Institute of Experimental Pharmacology and Toxicology

Center for Experimental Medicine

University Medical Center Hamburg-Eppendorf

Atrial Fibrillation Modelling and Targeted DNA Methylation Editing in Human Engineered Heart Tissue-Based Disease Models

---

Dissertation

Submitted to the Department of Chemistry

Faculty of Mathematics, Informatics, and Natural Sciences

University of Hamburg

For the degree of

Doctor of Natural Sciences

(Dr. rer. nat.)

By

PAN, BANGFEN

Hamburg, 2022

Reviewer 1: Prof. Dr. Elke Oetjen

Reviewer 2: Prof. Dr. Viacheslav Nikolaev

Disputation committee:

Prof. Dr. Elke Oetjen

Prof. Dr. Thomas Oertner

Prof. Dr. Friederike Cuello

Date of disputation: 07.10.2022

This dissertation was carried out at the Institute of Experimental Pharmacology and Toxicology, University Medical Center Hamburg-Eppendorf from November 2018 to August 2022.

Supervisor: Prof. Dr. Elke Oetjen

Co-supervisor: Prof. Dr. Thomas Eschenhagen

Practical supervisor: Dr. Dr. Justus Stenzig

I. List of publications

Publications:

Wu, D., Li, P.Y., **Pan, B.**, Tiang, Z., Dou, J., Williantarra, I., Pribowo, A.Y., Nurdiansyah, R., Foo, R.S.Y., and Wang, C. (2021). Genetic Admixture in the Culturally Unique Peranakan Chinese Population in Southeast Asia. Mol. Biol. Evol. 38, 4463–4474.

Pua, C.J.B., Tham, N., Chin, C.W.L., Walsh, R., Khor, C.C., Toepfer, C.N., Repetti, G.G., Garfinkel, A.C., Ewoldt, J.F., Cloonan, P.,…, **Pan, B.**, et al. (2020). Genetic studies of hypertrophic cardiomyopathy in singaporeans identify variants in TNNI3 and TNNT2 that are common in Chinese patients. Circ. Genomic Precis. Med. 424–434.

Tan, W.L.W., Anene-Nzelu, C.G., Wong, E., Lee, C.J.M., Tan, H.S., Tang, S.J., Perrin, A., Wu, K.X., Zheng, W., Ashburn, R.J., **Pan, B.**, et al. (2020). Epigenomes of human hearts reveal new genetic variants relevant for cardiac disease and phenotype. Circ. Res. 761–777.

Anene-Nzelu, C.G., Tan, W.L.W., Lee, C.J.M., Wenhao, Z., Perrin, A., Dashi, A., Tiang, Z., Autio, M.I., Lim, B., Wong, E., Tan, H.S., **Pan, B.**, et al. (2020). Assigning distal genomic enhancers to cardiac disease-causing genes. Circulation 910–912.

Congress abstracts:

Pan, B., Hansen, J., Stüdemann, T., Weinberger, F., Eschenhagen, T., Stenzig, J., A simple and flexible platform for optogenetic pacing in cardiac tissue engineering. XXIV World Congress International Society for Heart Research, 2022.

Pan, B., Ulmer, B.M., Shibamiya, A., Rössinger, J., Schweizer, M., Höppner, G., Stenzig, J., Eschenhagen, T., Effects of a sodium channel *SCN5A* mutation with associated proton leakage in 3-dimensional engineered heart tissue. 7th German Pharm-Tox Summit, 2022.

Pan, B., Hansen, J., Höppner, G., Stüdemann, T., Stoter, A.M.S., Christ, T., Lemoine, M.D., Foo, R.S.Y., Eschenhagen, T., Stenzig, J., Establishing an optogenetic *in vitro* model to study atrial fibrillation based on human engineered heart tissue. American Heart Association Scientific Sessions, 2021.

Pan, B., Werner, T.R., Löser, A., Braren, I., Höppner, G., Autio, M.I., Foo, R.S.Y., Hirt, M.N., Eschenhagen, T., Stenzig, J., Targeted DNA methylation manipulation in human engineered heart tissue. XXIII World Congress International Society for Heart Research, 2019.

II. Table of contents

III. List of abbreviations

2D	Two-dimensional
3D	Three-dimensional
4-AP	4-Aminopyridine

A

AAV	Adeno-associated virus
AAVS1	Adeno-associated virus integration site 1
ACTA2	Actin alpha 2
ACTN2	Actinin alpha 2
AF	Atrial fibrillation
ANP	Atrial natriuretic peptide
AP	Action potential
APA	Action potential amplitude
APC	Allophycocyanin
APD	Action potential duration
ATACseq	Assay for Transposase-Accessible Chromatin using sequencing
ATP2A2	ATPase sarco/endoplasmic reticulum Ca^{2+} transporting 2
AV	Atrioventricular

B

bFGF	Basic fibroblast growth factor
BMP4	Bone morphogenetic protein 4
BNP	Brain natriuretic peptide
bp	Base pair
BPM	Beats per minute
BSA	Bovine serum albumin
BTS	N-benzyl-p-toluenesulfonamide

C

$CaCl_2$	Calcium dichloride
CaMKII	Ca^{2+} calmodulin-dependent protein kinase type II
Cas9	CRISPR associated protein 9
CCh	Carbachol

ChIPseq	Chromatin immunoprecipitation sequencing
ChR	Channelrhodopsin
CNN1	Calponin 1
CM	Cardiomyocyte
CMV	Cytomegalovirus
COL1A1	Collagen type 1 alpha 1 chain
CRISPR	Clustered regularly interspaced short palindromic repeats
crRNA	CRISPR RNA
CTMV	Consulting Team Machine Vision
cTnT	Cardiac troponin T
Ctrl	Control
CV	Conduction velocity
CVD	Cardiovascular disease

D

DAD	Delayed afterdepolarization
DAPI	4',6-Diamidino-2-phenylindole
dCas9	Nuclease domain inactivated Cas9
DDR2	Discoidin domain receptor tyrosine kinase 2
DE	Differentially expressed
DMEM	Dulbecco's Modified Eagle Medium
DMSO	Dimethyl sulfoxide
DNA	Deoxyribonucleic acid
dNTP	Deoxynucleoside triphosphate
DPBS	Dulbecco's Phosphate Buffered Saline

E

EAD	Early afterdepolarization
EB	Embryoid body
E. coli	Escherichia coli
EC_{50}	Half maximal effective concentration
ECG	Electrocardiogram
ECM	Extracellular matrix
EDTA	Ethylenediaminetetraacetic acid

EF1α	Eukaryotic translation elongation factor 1 alpha 1
EGFP	Enhanced green fluorescent protein
EHT	Engineered heart tissue
ERP	Effective refractory period
ESC	Embryonic stem cell
ET-1	Endothelin-1
EYFP	Enhanced yellow fluorescent protein

F

F	Forward
FACS	Fluorescence-activated cell sorting
FCS	Fetal calf serum
FITC	Fluorescein isothiocyanate
FSC	Forward scatter
FSP-1	Fibroblast specific protein 1
FTDA	bFGF, TGF-β1, dorsomorphin and activin A-based hiPSC culture medium

G

g	Relative centrifugal force
GAPDH	Glyceraldehyde 3-phosphate dehydrogenase
gRNA	Guide RNA
GUSB	Glucuronidase beta

H

H&E	Hematoxylin and eosin staining
HAT	Histone acetyltransferase
HDAC	Histone deacetylase
HBSS	Hank's Balanced Salt Solution
HCl	Hydrochloric acid
HDFa	Primary adult human dermal fibroblasts
HEPES	4-(2-hydroxyethyl)-1-piperazineethanesulfonic acid
hESC	Human ESC
HF	Heart failure
hiPSC	Human induced pluripotent stem cell

HSA	Human serum albumin
Hz	Hertz

I

$I_{Ca,L}$	L-type calcium current
IEPT	Institute of Experimental Pharmacology and Toxicology
I_f	Pacemaker current
IF	Immunofluorescence
IHC	Immunohistochemistry
I_{K1}	Inward rectifier potassium current
$I_{K,ACh}$	Acetylcholine-activated potassium current
I_{Kr}	Rapid delayed rectifier potassium current
I_{Ks}	Slow delayed rectifier potassium current
I_{Kur}	Ultra-rapid delayed rectifier potassium current
I_{Na}	Sodium current
iPSC	Induced pluripotent stem cell
I_{ti}	Transient inward current
I_{to}	Transient outward current

K

kb	Kilobase
KCl	Potassium chloride
KCNA5	Potassium voltage-gated channel subfamily A member 5
KCNJ3	Potassium inwardly rectifying channel subfamily J member 3
KCNJ12	Potassium inwardly rectifying channel subfamily J member 12
kDa	Kilodalton
KLF4	Kruppel-like factor 4

L

LED	Light-emitting diode

M

M	Molar
µM	Micromolar

MgCl$_2$	Magnesium chloride
MHC	Myosin heavy chain
MLC2A	Myosin regulatory light chain 2, atrial isoform
MLC2V	Myosin regulatory light chain 2, ventricular/cardiac muscle isoform
mM	Millimolar
mN	Millinewton
MOI	Multiplicity of infection
mRNA	Messenger RNA
mW	Milliwatt
MYH	Myosin heavy chain

N

Na$_2$HPO$_4$	Disodium hydrogen phosphate
NaCl	Sodium chloride
NaHCO$_3$	Sodium hydrogen carbonate
ncRNA	Non-coding RNA
NGS	Next-generation sequencing
NPPA	Natriuretic peptide A
NPPB	Natriuretic peptide B

P

PAM	Protospacer adjacent motif
PCA	Principal component analysis
PCR	Polymerase chain reaction
PE	Phenylephrine
POSTN	Periostin
PS	Phase singularity

Q

qPCR	Quantitative real-time PCR

R

R	Reverse
RA	Retinoic acid

RNA	Ribonucleic acid
RNAseq	RNA sequencing
Rpm	Revolutions per minute
RPMI	Roswell Park Memorial Institute
RT	Relaxation time
RyR2	Ryanodine receptor 2

S

SA	Sinoatrial
SEM	Standard error of mean
SERCA2a	Sarco/endoplasmic reticulum Ca^{2+}-ATPase
SR	Sarcoplasmic reticulum
SSC	Sideward scatter
SSEA-3	Stage-specific embryonic antigen 3

T

TAE	Tris acetate EDTA
TET1	Ten-eleven translocation methylcytosine dioxygenase 1
TBS	Tris-buffered saline
tracrRNA	Trans-activating crRNA
TGF-β	Transforming growth factor beta
Tm	Melting temperature
TTP	Time to peak

U

U	Unit
UKE	University Medical Center Hamburg-Eppendorf
UTR	Untranslated region

V

V	Volt
v/v	Volume by volume
VChR1	*Volvox carteri* channelrhodopsin 1
VIM	Vimentin

W

W	Watt
WB	Western blot
WL	Wavelength
w/v	Weight by volume
WNT	Wingless-related integration site

1 Zusammenfassung

Vorhofflimmern (VHF) und Herzinsuffizienz sind weltweit für eine hohe und weiterhin steigende Morbidität und Mortalität verantwortlich. Trotz zahlreicher neuer therapeutischer Ansätze in den letzten Jahren sind die Behandlungserfolge weiterhin unbefriedigend. Viele Aspekte der Pathophysiologie des VHF sind noch immer sind noch immer nicht entschlüsselt, was teilweise einem Mangel an geeigneten Krankheitsmodellen geschuldet ist. Humanes künstliches Herzgewebe (*Engineered Heart Tissue*, EHT) aus Kardiomyozyten, die zuvor aus induzierten pluripotenten Stammzellen (hiPSC) differenziert werden, stellt ein mittlerweile sehr gut etabliertes Modell für die Krankheitsmodellierung und Arzneimittelerprobung (*drug testing*) dar. In dieser Arbeit sollten auf dem EHT beruhende Krankheitsmodelle für VHF und Herzinsuffizienz zunächst verfeinert und angepasst werden und dann dazu dienen, Strategien zur therapeutischen Manipulation von Chromatin-bezogenen Signalwegen, vor allem mit Bezug zur DNA-Methylierung, zu evaluieren.

Im ersten Abschnitt der Arbeit wurde ein Modell etabliert, in dem atriales EHT mittels optogenetischer Methoden für längere Zeit einer hohen Schlagfrequenz unterworfen wurde. Dieses einfache VHF-Modell wurde zunächst genau im Hinblick darauf, wie gut es Eigenschaften von VHF *in vitro* wiedergibt validiert. Im nächsten Schritt wurden erste Versuche unternommen, das Modell zu nutzen, um eine mögliche dynamische Regulation der Chromatinstruktur, allein durch eine Variation der Schlagfrequenz verursacht, mittels verschiedener Sequenzierverfahren zu untersuchen. Die optogenetische Erregbarkeit für ein *Pacemaking* mittels Lichtimpulsen wurde dadurch erreicht, dass eine ein Kanalrhodopsin (*volvox carteri* channelrhodopsin 1; VChR1, lichtsensitiver nicht-selektiver Kationenkanal) exprimierende hiPSC-Linie mittels CRISPR/Cas9-Genomeditierung hergestellt wurde. Die so entstandenen VChR1-iPSCs wurden dann mit einem optimierten, Embryoid-basierten Differenzierungsprotokoll zu atrialen Kardiomyozyten differenziert. Die atriale Spezifikation kam in diesem Protokoll durch eine Retinoat- (r*etinoic acid*, RA-) Behandlung und eine Veränderung der Konzentration der Wachstumsfaktoren Aktivin A und BMP4 zu Stande. In dieser Arbeit konnte erfolgreich gezeigt werden, dass die aus so differenzierten Zellen hergestellten RA-EHTs dem menschlichen Atrium in Bezug auf Transkription und Elektrophysiologie sehr nahekamen und vorherigen Versuchen zu atrialem EHT überlegen waren. Für die weiteren optogenetischen Versuche wurde im Rahmen dieser Arbeit eine flexible, digitalisierte optogenetische Schrittmacher-Plattform konstruiert. Im Folgenden wurden VChR1-RA-EHTs einem intermittierenden schnellen optogenetischen *Pacing* unterworfen, um einige der Effekte des VHF *in vitro* zu modellieren. Die dieser Intervention

unterzogenen EHTs zeigten eine niedrigere Kraft und eine höhere Freisetzung des Zellschaden-Markers Troponin I in das Zellkulturmedium als Kontrollen. Erste, vorläufige Ergebnisse aus Sequenziertechnologie-basierten Experimenten (RNA-Sequenzierung, ATAC-Seq, H3K27 ChIP-Seq) deuteten auf ein geändertes Genexpressionsmuster und eine geänderte Chromatinstruktur mit einer Rarefizierung von Regionen offenen Chromatins hin. Zusammenfassend konnten in diesem optimierten atrialen EHT-Modell einige Aspekte der Pathophysiologie von VHF rekapituliert werden und Hinweise auf neue Muster der Chromatindynamik bei VHF gefunden werden. Darüber hinaus kann das Modell als Grundlage für zukünftige Experimente dienen.

In einem zweiten Teil der Arbeit wurde die gezielte und Sequenz-spezifische Manipulation der DNA-Methylierung im EHT-basierten Krankheitsmodell untersucht. Die Korrektur pathologischer Genexpression mittels Beeinflussung der DNA-Methylierung könnte in Zukunft neue Therapiemöglichkeiten eröffnen, da mit diesem Verfahren Regulationsmechanismen in Angriff genommen werden können, deren Beeinflussung mit konventionellen Arzneistoffen bisher unmöglich war. Darüber hinaus könnte sich eine therapeutische Ansprache von pathologischer Transkription direkt am Ursprungsort als günstig in Bezug auf unerwünschte Nebenwirkungen und den zeitlichen Verlauf des Interventionseffektes erweisen. In diesem Teil der Arbeit wurden zwei weitere auf dem EHT beruhende Krankheitsmodelle optimiert und adaptiert. Zum einen wurden kardiale Fibroblasten aus hiPSC differenziert und dem gut etablierten ventrikulären EHT hinzugefügt, um Fibroblasten-haltiges CF-EHT als mögliches Fibrose-Modell herzustellen. Zum anderen wurde ein auf dem EHT beruhendes Modell der pathologischen kardialen Hypertrophie adaptiert, bei dem EHTs für 7 Tage mit den pro-hypertrophen Substanzen Phenylephrin und Endothelin-1 behandelt wurden. Zur gezielten, Sequenz-spezifischen Manipulation der DNA-Methylierung wurde eine nicht funktionale Defektvariante der Nuklease Cas9, dCas9, zusammen mit mehreren, die Zielsequenz bestimmenden guide-RNAs verwendet, bei der die defekte Nuklease mit DNA-Methylierung verändernden Enzymen fusioniert war. Es kamen DNMT3A und TET1 zur forcierten Methylierung beziehungsweise Demethylierung zum Einsatz. Diese Epigenom-Editierungswerkzeuge sollten mittels Transfer mit adeno-assoziierten Virus-Vektoren in die Kardiomyozyten beziehungsweise Fibroblasten transduziert werden. Da die Sequenz-Transportkapazität von AAV-Vektoren limitiert ist, wurden die dCas9-Fusionsgene in diesem Projekt geteilt und mit Intein-Sequenzen kombiniert, die eine Fusion der beiden Teile auf Protein-Ebene ermöglichen. Diese Strategie konnte zunächst erfolgreich in HEK293-Zellen validiert werden, wo eine Transfektion der codierenden Regionen der beiden Teile zur Expression und Fusion eines vollständigen dCas9-DNMT3A-Fusionskonstrukts führte. Dieses war außerdem

zusammen mit geeigneten guide-RNAs in der Lage, als Test-Sequenz die Promotor-Region des Gens IL6ST zu methylieren. In einem nächsten Schritt konnte nach AAV-mediiertem Gentransfer in HEK293-Zellen und hiPSC-Fibroblasten ebenfalls das dCas9-DNMT3A-Fusionskonstrukt nachgewiesen werden. Allerdings konnte hier keine nennenswerte Expressionsregulation von Zielgenen nachgewiesen werden. Der bisher ausbleibende Erfolg der Strategie beruht mutmaßlich auf einer in jedem Schritt (Transduktion, Fusion, Auffindung der Zielstruktur, Methylierung, Repression) unvollständigen Effizienz und hohen Variabilität. Weitere Optimierung der Transduktion, der Zielsequenz und der guide-RNAs wäre nötig, um dieses Problem auszuräumen. Dennoch konnten auch in diesem Teil der Arbeit zumindest wertvolle Modelle und Werkzeuge weiterentwickelt werden.

2 Summary

Atrial fibrillation (AF) and heart failure (HF) are significant contributors to morbidity and mortality worldwide. Effective treatments for these heart diseases are still limited. Furthermore, many aspects of AF pathophysiology remain incompletely understood due to a lack of suitable models. Human engineered heart tissue (EHT) derived from human induced pluripotent stem cells (hiPSCs) has proven its value as an in vitro model for disease modelling and exploration of novel therapeutic strategies. Thus, we set out to establish and refine models for AF and HF based on human EHT for both assessment and manipulation of chromatin-based signaling.

In the first part of this work, a chronic optical tachypacing model based on atrial-like EHT was established and the effects of tachypacing were evaluated, both with regard to model validation and beyond, probing chromatin signaling. To allow optical pacing, a channelrhodopsin (*volvox carteri* channelrhodopsin 1; VChR1) expressing hiPSC line was generated by inserting the transgene into the AAVS1 locus with CRISPR/Cas9 genome editing. VChR1-iPSCs were then differentiated into atrial-like cardiomyocytes (CMs) using an optimized embryoid body (EB)-based protocol involving retinoic acid (RA) treatment combined with reduced concentrations of activin A and BMP4. We demonstrated that RA-EHTs resembled the human atrium transcriptionally and electrophysiologically, especially compared to previous attempts of atrial tissue engineering. Next, a flexible digital optogenetic device was built for long-term optical stimulation. VChR1-RA-EHTs were then intermittently optically tachypaced to model AF. Paced EHTs displayed impaired contractile force and released more cardiac troponin I into the culture medium than unpaced EHTs. First results from next-generation sequencing (NGS) revealed altered gene expression and loss of chromatin accessibility in paced versus unpaced EHTs. In summary, our tachypaced atrial-like EHT model partially recapitulated AF pathophysiology, provided new insights into chromatin dynamics in AF and could be used to test new potential therapies.

In the second part, targeted DNA methylation editing in EHT disease models was investigated. Harnessing DNA methylation for therapy could open up new opportunities, as pathways previously considered not druggable could be addressed, targeting the root of the problem could prove favorable in terms of side effects, and the kinetics of the intervention could be especially suitable. To this end, besides the AF model mentioned above, two other disease EHT models of HF were generated or adapted in this study. Cardiac fibroblasts (CFs) were differentiated from hiPSCs and added into ventricular-like EHTs to produce fibroblast-EHTs (CF-EHTs) for fibrosis modelling. Meanwhile, a pro-hypertrophic EHT model was adapted with the treatment of ventricular-like EHTs with phenylephrine (PE) and endothelin-1 (ET-1) for 7 days. In order to

manipulate DNA methylation, split-dCas9-DNMT3A and split-dCas9-TET1 were created for methylation and demethylation of specific genes, respectively. These editing tools were designed for adeno-associated virus (AAV)-mediated delivery. To this end, dCas9 was split into dCas9N and dCas9C and fused with protein inteins in order to circumvent problems arising from a limited AAV packaging capacity. In an activity test in HEK 293 cells, transfection of split-dCas9-DNMT3A plasmids led to expression and fusion of full-length dCas9 and methylation of the targeted promoter region of *IL6ST*. Full-length dCas9-DNMT3A protein was also detected in both HEK 293 cells and CFs after plasmids co-transfection or AAV co-transduction. However, no regulation of expression could be detected for genes targeted by AAV in CFs, likely because the absolute effect was small and masked by variability. Taken together, in the second part of this thesis, we successfully adapted and optimized two further EHT-based models and established split-dCas9 targeted DNA methylation editing tools. However, optimization of the editing tools is still needed to achieve meaningful DNA methylation editing in CFs or CMs in EHTs by AAV delivery in the future.

3   Introduction

3.1   Cardiovascular diseases: atrial fibrillation and heart failure

Cardiovascular diseases (CVDs) are the leading cause of mortality worldwide, resulting in approximate 17.9 million deaths each year (World Health Organization, 2021). Moreover, they cause a large global disease burden. The total number of CVD cases in the world has almost doubled from 271 million in 1990 to 523 million in 2019 (Roth et al. 2020). In general, CVDs are a group of diseases affecting the heart and blood vessels. There are many types of CVDs involving the heart, including coronary heart disease, cardiac arrhythmia, HF, heart valve disease and other conditions. The focus of the present study was modelling heart diseases in vitro to better understand the pathophysiological processes and search for new potential therapies.

3.1.1   Atrial fibrillation

AF stands out as the most prevalent sustained cardiac arrhythmia. It is a significant contributor to global morbidity and mortality, associated with an elevated risk of thromboembolism, stroke, myocardial infarction, HF and other secondary diseases (Kannel et al. 1998; Piccini et al. 2012; Andrade et al. 2014). According to the Global Burden of Disease 2019 Study, the worldwide prevalence of AF and atrial flutter was 59.7 million cases in 2019, which doubled the number in 1990 (Kornej et al. 2021; Roth et al. 2020). AF risk correlates with various risk factors and traits, including age, sex, genetic factors, cardiovascular and non-cardiovascular disorders (January et al. 2014; Mahida 2014; Morin et al. 2016).

In the normal heart rhythm (figure 1 A), the regular electrical signals are initiated from spontaneous firing of the sinoatrial (SA) node and propagate through the heart, causing cardiac contraction. In the electrocardiogram (ECG), the atrial and ventricular activation are denoted by P waves and QRS complexes, respectively. However, in AF (figure 1 B), abnormal electrical impulses start from some locations (mainly pulmonary veins) other than the SA node, causing rapid and uncoordinated atrial activation with ineffective atrial contraction. Consequently, the ventricles respond with fast and irregular activities and weaker contraction. The ECG displays the absence of P waves and irregular QRS complexes (Wakili et al. 2011; January et al. 2014; Lip et al. 2016). Clinically, with regards to the episode duration, AF can be classified as: paroxysmal AF (terminates within 7 days), persistent AF (lasts more than 7 days), long-standing persistent AF

(lasts more than 1 year) and permanent AF (does not convert to normal sinus rhythm; Iwasaki et al. 2011; January et al. 2014; Kirchhof et al. 2016).
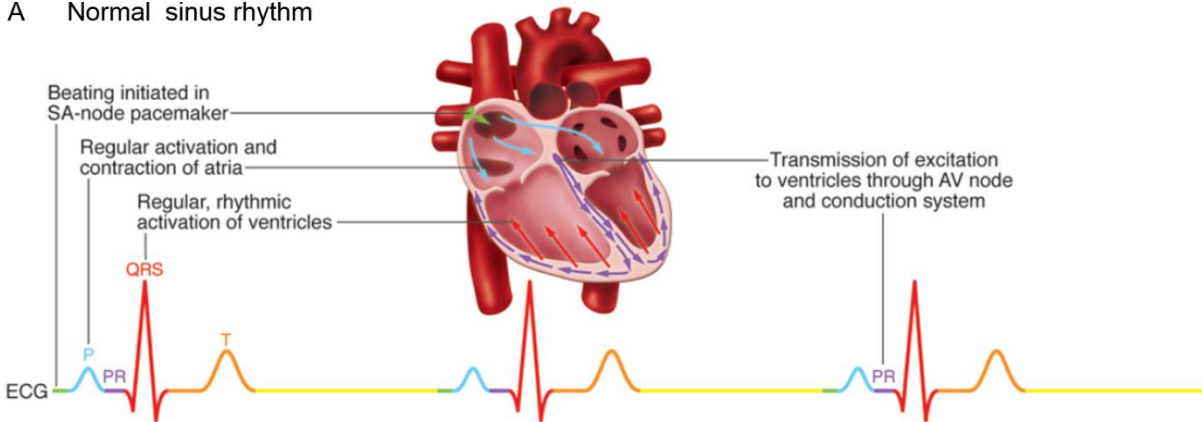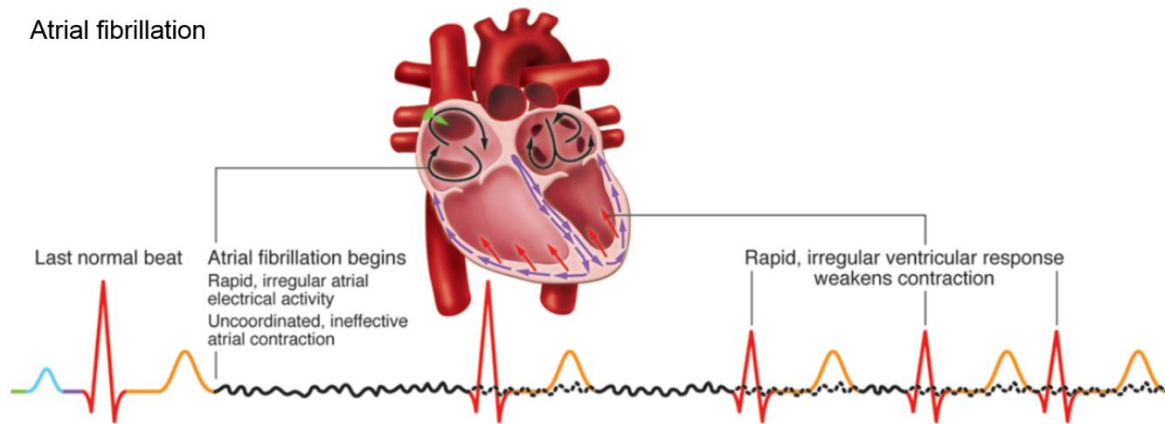
Figure 1: Schematic overview of the regular heart rhythm and atrial fibrillation. (A) Normal sinus rhythm. The electrical signals originate from the SA node pacemaker, travel through the atria and reach the ventricles via the atrioventricular (AV) node and the His-Purkinje conducting system. In the ECG, P waves indicate atrial activation, and QRS complexes correspond with ventricular activation. (B) Atrial fibrillation. Asynchronous impulses fire in the atria and cause ineffective atrial contraction. The distinct P waves are replaced by wavering lines. The ventricles display rapid and irregular electrical activity with weaker contraction. QRS complexes are irregular (adapted from Wakili et al. 2011).

3.1.2   AF mechanisms and atrial remodelling

A comprehensive understanding of AF mechanisms and pathophysiology is crucial in searching for potential therapies. The underlying mechanisms and pathophysiological processes are diverse. Over the past decades, many studies have shown that mechanisms to maintain the rapid and irregular rhythm of AF involve focal ectopic activity, single-circuit re-entry and multiple-circuit re-entry in the atria (Allessie et al. 1977; Nattel 2002; Comtois et al. 2005; Wakili et al. 2011; Nattel et al. 2020). Focal ectopic activity is likely caused by enhanced automaticity, delayed afterdepolarizations (DADs) and early afterdepolarizations (EADs). In normal sinus rhythm, the atrial action potential (AP; figure 2) is initiated through voltage-gated Na^+ channels, which produce the depolarizing Na^+ inward current (I_{Na}) and are responsible for the AP upstroke. The rapid depolarization is followed by an early fast repolarization phase, caused by the transient-outward K^+ current (I_{to}), and a plateau phase, maintained by the activation of inward L-type Ca^{2+} current ($I_{Ca,L}$). A series of time-dependent delayed-rectifier K^+ currents are involved in AP repolarization: the slow delayed-rectifier K^+ current (I_{Ks}), rapid delayed-rectifier K^+ current (I_{kr}), and ultrarapid delayed-rectifier K^+ current (I_{Kur}). The large background and acetylcholine-dependent inward-rectifier K^+ currents (I_{K1} and $I_{K,ACh}$), which overwhelm the inward pacemaker current (I_f; which also exists in atrial CMs other than the SA node), control final AP repolarization and maintain the resting membrane potential (RMP). However, enhanced automaticity, caused by decreased inward-rectifier K^+ currents and/or enhanced I_f, can accelerate the rate of spontaneous diastolic depolarization to reach threshold potential and result in focal ectopic firing (Iwasaki et al. 2011; figure 3A). EADs are abnormal cell membrane depolarizations preceding full repolarization (figure 3A). They can result from reactivation of the inward current $I_{Ca,L}$ during prolonged AP duration (APD) caused by loss of repolarizing K^+ currents or excessive late Na^+ current (Song et al. 2008; Nattel and Dobrev 2016). Conversely, DADs happen after the completion of AP repolarization and trigger new APs (figure 3A). They can arise from abnormal diastolic Ca^{2+} leakage from sarcoplasmic reticulum (SR) through a SR Ca^{2+} release channel, the ryanodine receptor 2 (RyR2; Wakili et al. 2011). The resulting excessive cytoplasmic Ca^{2+} activates the Na^+/Ca^{2+} exchanger (NCX) on the plasma membrane, with 3 Na^+ entering the cell for 1 Ca^{2+} extruded, subsequently creating a transient inward current (I_{ti}), leading to depolarization and the generation of an AP.
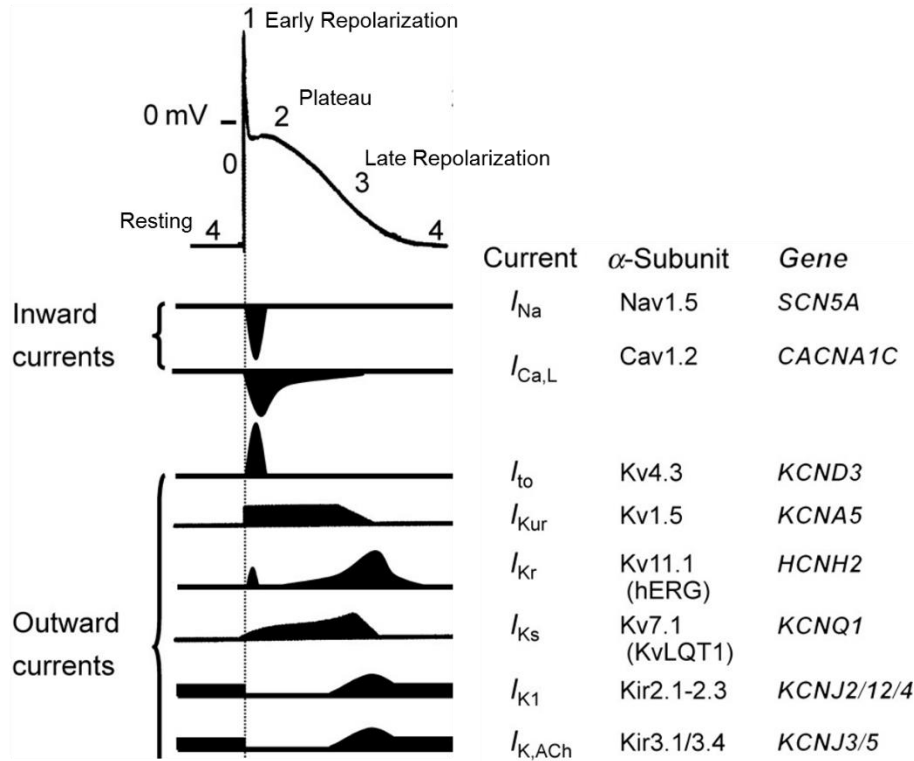
Figure 2: Atrial action potential in normal sinus rhythm. The principal transmembrane ionic inward and outward currents are listed (adapted from Jost et al. 2021).

Re-entry can be responsible for AF maintenance. It refers to continuous and repetitive AP propagation in a circular manner with or without anatomic obstacles. Re-entry requires an initial trigger and a vulnerable atrial substrate, and its maintenance depends on effective refractory period (ERP) and conduction velocity (CV) of the tissue. ERP is closely related to APD, and CV is determined by the function of ion channels and connexins. There are two main conceptual models of re-entry: the leading circle model and the spiral wave model (Waks and Josephson 2014). In the leading circle model (Allessie et al. 1977; Comtois et al. 2005), the electrical impulse travels in the smallest possible circuit that can maintain re-entry (figure 3B). The center of the re-entry zone is refractory and unexcitable by centripetally moving impulses. The impulse in the leading edge excites tissue as soon as excitation is possible. The circuit length (wavelength, WL) refers to the distance travelled by the electrical impulse in one ERP, which is the product of ERP and CV. The stability of AF depends on the number of simultaneous re-entry circuits that can be accommodated in the atria. Enlarged atria size, shortened ERP and reduced CV favor re-entry and perpetuate AF. The spiral wave model is a more complex and biophysical concept (Comtois et al. 2005; Pandit and Jalife 2013; Nattel et al. 2017). In this model, the curved wavefront revolves

around an excitable yet unexcited core and meets the wavetail at a focal point called phase singularity (PS), where the curvature of the wavefront is highest (figure 3B). The APD and CV are inversely proportional to the curvature of the wavefront. The reduced APD around the core can stabilize the spiral wave. The circuit in the leading circle model remains fixed at a location, while the spiral wave can move through space.
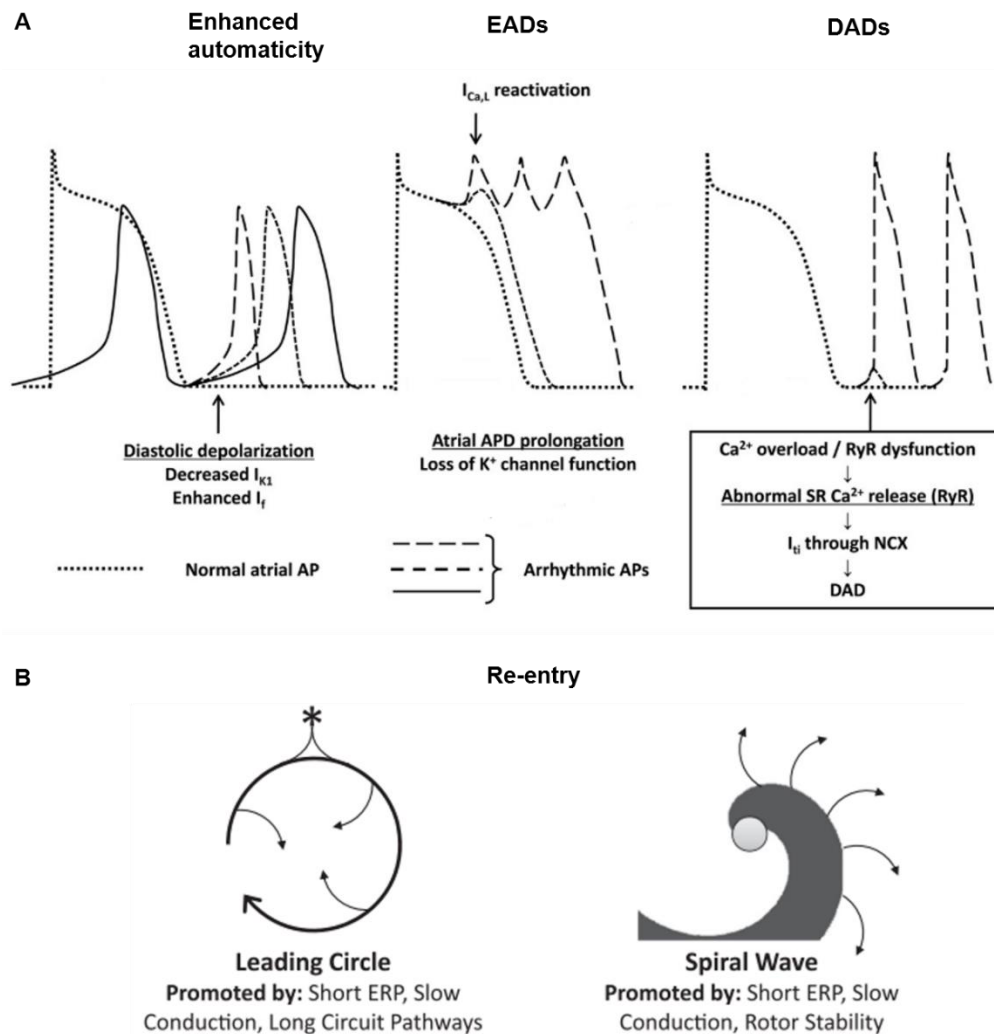
Figure 3: Overview of mechanisms of atrial fibrillation. (A) Focal ectopic activity. (B) Re-entry (adapted from Iwasaki et al. 2011 and Heijman et al. 2014).

The initiation and perpetuation of AF require atrial remodelling, for example, creating an AF-prone substrate for ectopic activity or re-entry. Moreover, pathophysiological remodelling of atrial tissue can arise from AF itself or other heart diseases. Alterations of electrophysiological properties in AF are referred to as electrical remodelling, involving changes in various ion channels. These

changes contribute to shortened atrial APD and refractoriness, and eventually stabilize re-entry and favor AF vulnerability. They mainly include downregulation of inward $I_{Ca,L}$ and transient outward I_{to}, upregulation of inward-rectifier K$^+$ current I_{k1} and activation of acetylcholine-dependent K$^+$ current $I_{K,ACh}$ (Allessie et al. 2002; Karle et al. 2002; Dobrev et al. 2005; Qi et al. 2008; Wakili et al. 2011). Abnormal calcium handling and resulting DADs can additionally cause ectopic firing (Nattel and Dobrev 2012). The abnormal Ca^{2+} release from the SR can be due to specific triggers in some conditions, such as SR Ca^{2+} overload and RyR2 dysfunction (hyperphosphorylation or mutation). In AF patients, it was observed that Ca^{2+} calmodulin-dependent protein kinase type II (CaMKII) was more activated than in control subjects, and RyR2 was more phosphorylated (Vest et al. 2005; Neef et al. 2010). AF moreover changes the expression or distribution of connexins, causing impulse conduction abnormalities, and in turn promotes re-entry (Wakili et al. 2011; Kato et al. 2012).

Structural remodelling is another major determinant and consequence of AF, referring to changes in atrial tissue properties, size and intracellular ultrastructure. Atrial fibrosis is a prominent feature of structural remodelling, resulting from aberrant activation, proliferation and differentiation of cardiac fibroblasts with the consequence of excessive production of extracellular matrix (ECM) components, particularly collagen (Polyakova et al. 2008; Yue et al. 2011; Gasparovic et al. 2014). Fibrosis provides physical barriers among atrial CMs, interrupts muscle bundle continuity, and disturbs impulse conduction. Heterogeneous fibroblast-cardiomyocyte coupling can also alter cardiac electrophysiological properties (Yue et al. 2011). Taken together, atrial fibrosis serves as a substrate of AF vulnerability and promotes ectopic activity or re-entry. As mentioned before, enlargement of the atria is one of the pivotal determinants of AF, increasing the likelihood of re-entry circuits and maintaining re-entry. The intracellular remodelling of atrial CMs comprises myolysis, glycogen deposition, mitochondrial disruption and redistribution, SR alterations, and nuclear chromatin remodelling (Kostin et al. 2002; Allessie et al. 2002). Moreover, atrial CMs from AF patients were found to display signs of apoptotic signaling (Aimé-Sempé et al. 1999; Gasparovic et al. 2014).

Atrial remodelling is multifaceted and associated with the time course of AF development. However, changes in the atria and underlying mechanisms remain incompletely elucidated. The factors that cause atrial remodelling are manifold and comprise intracellular Ca^{2+} overload and subsequent cell signaling pathways, gene expression changes, microRNAs, neurohumoral factors, oxidative stress, inflammation and atrial stretching (Lee 2013; Youn et al. 2013; Nattel

and Harada 2014). A detailed understanding of atrial remodelling contributes to developing therapeutic approaches and improving clinical management.

3.1.3 AF models

Since human samples are not readily accessible, modelling AF in model systems can facilitate the understanding of AF mechanisms and validate potential therapies in the experimental setting. Over the past decades, plenty of in vitro and in vivo models have been established. Despite the fact that human AF is heterogeneous and multifactorial, these models can recapitulate some aspects of the pathophysiological characteristics of human AF and significantly contribute to our knowledge of AF. Commonly used AF models involve small animals (mouse, rat, guinea pig, rabbit), large animals (goat, dog, sheep, pig and horse), and human stem cell-derived CMs.

AF is not as prevalent in animals as it is in humans. Animal AF models from different species vary widely in terms of duration of AF, ion channel expression and AP properties (Schüttler et al. 2020). The methods to induce AF in animal models include rapid atrial pacing, mitral regurgitation and intrapericardial methylcholine infusion (Morillo et al. 1995; Li et al. 1999; Benser et al. 2001; Verheule et al. 2003). For example, Morillo and colleagues performed continuous rapid atrial pacing at 400 beats per minute (bpm) for 6 weeks in dogs and induced sustained AF with shortened ERP (Morillo et al. 1995). Another group showed that right atrial pacing at 400 bpm for 1 week in a congestive HF dog model caused interstitial fibrosis to promote sustained AF (Li et al. 1999). In addition, with the development of genetic manipulation, many genetically modified mouse models were created to elucidate the roles of specific genes or non-coding regions in AF (Schüttler et al. 2020). However, using animal models provokes concerns in terms of cost and ethical considerations. Moreover, there are physiological and genetic differences between atrial CMs of animal origin and human atrial CMs, including channel expression, structural differences, baseline frequency and many others. Animal models cannot fully represent human AF and their translational value is limited.

HiPSCs and human embryonic stem cells (hESCs) provide great potential to study AF in a human-based physiologically relevant system. Patient-specific iPSC incorporating genome editing can provide the exact genetic background to study underlying mechanisms and AF-related mutations (Benzoni et al. 2020; Hong et al. 2021). Over the last years, atrial-like CMs and tissues derived from hiPSC or hESC have been established and emerged as AF models (Devalla et al. 2015; Lee et al. 2017; Laksman et al. 2017; Lemme et al. 2018). Rapid pacing has also been applied to

hiPSC-derived engineered heart tissues (EHTs) for arrhythmia modelling. Laksman and colleagues generated multicellular sheets with atrial-like CMs derived from hESC and induced re-entrant spiral wave geometries by rapid external pacing (Laksman et al. 2017). In our institute, Lemme and colleagues initially performed chronic intermittent tachypacing on ventricular-like EHTs derived from hiPSC and induced robust arrhythmia vulnerability to tachycardia in EHTs (Lemme et al. 2020). They then attempted to tachypace atrial-like EHTs and induced only limited electrical remodelling (Lemoine et al. 2020). In this regard, with further optimization, tachypacing on atrial-like EHTs is suggested allowing for several promising ways to model AF in EHT in future.

3.1.4   Heart failure and cardiac hypertrophy

HF is a clinical syndrome characterized by impaired cardiac function, in which the heart is unable to pump enough blood to sufficiently supply the body with oxygen and nutrients. It is a global pandemic with an increasing prevalence, affecting more than 64 million people (1%-3% in the adult population) and again resulting in great health and economic burden worldwide (Lippi and Sanchis-Gomar 2020; Bragazzi et al. 2021). There are a variety of cardiac conditions contributing to the development of this clinical syndrome, including ischaemic heart disease, hypertensive heart disease, valvular and rheumatic heart disease, cardiac arrhythmia, cardiomyopathy, congenital heart disease and other disease conditions (Ponikowski et al. 2016; Savarese et al. 2022). The symptoms and signs of HF result from structural and/or functional cardiac abnormalities (McDonagh et al. 2021). Under some of the above pathological conditions, cardiac hypertrophy occurs initially and often subsequently predisposes to the development of HF with either preserved or reduced ejection fraction. Therefore, cardiac hypertrophy modelling provides a useful platform for investigating new therapies for HF.

In general, there are two types of cardiac hypertrophy: physiological hypertrophy and pathological hypertrophy (reviewed in Nakamura and Sadoshima 2018). The former usually occurs during postnatal growth, pregnancy or physical training, represents an adaptive response to physiological stimuli and is reversible (except for postnatal growth). It is identified by a mild increase in ventricular volume and wall thickness with CM growth in both width and length, showing a preserved or enhanced pump function. In contrast, pathological hypertrophy is initially a compensatory response and marked by a reduction in ventricular chamber dimensions and an increase in wall thickness, with CM growth in width more than in length. It can further progress to

a maladaptive cardiac remodelling process, with dilatation of ventricular chamber, lengthening of CMs and impaired contractile function.

The progression of pathological hypertrophy is usually associated with several processes: reactivation of fetal gene expression, alterations of Ca^{2+} handling, mitochondrial dysfunction, metabolic reprogramming, altered sarcomere structure, myocardial fibrosis and cell death. Increased expression of fetal genes is one of the classical features of pathological hypertrophy. Typically regulated genes include natriuretic peptide A (*NPPA*), natriuretic peptide B (*NPPB*) and skeletal α-actin (Bernardo et al. 2010). Moreover, alterations in contractile proteins α- and β-myosin heavy chain (α- and β-MHC) result in an increased ratio of β-MHC/α-MHC, affecting cardiac contractility (Locher et al. 2011). Dysregulation of Ca^{2+} handling proteins and Ca^{2+} mediated signaling was observed during pathological hypertrophy. Of note, the expression level of the sarco/endoplasmic reticulum calcium-ATPase (SERCA2a), which mediates Ca^{2+} uptake into the SR, is regularly decreased, resulting in impaired Ca^{2+} cycling and contributing to contractile dysfunction (Hasenfuss et al. 1994; Meyer et al. 1995; Huang et al. 2014).

3.1.5 Heart failure and cardiac fibrosis

Cardiac fibrosis is a hallmark of both AF and HF and is characterized by excessive deposition of ECM proteins. Pathological hypertrophy is usually accompanied by the development of interstitial and perivascular fibrosis, with disproportionate collagen accumulation and myofibroblast activation (Nakamura and Sadoshima 2018). Increased collagen deposition stiffens the cardiac walls, perturbing systolic and diastolic function, and contributes to HF. In the normal heart, CFs are the predominant non-myocytes surrounding CMs. They are the main ECM-producing cells, play an important role in ECM protein homeostasis, and contribute to cardiac development, structure and function (Camelliti et al. 2005). Common morphological features are flatness, spindle-shape without a basement membrane, and abundant cytoplasmic granular material with extensive rough endoplasmic reticulum and a large Golgi apparatus (Camelliti et al. 2005). Due to the lack of a unique specific maker of CFs, they are usually identified by showing the expression of a set of cell surface markers or ECM proteins, for example, collagen, fibroblast specific protein (FSP-1), discoidin domain receptor 2 (DDR2), calponin 1 (CNN1), periostin (POSTN) and vimentin (VIM; Lajiness and Conway 2014). When exposed to some pathophysiologic stimuli, activated CFs can convert to myofibroblasts, which are the predominant matrix-producing cell type in the fibrotic heart. Various cells and molecules are involved in the process of cardiac fibrosis.

For instance, macrophages, mast cells, lymphocytes and endothelial cells can secrete a variety of fibrogenic mediators, including growth factors and matricellular proteins (Xia et al. 2009; Frangogiannis 2012; Carlson et al. 2017). Transforming growth factor β (TGF-β) is a major fibrogenic growth factor which induces CF activation and suppresses ECM degradation (Leask 2007). Thus, many properties of fibroblasts are known, which may become therapeutic targets in HF, and which may be modified in an epigenetic manner. In clinical trials, renin-angiotensin-system (RAS) inhibitors, TGF-β inhibitors and endothelin inhibitors have shown some efficacy in different diseases, yet to a limited extent (reviewed in Fang et al. 2017). Only RAS inhibitors are approved HF therapeutics. New potential strategies are thus needed to further improve the anti-fibrotic outcome. Epigenetic regulation of target genes, such as extracellular matrix proteins, could be a new direction.

3.2   Epigenetics and heart disease

Epigenetics studies heritable changes that affect gene expression regulation without altering the DNA sequence. Over the past few years, the advances in NGS have substantially improved our knowledge of epigenetics as a key regulator in cardiac development and disease. Epigenetic regulation is generally carried out by DNA methylation, post-translational modifications of histones, plasticity of chromatin structural organization, and regulatory non-coding RNAs (ncRNAs; Zhou et al. 2019).

DNA methylation is a process by which a methyl group is added to the C5 position of cytosine, mainly at CpG islands. In mammalian cells, this process is catalysed by DNA methyltransferases (DNMTs), among which DNMT1 is responsible for the maintenance of DNA methylation during cell division and DNA repair, while DNMT3A and DNMT3B are responsible for de novo methylation of previously non-methylated DNA (Okano et al. 1999). Reversely, the removal of the methyl group (demethylation) is conducted by ten-eleven translocation enzymes (TET1, TET2 and TET3; Ito et al. 2011). Often, methylation in a promoter region causes gene silencing by preventing transcription factor binding or mediating chromatin remodelling (Jones 2012). Two pioneering genome-wide cardiac DNA methylation studies have revealed differential DNA methylation signatures in failing human hearts compared with healthy human hearts (Movassagh et al. 2011; Haas et al. 2013). Moreover, in an epigenome-wide association study, significant changes in DNA methylation were identified in 59 CpG regions in the myocardium of patients with dilated cardiomyopathy compared to controls (Meder et al. 2017). More recently, Glezeva et al.

found 195 unique differentially methylated regions in cardiac tissue of heart failure patients by targeted DNA methylation sequencing, and validated them according to expression alterations of underlying genes/ncRNAs (Glezeva et al. 2019). Differential methylation of CpG sites was also associated with prevalent AF (Lin et al. 2017). Meanwhile, manipulation of DNA methylation in cardiac disease models has been attempted. Treatment with the non-specific, nucleosidic DNMT inhibitor 5-aza-2'-deoxycytidine was shown to reverse norepinephrine-induced cardiac hypertrophy in rats (Xiao et al. 2014). Stenzig and colleagues observed protective effects in rats that underwent transverse aortic constriction and were treated with the non-nucleosodic DNMT inhibitor RG108, and identified lower global DNA methylation in CMs (Stenzig et al. 2018). Moreover, in a recent study, knock-out of the gene encoding the DNA methyltransferase DNMT3A prevented functional impairment resulting from a pro-hypertrophic intervention in human EHT (Madsen et al. 2021). Taken together, manipulation of DNA methylation could be a therapeutic strategy in heart disease.

Chromatin is a complex of genomic DNA and proteins in the eukaryotic nucleus, which is formed by repeating units, the nucleosomes. Each nucleosome consists of about 145-147 base pairs of DNA wrapped around a histone octamer (two copies of each of the histone proteins H2A, H2B, H3 and H4). Histone modifications can regulate gene expression in response to upstream signaling pathways. To date, the known modifications include acetylation (ac) of lysine (K) residues, methylation (me) of lysine and arginine (R) residues, phosphorylation of serine (S) and threonine (T) residues, ubiquitylation and sumoylation (Peterson and Laniel 2004). They can modulate DNA accessibility to both regulatory cis-elements and trans-factors. Among these modifications, histone acetylation generally leads to transcription activation, while hypoacetylation mediates transcription repression. For instance, H3K27ac indicates acetylation of the lysine residue at N-terminal position 27 of the histone H3 and is associated with transcription activation. Therefore, it is defined as an active enhancer or promoter mark. The processes of acetylation and deacetylation are controlled by histone acetyltransferases (HAT) and deacetylases (HDAC), respectively (Lee and Workman 2007). Besides modifications of DNA and histones, epigenetic regulation additionally comprises any changes in 3-dimensional chromatin structure. For example, chromatin looping mediated by the DNA binding factor CTCF facilitates the interactions among distal cis-elements, a process that can also be considered epigenetic (Lee et al. 2019). Recently, NGS technologies combined with chromatin immunoprecipitation assay (ChIPseq), assay for transposase accessible chromatin (ATACseq) and chromosome conformation capture

technologies have been widely used to decipher chromatin dynamics (Bardet et al. 2011; de Wit and de Laat 2012; Buenrostro et al. 2015).

Histone modifications were shown to be associated with pathogenic gene expression regulation in heart diseases. For example, the effects of histone deacetylase inhibition have been investigated. The HDAC inhibitor, trichostatin A, reduced atrial fibrosis and arrhythmias in a mouse model of cardiac hypertrophy (Liu et al. 2008). The HDAC6 inhibitor tubastatin A treatment protected the atria from electric remodelling in an atrial tachypacing dog model (Zhang et al. 2014). Another HDAC inhibitor, valproic acid, attenuated atrial remodelling in transgenic mice (Scholz et al. 2019). In addition, a genome-wide association study (GWAS) of 60,620 AF patients and 970,216 controls identified AF-associated risk variants, and further elucidated some of them to correlate with active enhancer sequences, as indicated by histone acetylation H3K27ac, in the right atrium (Nielsen et al. 2018). Another study discovered that the histone-lysine N-methyltransferase enzyme and H3K27me3 were upregulated in chronic AF patients with atrial fibrosis (Song et al. 2019). However, the understanding of other aspects of chromatin remodelling in heart diseases, especially in AF, is still lacking.

Recently, regulatory ncRNAs have emerged as important epigenetic regulators, such as microRNAs (miRNA) and long ncRNAs (lncRNAs). MiRNAs are a group of small non-coding RNAs that regulate gene expression by translational repression and/or by mediating degradation of their target mRNAs. LncRNAs (longer than 200 nucleotides) govern gene expression by interacting with chromatin regulators, or interfering with miRNA pathways (Fatica and Bozzoni 2013). Over the last years, a number of ncRNAs have been identified to be involved in myocardial remodelling and pathophysiology.

3.3   Human induced pluripotent stem cells

Due to the limited availability of human primary cells and the suboptimal translational value of animal models in recapitulating the pathophysiology of complex diseases, the discovery of human iPSCs, reprogrammed from somatic cells, has revolutionized the field of human disease research. In 2007, Yamanaka and colleagues generated hiPSCs from human dermal fibroblasts by retroviral transduction of only four transcription factors (Oct3/4, Sox2, Klf4 and c-Myc; Takahashi et al. 2007). Subsequently, genome integration-free delivery of these reprogramming factors by Sendai virus was developed, in order to replace retroviral delivery (Fusaki et al. 2009). Human iPSCs resemble human ESCs in many aspects: morphology, growth properties, marker genes, and the

potential to differentiate into all cell types of the three germ layers (endoderm, mesoderm and ectoderm; Takahashi et al. 2007). Combined with genome engineering technology, nowadays, hiPSCs are widely utilized from basic research to clinical applications. For example, patient-specific or genetically modified hiPSC lines can be used for disease modelling, drug development or precision medicine.

3.3.1 Cardiac differentiation

Given the differentiation potential of hiPSCs to derivatives of all three germ layers *in vitro*, various protocols have been established and improved to differentiate hiPSCs into desired cardiac lineages over the last decade. This provides unprecedented opportunities for cardiovascular research and therapies. In general, for cardiac differentiation, specific signaling pathways are manipulated in order to recapitulate the sequential stages of embryonic cardiac development. First, hiPSCs are pushed from the pluripotent stage towards the mesodermal lineage via GSK-3β inhibition by CHIR99021, or by canonical WNT signaling pathway activation by growth factors (bFGF, BMP4 and activin A). This step is followed by WNT signaling inhibition to induce further differentiation into the cardiac progenitor lineage. Afterwards, the direction of differentiation is continuously governed by WNT signaling. With the activation of the WNT pathway, the epicardial lineage is generated, which can be further differentiated in to CFs (Witty et al. 2014). Conversely, the absence of the WNT pathway leads to CMs, which usually display ventricular-like features (Paik et al. 2020). Additionally, on the way to CMs, RA was shown to drive mesodermal progenitors towards the atrial subtype (Devalla et al. 2015). Cardiac differentiation protocols can be divided into two groups: EB-based and monolayer-based protocols. Initially, mainly EB-based protocols were employed for cardiac differentiation with hiPSCs forming small cell aggregates in suspension culture, and suitable for stable and large-scale production after substantial optimization (Burridge et al. 2007; Breckwoldt et al. 2017). Alternatively, monolayer-based differentiation protocols have the advantage of reduced procedural steps, but at the expense of lower yield (Lian et al. 2013; Mosqueira et al. 2018).

3.3.2 Engineered heart tissue

Cardiac tissue engineering techniques enable CMs to grow in a 3-dimensional (3D) and thus more physiological environment, which can lead to improved maturation and closer resemblance to the native heart than in monolayer culture. In 1997, the first engineered heart tissue was established,

employing embryonic chick CMs in a 3D collagen matrix (Eschenhagen et al. 1997). In the following years, neonatal rat CMs and mouse CMs were used to generate cardiac tissue constructs (Zimmermann et al. 2000, 2002; Stöhr et al. 2013). To date, in our institute, EHTs are especially well established in 24-well format with fibrin-based matrix, CMs from neonatal animal hearts or human iPSC-derived CMs, and automated contractile analysis (Hansen et al. 2010; Schaaf et al. 2011; Mannhardt et al. 2016; Breckwoldt et al. 2017; figure 4). In recent years, additional modifications of EHT to model disease have been exploited in our institute. Lemme and colleagues established atrial-like EHTs for atrial fibrillation study (Lemme et al. 2018). Moreover, an optogenetic tool was introduced into ventricular-like and atrial-like EHTs for arrhythmia modelling (Lemme et al. 2020; Lemoine et al. 2020). In addition, we have successfully generated non-cardiomyocytes from hiPSCs and included them into EHTs for disease modelling (Werner 2018). Epicardial cells are essential non-cardiomyocytes for the heart's normal development and disease progression. For instance, to model fibrosis, CFs which are the main ECM-producing cells could be added into EHTs. Taken together, EHTs have been proven to be useful for cardiac disease modelling and in vitro drug testing and novel modification broaden the spectrum of disease modelling and render the model more physiological (Saleem et al. 2020; Mannhardt et al. 2020).
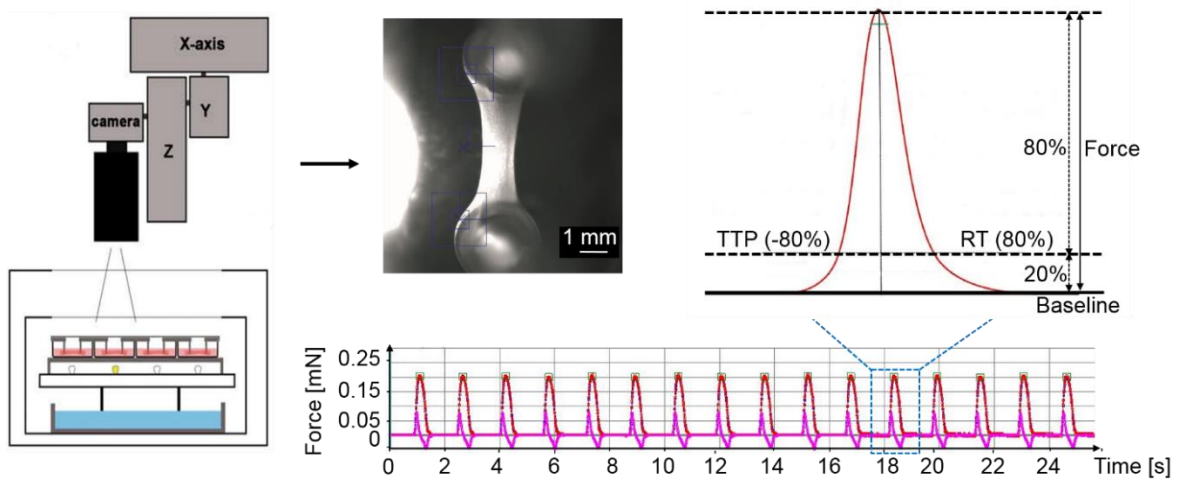

Figure 4: Video-optical analysis of EHT contractility. (Left) Schematic of the video-optical system for recording. (Right) EHT image and contraction peak recorded by the contractility analysis software (EHT Technologies/CTMV; adapted from Mannhardt et al. 2017).

3.4 Optogenetics and heart disease modelling

Over the last decade, applications of optogenetics have emerged in cardiovascular research and medicine, for example, optical cardiac pacing, optical cardioversion, heart contractility control, and high-throughput drug screening (Arrenberg et al. 2010; Funken et al. 2019; Dwenger et al. 2019; Paci et al. 2020; Zgierski-Johnston et al. 2020). Optogenetic tools can be divided into two groups: optogenetic sensors and optogenetic actuators. The first group includes genetically encoded voltage indicators and calcium indicators, which can monitor changes in membrane voltage and intracellular calcium concentration (Tan et al. 2015; Jiang et al. 2018). The second group consists of depolarizing and hyperpolarizing opsins. Channelrhodopsins (ChRs) are the most widely used opsins. They are light-activated non-selective cation (H^+, Na^+, K^+ and Ca^{2+}) channels from algae and can cause depolarization with the transmembrane ion flux when excited by light of a certain wavelength (Lin 2012). In 2005, channelrhodopsin-2 (ChR2) was engineered as the first optogenetic tool (Boyden et al. 2005; Nagel et al. 2005). Subsequently, a number of the ChR variants were developed as research tools with changes in their optical spectrum, kinetics and dynamic range, for example, ChR2 with H134R mutation (ChR2/H134R), ChR2 with E123T mutation (ChETA), *Volvox carteri* channelrhodopsin-1 (VChR1), *Volvox carteri* channelrhodopsin-2 (VChR2) and a blue-shifted ChR (CheRiff; Lin 2012; Hochbaum et al. 2014). As optogenetic tools, the major limitation of ChRs is desensitization. Their recovery time and efficiency after stimulation decide their effectiveness for various applications. Compared to ChR2, ChR2/H134R has a similar excitation wavelength around 470 nm, but slower closing rate, reduced desensitization, and increased light sensitivity (Lin et al. 2009). Of note, ChR2/H134R was utilized in human EHTs to manipulate the beating rate for in vitro arrhythmia studies (Lemme et al. 2020). VChR1 is a red-shifted ChR variant with higher light sensitivity and a broader excitation spectrum. Although the peak response is around 530 nm, VChR1 was shown to be also strongly excited at 470 nm (Zhang et al. 2008). Despite the limitations of slow channel kinetics and incomplete recovery from the desensitized state, VChR1 is still a useful tool with better tissue penetration compared to blue light-activated ChRs. Moreover, VChR1 was engineered as a fusion construct with Gaussia luciferase to produce larger photocurrents than ChR2 (Berglund et al. 2013).
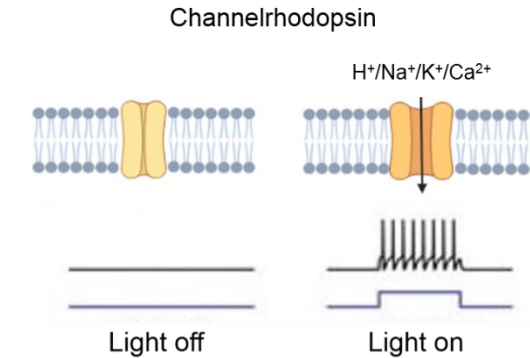
Channelrhodopsin

Figure 5: Basic principle of channelrhodopsin. ChR is a non-selective cation channel. When activated by light at a certain wavelength, it allows the influx of cations, which depolarizes cell membrane and further triggers action potentials.

As described previously, rapid atrial pacing is a common method to model AF in animal models. However, animal models do not accurately represent the physiology of human CMs. With the introduction of optogenetics into human EHTs derived from hiPSCs, chronic tachypacing atrial-like EHTs could be a promising tool to model AF in the future (Lemme et al. 2018, 2020).

3.5   CRISPR/Cas9 genome and epigenome editing

The development of this technique based on clustered regularly interspaced short palindromic repeats (CRISPR)-associated (Cas) systems from bacteria and archaea was a breakthrough in both targeted and large-scale manipulation of the genome, especially when applied to hiPSC. Originally, CRISPR/Cas serves as a microbial adaptive immune system using RNA-guided nuclease to cleave foreign DNA. To date, the CRISPR/Cas9 system is one of the best characterized systems for developing into genome editing tools (Jinek et al. 2012; Ran et al. 2013). It most commonly consists of the nuclease Cas9 from *Streptococcus pyogenes*, the CRISPR RNA (crRNA) array encoding a 20 nt guide RNA (gRNA), and the auxiliary trans-activating crRNA (tracrRNA). The gRNA directs Cas9 to a 20 bp DNA target (protospacer) by complementary base pairing. To adapt this system to human cells and to allow for efficient genome editing, a human codon-optimized Cas9 was created, and the gRNA and tracrRNA were fused into a chimeric, single-guide RNA. Cas9 cleavage requires the presence of a 5'-NGG protospacer adjacent motif (PAM) downstream of the target DNA.

In general, the applications of the CRISPR/Cas9 system can be grouped into three categories (Hanna and Doench 2020). The first category is performing precise and specific alterations in the genome, relying on high-fidelity homology-directed repair machinery and an exogenous DNA repair template. It is widely used to create isogenic hiPSC lines with the same underlying genetic background by correcting or introducing pathogenic mutations (Grobarczyk et al. 2015). Another application is to generate transgenic cell lines by inserting a specific gene in a safe harbor site without causing further alterations in the genome. For example, it can be used to generate a ChR knock-in iPSC line to allow for optical stimulation of EHTs in this study. The second category is making knock-out alleles by introducing random mutations (insertion or deletion) in the target sites, for example, in coding regions or transcription factors binding sites. This process occurs with imperfect DNA repair of double-stranded DNA breaks created by Cas9 in the absence of a repair template. The last category is the application of CRISPR/dCas9. Here, a nuclease domain inactivated Cas9 (dCas9) protein is fused with effector proteins, which can be used for base editing, transcription regulation or epigenetic modification.

The applications of CRISPR/dCas9 have emerged over the last years. Among them, base editing tools have been developed, which comprise fusion proteins of dCas9 and a base modification enzyme to generate precise point mutations in the genome (Komor et al. 2016). By fusing dCas9 with transcription activators or repressors, dCas9 can be harnessed to target gene activation or repression (Perez-Pinera et al. 2013; Thakore et al. 2015). Moreover, CRISPR/dCas9 can be exploited for epigenome editing to regulate gene expression. For instance, targeted DNA methylation editing can be achieved by dCas9 fusion with the catalytic domain of DNMT3A or TET1 (Liu et al. 2016; figure 6). Combined with an AAV delivery system, these dCas9 tools could be used for clinical applications as potential therapeutic approaches for heart diseases. In contrast to epigenetic inhibitors or drugs, epigenetic manipulation with CRISPR/dCas9 can achieve precise targeting, avoid drug resistance and have a long-term but not permanent effects on gene expression (Vojta et al. 2016; Shi et al. 2022).
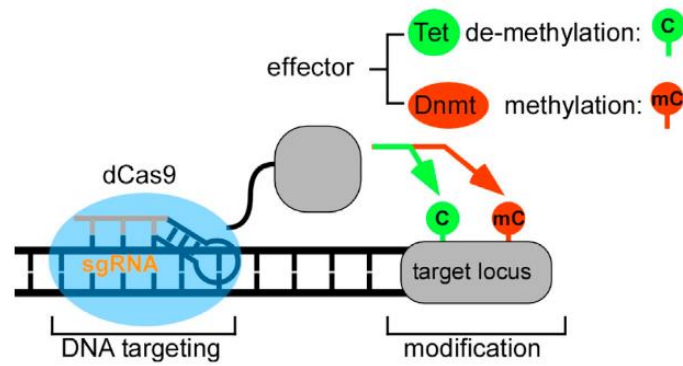
Figure 6: Schematic of CRISPR/dCas9-effector for site-specific manipulation of DNA methylation. A dCas9 fused with TET1 for erasing DNA methylation, or with DNMT3A for de novo methylation, is driven by gRNA to the targeted DNA region (adapted from Liu et al. 2016).

4   Objectives of the thesis

To date, many aspects of AF pathophysiology remain incompletely understood. An improved understanding of the underlying mechanisms of AF is needed to develop novel therapeutic approaches. However, there is no perfect model to reproduce human AF in vitro. Aiming to reduce the complexity of AF in vitro, we set out to establish a human atrial-like EHT-based tachypacing model to simply recapitulate one or several aspects of AF pathophysiology. To this end, an optogenetic approach was developed for chronic tachypacing of atrial-like EHTs. Effects of chronic tachypacing were investigated to evaluate this model. Additionally, NGS (RNAseq, ATACseq and ChIPseq of H3K27ac) was performed to study the possible alterations of transcriptome and chromatin accessibility after chronic tachypacing to explore the role of epigenetic regulation during AF.

As mentioned above, the pathophysiological processes of AF and HF are associated with aberrant gene expression, and epigenetic processes participate in regulating gene expression. The second objective of the thesis was to investigate targeted manipulation of DNA methylation as a potential therapeutic strategy in AF and HF. To this end, an EHT-based fibrosis model and an EHT-based hypertrophy model were generated, based on previous experience in ventricular-like EHTs to model different aspects of HF in our institute. CRISPR/dCas9-DNMT3A and CRISPR/dCas9-TET1 tools were then created for targeted DNA methylation editing in these disease EHT models.

5   Materials and methods

A detailed list of media, materials, reagents and devices used for this project can be found in the supplementary data.

5.1   Cell culture

5.1.1   Basic cell culture

HEK 293 and HEK 293T cells were kindly provided by Dr. Ingke Braren (Vector Facility, UKE, Hamburg, Germany). Cells were cultured in DMEM supplemented with 10% FCS, 1% penicillin/streptomycin and 1% L-glutamine (HEK cell medium) in a humidified incubator at 37 °C and 5% CO_2 / 95% air. They were split with 0.05% trypsin when reaching 90-100% confluence and seeded into tissue culture plates for further experiments.

5.1.2   Stem cell culture

The established in-house control hiPSC line ERC001 was used for most experiments. It is registered as UKEi001-A in a global registry for human pluripotent stem cell lines (https://hpscreg.eu/cell-line/UKEi001-A). It was generated from a skin biopsy of a healthy donor with the CytoTune-iPS Sendai Reprogramming kit (ThermoFisher). This work was performed by UKE Stem Cell Core Facility. The studies based on this hiPSC line were approved by the Ethics Committee of the Hamburg Physicians' Chamber, responsible for the University Medical Center Hamburg-Eppendorf (Az. PV4798/28.10.2014). The genetically engineered optogenetic hiPSC line VChR1 was kindly provided by Dr. Tim Stüdemann (IEPT, UKE, Hamburg, Germany). It was created by CRISPR/Cas9 genome editing and homology-directed repair on the AAVS1 locus in the cell line ERC001 (Stüdemann et al. 2021). Fluorescently labeled Venus-iPSC and dKatushka2-iPSC were generated from ERC001 by the method of RGB marking (Weber et al. 2012). In brief, ERC001 cells were transduced with lentivirus encoding fluorescent proteins Venus and dKatushka2, respectively (see section 5.2.1).

The stem cell culture work was performed as previously described (Breckwoldt et al. 2017; Shibamiya et al. 2020). In brief, hiPSCs were maintained in FTDA medium (Frank et al. 2012) in Geltrex (Gibco)-coated T75 flasks under hypoxia conditions (37 °C, 5% O_2, 5% CO_2 and 95% humidity). PCR-based mycoplasma detection was regularly conducted (see section 5.8.1). Pluripotency was checked by staining the cell surface marker SSEA-3 and analyzed by flow

cytometry (see section 5.8.5). Standard passaging was performed twice per week when cells were confluent. Cells were dissociated into single cells with Accutase (Sigma-Aldrich). After centrifugation at 200 g for 2 minutes and removal of the supernatant, cells were resuspended in fresh FTDA with 10 µM Y-27632. Subsequently, the total cell number was determined by manually counting with a Neubauer chamber with trypan blue staining. Two seeding densities were used: 4.5×10^6 or 6.5×10^6 cells per T75 flask for culturing for 4 days or 3 days, respectively. Cell culture medium was replaced with fresh FTDA daily (table 1). When reaching confluency, the medium was changed twice at a 7-hours interval (table 1).

Table 1. HiPSC media change schedule

	4.5×10^6 cells per T75 flask	6.5×10^6 cells per T75 flask
Day 0	15 mL FTDA+10 µM Y-27632	20 mL FTDA+10 µM Y-27632
Day 1	20 mL FTDA	20 mL FTDA
Day 2	20 mL FTDA	15 mL+25 mL FTDA
Day 3	15 mL+25 mL FTDA	Passage
Day 4	Passage	

For freezing hiPSC, cells were split and counted when the confluency was around 80%-90%. They were resuspended in the freezing medium (10% heat-inactivated FCS+90% DMSO) as 1×10^6 cells per mL, then transferred into cryotubes (1 mL per tube). The cryotubes were kept in the freezing container (Mr. Frosty) at -80 °C for 24 hours, then transferred to -150 °C for long-term storage.

For thawing hiPSC, each cryotube was thawed in a water bath at 37 °C for 2-3 minutes without shaking. After removal from the water bath, the tube was sprayed with 70% ethanol. A 5 mL pipette was filled up with 5 mL pre-warmed medium (FTDA+10 µM Y-27632), then placed into the cryotube to aspirate the cell suspension. Afterwards, the resulting 6 mL cell suspension was slowly transferred to a 15 mL tube and centrifuged at 200 g for 2 minutes. Cells were seeded into one or two wells of a Geltrex-coated 6-well plate in FTDA+10 µM Y-27632.

5.2 Virus transduction

5.2.1 Lentivirus transduction

For fluorescent labeling by lentiviral transduction, ERC001-iPSCs were seeded into a Geltrex-coated 6-well plate at a density of 3×10^5 cells per well and cultured for 3 days in FTDA with daily medium change. To perform transduction, culture medium was changed to 2 mL fresh FTDA with 800 µL Lenti-Venus (2.5×10^6 TU/mL) or Lenti-dKatushka2 (1.6×10^6 TU/mL). The lentiviruses containing EF-1α promoter, coding sequences of the respective fluorescence protein and puromycin-resistance gene were kindly provided by Dr. Kristoffer Riecken (Stem Cell Transplantation Research, UKE, Hamburg, Germany). After 6 hours, the virus-containing medium was replaced by 3 mL fresh FTDA. After 2 days, selection of transduced cells by puromycin treatment was started. 2 µg/mL puromycin were applied on both untransduced and transduced cells for 5-7 days until untransduced cells were completely killed by puromycin. Then Venus-iPSCs and dKatushka-iPSCs were expanded and frozen for further experiments.

5.2.2 Adeno-associated virus transduction

The AAV serotype AAV-DJ, containing split dCas9-DMNT3A sequence, was produced by Dr. Ingke Braren. CMs or CFs were seeded into Geltrex-coated 12-well plates at a density of 1×10^5-2×10^5 cells per well. They were cultured in HEK cell medium for approximately 3 days until they attached well to the cell culture plate surface. Then culture medium was changed to 500 µL fresh medium. AAV-DJ was added into the fresh medium with the desired MOI of 1×10^5. After 24 hours, each well was topped up with 500 µL fresh medium. After 3 days of transduction, 1.5 µg/mL puromycin selection was started until untransduced cells were completely killed by puromycin.

5.3 Plasmids co-transfection

HEK 293 cells were seeded in a 24-well plate at a density of 1×10^5 cells per well for 24 hours. 2.4 µg of total plasmid DNA (1.2 µg of split-dCas9N with gRNAs and 1.2 µg of split-dCas9C plasmids) were diluted in 100 µL DMEM. 2.8 µL of TurboFect Transfection Reagent (Thermo Scientific) were then added into the DNA mix and mixed thoroughly by vortexing. Afterwards, the mixture was added into each well in a drop-wise manner. After 48 hours, 1.5 µg/mL puromycin selection was performed on cells transfected with pAAV-SMVP-dCas9C-DNMT3A-2Apuro and pAAV-SMVP-dCas9C-inactiveDNMT3A-2Apuro. Transfection efficiency was assessed by

checking BFP expression with confocal microscopy in cells transfected with pAAV-dCas9C-DNMT3A-2ABFP. After 8 days of transfection, cells were harvested for analysis of DNA methylation and gene expression.

5.4 Karyotyping

5.4.1 NanoString nCounter karyotype assay

Genomic DNA was extracted from each hiPSC line using the DNeasy Blood & Tissue Kit (QIAGEN). Further sample processing procedures were performed by Elisabeth Krämer (Nanostring Core Facility, UKE, Hamburg, Germany) according to the manufacturer's instructions. In brief, 250 ng genomic DNA were fragmented by restriction enzyme digestion at 37 °C for 1-2 hours and subsequently denatured at 95 °C for 5 minutes. Then, the fragmented DNA was hybridized with probes of a fixed-content panel from the kit at 65 °C for 16 hours. Afterwards, the hybridized DNA complexes were purified by the nCounter Prep Station, and fluorescently labeled reporter codes were counted by nCounter Digital Analyzer. The data analysis was done by Dr. Giulia Mearini (IEPT, UKE, Hamburg, Germany).

5.4.2 Giemsa-banding cytogenetic analysis

For karyotyping, hiPSCs were first cultured in a 6-well plate under standard conditions. When reaching 70-80% confluency, they were transferred to the Institute of Human Genetics (UKE, Hamburg, Germany) for karyotype analysis by Giemsa-banding (G-banding) as previously described (Breckwoldt et al. 2017).

5.5 Cardiac differentiation

5.5.1 Embryoid body-based cardiomyocyte differentiation

The differentiation of hiPSC to control cardiomyocyte (Ctrl-CM) was performed with an EB-based differentiation protocol (Breckwoldt et al. 2017). Undifferentiated hiPSCs were expanded in T75 flasks. On day 0 of differentiation, cells with 100% confluency were pre-treated with 10 µM Y-27632 for one hour. They were dissociated into single cells with 0.5 mM EDTA or Accutase and transferred into spinner flasks at a density of 30-35 million cells per 100 mL EB-formation medium. In order to form EBs, the cell suspension was constantly stirred (40 rpm) on a magnetic plate.

After 24 hours, the EBs were washed and the total EB volume was estimated. 200-250 µL EBs were transferred into one T175 flask coated with 1% Pluronic F-127 (Sigma-Aldrich) for mesodermal differentiation. They were cultured in mesoderm induction medium for 3 days with a daily medium change of half of the medium volume under hypoxic conditions. 10 ng/mL BMP4, 3 ng/mL activin A and 5 ng/mL bFGF were used to induce mesoderm. The cardiac differentiation was induced using the Wnt-signaling inhibitor XAV939 under normoxic conditions. EBs were washed and the total EB volume was estimated again. 200-250 µL EBs per T175 flask were cultured in cardiac differentiation medium I for 3 days and cardiac differentiation medium II for 4 days. The onset of beating between day 9 and day 11 indicated successful differentiation. Subsequently, EBs were cultured in cardiac differentiation medium III without XAV939 for 5 more days.

The EB-based atrial differentiation was established in the institute previously by adding RA (1 µM) into the cardiac differentiation medium I for 3 days (Lemme et al. 2018). This protocol was further optimized in the present study by changing concentrations of BMP4 and activin A. The details are shown in the results section.

5.5.2 Monolayer-based cardiomyocyte differentiation

In protocol I, hiPSCs were seeded into a Matrigel (Corning)-coated 6-well plate at a density of 5×10^5 to 6×10^5 cells per well and cultured in 3 mL FTDA medium with 10 µM Y-27632 for 24 hours. At day 0, when cells reach 50%-70% confluency, FTDA medium was replaced by 1.5 mL/well Stg0 medium containing StemPro-34 for preconditioning. After 12-16 hours, 2 mL/well Stg1 medium with activin A and BMP4 was used for mesodermal induction for two days. At day 3, Stg1 medium was rinsed off with RPMI 1640 and then replaced by 3 mL/well Stg2.1 medium with XAV939 and B-27 minus insulin for cardiac induction for 48 hours. For an atrial differentiation protocol test, 0.5 µM or 1 µM RA was included in the Stg2.1 medium. Afterwards, cells were cultured in 3 mL/well Stg2.2 medium with XAV939 and B-27 plus insulin for another 2 days. From day 7, cells were maintained in RDM until they started to beat.

In protocol II, hiPSCs were seeded into a Matrigel-coated 6-well plate with about 1×10^6 cells per well and cultured in 3 mL mTeSR1 medium for two days with daily medium change. Mesoderm was induced by treatment with GSK3 inhibitor CHIR99021. At day 0, when the confluency reached 80%-90%, the culture medium was changed to RPMI1640 supplemented with B-27 minus insulin and 10 µM CHIR99021 for 24 hours. Afterwards, CHIR99021 was removed and cells were

cultured in fresh RPMI1640 with B-27 minus insulin for 2 days. At day 3, a mixed medium was used to induce cardiac differentiation for 2 days, which contained 2 mL/well old medium and 2 mL fresh RPMI1640 with B-27 minus insulin and was supplemented with 5 μM XAV939. For the atrial differentiation protocol test, 0.5 μM or 1 μM RA was added from day 3 to day 5. At day 5, XAV939 containing medium was replaced by fresh RPMI1640 with B-27 minus insulin for 2 days. From day 7, cells were maintained in RDM until they started to beat.

5.5.3   Dissociation of cardiomyocytes

For dissociation of CMs from both EB and monolayer-based protocols, cells were washed twice with HBSS and then treated with dissociation buffer containing 200 U/mL collagenase II, 30 μM N-benzyl-p-toluenesulfonamide (BTS) and 10 μM Y-27632. For one T175 flask, 20 mL of dissociation buffer were used. For one well of a 6-well plate, 1 mL of dissociation buffer was used. Afterwards, flasks or plates were placed in a cell culture incubator for 2-3 hours and regularly checked for dispersing cells under the microscope. After collagenase digestion, blocking buffer with the same volume as dissociation buffer was added. Cells were further dispersed by pipetting and centrifuged at 100 g for 8 minutes. Then single cells were washed twice with RPMI 1640 before manually counting with a Neubauer chamber. Eventually, they were used for EHT casting, cryopreservation, flow cytometer analysis or other experiments.

5.5.4   Cardiac fibroblast differentiation

The CF differentiation was adapted from a previous doctoral thesis from the institute (Werner 2018). EB formation and mesoderm induction procedures were the same as Ctrl-CM differentiation. After the mesoderm stage, 50 mL EBs were seeded into a Geltrex-coated T75 flask in 20 mL Epi-medium (supplemented with 10 ng/mL BMP4, 5 ng/mL VEGF, 4 μM CHIR99012 and 5.4 μM SB-431542) for 2 days. EBs attached to the surface and formed a monolayer. Afterwards, cells were cultured in 20 mL Epi-medium with 5 ng/mL VEGF for 8 days and the medium was changed for every other day. On day 15, cells were detached with collagenase II and 0.05% trypsin. 2×10^6 cells were seeded in a Geltrex-coated T75 flask in 20 mL Epi-medium with 10 μM Y-27632. From day 16 to day 24, cells were cultured in the Epi-medium with 10 ng/mL bFGF, and the medium was changed every other day. CF dissociation was carried out with Accutase on day 24.

5.6   EHT generation and analysis

5.6.1   EHT generation

Human EHTs were generated according to a published protocol (Mannhardt et al. 2017). EHT casting molds were made by placing polytetrafluoroethylene (PTFE) spacers into a 24-well plate pre-filled with 2% agarose/DPBS solution. After agarose solidification at room temperature, the spacers were gently removed, and PDMS racks were placed into the agarose casting molds. The EHT master mix contained hiPSC-CMs, Y-27632, 2x DMEM and fibrinogen (table 2). First, 100 μL the master mix were added into a 200 μL microtube containing 3 μL thrombin and pipette-mixed twice. Then 100 μL of the mixture were added into each mold between the two silicon posts. To cast CFs containing EHTs (CF-EHTs), each EHT master mix contained both hiPSC-CMs and hiPSC-CFs with a total cell number of $1x10^6$. After fibrin polymerization in a cell culture incubator for 1-1.5 hours, 300 μL pre-warmed medium were added into each well for 30 minutes to facilitate the detachment of EHTs from the molds. In the end, the silicon racks with EHTs attached were transferred to a new plate with fresh standard EHT culture medium. EHTs were cultured in the humidified incubator at 37 °C, 7% CO_2, 40% O_2 and the medium was changed on Mondays, Wednesdays and Fridays.

Table 2. EHT master mix per single EHT

Component	Volume
CMs with or without CFs	1.0×10^6
EHT casting medium	97.6 μL
2x DMEM	6.2 μL
0.1% Y-27632	0.11 μL
Fibrinogen	2.8 μL

5.6.2   Contractility measurement

The contractility of EHTs was analyzed in a well-established video-optical analysis set-up as described previously (Hansen et al. 2010; Schaaf et al. 2011). EHTs in a 24-well plate were placed into a glass-roof humidified incubator (37 °C, 7% CO_2, 40% O_2 and 53% N_2) and back-illuminated by 24 individual white light-emitting diodes (LEDs). For measuring the contractility of light-sensitive EHTs derived from VChR1-iPSCs, the original white LED board was replaced by a specific tri-color LED board and red LEDs were used for illumination. A video camera was

mounted onto a motorized XYZ-axis above the incubator to record a video of each EHT. Each video was analyzed with custom-designed software (Consulting Team Machine Vision, CTMV) based on automated figure recognition. By tracking the movement of the two silicon posts caused by the EHT contractions over time, the software calculates the beating frequency, contraction force, kinetics (contraction/relaxation time and velocity) and beating regularity (interdecile range of beat-to-beat interval length; RR scatter).

5.6.3 Optical pacing

The device used for optical pacing was designed and built by Julius Hansen (Sarcura GmbH, Klosterneuburg, Austria). The details were described in the result section (section 6.4). In brief, the wavelength, light pulse duration, frequency and interval were controlled by a microcontroller platform (Arduino). The parameters were set from a computer connected to the microcontroller board via USB-Serial port using a simple text-based interface. Codes c: 255:0:0, c:0:255:0 and c:0:0:255 represented red, green and blue light on full intensity, respectively. Code t:60:140 was 25 milliseconds of pulse duration and 5 Hz. Code i:25:10 indicated 25 seconds of pacing and 10 seconds break.

5.6.4 Electrical pacing

Electrical pacing was used to standardize EHT beating frequency during some experiments. The electrical stimulation procedure was established in the institute previously (Hirt et al. 2014). To this end, 24-well plates with desired medium (2 mL/well) were pre-equilibrated in an EHT incubator overnight or for at least 2 hours before experiments. Then, EHTs with silicone racks were mounted onto custom-made carbon electrodes and placed into the 24-well plate (figure 7). The electrical stimulation was controlled by the Grass S88X Dual Output Square stimulator (Natus Neurology Incorporated). EHTs were paced at different frequencies at 2.5 V and 4 ms biphasic pulse duration.
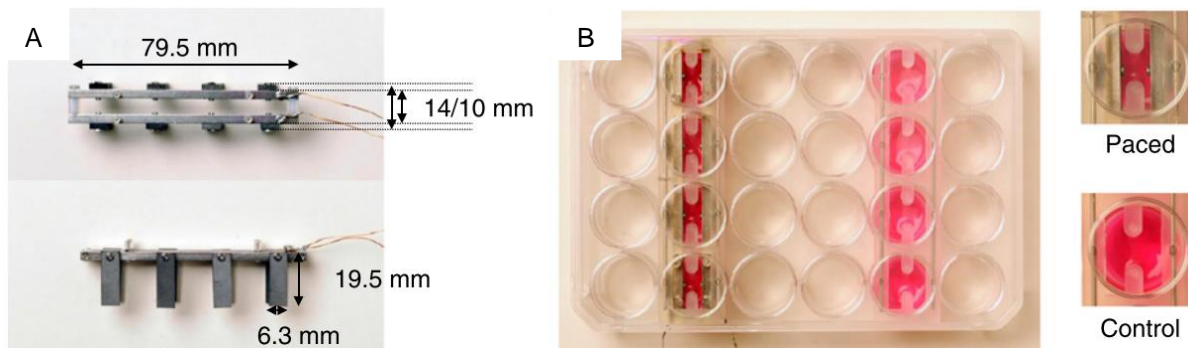
Figure 7: Setup of electrical stimulation of EHTs. (A) Carbon electrodes pacing unit for 4 EHTs. (B) EHTs with or without pacing unit (adapted from Marc et al. 2014).

5.6.5 EHT calcium concentration-response curve

This experiment was performed in PAN DMEM (PAN-Biotech, without calcium) supplemented with 25 mmol/L HEPES. For baseline measurements, EHTs were incubated in DMEM with 1.8 mM $CaCl_2$ for 30 minutes and the contractility was recorded both with and without electrical stimulation. The following measurements were all carried out under electrical stimulation. The medium with low calcium concentration (0.1 mM or 0.2 mM $CaCl_2$) was used to wash out the remaining calcium from EHTs. During this process, EHTs were closely monitored by video-optical recording until the force reached the minimal force threshold of 0.02 mN. Subsequently, contractility of EHTs was measured consecutively at calcium concentrations of 0.3 mM, 0.4 mM, 0.5 mM, 0.6 mM, 0.7 mM, 0.8 mM, 1.0 mM, 1.2 mM, 1.4 mM, 1.8 mM, 2.4 mM, 3.3 mM and 5.5 mM. For each calcium concentration, EHTs were incubated in the medium for 20 minutes before contractility measurement. Calculation of the calcium EC_{50} was done with GraphPad Prism 7 with the non-linear regression function 'log(agonist) vs. normalized response – variable slope'.

5.6.6 EHT force-frequency relationship

First, PAN DMEM (supplemented with 25 mM HEPES) was pre-equilibrated overnight (37 °C, 7% CO_2, 40% O_2). EHTs were incubated in the medium with 1.8 mM calcium for 30 minutes and baseline measurements were performed with and without pacing. Afterwards, EHTs were transferred into the low calcium medium for washing out calcium (see section 5.6.5). Next, EHTs were transferred into the medium containing calcium at the concentration determined as EC_{50} of the EHT force for 30 minutes. For analysis of force-frequency relationship (FFR), EHTs were

electrically stimulated stepwise from 2.25 to 4.0 Hz with 0.25 Hz increments, and from 4.0 to 6.5 Hz with 0.5 Hz increments after each measurement. EHT contractions were recorded for 10 seconds at each stimulation frequency.

5.6.7 Pro-hypertrophic intervention

The pro-hypertrophic intervention was started when the force of EHTs reached its plateau. EHTs were switched from standard EHT culture medium to serum-free EHT medium to prevent possible interfering pro-hypertrophic serum-effects. Serum-free EHT medium was prepared freshly and supplemented with 20 µM PE and 50 nM ET-1. EHTs were treated for 7 days and the medium was changed daily. Contractility was measured 2 hours after each medium change.

5.6.8 Action potential recording

APs were recorded in intact EHTs (30-60 days old) with standard sharp microelectrodes as previously described (Lemoine et al. 2017). EHT was placed in a small recording chamber, fixed with two needles at each end and superfused with Tyrode's solution equilibrated with 95% O_2 / 5% CO_2 at 36.5±0.5 °C. APs were recorded by sharp microelectrodes pulled from filamented glass (Hilgenberg, DMZ Puller) with a tip resistance ranging from 20 to 50 MΩ when filled with 2 mol/L KCl solution. Before AP measurements, tissues were superfused with Tyrode's solution at 36.5±0.5 °C for at least 30 minutes. 10 µM carbachol (CCh) and 50 µM 4-aminopyridine (4-AP) were used to discriminate between atrial and ventricular phenotypes. CCh was dissolved in DMSO as a stock solution of 10 mM and then stored at -20 ºC. 4-AP was prepared as a 1 mM stock solution in Tyrode's solution and stored at 4 ºC. Parameters of APs were analyzed using Lab-Chart software, for example, APD and plateau potential (Plateau V1).

5.6.9 EHT dissociation

EHTs were removed from silicon posts and washed twice with pre-warmed HBSS in a 24-well plate. They were then transferred to new wells containing 0.5x papain solution and placed in an EHT culture incubator for 10 minutes. Afterwards, EHTs were checked every 5 minutes under microscopy until they ruptured and single cells were released. 1 mL HBSS with 10% FCS was then added into each well. EHTs were further dissociated into single cells by pipetting 4-5 times. Cells were then transferred to 15 mL tube. 5 mL HBSS with 10% FCS were added into the tube

and cells were centrifuged at 100 g for 5 minutes. Then cells were resuspended in 500 μL cold HBSS for each EHT and manually counted with trypan blue staining with a Neubauer chamber.

5.7 Molecular cloning

5.7.1 Construction of dCas9N and dCas9C plasmids

The cloning information of the constructs is listed in table 3 and table S10. All construct maps were built with the software CLC Main Workbench (QIAGEN). Inserts were PCR amplified by Q5 High-Fidelity 2X Master Mix (NEB). Primers with 15-20 bp overlaps were designed using an online tool (https://nebuilder.neb.com/) and ordered from Eurofins Genomics or Microsynth Seqlab (table S6). Vectors were linearized by respective restriction enzymes (table 3, S10). The ligation reactions were conducted using NEBuilder HiFi DNA Assembly Master Mix (NEB; table 4), then transformed into NEB 5-alpha competent *E. coli* cells (NEB) by 42 °C heat-shock for 30 seconds. The transformation reaction mix was plated onto an ampicillin LB agar plate and incubated at 37 °C for 12-16 hours. On the next day, 3 single colonies from each reaction were inoculated into 15 mL tubes with 5 mL ampicillin LB and cultured at 37 °C with 200 rpm shaking overnight. Plasmids were extracted from the *E. coli* cells by FavorPrep Plasmid Extraction Mini kit (Favorgen). Finally, Sanger sequencing (conducted by Eurofins Genomics or Microsynth Seqlab) was used to verify the correct clones.

DCas9N and dCas9C constructs were generated from plasmids pAAV-SMVP-Cas9N (Addgene plasmid # 80930) and pAAV-CMV-Cas9C-VPR (Addgene plasmid # 80933), gifts from George Church (Chew et al. 2016). DNA fragments TET1CD and P2A-tagBFP were PCR amplified from plasmid pFuw-dCas9-Tet1CD-P2A-tagBFP (Addgene plasmid # 108245), a gift from Rudolf Jaenisch (Liu et al. 2018). DNA fragments DNMT3A and FLAG were PCR amplified from plasmid pdCas9-DNMT3A-EGFP (Addgene plasmid # 71666), a gift from Vlatka Zoldoš (Vojta et al. 2016). The BmsBI chimaeric gRNA cassette with human U6 promoter was obtained from plasmid pMIA3 1sg-eSpCas9-2AmRuby2-2Amp53DD, a gift from Dr. Matias I. Autio from Genome Institute of Singapore. T2A-puro and cTNT promoter were obtained from plasmid pVC178-pSico-Ef1a-RIP1-2Apuro and plasmid pVC525-pGG2-cTnT-HA-TTL, respectively. Both plasmids were kindly provided by Dr. Ingke Braren.

Table 3: Cloning information of dCas9N and dCas9C constructs

pAAV-SMVP-FLAG-dCas9N

Plasmid	Insert		Vector	
	Primer	Template	Backbone	RE
StepI-pAAV-SMVP-Cas9N-Amp	AmpN-F AmpN-R	pAAV-SMVP-Cas9N	pAAV-SMVP-Cas9N	PvuII
	AmpC-F AmpC-R	pAAV-SMVP-Cas9N		
StepII-pAAV-dCas9N-Amp	hU6-BsmBI-sgRNA-F hU6-BsmBI-sgRNA-R	pMIA3 1sg-eSpCas9-2AmRuby2-2Amp53DD	StepI-pAAV-SMVP-Cas9N-Amp	SphI/EcoRV
	CMV-Intein F dCsa9-EcoRV-R	pAAV-SMVP-Cas9N		
StepIII-pAAV-dCas9N-Amp	dCas9N-SalI-F dCas9N-BsaI-R	pAAV-SMVP-Cas9N	StepII-pAAV-dCas9N-Amp	SalI/BamHI
	dCas9-BsaI-BamHI-F dCas9-BamHI-R	pAAV-SMVP-Cas9N		
pAAV-SMVP-dCas9N	hU6-BsmBI-sgRNA-F hU6-BsmBI-sgRNA-R	pMIA3 1sg-eSpCas9-2AmRuby2-2Amp53DD	StepIII-pAAV-dCas9N-Amp	SphI/SpeI
	CMVenhancer-F CMV-R	pAAV-SMVP-Cas9N		
pAAV-SMVP-FLAG-dCas9N	FLAG-dCas9N-F FLAG-dCas9N-R	dCas9-DNMT3A-EGFP	pAAV-SMVP-dCas9N	NheI/PstI
	dCas9N-PstI-F dCas9N-PstI-R			
pAAV-cTNT-FLAG-dCas9N	cTNT-F cTNT-R	pVC525-pGG2-cTnT-HA-TTL	pAAV-SMVP-FLAG-dCas9N	SpeI

pAAV-CMV-dCas9C-Tet1 and pAAV-SMVP-dCas9C-DNMT3A

Plasmid	Insert		Vector	
	Primer	Template	Backbone	RE
StepI-pAAV-CMV-dCas9C-VPR	pAAV-CMV NdeI F pAAV-CMV R	pAAV-CMV-Cas9-VPR	pAAV-CMV-Cas9-VPR	NdeI/PmlI
	IntC F Int C dCas9 R	pAAV-CMV-Cas9-VPR		
	dCas9 C F dCas9 C R	pAAV-CMV-Cas9-VPR		
pAAV-CMV-dCas9C-TET1	Cas9 C-NLS F Cas9 C-NLS R	pAAV-CMV-Cas9-VPR	StepI-pAAV-CMV-dCas9-VPR	AscI/Mph1103I
	Tet1CD F Tet1CD-R	pFuw-dCas9-Tet1CD-P2A-tagBFP		
pAAV-CMV-dCas9C-DNMT3A	Cas9C-NLS F cas9C-NLS-Gly4 R	pAAV-CMV-Cas9-VPR	StepI-pAAV-CMV-dCas9-VPR	AscI/Mph1103I
	DNMT3A-F DNMT3A-R	pdCas9-DNMT3A-EGFP		
pAAV-SMVP-dCas9C-DNMT3A	NdeI-pAAV-CMV-enhancer-F NdeI-pAAV-CMV-R	pAAV-SMVP-dCas9N	pAAV-CMV-dCas9C-DNMT3A	NdeI

Table 4: Ligation reaction

	Amount
DNA molar ratio	Vector:insert=1:2
Vector	50 ng
Inserts	m=size (insert)/ size (vector) x 2 x 50 ng
NEBuilder Master Mix	5 µL
Nuclease free H_2O	Top up to 10 µL
Incubated at 50 °C for 30 minutes, then transformed into NEB 5-alpha competent cells	

5.7.2   Design and cloning of gRNA

The genomic sequence of the promoter region of human *COL1A1* (hg38_chr17:50200862-50201862) was uploaded to CRISPOR (http://crispor.tefor.net/), and gRNAs were designed by the online search algorithm. The sequences of human *IL6ST* gRNAs and non-targeting gRNAs were published previously (Vojta et al. 2016). Oligonucleotides of the gRNA sequence and the complementary sequence, with CACC- and AAAC- added to the 5' end of each oligonucleotide, were purchased from Eurofins Genomics or Microsynth Seqlab (table S7). The mixture of 10 µM of each oligonucleotide was incubated at 95 °C for 5 minutes, then cooled down to room temperature gradually, and inserted into Esp3I digested dCas9N plasmids (table 5). The sequences of inserts were verified by Sanger sequencing with standard primer CMV-rev (AGTAGGAAAGTCCCGTAAGG) or U6-fwd (GAGGGCCTATTTCCCATGATTCC).

Table 5. gRNA cloning reactions

Reagent	Amount
10x RE buffer (Cutsmart)	1 µL
Vector	300-500 ng
Esp3I	0.5 µL
Nuclease-free H_2O	Top up to 10 µL
Incubated at 37 °C for 30 minutes, then added:	
10x T4 ligase buffer	1.25 µL
Annealed oligonucleotide (10 µM)	0.5 µL
T4 DNA ligase	0.75 µL
Incubated at room temperature for 30 minutes, then transformed into NEB 5-alpha competent cells	

5.8   Molecular analysis

5.8.1   Mycoplasma test

Possible mycoplasma contamination was regularly screened during standard stem cell culture. Stem cells were cultured without medium change for 3 days. 1 mL of culture medium was collected and incubated at 100 °C for 10 minutes. After centrifugation at 250 g for 5 minutes, 2 µL of the supernatant were added into the PCR reaction (table 6, 7). Water was used as a negative

control, while a contaminated supernatant was used as a positive control. The PCR products were identified by 1% (w/v) agarose gel electrophoresis in TAE buffer. This work was kindly performed by June Uebeler and Anna Steenpass (IEPT, UKE, Hamburg).

Table 6: PCR reaction mix for mycoplasma test

Component	50 µL reaction
Nuclease-free H_2O	25.75 µL
10x buffer	5 µL
Q-solution	10 µL
$MgCl_2$ (25 mM)	4 µL
Primer pool Myco-dw (10 pM)	1 µL
Primer pool Myco-up (10 pM)	1 µL
dNTPs	1 µL
Template	2 µL
Taq DNA polymerase	0.25 µL

Table 7: PCR thermocycling conditions

Step	Temperature	Time
Initial denaturation	95 °C	15 minutes
40 cycles	94 °C	30 seconds
	56 °C	30 seconds
	72 °C	1 minute
Final extension	72 °C	10 minutes
Hold	4 °C	-

5.8.2   RNA extraction

For total RNA isolation with the RNeasy Mini Kit (QIAGEN), 350 µL RLT buffer with 1% 2-mercaptoethanol was used for one EHT or cells from one well in a 12 or 6-well plate. An additional homogenization step was performed for EHT samples. To this end, a steel bead was added into a 2 mL microcentrifuge tube containing the EHT sample and the tissue was disrupted and homogenized with a TissueLyser disruptor device (QIAGEN) for 2 minutes at 30 Hz. The lysate was further processed according to the manufacturer's instructions.

For total RNA isolation with TRIzol reagent (Life Technologies), cell and EHT samples were dissolved in 1 mL TRIzol. The homogenization of EHT samples were performed as described above with the TissueLyser disruptor device. Afterwards, 200 mL chloroform were added into each lysate and thoroughly mixed by shaking. After incubation for 2 minutes at room temperature, the samples were centrifuged at 12,000 g and 4 °C for 15 minutes. The aqueous phase containing RNA was transferred to a new reaction tube. The RNA was precipitated with isopropanol, washed in 70% ethanol and reconstituted in 20 µL RNAse-free water.

5.8.3   Reverse transcription and quantitative real-time PCR

100 ng of total RNA (quantified by Nanodrop 1000 Spectrophotometer) were reverse transcribed into cDNA with High-Capacity cDNA Reverse Transcription Kit (Applied Biosystems; table 8, 9). Subsequently, cDNA was diluted 5-10 times for quantitative real-time PCR (qPCR). The qPCR was performed on an ABI PRISM 7900HT Sequence Detection System (Applied Biosystems; table 10, 11).

Table 8: Reverse transcription reaction mix

Component	25 µL reaction
10x RT buffer	2.5 µL
10x Random primer	2.5 µL
25x dNTPs (100 mM)	1 µL
MultiScribe reverse transcriptase (50 U/ µL)	1 µL
RNA	100 ng
Nuclease-free H$_2$O	Top up to 25 µL

Table 9: Reverse transcription thermocycling conditions

Step	Temperature	Time
1	25 °C	10 minutes
2	37 °C	120 minutes
3	85 °C	5 minutes
4	4 °C	-

Table 10: qPCR reaction mix

Component	10 µL reaction
EvaGreen master mix	5 µL
10 µM primer mix	0.5 µL
cDNA	2 µL
Nuclease-free H_2O	5.5 µL

Table 11: qPCR thermocycling conditions

Cycles	Temperature	Time
1	50 °C	2 minutes
1	95 °C	10 minutes
40	95 °C	15 seconds
	60 °C	1 minute
1% ramping rate	95 °C	15 seconds
	60 °C	15 seconds
	95 °C	15 seconds

5.8.4 Western blot

For sample preparation, cells in 12 or 6-well plates were washed twice with cold DPBS. After removal of DPBS, cells in the plate were stored at -80 °C or directly dissolved in 1x Kranias buffer (with 0.1% DTT, 50-100 μL per well). The lysate was transferred into a 1.5 mL microtube and heated at 95 °C for 5-10 minutes to reduce the viscosity. Subsequently, the total protein amount was quantified by Bradford assay. The standard protein solution was obtained by a serial dilution of 1 mg/mL BSA solution into the following concentrations: 1 mg/mL, 0.8 mg/mL, 0.6 mg/mL, 0.4 mg/mL, 0.2 mg/mL and 0 mg/mL. Meanwhile, samples were prepared in a dilution of 1:10 and 1:100. 10 μL of each standard protein or sample was pipetted into a 96-well plate in duplicates. 200 μL coomassie dye reagent (1:50; Bio-Rad) were then added into each well. Afterwards, protein-dye mixtures were incubated at room temperature for 5 minutes. The absorbance at 595 nm was measured using a plate reader photometer (TECAN). The concentration of each sample was calculated according to the standard curve and adjusted to the same concentration with 1x Kranias buffer.

8-20 μg sample were used for SDS-PAGE gel electrophoresis. First, laemmli buffer was added to each sample. The mixture was then heated to 95 °C for 2 minutes and loaded into 10% SDS-PAGE gel. The samples were running at 70-100 V in the stacking gel and at 120 V in the separating gel. After separation, proteins were transferred onto a nitrocellulose membrane (0.45 μm) with cold transfer buffer for 2 hours at 350 mA. The blot was stained with Ponceau S solution to allow for inspection of all bands. Afterwards, the blot was blocked with 5% (w/v) BSA in TBST (0.1% Tween 20) for 45 minutes and subsequently incubated with primary antibodies at 4 °C overnight. The blots were incubated with anti-rabbit or anti-mouse IgG peroxidase-conjugated secondary antibodies (Sigma) under shaking at room temperature for 2 hours before proteins were visualized with Pierce ECL Western Blotting Substrate (Thermo Fisher) on the Bio-Rad ChemiDoc Touch Imaging System (Bio-Rad Laboratories).

5.8.5 Flow cytometry

For flow cytometry analysis of cell surface marker, SSEA-3 was regularly used to assess hiPSC pluripotency. 5×10^5 to 1×10^6 fresh hiPSCs first were blocked in 1 mL FCS at 4 °C for at least 15 minutes. Then cells were split into two fluorescence-activated cell sorting (FACS) tubes, washed with 2 mL cold DPBS and centrifuged at 200 g for 2 minutes. Afterwards, cells were resuspended in 100 μL FACS buffer containing antibody and incubated on ice for 45 minutes.

Cells were then washed twice with 2 mL DPBS as described above to remove unbound antibodies. Finally, cells were resuspended in 250 µL cold DPBS. For the analysis of intracellular markers, NANGO and KLF4 were used to assess hiPSC pluripotency, and cTNT was used to determine CM differentiation efficiency. 4×10^5 hiPSCs or CMs were fixed in 4% formaldehyde (Roti-Histofix) for 20 minutes and the cell membrane was then permeabilized overnight in FACS buffer containing 5% fetal bovine serum, 0.5% saponin and 0.05% sodium azide. Afterwards, cells were split into two FACS tubes and stained with respective antibodies as described above. An appropriate isotype antibody was used as a negative control. Finally, cells were analyzed with FACSCanto II Flow Cytometer (BD Biosciences) in FACS Core Facility (UKE, Hamburg, Germany). Acquired data were analyzed with FlowJo V7 or FASCDiva.

5.8.6 Immunohistochemistry and immunofluorescence

First, for relaxation of EHTs, 40 mM KCl or 30 mM BDM was added into the medium until EHTs stopped beating. EHTs were then washed with DPBS and fixed in 4% formaldehyde overnight at 4 °C. EHTs were gently removed from the silicon posts and transferred to a 2 mL microtube containing 1 mL TBS-sodium azide for long-term storage at 4 °C.

For longitudinal sections, the EHTs in the 2 mL microtubes were directly passed to Dr. Kristin Hartmann (Mouse Pathology Core Facility, UKE, Hamburg, Germany) for further procedures. In brief, EHTs were dehydrated and embedded in paraffin using Leica ASP300S tissue processor with Leica EG1160 embedding station. Paraffin tissue sections were then cut at 2 µm. H&E staining was performed according to standard procedures. Alternatively, sections were processed for immunohistochemical staining. After dewaxing and inactivation of endogenous peroxidases in DPBS/3% hydrogen peroxide, antibody-specific antigen retrieval was carried out using the Ventana Benchmark XT machine (Ventana). Sections were then incubated with primary antibodies for 1 hour. UltraView Universal DAB Detection Kit (Roche) was used for secondary antibody, which contained both anti-mouse and anti-rabbit secondary antibodies. To stain dystrophin in cross-sections, each EHT was embedded in 4% (w/v) agarose/DPBS in a well of a 6-well plate. After agarose solidification, agarose containing the EHT was cut out and transferred into a 2 mL microtube filled with DPBS for further staining processes. All microscopic images were acquired with LEICA DMD 108 microscope (LEICA).

For immunofluorescence staining of EHT vibratome sections, fixed EHTs were first embedded in 4% agarose. EHT sections were cut at 100 µm by Leica VT1000 S Vibrating blade microtome

(Leica). Sections were blocked in antibody solution with 10% goat serum at room temperature for 1.5 hours, then incubated with primary antibodies overnight at 4 °C. After 3 times washing with DPBS, sections were incubated with secondary antibodies and DAPI at room temperature for 1.5 hours. Finally, stained EHTs were washed 3 times with DPBS and embedded in Fluoromount-G (Invitrogen) in HistoBond microscope slides (Marienfeld). To stain hiPSCs or CMs in 96-well plates, cells were first fixed in 4% formaldehyde overnight. Subsequent staining procedures were same as vibratome sections staining. All immunofluorescence images were captured using the laser scanning microscope Zeiss LSM 800 (Zeiss).

5.8.7 Glucose and lactate quantification

To quantify glucose consumption and lactate production of EHTs, the concentrations of glucose and lactate in EHT culture medium were measured with an ABL90 FLEX blood gas analyzer. 0.5 mL medium were injected into the instrument with a 1 mL syringe. Glucose consumption was calculated with the formula: 5 mM (glucose concentration from fresh medium) - glucose concentration in each culture medium. Lactate production/glucose consumption ratio was calculated to estimate the anaerobic and aerobic respiration.

5.8.8 Troponin I measurement

For cardiac troponin I quantification, 3-day old culture medium was collected, and a two-step ARCHITECT STAT High Sensitive Troponin-I immunoassay was carried out. This work was kindly done by the working group of Prof. Tanja Zeller (Molecular Cardiology, University Heart and Vascular Center Hamburg, Hamburg, Germany).

5.8.9 DNA methylation measurement

After transfection of split-dCas9-DNMT3A with specific gRNAs targeting *ILST6* in HEK 293 cells, genomic DNA was extracted using DNeasy Blood & Tissue kit (QIAGEN). The DNA concentration was then quantified using Qubit dsDNA BR Assay kit (Life technologies) on a Qubit 3.0 Fluorometer (Life technologies). 200 ng DNA were used for bisulfite-conversion reaction with EZ DNA Methylation-Gold kit (Zymo Research) according to the manufacturer's instructions. In brief, 20 µL DNA samples were mixed well with 130 µL CT Conversion Reagent and incubated in a thermal cycler at 98 °C for 10 minutes, 64 °C for 2.5 hours and 4 °C for up to 20 hours. Afterwards,

DNA samples were bound to Zymo-Spin IC Coulumn pretreated with M-Binding Buffer. After washing, desulphonation and elution, PCR amplification of the targeted region was performed using EpiMark Hot Start Taq Polymerase (NEB) according to the manufacturer's instructions. The primer information is listed in table S8. The desired PCR products were cloned into a pMiniT 2.0 vector using NEB PCR Cloning kit (NEB) and 10 clones for each PCR product were sequenced by Microsynth Seqlab. Finally, unmethylated cytosine was represented as thymine in the sequencing results. DNA methylation level was calculated based on the percentage of cytosine vs cytosine + thymine at positions where cytosine would be expected in the reference sequence.

5.9   High throughput sequencing

5.9.1   ATACseq

To assess the chromatin openness state at different regions, ATACseq was performed according to a previously published protocol (Jonsson et al. 2016). Each EHT was dissociated into single cells with papain solution (section 5.6.9). After counting, 25,000 living cells were washed with 1 mL cold DPSB and centrifuged at 500 g for 5 minutes at 4 °C. The cells were then resuspended in 100 µL ATAC-lysis buffer per sample (5 µL 10% NP40, 5 µL 10% Tween 20, 0.5 µL 1 % digitonin, 89.5 µL ATAC-resuspension buffer), and incubated on ice for 10 minutes. 1 mL cold ATAC-resuspension buffer containing 0.1% Tween 20 was then added to wash out the lysis buffer. The resulting nuclei were pelleted at 500 g for 5 minutes and resuspended in 50 µL transposition reaction mixture containing 25 µL of 2x TD buffer, 16.5 µL of DPBS, 5 µL H_2O, 0.5 µL of 1% digitonin, 0.5 µL of 10% Tween-20 and 2.5 µL of transposase (Illumina Tagment DNA enzyme 1). The reaction was incubated at 37 °C for 30 minutes with 1000 rpm shaking. DNA was then extracted using the NEB Monarch PCR & DNA clean up kit (NEB) and stored at -20 °C. The further steps were kindly performed by Dr. Chukwuemeka George Anene-Nzelu at the Genome Institute of Singapore in Singapore. For library preparation, PCR reactions were performed using the Illumina/Nextera primers and followed by Ampure XP beads clean up. The resulting library was sequenced on Novaseq sequencing instrument (Illumina). Data analysis was performed by Dr. Mick Lee (Genome Institute of Singapore, Singapore) and Dr. Wen Wang (Tong Ji University, Shanghai, China).

5.9.2 RNAseq

The remaining cells from the ATACseq preparation were used for total RNA extraction using TRIzol reagent (section 5.8.2). The following steps were kindly performed by Dr. Chukwuemeka George Anene-Nzelu. In brief, RNA concentration and quality were determined using the Agilent 2100 RNA Nano Chip. RNA sequencing libraries were prepared using the Illumina TruSeq stranded mRNA kit according to the manufacturer's instructions. Libraries were sequenced on a Novaseq sequencing instrument to a depth of 25 million 150 bp paired-end reads per biological sample. Data analysis was performed by Dr. Mick Lee. Fastq files were aligned against the human reference genome (hg38) using the STAR aligner tool with default parameters. Differential gene expression analysis was performed using EdgeR.

5.9.3 ChIPseq

The H3K27ac ChIP-seq and QC protocol used in this work has been previously published (Tan et al. 2020). Briefly, EHTs were dissociated into single cells with papain solution (section 5.6.9). Cells were cross-linked with 1% formaldehyde for 10 minutes at room temperature, subsequently quenched with glycine (125 mM) for 5 minutes at room temperature and rinsed twice with cold DPBS. The following steps were performed by Dr. Chukwuemeka George Anene-Nzelu at the Genome Institute of Singapore. Cells were lysed in lysis buffer (50 mM Tris-HCl, pH 7.5, 150 mM NaCl, 1 mM EDTA, 0.1% sodium deoxycholate, 1% Triton X, 0.1% SDS, 1x protease inhibitor) and centrifuged at 4000 rpm for 10 min at 4 °C to collect the nuclei pellet. Nuclei were microscopically inspected after each preparation. Nuclei were lysed in nuclei lysis buffer (50 mM Tris-HCl, pH 7.5, 150 mM NaCl, 1 mM EDTA, 1% Triton X, 0.1% sodium deoxycholate, 1% SDS, 1x protease inhibitor) and sonicated with a Bioruptor sonicator device (Diagenode) to obtain chromatin fragments between 200 to 500 bp. Sheared chromatin was immunoprecipitated with 5 µg H3K27ac antibody (Abcam) with 50 µL protein G beads (Invitrogen) overnight at 4 °C. Beads were then washed and eluted in 200 µL of elution buffer (50 mM Tris-HCl, pH 7.5 and 10 mM EDTA). De-crosslinked was performed overnight at 65 °C. Pulldown DNA was purified by ethanol precipitation with standard Phenol-Chloroform extraction. Library preparation was carried out with the NEB Ultra II Library Preparation kit according to the manufacturer's protocol. 10-12 PCR cycles were performed using indexed primers. The libraries with 300 to 500 bp were selected and underwent paired-end sequencing at 2 x 150 bp read length on an Illumina Novaseq sequencing instrument. Data analysis was kindly performed by Dr. Mick Lee and Dr. Wen Wang.

5.10 Statistics

Statistical analyses of the results were conducted with GraphPad Prism 7. Data are presented as mean ± SEM. Differences between groups were analyzed by unpaired t-test, one or two-way ANOVA plus Bonferroni's multiple comparisons test when appropriate. A P-value less than 0.05 was considered to be statistically significant.

6   Results I: Establishment of a chronic tachypacing model in atrial-like EHT

6.1   Characterization of VChR1-iPSC

In the first part of this study, we employed VChR1 that is a type of ChR for chronic optical tachypacing of atrial-like EHTs to model AF and to study the effects in human atrial-like EHTs with high beating frequency. In order to obtain atrial-like CMs expressing VChR1, the transgene VChR1 was inserted into the hiPSCs genome, and VChR1-iPSCs were then differentiated into atrial-like CMs to generate atrial-like EHTs. The VChR1-iPSC line was obtained by CRISPR/Cas9 cleaving the safe harbor AAVS1 locus and inserting the transgene VChR1 with homology-directed repair. The genome editing work was done by Dr. Tim Stüdemann, as a part of his doctoral thesis. The donor plasmid was constructed by inserting the expression cassettes of puromycin resistance and Luc-VChR1-EYFP between 3' and 5' homology arms of the target site in the AAVS1 locus, which is used as a safe harbor for transgene integration in the human genome. Then, a specific gRNA (5' GTCACCAATCCTGTCCCTAG 3') was chosen to drive the DNA endonuclease Cas9 to cleave the targeted region, and the subsequent homology-directed repair led to the insertion of the transgene (figure 8). The transcription of the Luc-VChR1-EYFP fusion transcript is driven by a ubiquitously active promoter, the CAG promoter. The transcript encodes a fusion peptide including a luciferase, VChR1 and EYFP (figure 8). The luciferase was not used for this project but for other research purposes (Park et al. 2020).
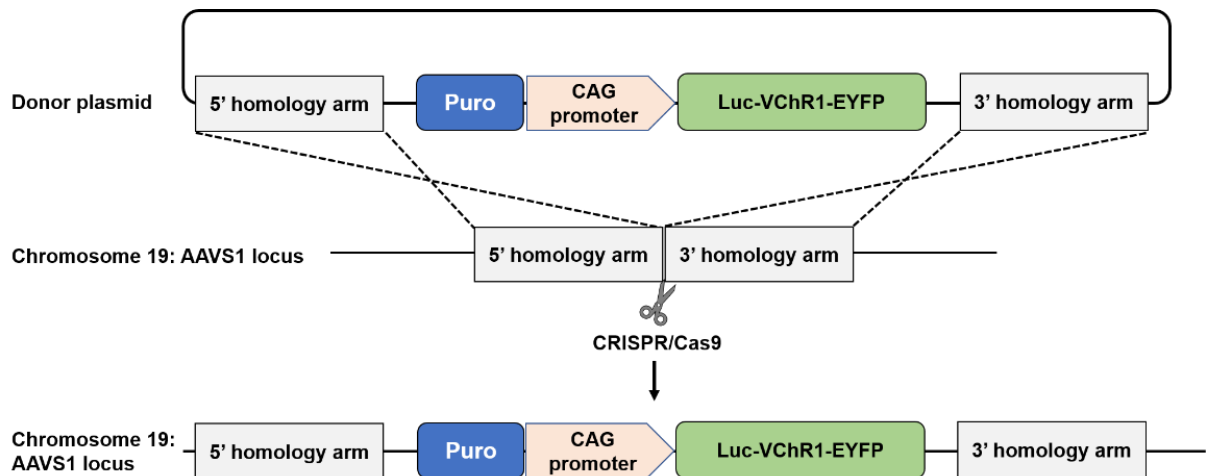

Figure 8: Generation of VChR1-iPSC line. Schematic illustration of the CRISPR/Cas9 strategy to insert the transgene VChR1 into the AAVS1 locus. Puro: the puromycin resistance cassette for the purpose of screening successfully edited clones.

Afterwards, a deep characterization of this cell line was carried out in the present study. During genome editing, a successfully edited clone of VChR1-iPSC (named LMO-AF10) was identified as heterozygous by several specific PCR reactions from genomic DNA. To distinguish the unedited allele from the knock-in allele, primers were designed to bind to outside and inside the inserted DNA (figure 9, top). The PCR product of the unedited allele (1373 bp) from primer pair HA-L for and HA-R rev was found in both ERC001 and LMO-AF10, indicating the presence of one unedited allele (figure 9, bottom). However, the whole insert (7077 bp) could not be amplified in the current PCR condition. The product (1321 bp) of the 5' homology arm and part of the insert was exclusively amplified with primers HA-L for and HA-L rev from the LMO-AF10 genome. Furthermore, the VChR1 region was amplified with primers Gaussia for and EYFP rev from the LMO-AF10 genome and the sequence was validated by Sanger sequencing. In addition, flow cytometry analysis and confocal microscopy both confirmed that the VChR1 tagged with EYFP was stably expressed in the iPSCs and mainly localized on the cellular membrane (figure 10).
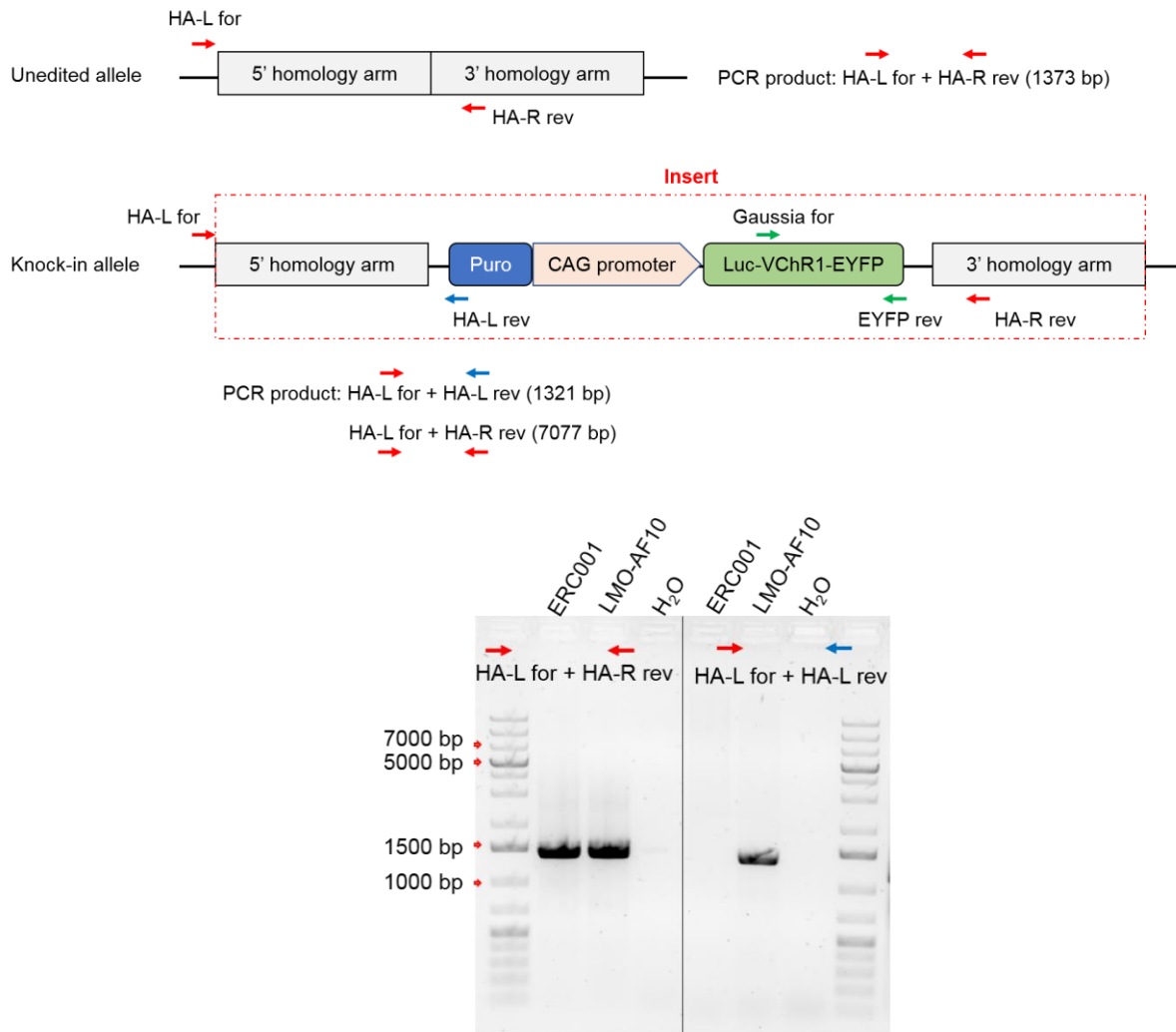
Figure 9: Insertion validation by PCR. Top: schematic illustration of primer binding sites and predicted PCR products in unedited and knock-in alleles. Primer binding sites are illustrated through red, blue and green arrows. Bottom: DNA agarose gel of PCR products by primer pairs HA-L for+HA-R rev, HA-L for+HA-L rev. Templates were genomic DNA from ERC001 and LMO-AF10 iPSCs. H_2O (no template) as negative control.
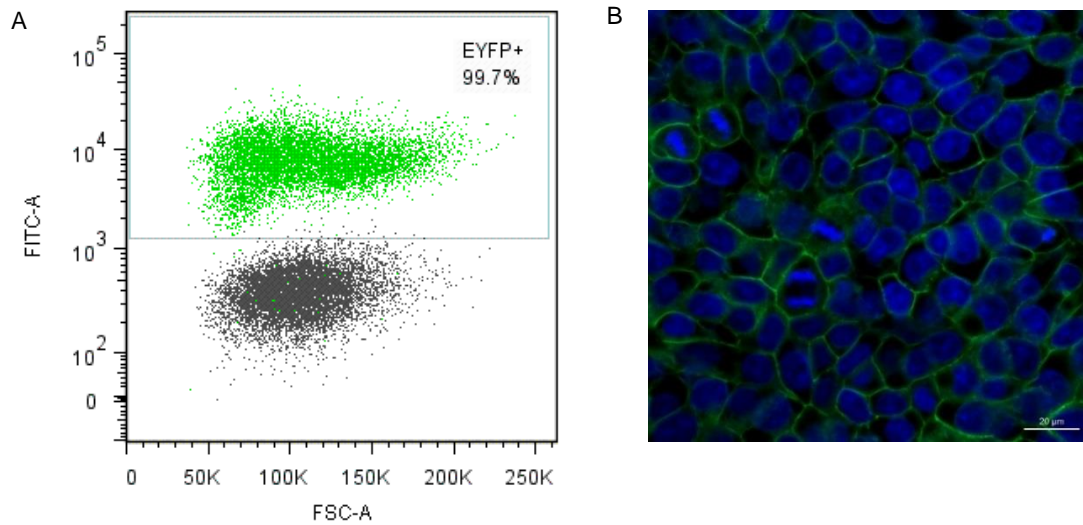
Figure 10: VChR1-iPSC line stably expressing EYFP. (A) Flow cytometry analysis of EYFP signal of VChR1 cells (green). ERC001 cells were used as the control for gating (grey). (B) Confocal image of VChR1-iPSCs. Green is VChR1-EYFP. Blue is the DAPI staining of nuclei. The scale bar is 20 μm.

Next, the quality of this iPSC line was assessed regarding sterility, pluripotency and karyotyping. Cells were maintained in an antibiotics-free medium and showed a negative mycoplasma test result (figure 11). The pluripotency status was assessed by analyzing the expression of marker proteins. To this end, cells were collected for flow cytometry analysis during expansion, or seeded into a 96-well plate with glass bottom and black walls for immunofluorescence microscopy (figure 12). The percentage of cells expressing the pluripotency markers SSEA-3, NANOG and KLF4 was assessed by flow cytometry and ranged between 93.1% and 98.7%. In addition, cells in the 96-well plate were fixed and stained for NANOG. Confocal microscopy images confirmed most of the cells expressing NANOG.
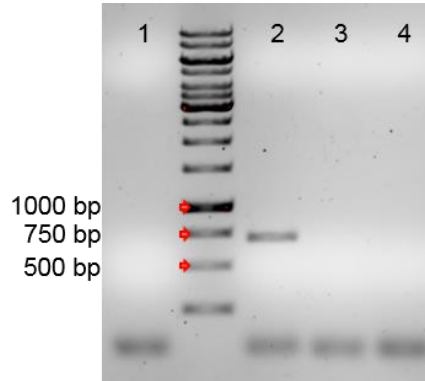
Figure 11: PCR-based mycoplasma test result. Lane 1: ERC001-iPSC, lane 2: positive control, lane 3: H$_2$O, lane 4: VChR1-iPSC.
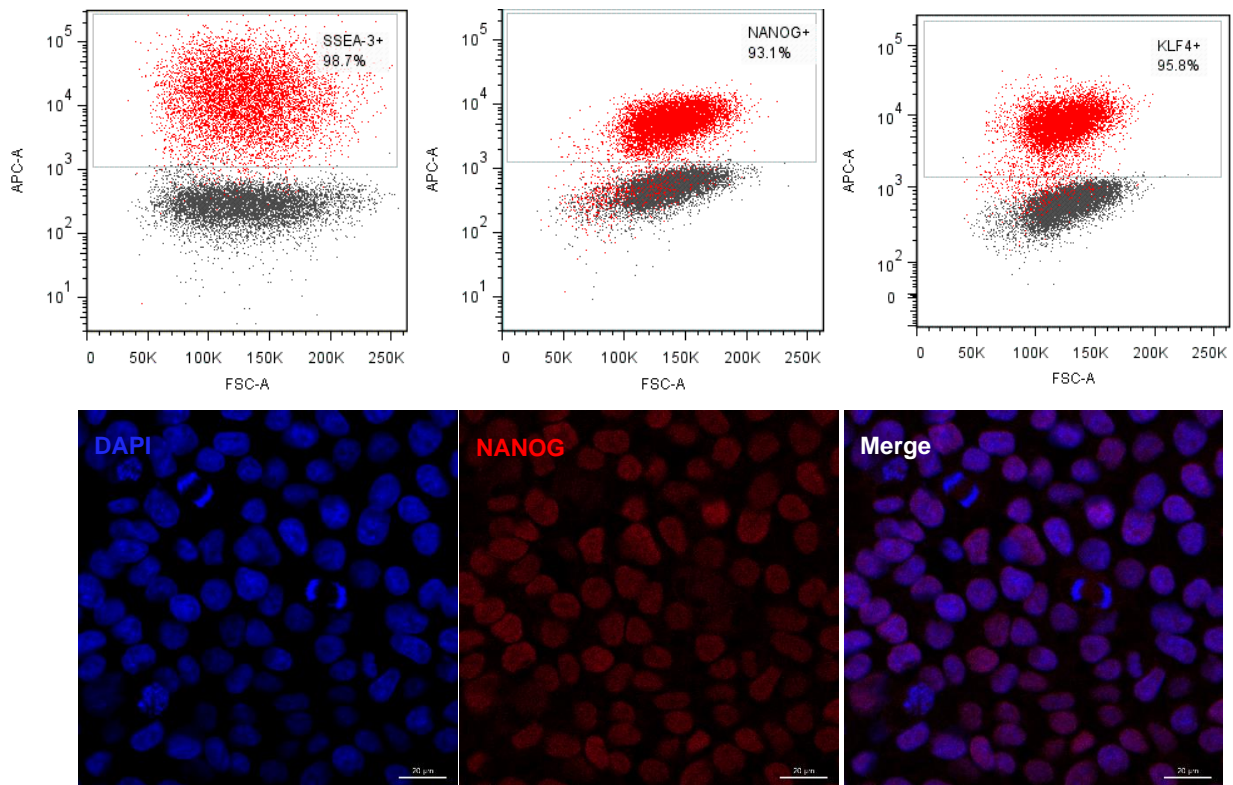
Figure 12: Expression of pluripotency markers in VChR1-iPSC. Top row: flow cytometry analysis. All antibodies were conjugated with the fluorochrome APC. The grey populations represent cells stained with an APC-labeled isotype control antibody for gating control. The red populations represent cells stained with anti-SSEA-3, NANOG and KLF4 antibodies from left to right. Bottom row: images of confocal microscopy. Staining of DAPI and NANOG. Blue is DAPI (nuclei). Red is NANOG. The scale bar is 20 µm.

Human iPSCs are prone to accumulate karyotypic abnormalities during long-term culture or genome editing. We thus investigated the karyotype of this cell line by two different methods: NanoString nCounter karyotype assay and G-banding cytogenetic analysis. In the nCounter assay, a panel of fixed content of probes were used to target invariant regions covering all human chromosomes. The copy number of all chromosomes was then analyzed and displayed no significant changes in probe number from each chromosome (figure 13, top). For G-banding, 15 cells in metaphase were karyotypically analyzed with 450-500 bands per haploid set resolution. The result confirmed a normal female karyotype (46, XX) without numerical or structural chromosomal aberrations (figure 13, bottom).
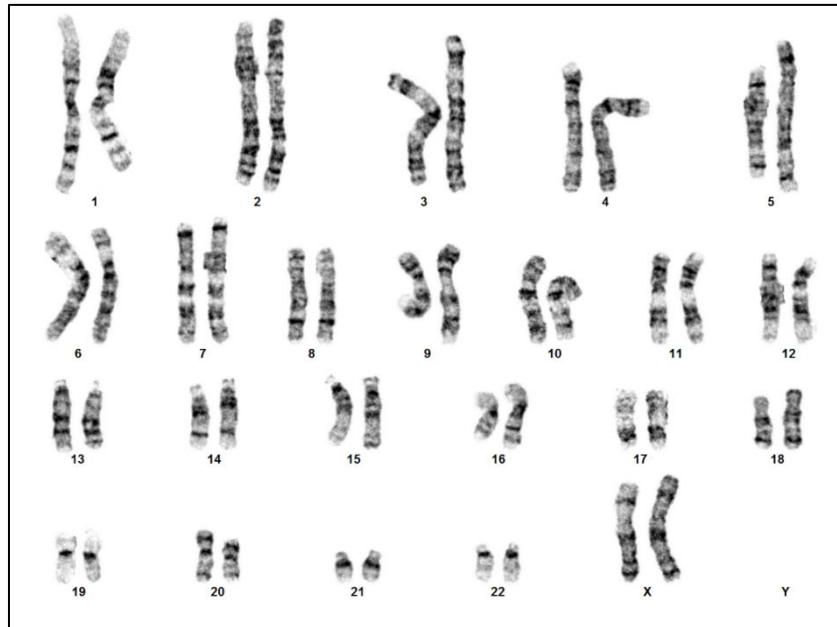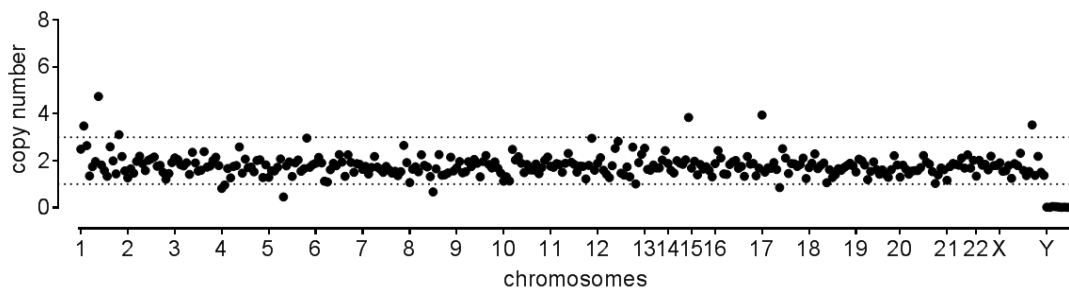

Figure 13: Karyotype of VChR1-iPSC. Cells were expanded at least 2 passages after thawing from the working cell bank. Top: NanoString nCounter karyotype assay. Each dot represents one probe. The copy number of targeted regions is 2 across all chromosomes, indicating a normal chromosome number. Bottom: cytogenetic analysis by G-banding. It shows a normal female karyotype (46, XX).

6.2 Optimization of atrial-like cardiomyocyte differentiation

6.2.1 Optimization of embryoid body-based differentiation protocol

The differentiation of atrial-like CMs was conducted by adding RA (1 μM) at the cardiac induction stage in a standard EB-based protocol established previously (Lemme et al. 2018). The CMs and EHTs generated before with this protocol had displayed high expression of atrial-selective markers on both the mRNA and protein levels. However, the electrophysiological properties of atrial-like EHTs only partially resembled those of the human atrium in sinus rhythm (Wettwer et al. 2004; Lemme et al. 2018). Meanwhile, Lee and colleagues had shown that a high concentration of activin A inhibited the deviation of the atrial lineage (Lee et al. 2017). Hence, we aimed to optimize the current atrial differentiation protocol using different concentration combinations of growth factors (BMP4 and activin A) in the present study. CMs from the standard EB-based protocol with 10 ng/mL BMP4 + 3 ng/mL activin A were used as a control group. CMs from the differentiation procedure with RA treatment were defined as a RA group. Three different RA groups were created: 10 ng/mL BMP4 + 3 ng/mL activin A (10B/3A+RA), 6 ng/mL BMP4 + 2 ng/mL activin A (6B/2A+RA), and 3 ng/mL BMP4 + 2 ng/mL activin A (3B/2A+RA). Two differentiation batches of VChR1-iPSC and two batches of ERC001-iPSC were conducted in total.

First, the gene expression of atrial and ventricular markers, *MYL7* (MLC2A) and *MYL2* (MLC2V), was assessed in control-CMs and RA-CMs after cardiac differentiation. Moreover, the ratio of *MYL7*/*MYL2* was compared between control and RA groups. We observed similar results from each batch of both iPSC lines. Results from one batch are shown here (figure 14). Cells from all differentiation groups had a certain degree of expression of *MYL7*, which is both an atrial marker and an immaturity marker (Bedada et al. 2014). Importantly, the control group showed a high expression level of the ventricular marker *MYL2*, while all RA groups had very low expression of *MYL2*. Moreover, in line with previous results from our institute, CMs from RA groups had a high ratio of *MYL7*/MYL2, while control groups had a low ratio.
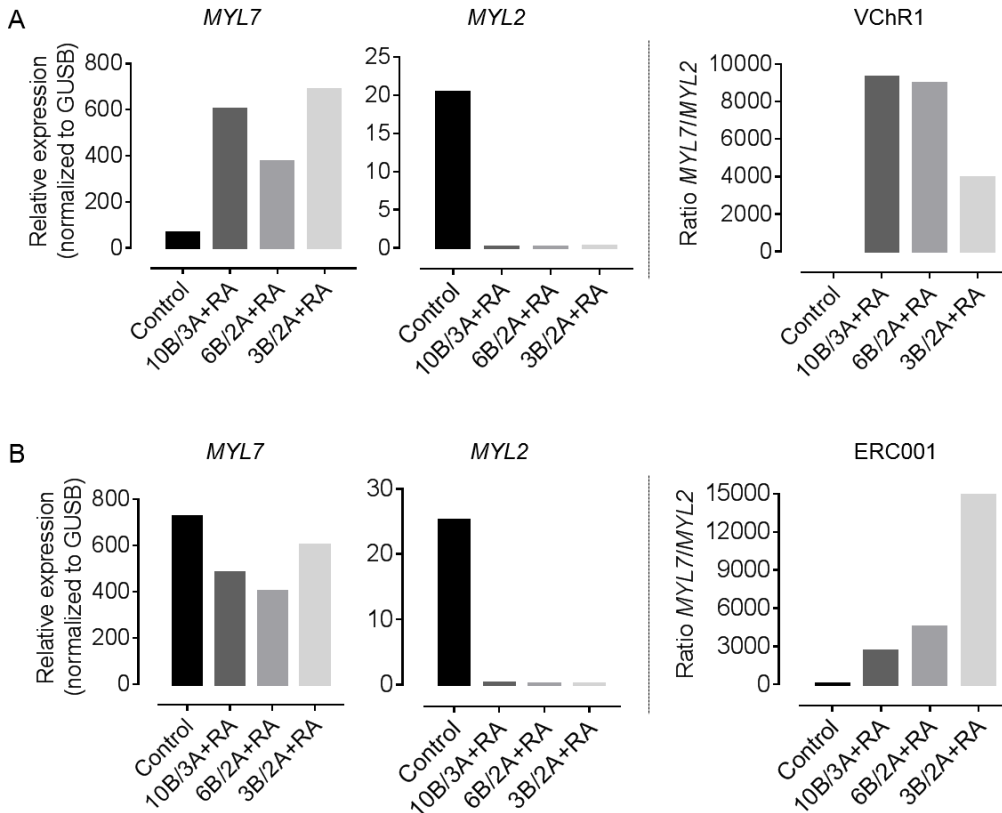
Figure 14: Gene expression analysis of *MYL7* and *MYL2* by qPCR for different EB-based differentiation protocols. CMs samples from control and RA groups were processed directly after differentiation. Ct values of target genes were normalized to the housekeeping gene GUSB. 2^-delta Ct is shown. Ratios of *MYL7*/*MYL2* were calculated and displayed on the right panel. (A) VChR1-CM. (B) ERC001-CM.

Since the expression of marker genes does not perfectly correspond to typical atrial action potentials in sinus rhythm, electrophysiological experiments were conducted to further evaluate the atrial features of CMs from RA groups. To this end, EHTs were generated after cardiac differentiation. RA-EHTs showed a higher spontaneous beating frequency than control-EHTs in a previous study (Lemme et al. 2018). Similarly, EHTs from all RA groups of both cell lines beat faster than those from the control group in the present study (figure 15). Next, APs of ERC001-RA-EHTs were recorded using standard sharp microelectrodes, with and without pharmacological treatment. The baseline APs from all RA groups displayed spike-and-dome shapes, with short APD at 20% of repolarization (APD$_{20}$, varying from 3.04 to 9.17 ms) and negative plateau potentials (varying from -18.65 to -9.94 mV; figure 16). Moreover, the selective blocker of atrial

ultra-rapid outward current I_{Kur}, 4-AP, was applied to the RA-EHTs during AP recording. In accordance with previous results, in the presence of 4-AP (50 μM), APD_{20} was prolonged and the plateau potentials were shifted to more positive values (figure 16). However, changes in APD_{90} of the three RA groups differed. Only in the 3B/2A+RA group, a significant decrease of APD_{90} was observed (from 138.5 ± 8.4 to 107.1 ± 4.4 ms; figure 16). The acetylcholine-activated potassium current $I_{K,ACh}$ is a hallmark of atrial CMs and can be activated by CCh. In the presence of 10 μM CCh, all RA-EHTs had a shortened APD (figure 17). Taken together, the 3B/2A+RA protocol yielded more atrial-like EHTs, especially the effect of 4-AP with prolonged APD_{20} and shortened APD_{90} resembled APs in sinus rhythm.
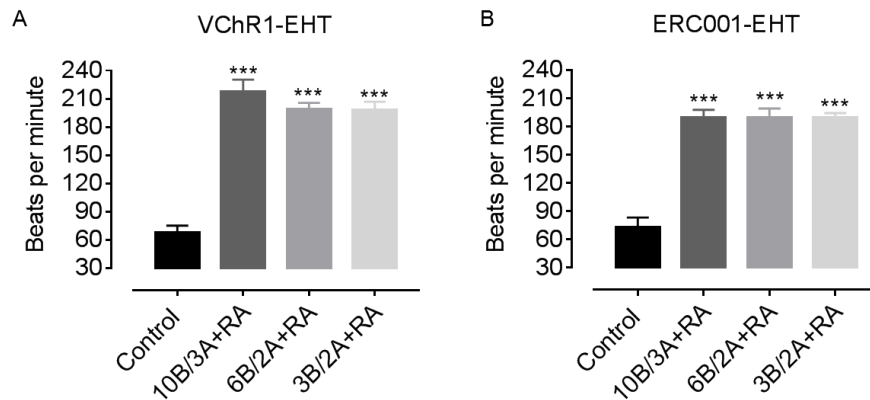
Figure 15: EHT Beating frequency. EHTs (from day 24 to day 30) from control and RA groups were compared. (A) VChR1-EHT, n=4 from one batch. (B) ERC001-EHT, n=6-8 from 2 batches. Data are presented as mean ± SEM. ***p<0.001 by one-way ANOVA plus Bonferroni's multiple comparisons test.
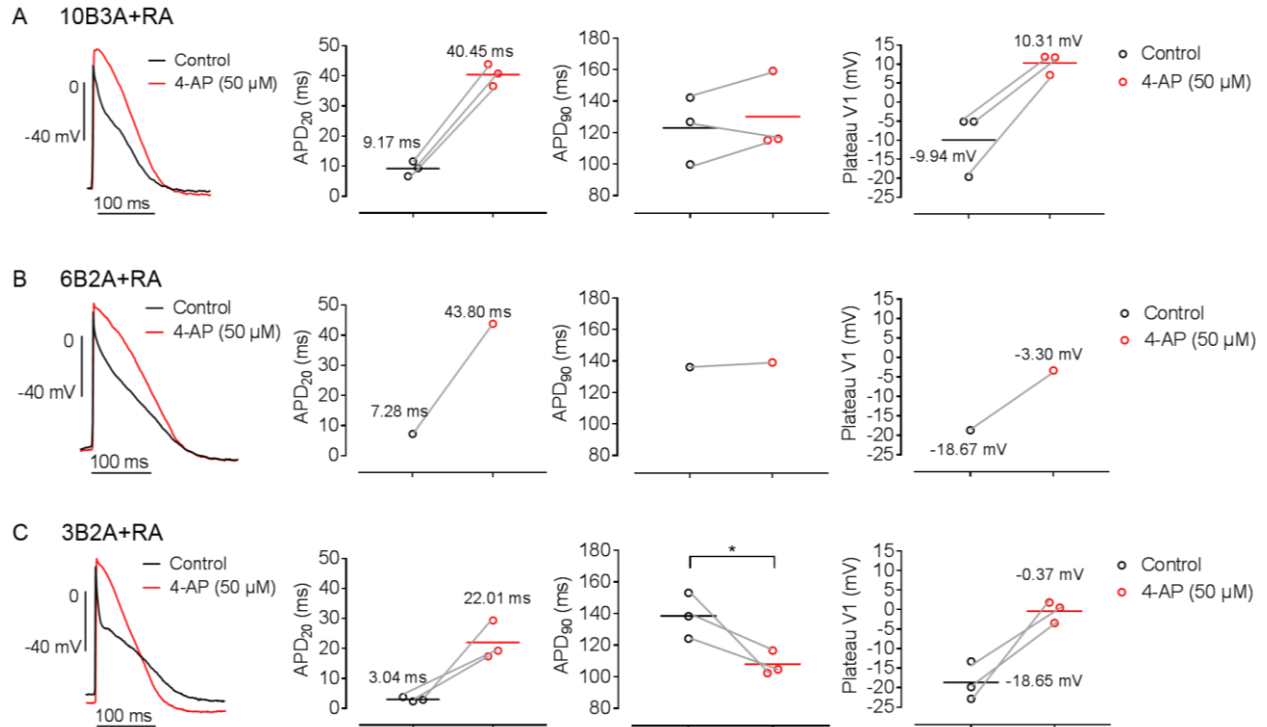
Figure 16: Effect of 4-aminopyridine on action potentials. ERC001-RA-EHTs were from the three RA groups from day 30 to day 40. APs were recorded with sharp microelectrodes before and after 15 minutes exposure to 50µM 4-AP. From left to right panels: representative AP shapes, changes of APD at 20% and 90% of repolarization (APD_{20} and APD_{90}), and plateau potentials (Plateau V1). Line represents mean of each group. Circle represents individual EHT. (A) Group 10B/3A+RA. (B) Group 6B/2A+RA. (C) Group 3B/2A+RA. *$p<0.05$ by unpaired t-test.
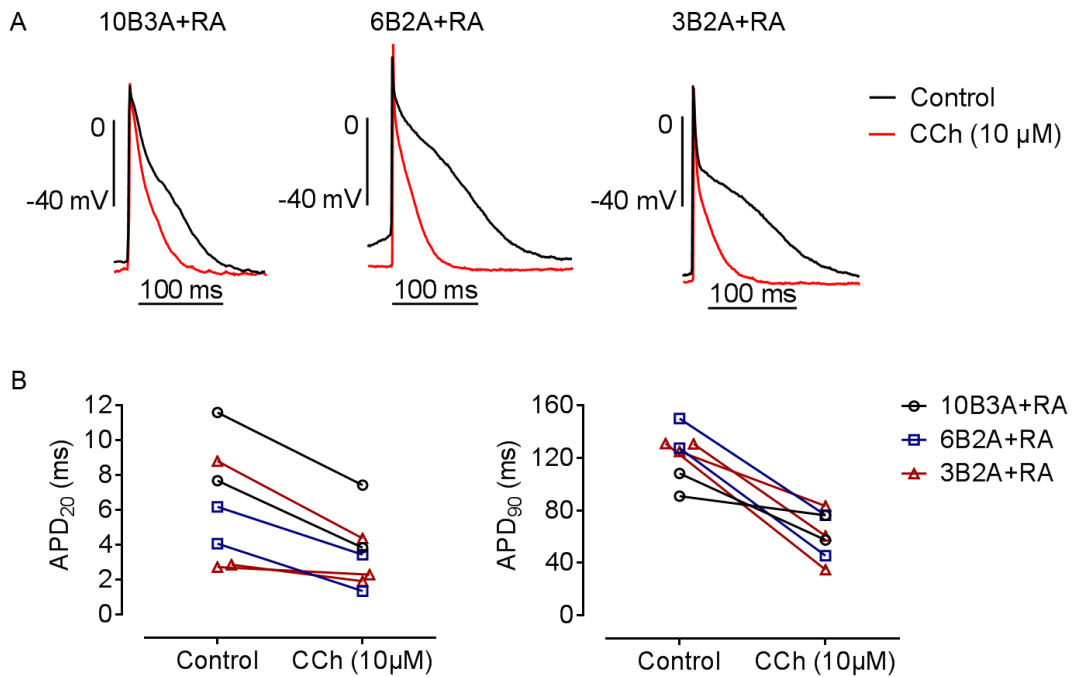
Figure 17: Effect of carbachol on action potentials. ERC001-RA-EHTs from the three RA groups from day 30 to day 40. APs were recorded with sharp microelectrodes before and after 2 minutes exposure to 10 µM CCh. n=2-3 EHTs per group. (A) Representative AP shapes. (B) Changes of APD_{20} and APD_{90} in individual EHT. All EHTs displayed shortened APD_{20} and APD_{90}.

6.2.2 Optimization of monolayer-based differentiation protocol

In a previous study, RA treatment was also used to induce atrial subtype specification in monolayer-based CM differentiation (Cyganek et al. 2018). Generally, monolayer-based differentiation is less laborious than EB-based differentiation. Therefore, we applied RA treatment in two well-established monolayer-based protocols for ERC001 and VChR1-iPSC lines in the present study. In protocol I, mesodermal lineage was induced with growth factors activin A and BMP4, while in protocol II mesodermal induction was conducted with CHIR99021 (figure 18; Lian et al. 2013; Mosqueira et al. 2018). To carry out atrial differentiation based on these two protocols, two different concentrations (0.5 µM and 1 µM) of RA were introduced at the cardiac induction stage, but without changes in mesodermal induction. In line with results from the EB-based protocol, VChR1-RA-CMs and ERC001-RA-CMs displayed high *MYL7*/*MYL2* ratio in all RA groups from two monolayer-based protocols (figure 19). The difference of relative level of *MYL2*

between control and RA groups in the VChR1 cell line from protocol I was not as pronounced as that in the ERC001 cell line from protocol I and II (figure 19). Spontaneous beating frequency of RA-EHTs was higher than that of control-EHTs from two protocols (figure 20). However, EHTs from protocol I beat faster than respective EHTs from protocol II (figure 20).
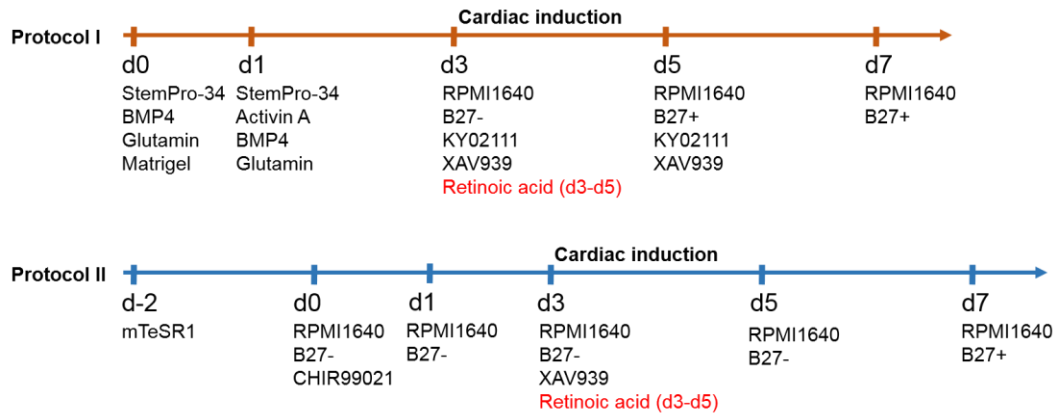
Figure 18: Schematic of monolayer-based differentiation protocols. 0.5 μM and 1 μM of RA were included at the cardiac induction stage in both protocols. Protocol I: StemPro-34 medium, growth factors (activin A and BMP4) and WNT inhibitors (KY02111 and XAV939). Protocol II: mTeSR1 medium, GSK3 inhibitor (CHIR99021) and XAV939.
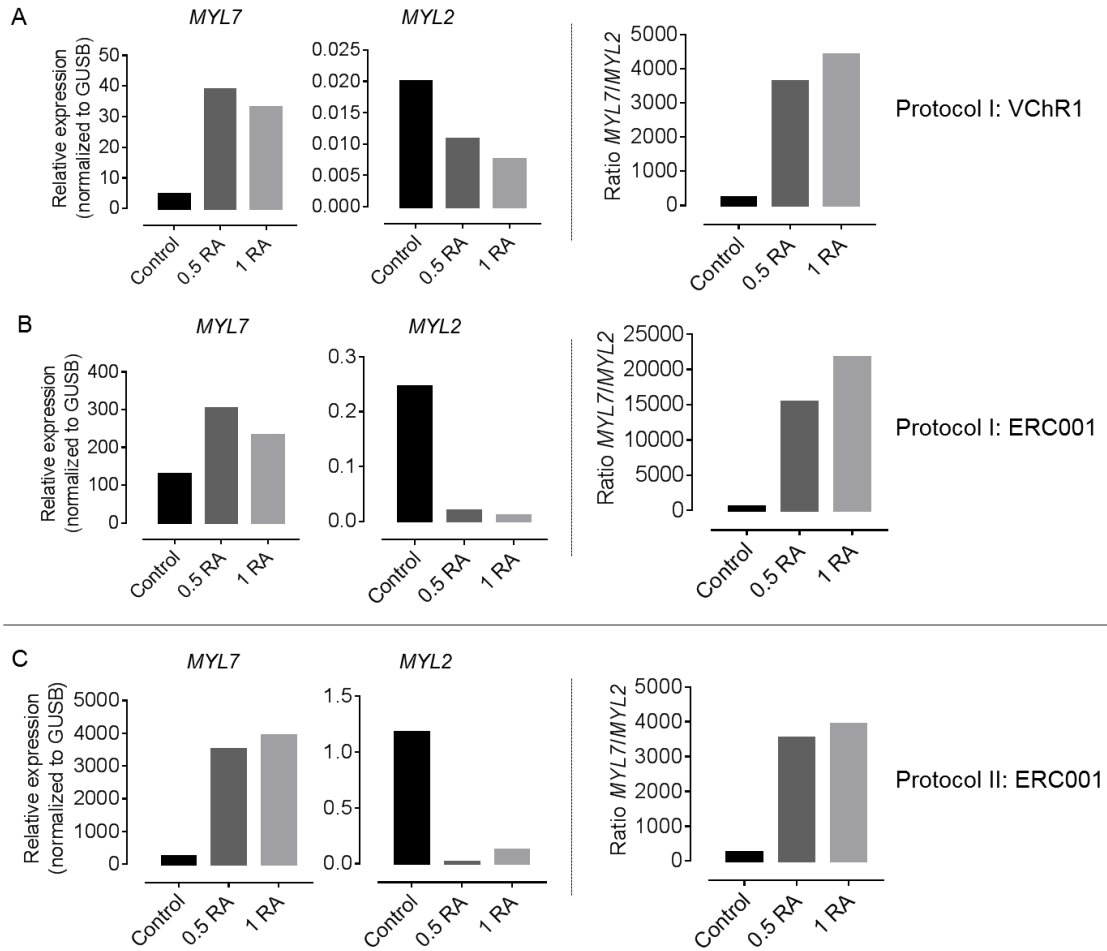
Figure 19: Gene expression analysis of *MYL7* and *MYL2* by qPCR for monolayer differentiation protocols. 0.5 RA: 0.5 µM RA. 1 RA: 1 µM RA. CMs samples were processed immediately after differentiation. Ct values of target genes were normalized to the housekeeping gene GUSB. 2^-delta Ct is shown. Ratios of *MYL7*/*MYL2* are displayed on the right panel. (A) Protocol I: VChR1-CMs. (B) Protocol I: ERC001-CMs. (C) Protocol II: ERC001-CMs.

Protocol I: ERC001
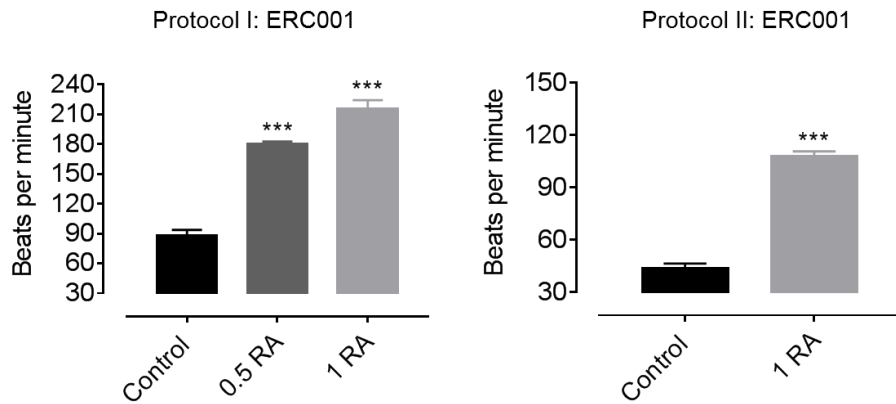
Protocol II: ERC001

Figure 20: Beating frequency of EHTs generated from monolayer-based protocols. Contractility of EHTs from ERC001-CMs was measured after 3 weeks of culture (n=4 from one batch for both protocols). 0.5 RA: 0.5 µM RA. 1 RA: 1 µM RA. Data are presented as mean ± SEM. ***$p < 0.001$ by one-way ANOVA plus Bonferroni's multiple comparisons test.

A Protocol I: 0.5 RA   Protocol I: 1 RA   Protocol II: 1 RA

B
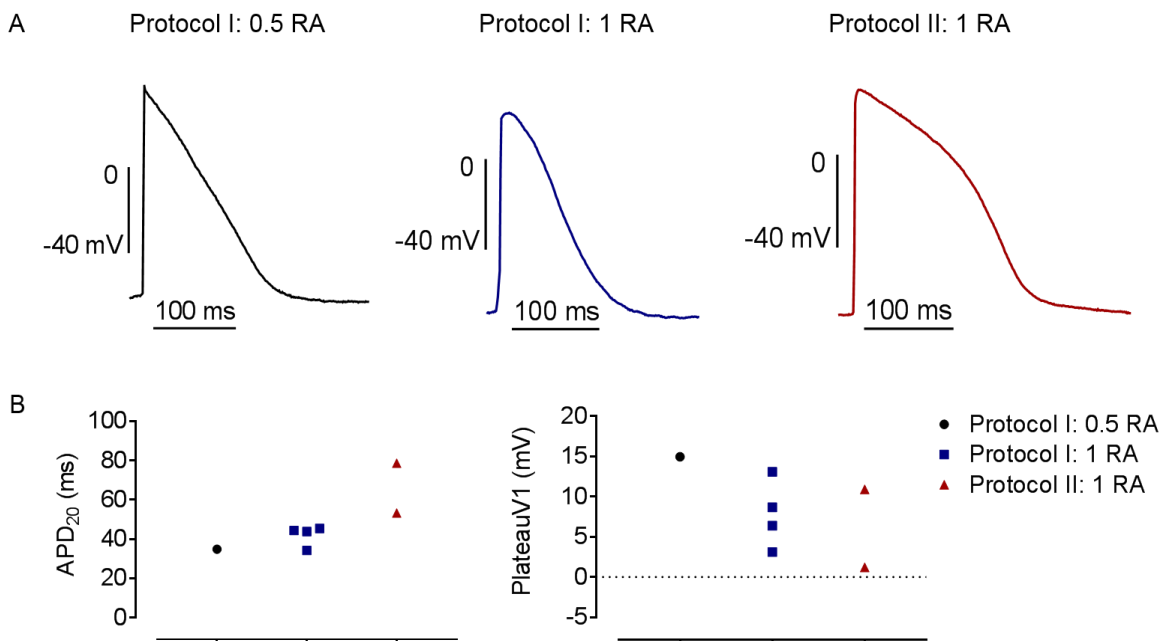
Figure 21: Characteristics of action potentials of ERC001-RA-EHTs generated from monolayer protocols. (A) Representative examples of AP from each RA-EHT group. (B) Left: AP duration at 20% repolarization (APD$_{20}$). Right: plateau potential (PlateauV1).

The results of monolayer-based protocols were similar to the EB-based protocols in terms of gene expression and EHT beating frequency. However, APs of RA-EHTs from monolayer-based protocols displayed atypical and triangular shapes, long APD_{20} (above 20 ms) and large plateau potentials (above 0 mV; figure 21). Therefore, RA-EHTs from monolayer-based protocols with tested conditions were not electrophysiologically close to the human atrium.

6.3   Generation and characterization of VChR1 atrial-like CMs and EHTs

Based on the results above, the 3B/2A+RA EB-based differentiation protocol was used to produce atrial-like CMs for this project, while the established standard EB protocol was used to produce control CMs (ventricular-like). Next, EHTs from VChR1-CMs were generated and deeply characterized after cardiac differentiation. First, CMs from both control and RA groups were seeded in 96-well plates for monolayer culture. After 4 weeks of spontaneous maturation, the expression of myosin light chain isoforms 2a (MLC2A, atrial isoform) and 2v (MLC2V, ventricular isoform) was examined by immunofluorescence staining. Similar to the characterization results of ERC001-CMs and human cardiac tissues (Lemme et al. 2018), Ctrl-CMs showed a high expression level of MLC2V and a low expression level of MLC2A, while RA-CMs displayed the opposite expression pattern (figure 22). In addition, the expression of the cation channel VChR1 was observed in the CMs through the EYFP fluorescence signal (figure 22).
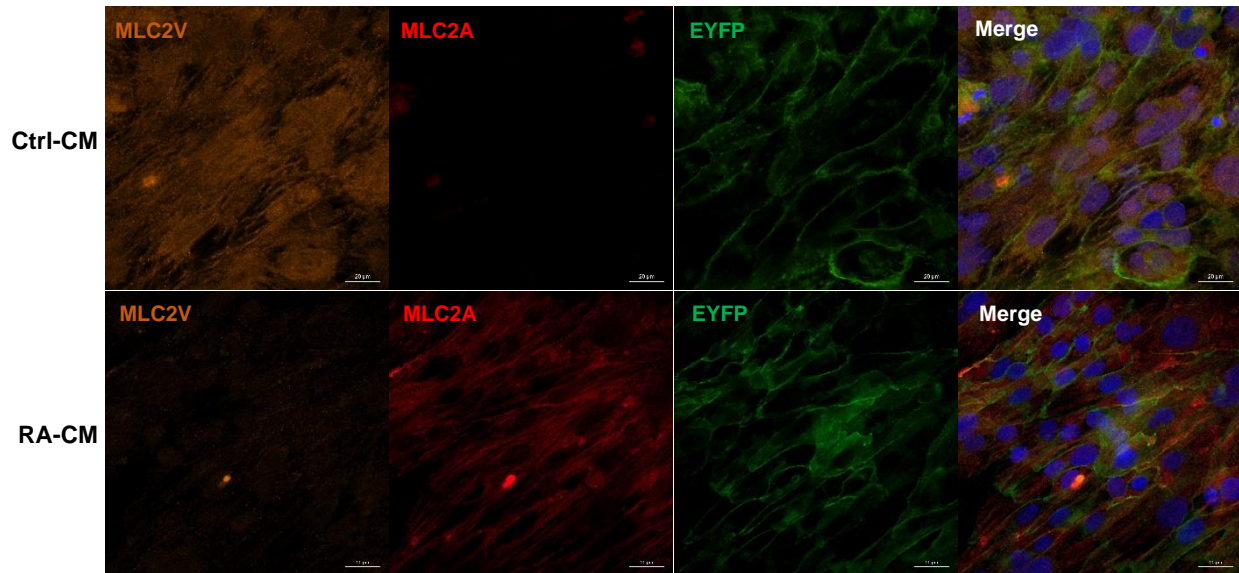
Figure 22: Immunofluorescence of MLC2V and MLC2A in CMs derived from VChR1-iPSC. Confocal images of monolayer CMs from control and RA groups at day 30. Staining of MLC2V (orange), MLC2A (red) and DAPI (blue). EYFP represents VChR1. The scale bar is 20 μm.

More experiments to characterize the atrial phenotype were then performed in VChR1-EHTs as quality control, as previous experiments had indicated a variable degree of atrial features after differentiation. Several ventricular and atrial specific markers were analyzed by qPCR in VChR1-Ctrl-EHTs and VChR1-RA-EHTs at day 30. Compared to Ctrl-EHTs, RA-EHTs showed significantly lower abundance of ventricular markers (*MYL2* and *IRX4*) and higher abundance of atrial markers (*NPPA*, *MYL7*, *KCNJ3*, *KCNA5*, *NR2F1*, *NR2F2* and *PITX2*; figure 23). The protein levels of MLC2V, MLC2A and ANP were assessed by immunohistochemical staining (figure 24). Due to the technical obstacles of AP recording in light-sensitive VChR1-EHTs, AP signals were not stable for an adequate time to allow for atrial specific drug application and parallel AP recording. At baseline, however, VChR1-RA-EHTs displayed a typical atrial AP shape with short APD_{20} and negative plateau potential (figure 25).
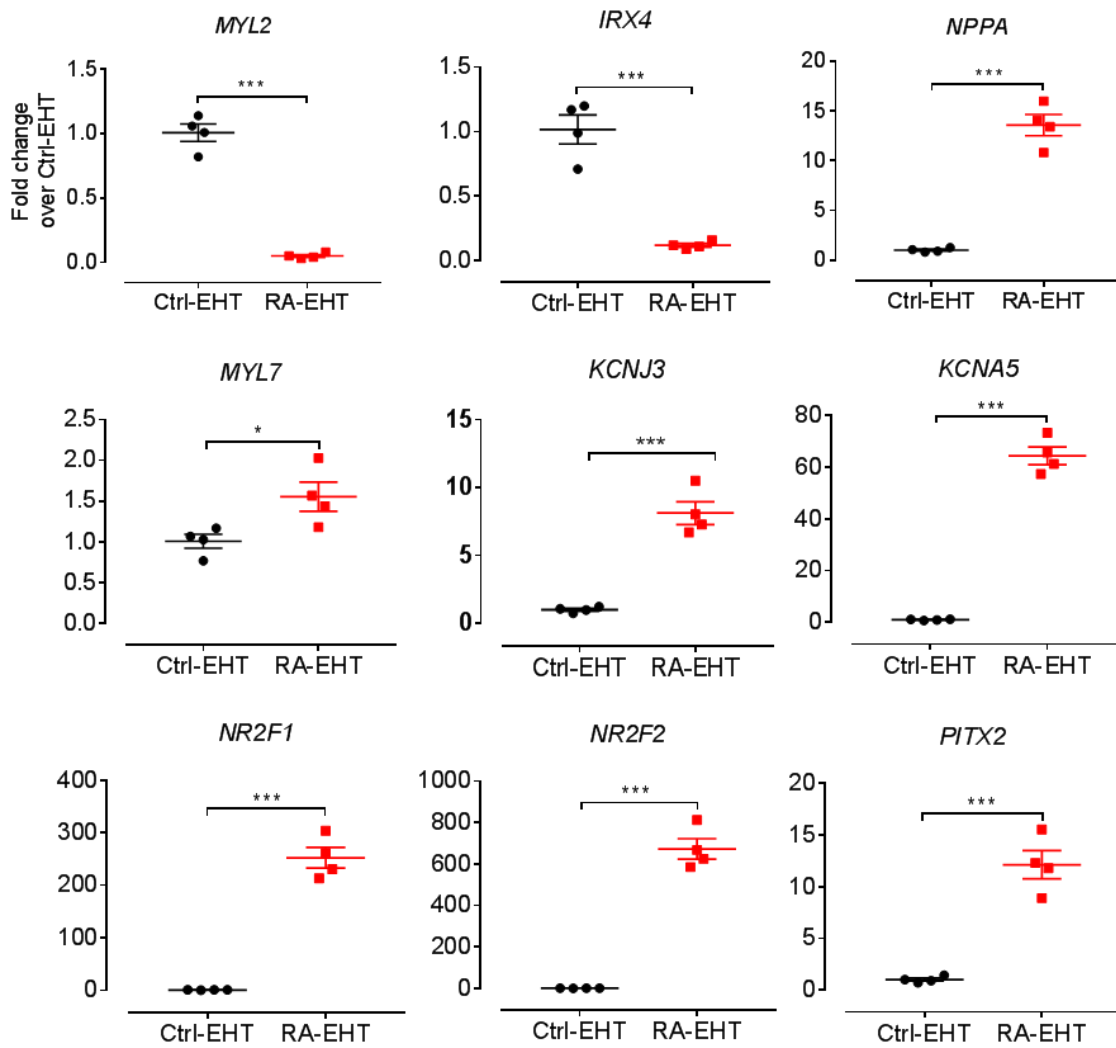
Figure 23: Gene expression analysis of VChR1-Ctrl-EHTs and VChR1-RA-EHTs. qPCR of selected ventricular *(MYL2* and *IRX4)* and atrial (*NPPA*, *MYL7*, *KCNJ3*, *KCNA5*, *NR2F1*, *NR2F2* and *PITX2*) marker genes in VChR1-Ctrl-EHTs and VChR1-RA-EHTs at day 30 (n=4 from 3 batches). Ct values of target genes were normalized to housekeeping gene GUSB and to Ctrl-EHT. Data are presented as mean ± SEM. *p<0.05, **p<0.01, ***p<0.001 by unpaired t-test.
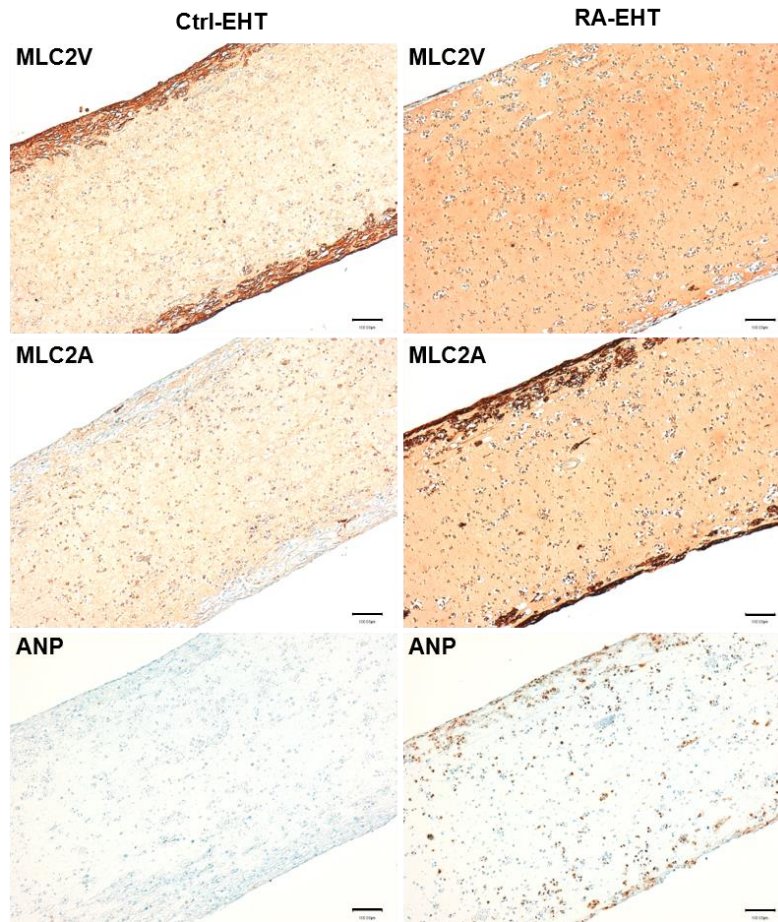
Figure 24: Immunohistochemistry of ventricular and atrial specific markers. Staining of MLC2V, MLC2A and ANP in VChR1-Ctrl-EHT (left column) and VChR1-RA-EHT (right column) at day 30. The scale bar is 100 µm.
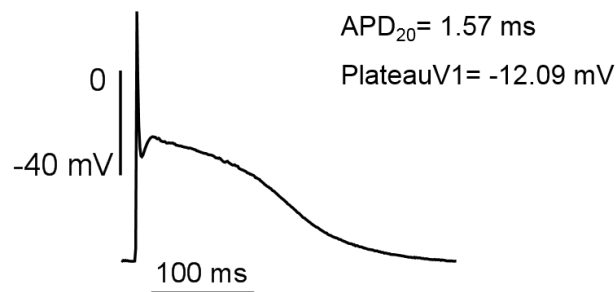
Figure 25: Action potential of VChR1-ER001 RA-EHT. AP duration at 20% of repolarization (APD_{20}) was 1.57 ms. Plateau potential was -12.09 mV.

In order to assess whether VChR1-RA-EHTs differed from VChR1-Ctrl-EHTs in contractility, as demonstrated in previous studies with other cell lines, spontaneous contractions of VChR1-EHTs were recorded with a video-optical analysis setup two hours after each medium change over time. In line with previous results of ERC001-Ctrl- and RA-EHTs (Lemme et al. 2018), VChR1-RA-EHTs showed higher beating frequency, shorter contraction time and relaxation time than VChR1-Ctrl-EHTs (figure 26). VChR1-RA-EHTs displayed slower remodelling and reached a plateau phase later than VChR1-Ctrl-EHTs (figure 27). Moreover, in the early phase of EHT development, VChR1-RA-EHTs had lower contractile force than VChR1-Ctrl-EHTs, which is in line with the previous results of ERC001-Ctrl- and RA-EHTs. Nevertheless, exceeding previous observations, the plateau forces of VChR1-Ctrl- and RA-EHTs eventually reached a similar level (figure 27).
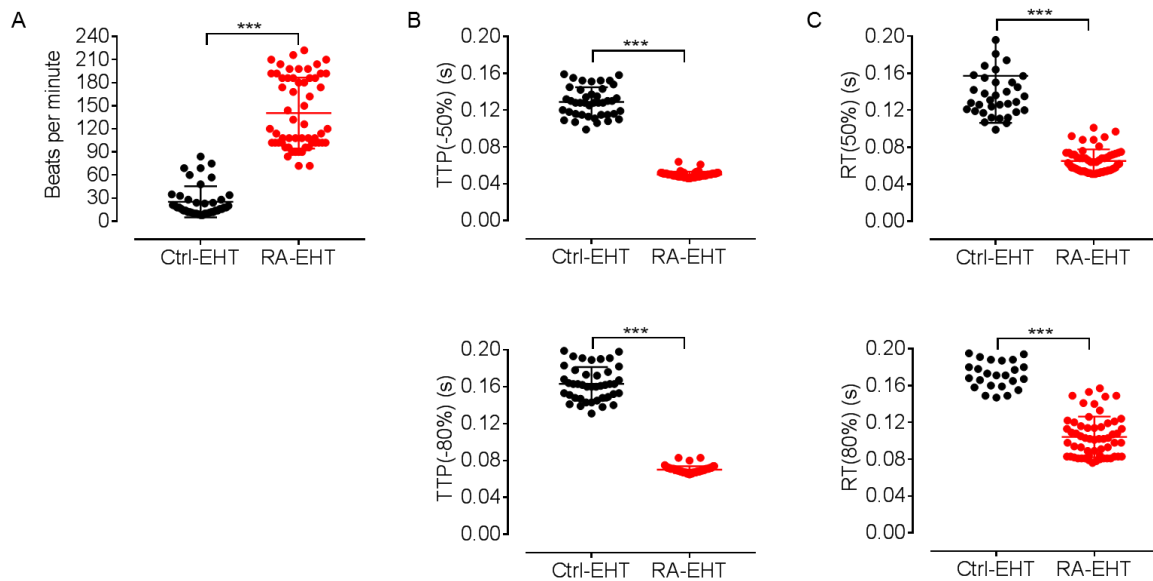
Figure 26: Spontaneous contractility analysis of VChR1-Ctrl-EHTs and VChR1-RA-EHTs. Ctrl-EHTs (n=42 from 4 batches) and RA-EHTs (n=58 from 5 batches) at day 42. RA-EHTs developed faster beating frequency and faster contraction and relaxation kinetics than Ctrl-EHTs. (A) Spontaneous beating frequency. (B) Contraction time TTP (-50%) and TTP (-80%). (C) Relaxation time RT (50%) and RT (80%). Data are presented as mean ± SEM. ***$p < 0.001$ by unpaired t-test.
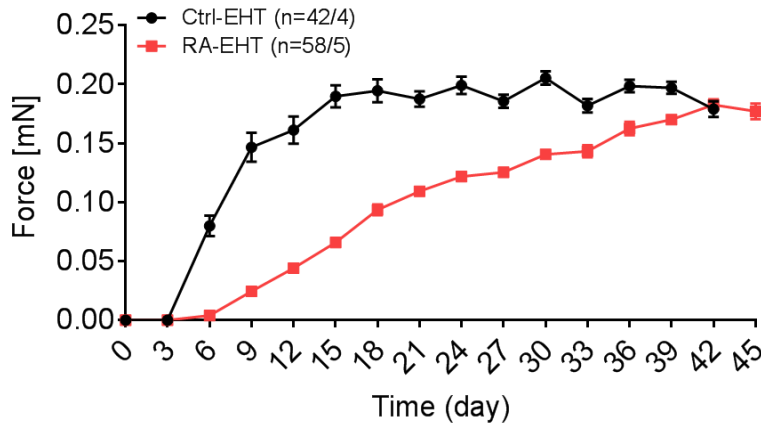
Figure 27: Force development of VChR1-Ctrl-EHTs and VChR1-RA-EHTs over time. Spontaneous EHT contractility was measured two hours after each medium change. n=number of EHTs / number of EHT batches.
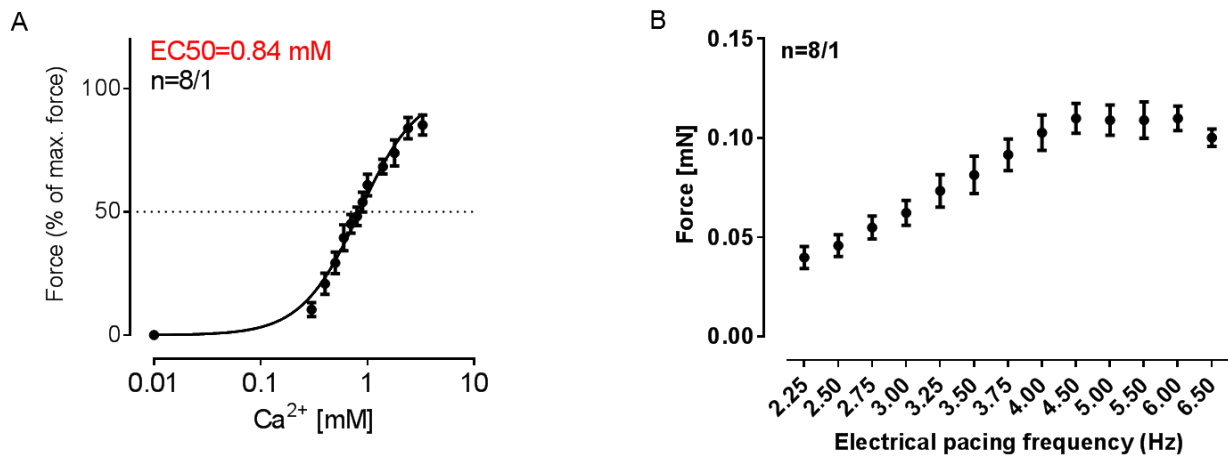
Figure 28: Calcium concentration-response curve and force-frequency relationship of VChR1-RA-EHTs. (A) Calcium concentration-response curve. Calculation of the EC_{50} yielded 0.84 mM. (B) Force-frequency relationship. Force was measured under electrical stimulation from 2.25 to 6.5 Hz. n=8 EHTs from one batch.

VChR1-RA-EHTs were further characterized regarding calcium handling and FFR. Calcium concentration-response curve experiments were conducted when VChR1-RA-EHTs reached their force plateau phase. EHTs showed a concentration-dependent positive inotropic response with a Ca^{2+} EC_{50} of 0.84 mM (figure 28A). FFR is a critical intrinsic regulatory mechanism of cardiac

contractility. To leave enough room for force increments to detect a positive FFR, measurements were carried out at initially submaximal force at EC_{50} Ca^{2+} concentration. After recovery from the experiment above, EHTs were electrically paced incrementally from 2.25 Hz to 6.50 Hz in 0.84 mM Ca^{2+}. VChR1-RA-EHTs showed a positive FFR from 2.25 Hz to 4.50 Hz, then a negative FFR at high frequency (figure 28B).

The cation channel protein VChR1 plays a crucial role in the following pacing experiments. Therefore, we assessed the expression of VChR1 by confocal microscopy imaging by detecting the fluorescent signal of the fused EYFP. Figure 29 shows that VChR1 was still expressed in the EHT at day 100, and not affected by CM differentiation, EHT generation and EHT development. Collectively, we optimized an established EB-based atrial differentiation protocol and assessed the atrial specificity of the resulting cells by comparing expression of chamber-specific genes and AP properties. The protocol yielded atrial hiPSC-derived EHTs with unprecedented human-like electrophysiology. We also showed that knock-in of VChR1 into the AAV1 safe harbor locus had no major adverse effects on electrophysiology and contractile function of hiPSC-EHTs.
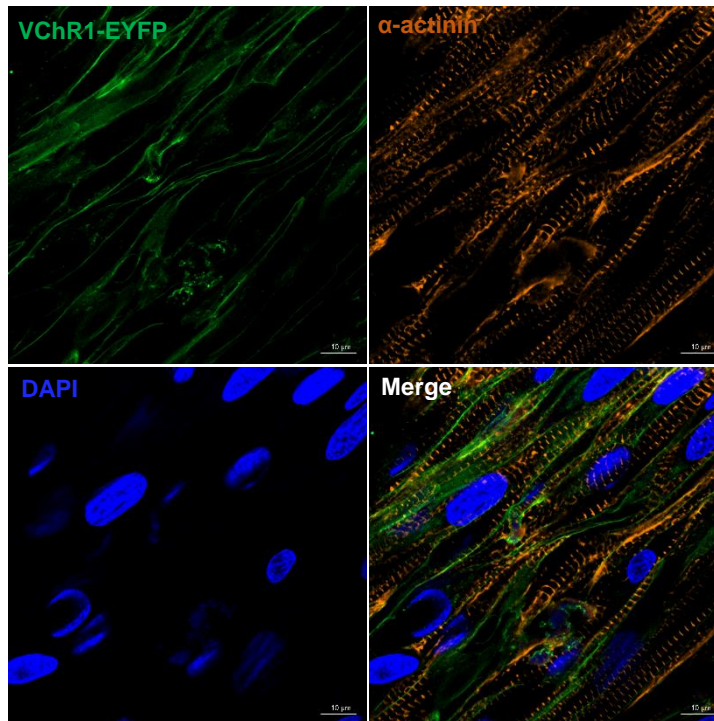
Figure 29: Expression of VChR1-EYFP in RA-EHT. EYFP (green) signal of VChR1-RA-EHT was analyzed by confocal microscopy imaging at day 100. Staining of α-actinin (orange) and DAPI (blue). The scale bar is 10 μm.

6.4   Establishment of a novel optical pacing device for VChR1-RA-EHTs

The standard video-optical recording system in the institute which uses the white light for illumination during recording is not suitable for either baseline recording or optical pacing of EHTs expressing the light-activated channel VChR1. To counteract this problem, we constructed a simple and cost-effective, novel customized digital optogenetic pacing and illumination platform with the help of Julius Hansen (Sarcura GmbH, Klosterneuburg, Austria; figure 30). 24 digitally addressable tri-color light-emitting diodes (LEDs, APA102) were mounted on a low-cost customized circuit board. The circuit board was designed using free and open-source software (KiCAD v5) and manufactured by a rapid-prototyping service (JLCPCB). The LEDs with three different wavelengths (470 nm, 525 nm and 625 nm) were controlled by a microcontroller programmed with the well-known open-source Arduino platform in the C programming language. The blue or green light was used to control the channel VChR1 activity, while the red light was for illumination. For the user, a simple text-based serial interface enabled the configuration of pacing pulse duration, interval between pacing pulse trains and light intensity from a connected computer. Furthermore, the configuration could be saved on the microcontroller for stand-alone operation without a connected computer. The device could be integrated into our standard video-optical system for EHT contractility measurements by replacing the original LED board used for illuminating the EHTs during recording. The device was also used to chronically and optically pace VChR1-RA-EHTs in an incubator by placing the circuit board underneath the EHT culture plate with pre-saved configuration in the microcontroller.
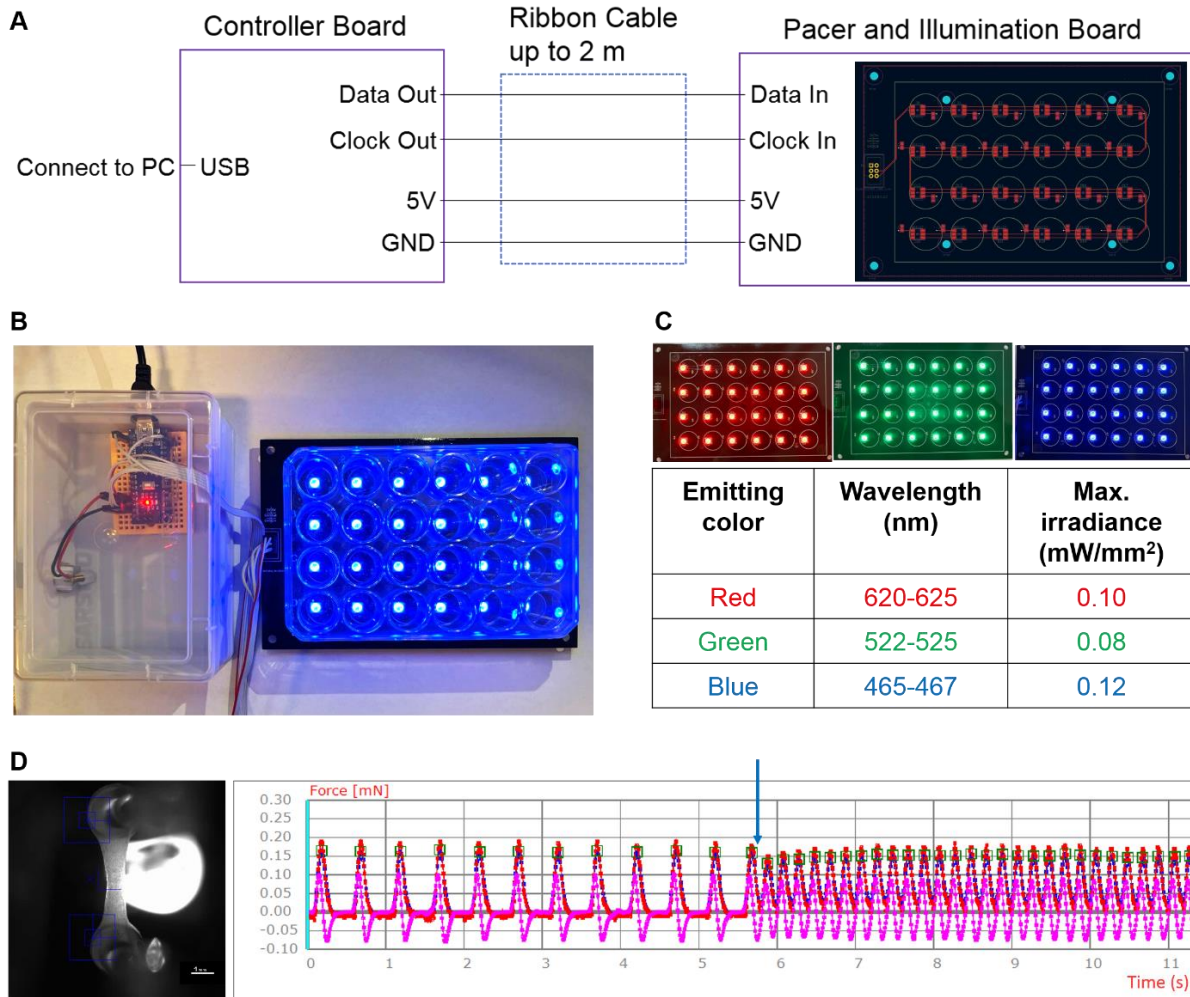
Figure 30: Design of the optical device and optical pacing. (A) Design and layout of the optical device. The black board is a 24-well format circuit board. (B) Image of the device. Left is the microcontroller. Right is a 24-well EHT culture plate on the circuit board with 24 RGB LEDs. (C) Wavelength and max irradiance of each RGB LED. (D) VChR1-RA-EHT contractility was recorded without or with optical pacing at 5 Hz. Left: EHT image. Scale bar is 1 mm. Right: contraction peaks. Blue arrow represents the starting of optical pacing.

Next, the compatibility of the new device with VChR1-RA-EHTs was assessed. In accordance with the ion channel properties of VChR1, the minimal necessary pulse duration of both blue (0.12 mW/mm^2) and green (0.08 mW/mm^2) light needed to trigger the contraction of EHTs was assessed (figure 31). Above 6 ms light pulse duration, both blue and green light were able to sufficiently activate VChR1 and induce contractions at 3 Hz. Moreover, EHTs were shown to follow optical pacing from 2 Hz under the blue light and from 2.5 Hz under the green light to higher frequencies, though at a longer light pulse duration (figure 31). In summary, both blue light and green light were able to activate channel VChR1 and pace VChR1-RA-EHTs at certain frequencies and increasing pulse duration was necessary at increasing frequency.
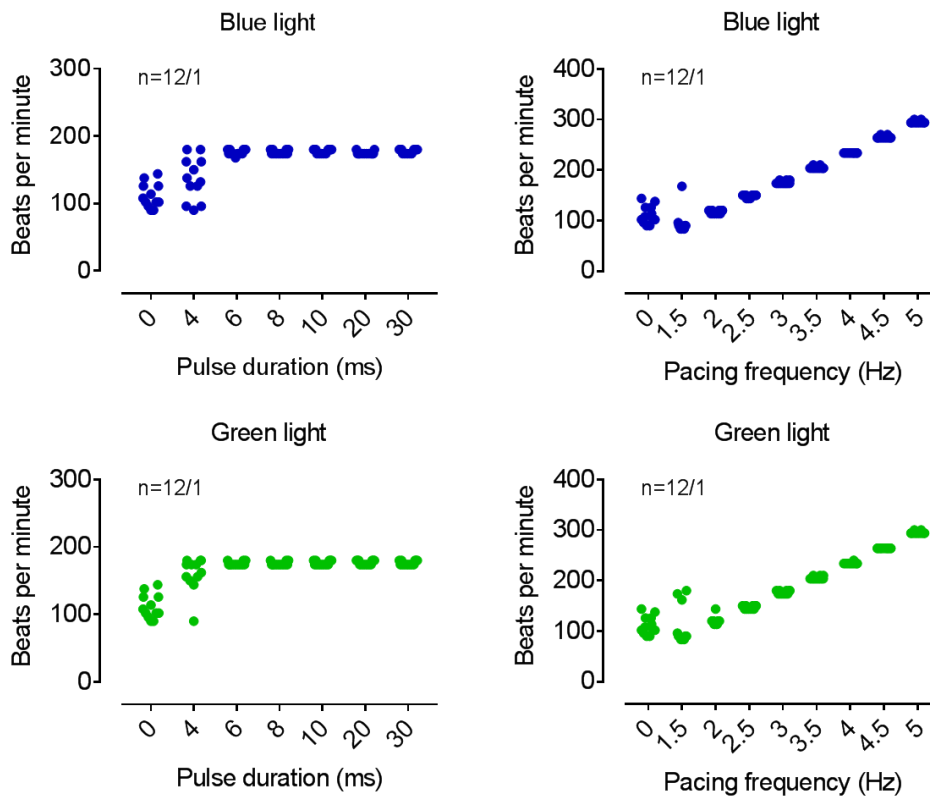
Figure 31: Optical stimulation by the new optical device. VChR1-RA-EHTs were optically paced by the new device for 10 seconds (n=12 EHTs). Left panel: EHTs were stimulated at 3 Hz and followed pacing when the pulse duration of blue or green light was higher than 6 ms. Right panel: pacing capture at 60 ms pulse duration.

Since the red light was used for illumination for video-optical recording, a potential response of VChR1-RA-EHTs to the red light was evaluated. EHTs were positioned at two different locations above the LEDs (right on the top and slightly offset to the side) and exposed to the red light of different light intensities for recording (figure 32A). EHT contraction force, frequency, TTP (-80%) and RT (80%) were compared between the positions (figure 32B). The results showed no significant differences of these parameters. Therefore, we concluded that the red light did not have a relevant effect on VChR1-RA-EHTs during recording. Taken together, we successfully created a digital and tailor-made optogenetic pacing device and were able to use it to pace VChR1-RA-EHTs by blue light or green light pulses.
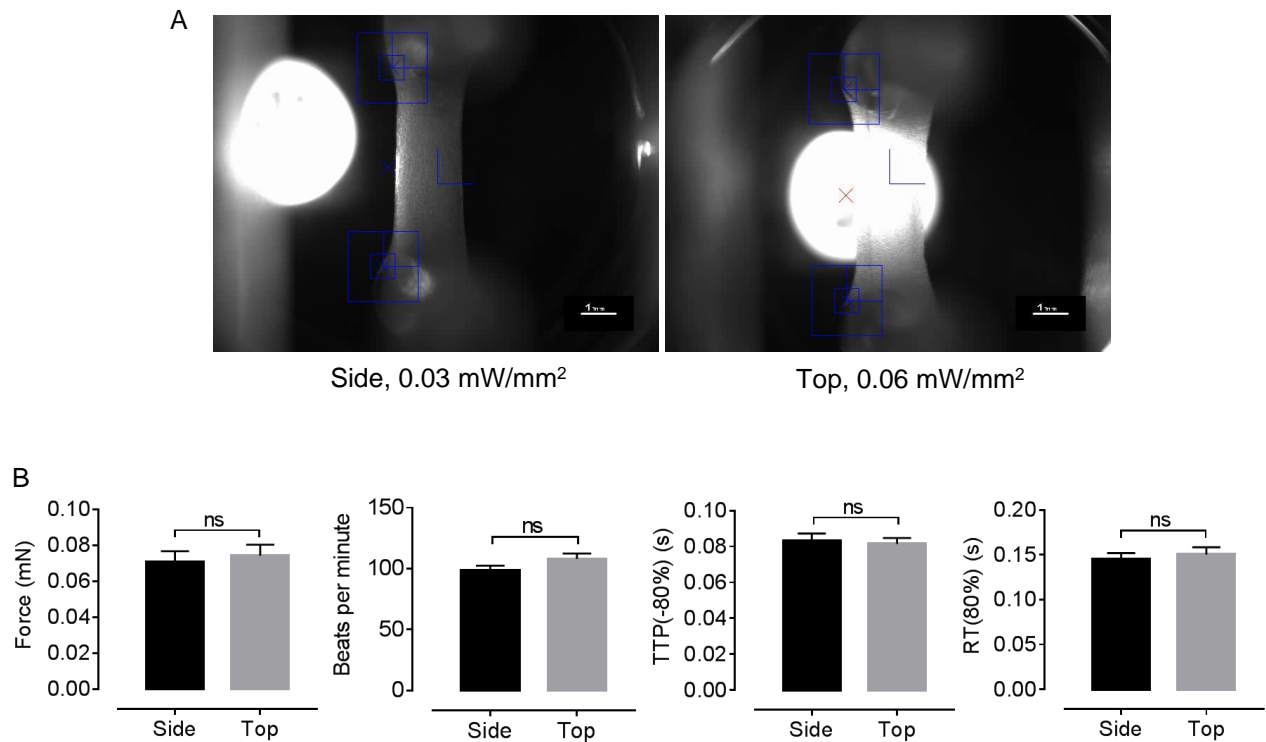
Figure 32: Evaluation of the influence of the red light on VChR1-RA-EHTs. (A) left: EHTs were placed towards the side of the LEDs (Side group) and exposed to red light at 0.03 mW/mm². Right: EHTs were placed directly on the top of the LEDs (Top group) and exposed to red light at 0.06 mW/mm². The scale bar is 1 mm. (B) Contractility parameters (force, BPM, TTP and RT at 80%) of VChR1 RA-EHTs were compared between Side and Top groups (n=11 EHTs per group). Data are presented as mean ± SEM. ns: not significantly different by unpaired t-test.

6.5 Optimization of long-term optical tachypacing of VChR1-RA-EHT

One aim of this study was to assess the influence of chronic optical tachypacing on different aspects of fibrillation induced remodelling, further focusing on exploration of transcriptome and chromatin structure in the paced CMs. After optimization of atrial differentiation, characterization of a suitable optogenetically excitable cell line and the construction of a new optogenetic device, pacing conditions, including pacing start time and pacing frequency had to be established under the standard EHT culture conditions. In an effort to determine a suitable starting time point for the onset of chronic stimulation, EHTs were first paced from day 8 on, when twitching of cells was visible. However, early pacing prevented EHT structural and contractile development (figure 33A). Therefore, in all following experiments, optical pacing was started when EHTs reached a force above 0.10 mN, which usually occurred around 3 weeks of culture. As mentioned previously, ChRs can be desensitized and recover incompletely (Lin 2012). Hence, different intermittent pacing protocols were evaluated. With a pacing protocol consisting of chronic stimulation with 10 seconds of blue light pulse trains, separated by 10 seconds of breaks, no effect on the contractile force could be observed (figure 33B). However, when EHTs were paced for 25 seconds with 10 seconds of break, a decline of force over time was observed (figure 33C). To further determine a suitable tachypacing frequency, VChR1-RA-EHTs were optically paced at frequencies from 3.0 Hz to 6.5 Hz. Based on the observation of a negative FFR of VChR1-RA-EHTs at high frequency, a reduction of force to 80% of baseline was chosen as the criterion for tachypacing, as a compromise between still visible and measurable contraction on the one hand and a measurable stress-induced force reduction on the other hand. Therefore, 5 Hz was determined as the optimal pacing rate derived from the data shown in figure 34, which is the same frequency as used in a previous study (Lemme et al. 2020). In summary, the following conditions were used for chronic pacing in this study: frequency 5 Hz, intermittent light bursts (90, 40 or 25 seconds on and 10 seconds off) and total pacing time up to 40 days. Desensitization was monitored regularly, and in case of incomplete pacing capture, the duration of blue light bursts was gradually adjusted from 90 seconds to 25 seconds. When desensitization occurred, EHTs skipped some pacing pulses, resulting in an arrhythmic contractile pattern (figure 35).

Figure 33: Optimization of optical stimulation. (A) Force and beating frequency of VChR1-RA-EHTs paced from day 8 for 7 days (5 Hz 1 day, 4 Hz 2 days and 3.5 Hz 2 days). VChR1-RA-EHTs from EB-based 3B/2A protocol. Paced EHTs did not show force development. n=8 EHTs per group. (B) 3-week old EHTs were paced for 48 hours at 6 Hz with cycles of 10 seconds optical pacing followed by 10 seconds without pacing. The force was not affected. (C) 3-week old EHTs paced for 48 hours at 5 Hz with cycles of 25 seconds of optical pacing followed by 10 seconds without pacing, force was lower in the paced group. n=8 EHTs. Data are presented as mean ± SEM. ns: not significantly different, ***p<0.001 by unpaired t-test.

Figure 34: Force-frequency relationship under optical stimulation. VChR1-RA-EHTs were optically paced at frequencies from 3.0 Hz to 6.5 Hz (n=21 from 3 batches) with 60 ms blue light pulse duration and paced for 10 seconds. Force is presented as a percentage of baseline force without pacing. EHTs displayed 80% of baseline force at 5 Hz.
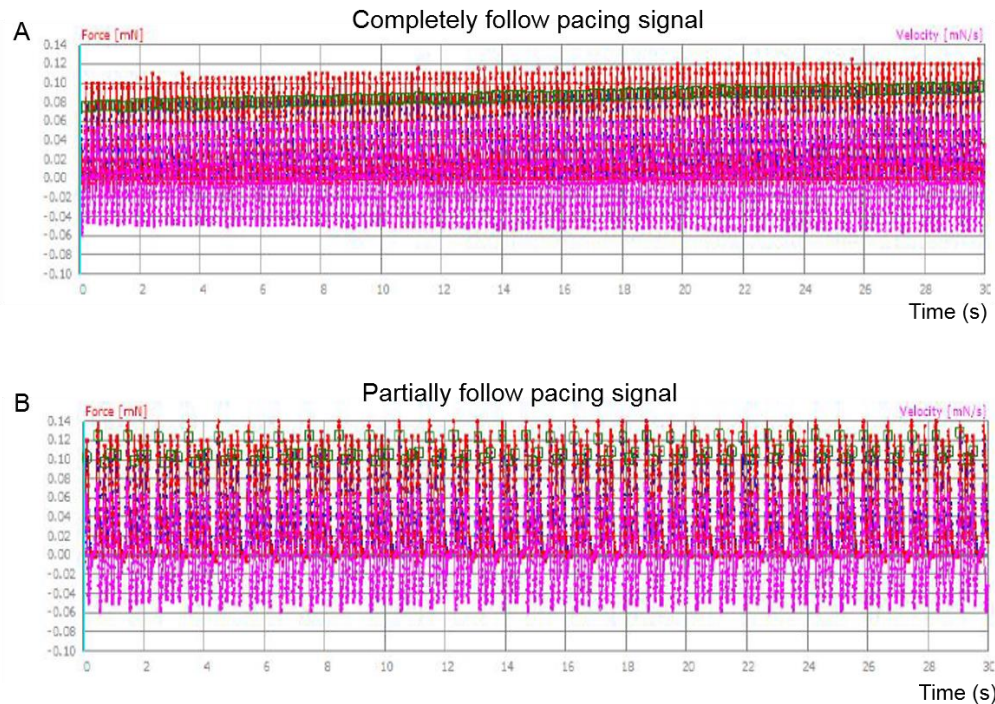
Figure 35: Representative original recording traces of optically paced EHT. (A) Example of EHT following the pacing signal (5 Hz) completely. (B) EHT partially following the pacing signal (5 Hz), resulting in an arrhythmic beating pattern. Red peaks represent contraction peaks, pink traces represent contraction velocity.

6.6   Effects of long-term optical tachypacing on VChR1-RA-EHT

To establish an atrial tachypacing model for AF studies, VChR1-RA-ETHs were optically paced at 5 Hz for as long as possible. The baseline contractility was monitored repeatedly over the whole EHT culture time. Each baseline recording was conducted without any stimulation of EHTs. In the tachypaced group, the spontaneous contractile force of paced EHTs started to decline and was significantly lower than that of unpaced EHTs from day 33 on (pacing started on day 30; figure 36).
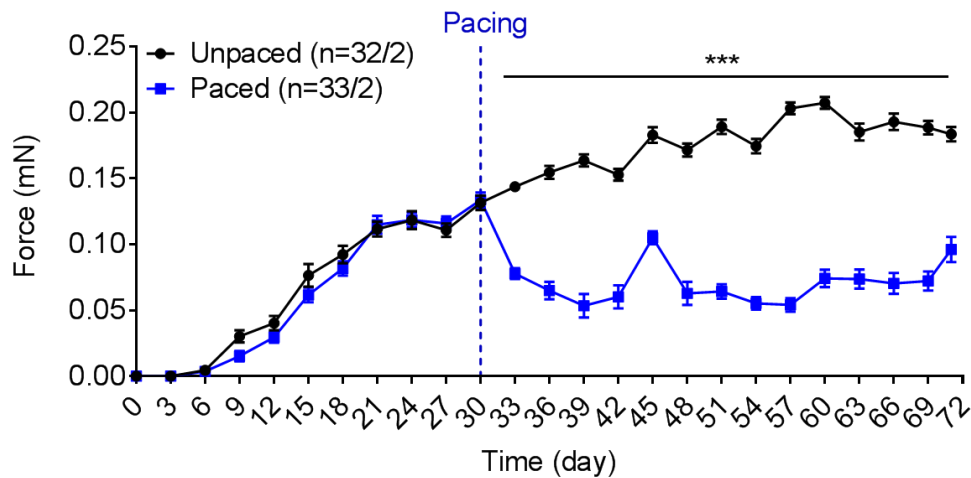
Figure 36: Force development during long-term optical stimulation. VChR1-RA-EHTs were paced at 5 Hz from day 30 to day 70. The dotted line indicates onset of pacing. Paced EHTs showed a lower force compared with unpaced EHTs immediately after onset of tachypacing. n=32-33 EHTs from 2 batches. Data are presented as mean ± SEM. ***$p < 0.001$ by two-way ANOVA plus Bonferroni's multiple comparisons test.

Prompted by the observation of impairment of force development by tachypacing, we quantified the concentration of cardiac troponin I in the EHT culture medium at day 70, which is a marker of cardiac injury and released by damaged and dying CMs. Our results showed that paced EHTs released more cardiac troponin I into the medium than unpaced EHTs (figure 37). Furthermore, at the end of pacing, EHT culture medium that had been in contact with EHTs for 2-days were collected to evaluate the status of metabolism by quantifying the concentration of glucose and lactate in the medium (figure 38). Paced EHTs consumed more glucose and produced more lactate after 2-days of culture, compared with unpaced EHTs. Moreover, the lactate production/glucose consumption ratio (lactate/glucose) can be used to assess the anaerobic and

aerobic respiration of CMs. Paced EHTs had a lower ratio than unpaced EHTs, which indicated that EHTs after tachypacing had more aerobic respiration (figure 38).
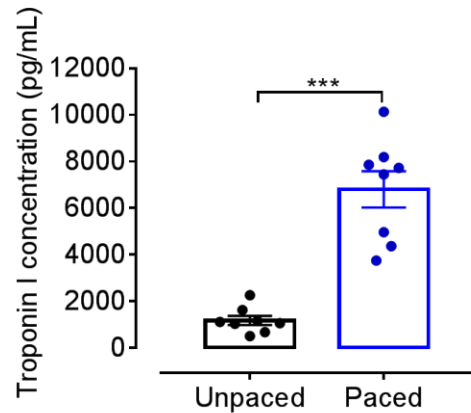
Figure 37: Concentration of cardiac troponin I from culture medium of unpaced and paced EHTs after chronic tachypacing. 2-days EHT culture media were collected on day 70. n=9 EHTs for each group. Data are presented as mean ± SEM. ***p<0.001 by unpaired t-test.
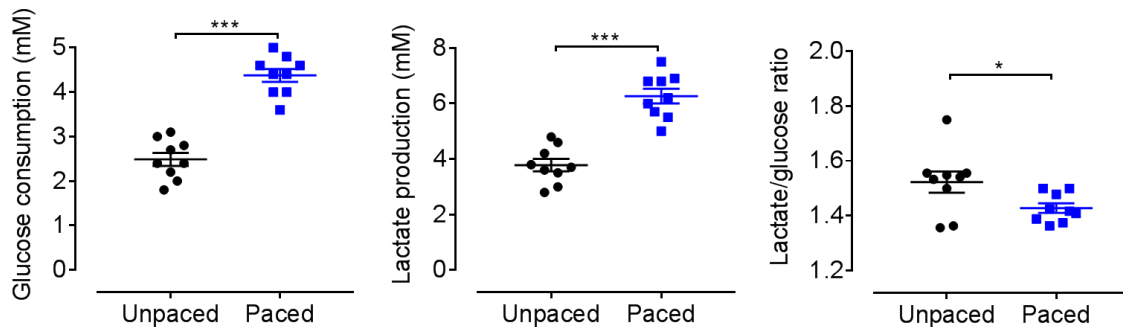
Figure 38: Glucose consumption and lactate production. Concentrations of glucose and lactate were quantified in culture medium after 2 days of culture at day 70. Glucose consumption = original glucose concentration (5 mM) - glucose concentration in the medium. Lactate production = lactate concentration in the medium. Lactate/glucose ratio = lactate production/glucose consumption. n=9 EHTs per group. Data are presented as mean ± SEM. ns: not significantly different, *p<0.05, ***p<0.001 by unpaired t-test.

Histological analysis was performed to identify potential structural differences between unpaced and paced EHTs. H&E staining on longitudinal sections and dystrophin staining on cross sections were carried out, respectively. In figure 39, the paced EHT was thinner and displayed a slightly higher apparent cell density towards the center than unpaced EHT. However, the diameters of EHTs in unpaced and paced groups were inconsistent and thinner EHTs appeared in both groups. Taken together, in both groups cells mainly clustered at the surface of EHTs, as usually observed in EHT (figure 39). Moreover, the staining results of ventricular and atrial markers consistently showed that CMs retained a high expression of MLC2A and a very low expression of MLC2V (figure 40). In summary, cells were aligned along the force lines on the surface of EHT but with no visible differences between the two groups.
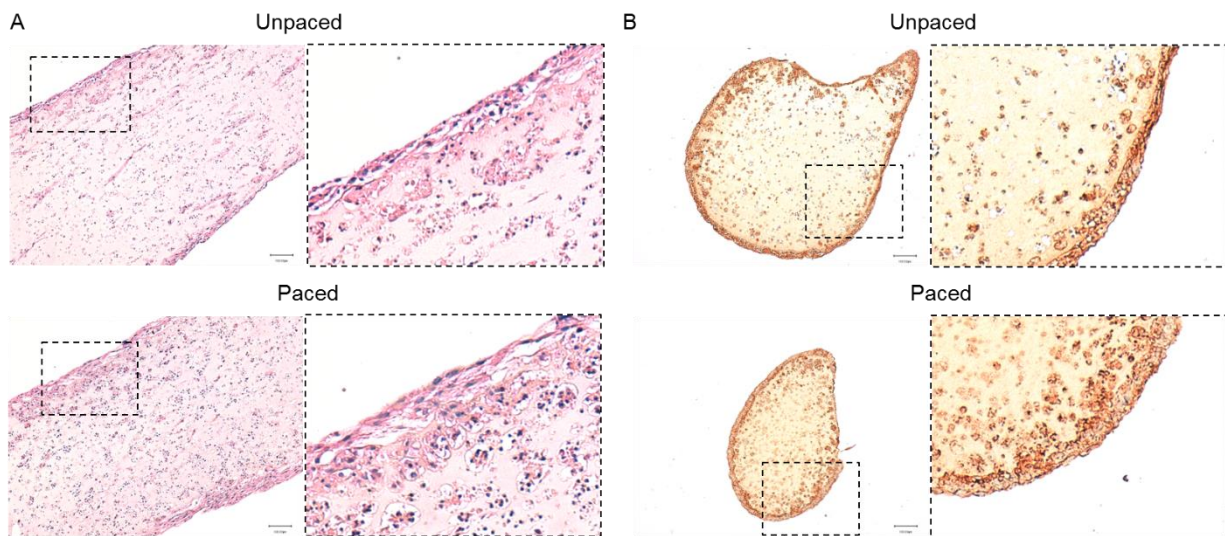
Figure 39: Histological images of unpaced and paced VChR1-RA-EHTs after chronic tachypacing.
(A) H&E staining of longitudinal sections. (B) Dystrophin immunohistochemistry staining of cross sections. The membrane skeleton protein dystrophin was used to visualize CM distribution. The scale bar is 100 μm.
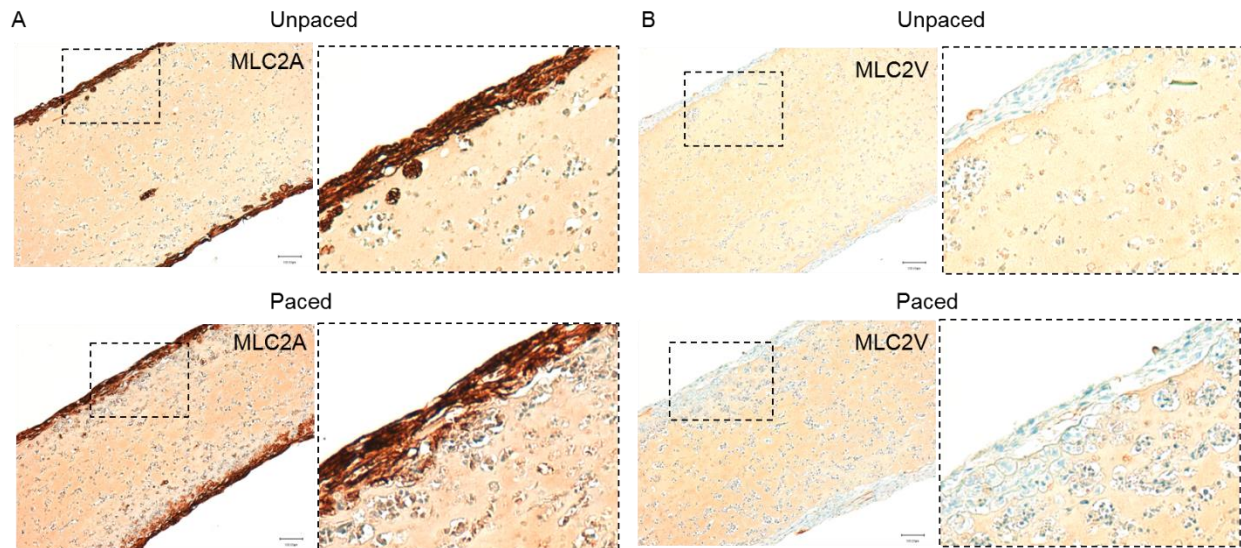
Figure 40: Staining of MLC2A and MLC2V of unpaced and paced EHTs after chronic tachypacing.
(A) MLC2A, (B) MLC2V staining of longitudinal sections. The scale bar is 100 μm.

6.7 Next-generation sequencing of unpaced and paced EHTs

After extensive validation of the model, we aimed to further assess the consequences of chronic tachypacing on cultured hiPSC-derived CMs, with a focus on nuclear signaling. To this end, different next-generation sequencing-based experiments were performed to study both the transcriptome and chromatin accessibility. Dr. Chukwuemeka George Anene-Nzelu and Dr. Mick Lee from the group of Prof. Roger Foo at Genome Institute of Singapore (Singapore), and Dr. Wen Wang from Tong Ji University (Shanghai, China) kindly provided help for this part of work.

Bulk RNAseq was performed to study transcriptomic changes. After sequencing and raw data processing, we first applied principal component analysis (PCA) to visualize global gene expression variation across different samples in minimized defined principal components (PC). There was a clear segregation between the unpaced and the paced group (figure 41A). Notably, with differential expression analysis and clustering across all EHTs from the two groups, we observed numerous genes differentially expressed (DE) in the chronic tachypacing and control group (figure 41B). Gene-Ontology (GO) enrichment analysis using R revealed that upregulated DE genes in paced EHTs were related to collagen-containing extracellular matrix, cation channel complex and cell-cell contact zone, while downregulated DE genes were associated with collagen-containing extracellular matrix (including different ECM-related genes; figure S1),

microtubule and condensed chromosome (figure 42). Furthermore, we performed qPCR to confirm the expression changes of a subset of the DE genes, including *NPPA*, *NPPB*, *KCNJ3* and *KCNJ12* (figure 43). Collectively, gene expression analysis demonstrated that paced EHTs mainly underwent expression alterations with regard to ion channels and extracellular matrix, as observed in human atrial fibrillation.
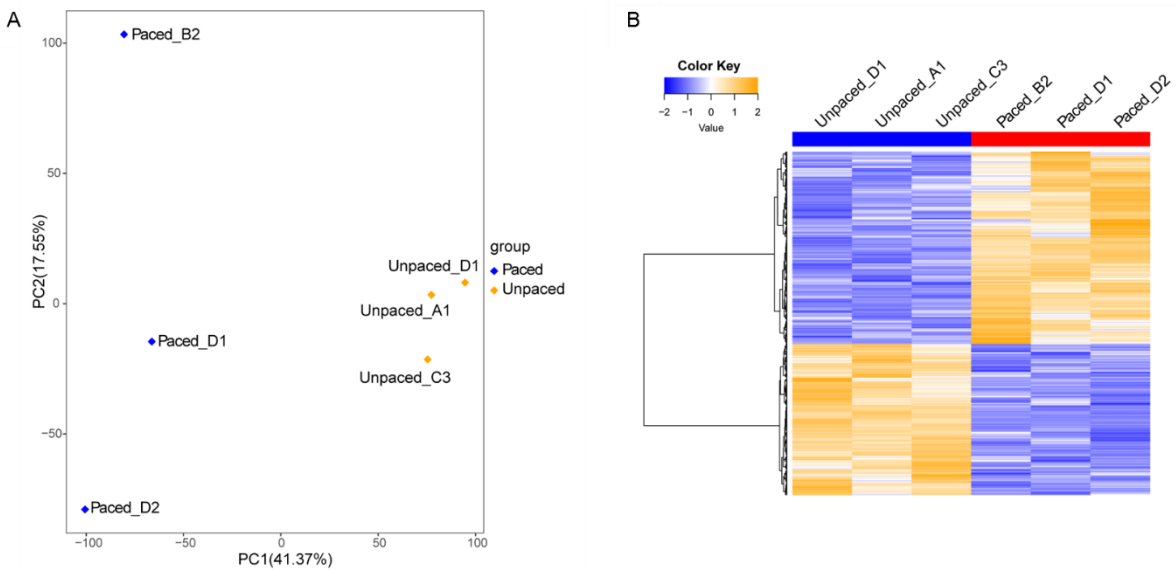
Figure 41: Global transcriptomic changes after chronic tachypacing analyzed by RNA sequencing. (A) PCA analysis of all 6 samples between unpaced and paced EHTs. (B) Heatmap and clustering of differentially expressed genes.
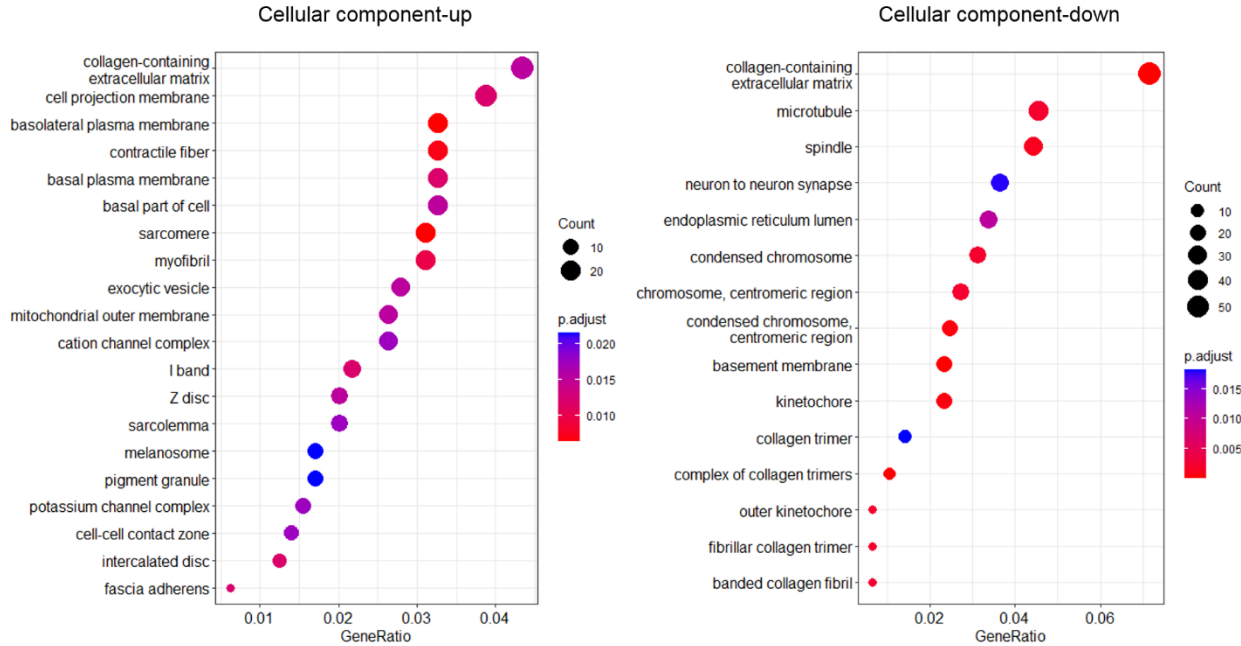
Figure 42: Analysis of Gene Ontology terms of DE genes. Paced EHTs versus unpaced EHTs. Left: upregulated GO terms. Right: downregulated GO terms.
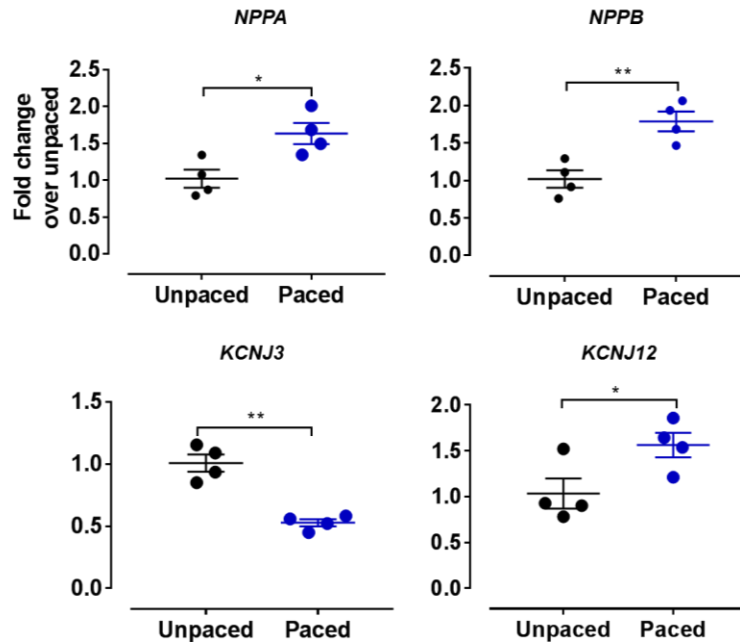
Figure 43: Gene expression analysis of unpaced and paced EHTs by qPCR. Ct values of target genes were normalized to housekeeping gene GUSB and to the upaced group. Data are presented as mean ± SEM. *p<0.05, **p<0.01 by unpaired t-test.

Last, chromatin accessibility in atrial-like EHTs after chronic tachypacing was assessed. We performed ATACseq and ChIPseq (H3K27ac) to map open (ATACseq) and active (H3K27ac) chromatin regions. Peaks captured by ATACseq represent open, active regulatory or transcriptionally active chromatin regions. Our ATACseq data revealed that paced EHTs had fewer open chromatin regions (338 unique peaks) than unpaced EHTs (773 unique peaks; figure 44A). Unfortunately, ATACseq libraries had a shortage of sequencing depth. More experiments need to be performed to confirm and refine these results, and to identify specific regulatory regions in the chromatin related to AF. ChIPseq of histone acetylation mark H3K27ac is used to detect H3K27ac binding DNA regions, which are usually located in active promoter or enhancer regions. We performed differential peak analysis and identified differential histone modification regions between paced and unpaced EHTs. The data showed fewer differentially bound peaks in paced EHTs (6812 peaks) than unpaced EHTs (12562 peaks; figure 44B), which was similar to the ATACseq results. Taken together, atrial-like EHTs displayed chromatin remodelling with reduced open regions after chronic tachypacing. Further, a more detailed analysis of the nature of the regions is necessary.
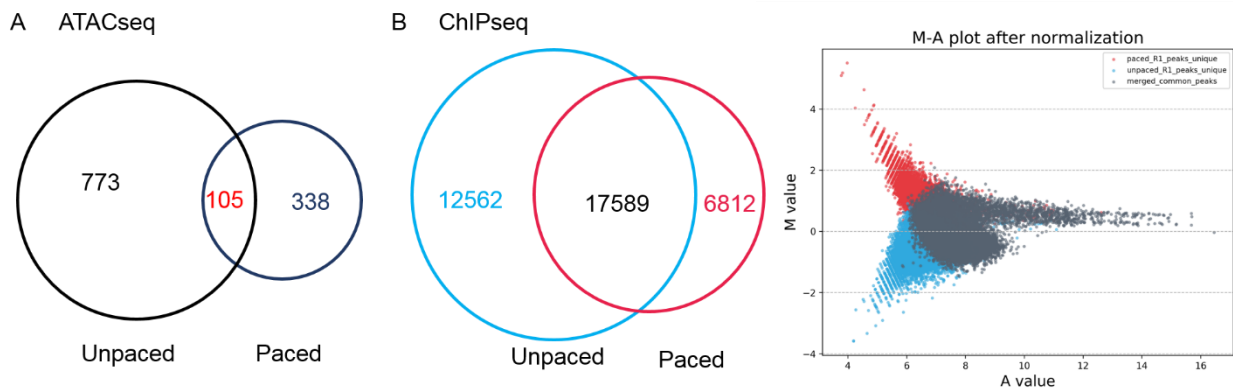
Figure 44: Altered chromatin accessibility after tachypacing. (A) Venn diagram of ATACseq peaks in unpaced and paced EHTs. (B) ChIPseq of histone acetylation H3K27ac showing differentially bound peaks. Left: Venn diagram showing overlap of unpaced and paced EHTs ChIP peaks. Right: M-A plot of ChIPseq peaks. Each dot represents a single peak. Grey: common peaks. Red: differentially bound peaks in paced EHTs. Blue: differentially bound peaks in unpaced EHTs.

7 Results II: Targeted DNA methylation editing on human EHT models

7.1 Generation of two-cell type EHT (fibroblast-EHT)

7.1.1 Cardiac fibroblast differentiation

As mentioned in the introduction, fibrosis is among the main morphologic alterations in the heart during the progression of AF (atria) and HF (ventricles). In our institute, ventricular-like EHTs are well-established, which are generated from CMs derived using a standard EB-based protocol as described above. Disease modelling on ventricular-like EHTs for different stages of HF has been previously attempted. Owing to the wealth of existing data for comparison and well standardized handling, we first investigated targeted DNA methylation editing as a potential therapeutic method in ventricular-like EHT-based disease models. Capitalizing on this model, fibroblast-EHT consisting of CFs and ventricular-like CMs was re-established and refined in this part of the study. In this model, we aimed to down-regulate the expression of ECM proteins by manipulating DNA methylation. To this end, CFs derived from hiPSCs were introduced into EHT for fibrosis modelling. An EB-based cardiac fibroblast differentiation protocol, which had been previously established in our institute (Werner 2018) was used to produce CFs in this study. To visualize CFs and CMs in the EHTs, ERC001-hiPSCs used for cardiac differentiation were labeled to constitutively express a green fluorescent protein (Venus) or a red fluorescent protein (dKatushka2) by lentiviral transduction, respectively. Venus-labeled iPSCs were differentiated into CFs, while dKatushka2-labeled iPSCs were differentiated into CMs (figure 45). Gene expression analysis confirmed iPSC-CFs expressed several fibroblast marker genes (*COL1A1*, *CNN1*, *DDR2*, *POSTN*, *VIM*; figure 46), similarly as primary adult human dermal fibroblasts (HDFa), used as a control. Conversely and as expected, hiPSC-CMs did not show high expression of these genes but had a high expression of the cardiac marker gene actinin alpha 2 (*ACTN2*; figure 46).
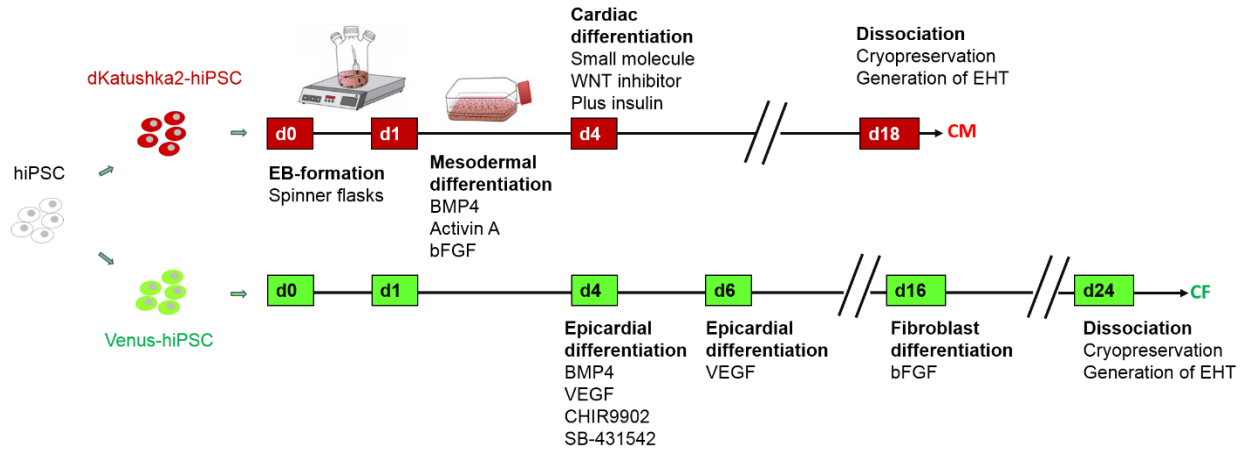
Figure 45: Schematic of cardiac differentiation from fluorescently labeled iPSCs. CMs were derived from dKatushaka2-iPSC (shown in red) by the EB-based differentiation protocol. CFs were derived from Venus-iPSC (shown in green), and cells were driven to epicardial differentiation by BMP4, VEGF, CHIR9902 and SB-431542 after mesodermal differentiation. bFGF was applied for fibroblast differentiation.
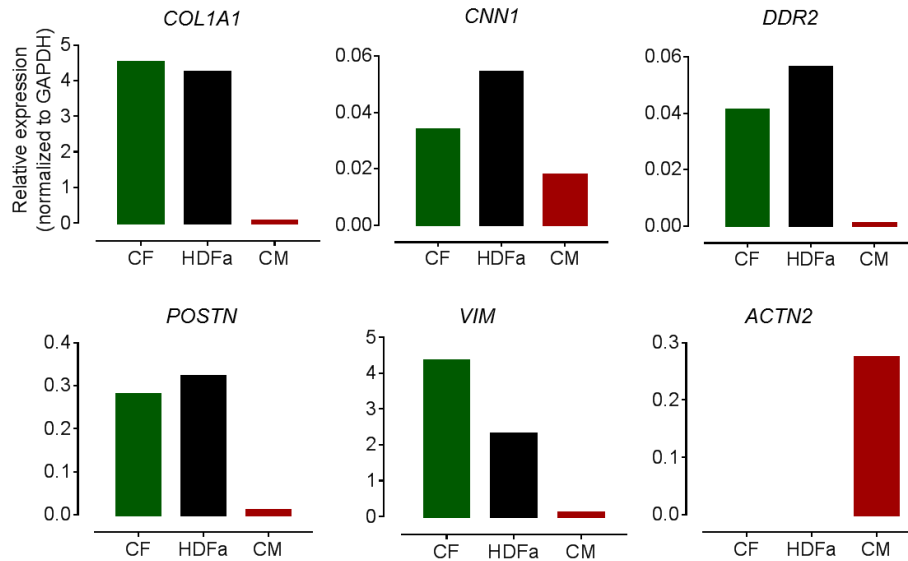
Figure 46: Gene expression analysis of fibroblast markers by qPCR. CF: iPSC-CF. HDFa (primary adult human dermal fibroblasts) and CM (iPSC-CM) were used as control. Ct values of target genes were normalized to Ct values of *GAPDH*. Individual samples were analyzed. 2^-delta Ct is shown.

7.1.2   Generation of fibroblast-EHT

The current standard human EHT contains CMs only and very few undefined non-CMs derived from hiPSCs. Without CFs, the collagen content in standard EHT would have been unpredictable and probably negligible. Therefore, we introduced hiPSC-CFs to create a two-cell type EHT (fibroblast-EHT, CF-EHT). To keep the total cell number in the EHT constant, the amount of CMs was reduced according to the percentage of CFs. Different percentages (from 5% to 20%) of CFs in the CF-EHTs were tested in 3 batches (Batch A, B, C). In Batch A, all CF-EHTs had a lower final diameter than EHTs (figure 47A). At day 21, 5% and 10% CF-EHTs developed higher contractile force than EHTs (figure 47B). 4 out of 6 10% CF-EHTs were broken, while all 6 20% CF-EHTs were broken (figure 47B). In Batch B (figure 48), all CF-EHTs had a shorter final length than EHTs and displayed lower force. Especially 20% CF-EHTs became unusually short and stopped beating. However, when treated with an inhibitor of TGF-β type I receptor (SB-431542, 10 µM) during CF-EHT culture to inhibit CF activation, the force of 10% CF-EHT+SB group was higher than that of 10% CF-EHT group but still lower than that of EHT group (figure 48B). In Batch C (figure 49), 10% and 20% CF-EHTs again had a shorter final length than EHTs and displayed lower force. However, in this batch, compared with EHTs, 5% CF-EHTs showed no significant difference in force (figure 49B). Collectively, the morphology of CF-EHTs differed from batch to batch in terms of thickness and length. In conclusion, 5% CF-EHTs developed a more regular shape with a tendency towards higher force than CF-EHTs from other groups.
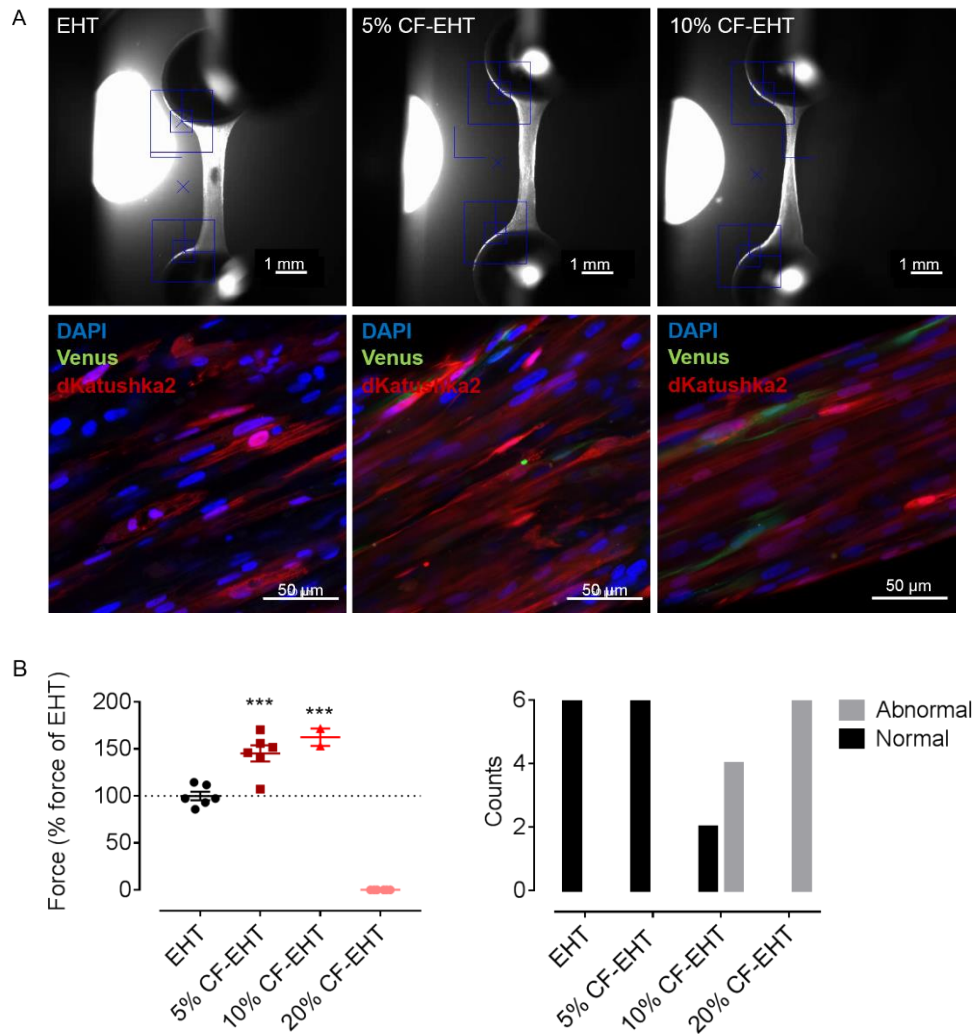
Figure 47: CF-EHTs from Batch A at day 21. (A) Morphology of EHT, 5% CF-EHT and 10% CF-EHT. Images were acquired by the video-optical recording system (top row, scale bar 1 mm) and confocal microscope (bottom row, scale bar 50 µm). DAPI (blue), Venus-iPSC-derived CF (green), and dKatushka2-iPSC-derived CM (red). (B) Left column: force % (normalized to EHT). 20% CF-EHTs became very thin and eventually ripped before day 21. n=6 EHTs per group. Data are presented as mean ± SEM. ***$p<0.001$ by one-way ANOVA plus Bonferroni's multiple comparisons test. Right column: counts of broken ("abnormal") and intact ("normal") EHT or CF-EHT, respectively.
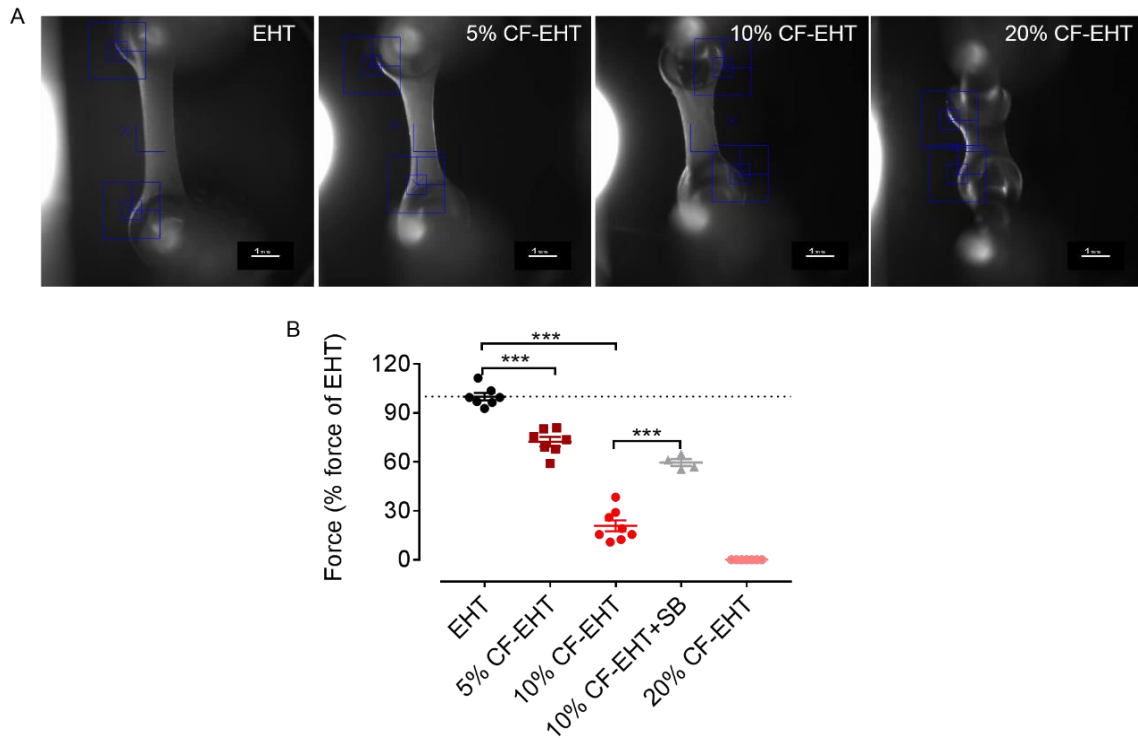
Figure 48: CF-EHTs from Batch B at day 20. (A) Morphology of EHT, 5% CF-EHT, 10% CF-EHT and 20% CF-EHT. Images were acquired by the video-optical system (scale bar 1 mm). (B) Force % (normalized to EHT). 20% CF-EHTs were very short and therefore not able to deflect the mounting posts further. 10% CF-EHT+SB is 10% CF-EHT treated with the TGF-β1 receptor inhibitor SB-431542 (10 μM). n=4-8 EHTs per group. Data are presented as mean ± SEM. ***$p < 0.001$ by one-way ANOVA plus Bonferroni's multiple comparisons test.
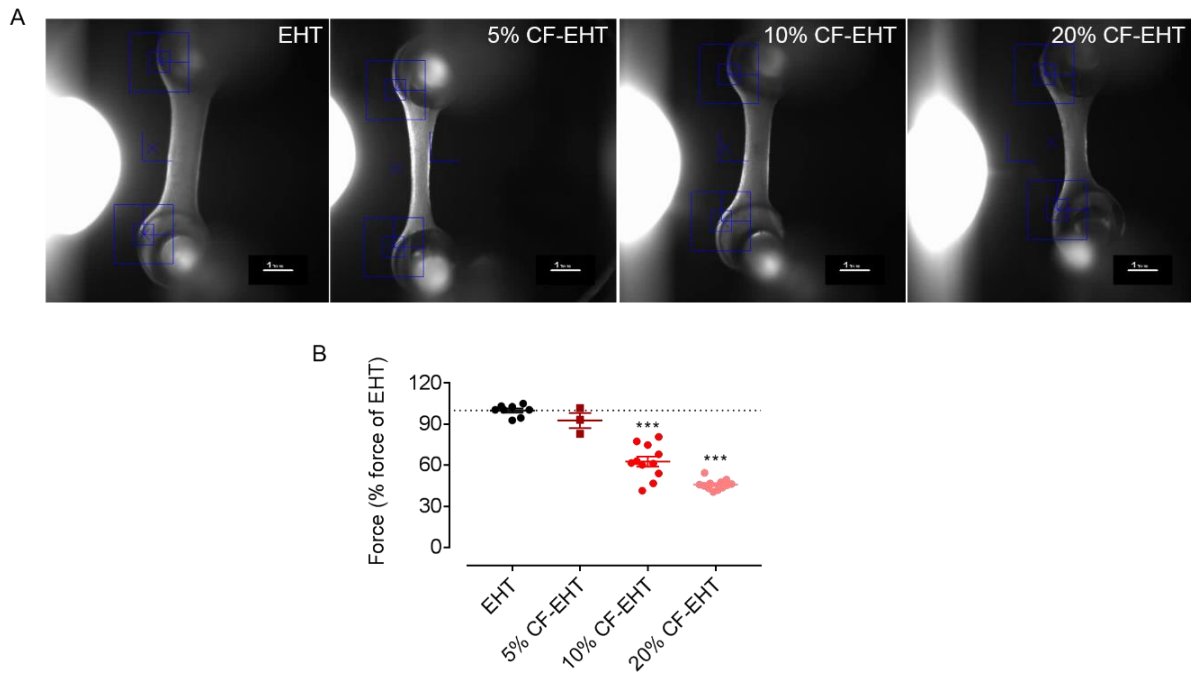
Figure 49: CF-EHTs from Batch C at day 17. (A) Morphology of EHT, 5% CF-EHT, 10% CF-EHT and 20% CF-EHT. Images were acquired by the video-optical recording system (scale bar 1 mm). (B) Force % (normalized to EHT). 20% CF-EHTs were very short and therefore hardly able to deflect the mounting posts further. n=3-12 EHTs per group. Data are presented as mean ± SEM. ***p<0.001 by one-way ANOVA plus Bonferroni's multiple comparisons test.

Next, to identify if CF-EHTs expressed collagen, we performed immunohistochemistry analysis with collagen staining. The result confirmed that collagen was present in CF-EHTs cultivated in the standard EHT medium (figure 50).
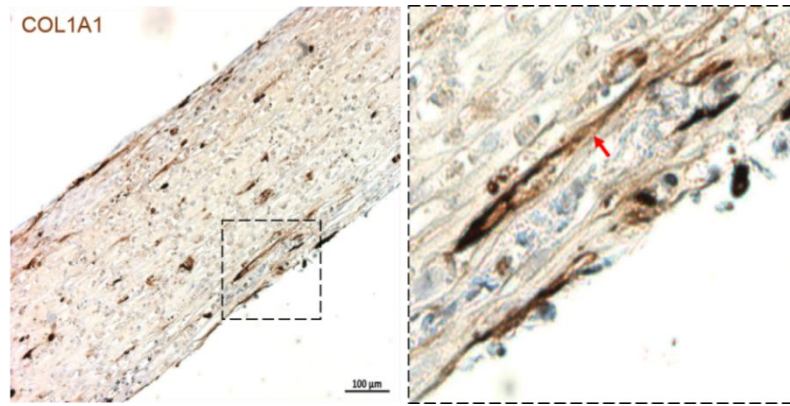
Figure 50: Staining of COL1A1. Immunohistochemistry analysis of 10% fibroblasts-containing CF-EHT. CF-EHT expressed COL1A1. Red arrow indicates collagen signal. The scale bar is 100 µm.

7.2 Generation of an EHT-based hypertrophy model

As a second test system for DNA methylation editing, a pro-hypertrophic EHT model was adapted. While the CF-EHT model should serve to test DNA methylation editing in CFs, the pro-hypertrophic model should serve to evaluate the strategy directly in CMs. This cardiac hypertrophy model based on pharmacological treatment had been established previously in our institute (Madsen et al. 2021). In this study, the same intervention was applied on dKatushka2-EHTs. When the force of EHTs reached a plateau phase in a standard culture medium with serum for 18 days, EHTs were switched to serum free medium to avoid potential pro-hypertrophic serum-effects and treated with 20 µM phenylephrine and 50 nM endothelin-1 for 7 days. In line with results of the previous study, during treatment, the force of control EHTs (untreated) slightly increased further in serum free medium, while the force of treated EHTs declined (figure 51). Compared to control EHTs, treated EHTs showed a significantly lower force and higher beating frequency (figure 51, 52). Moreover, typical hypertrophic gene expression changes were detected by qPCR. Treated EHTs had higher expression levels of *NPPA* and *NPPB*, but lower expression level of *ATP2A2* (figure 53). In summary, after treatment dKatushka2-EHTs displayed pro-hypertrophic signs, and this EHT model seemed suitable to serve as another platform to evaluate DNA methylation editing.
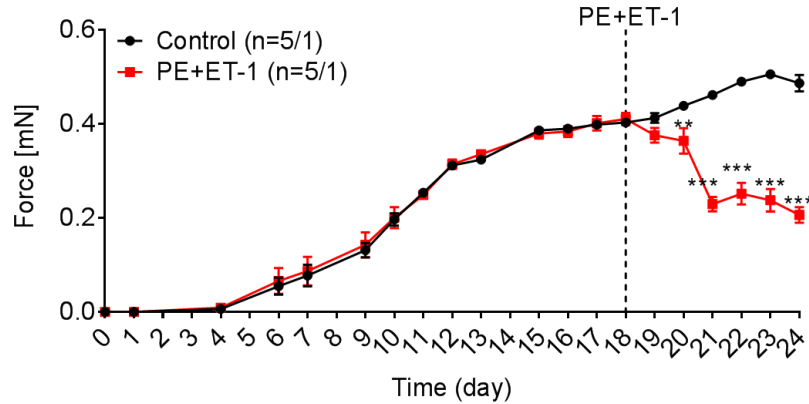
Figure 51: Force development of dKatushka2-EHTs with pro-hypertrophic intervention. EHTs were cast on white silicon posts (force=2.14 x force on standard silicon posts). The treatment with PE and ET-1 was initiated on day 18 (dotted line). Force of treated EHTs decreased and was significantly lower than control EHTs already after 2 days. n=5 EHTs from one batch for each group. Data are presented as mean ± SEM. **p<0.01, ***p<0.001 by two-way ANOVA plus Bonferroni's multiple comparisons test.
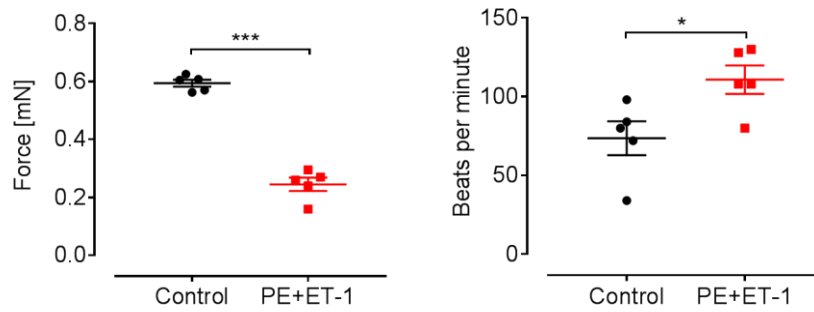
Figure 52: Effects of pro-hypertrophic intervention on contractility. EHTs were treated with PE and ET-1 for 7 days. Force and beating frequency were compared between control and PE+ET-1 EHTs. n=5 EHTs from one batch for each group. Data are presented as mean ± SEM. *p<0.05, ***p<0.001 by unpaired t-test.
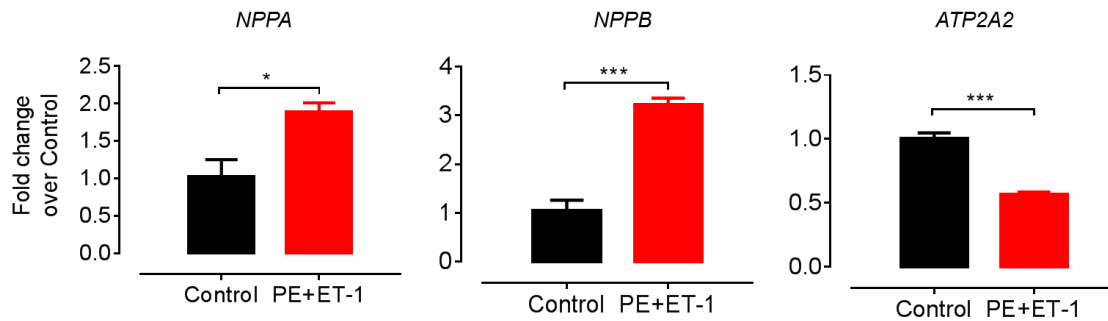
Figure 53: Gene expression analysis after pro-hypertrophic intervention by qPCR. Fold change of *NPPA*, *NPPB* and *ATP2A2* in control and PE+ET-1 EHTs. n=3 EHTs per group. Ct values of target genes were normalized to housekeeping gene *GUSB* and to control. Data are presented as mean ± SEM. *p<0.05, ***p<0.001 by unpaired t-test.

7.3 Establishment of targeted DNA methylation editing tool

7.3.1 Adeno-associated virus-split-dCas9 strategy

Previous studies have demonstrated that fusion of the dCas9 and the catalytic domain of DNMT3A or TET1 enables targeted DNA methylation or demethylation (Liu et al. 2016, 2018; Vojta et al. 2016). AAV vectors are commonly used for gene in vivo delivery. In the present study, we set out to create the editing tools AAV-dCas9-DNMT3A and AAV-dCas9-TET1 and deliver

them to EHTs by AAV transduction. However, gene delivery by AAV transfer plasmids has a packaging limitation (~5.0 kb, including ITRs; Wu et al. 2010) and the length of dCas9-DMNT3A and dCas9-TET1 both exceed 5 kb. In order to address this limitation, Chew and colleagues split SpCas9 at site V713-D714, fused the Cas9 N-terminal lobe with the *Rhodothermus marinus* N-split intein and the C-terminal lobe with C-split intein, and proved that the split-inteins allowed seamless reconstitution of full-length SpCas9 in the cells from two shorter peptides by protein splicing (Chew et al. 2016). Compared to SpCas9, dCas9 contains two point-mutations, D10A and H840, for endonuclease inactivation (Addgene: CRISPR Guide). Therefore, the same site and split-inteins of split-SpCas9 were employed to create split-dCas9 editing tools in this study (figure 54).
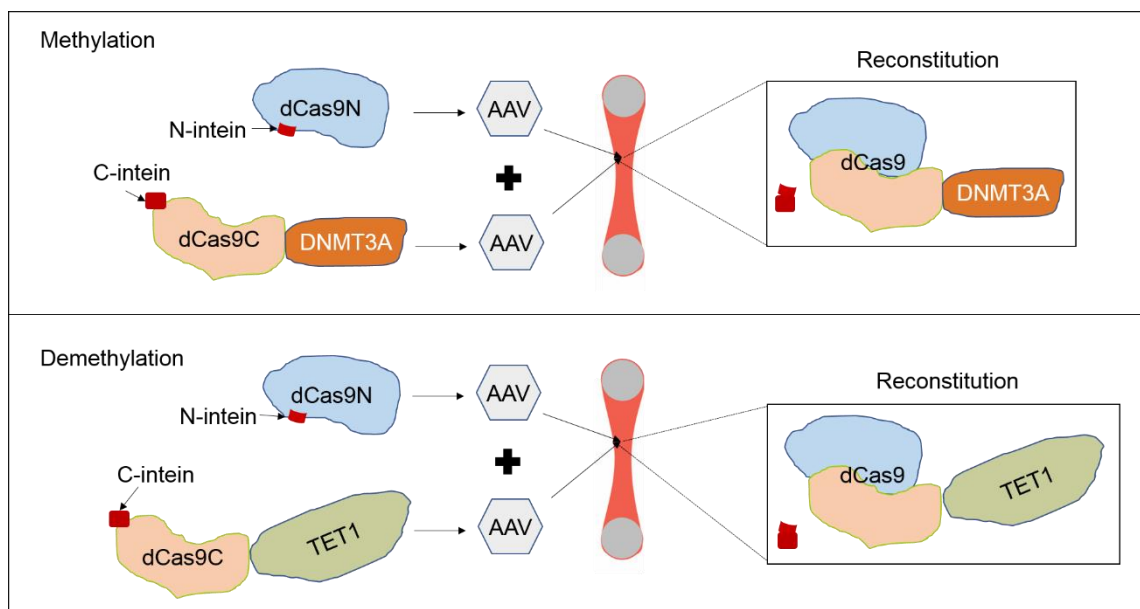
Figure 54: Schematic of AAV-split-dCas9 strategy. dCas9N (1-713 aa): dCas9 N-terminal, dCas9C (714-1368 aa): dCas9 C-terminal, DNMT3A: DNA methyltransferase 3 alpha catalytic domain, TET1: DNA demethylation enzyme, ten-eleven translocation dioxygenase 1 catalytic domain. dCas9N and dCas9C are co-delivered to EHT through separate AAV vectors and scarlessly reconstitute in the cells.

7.3.2   Generation of split-dCas9

The construction of split-dCas9 plasmids was based on split-Cas9 plasmids: pAAV-SMVP-Cas9N and pAAV-CMV-Cas9C-VPR (Chew et al. 2016). Assembly was performed using the NEBuilder

HiFi DNA Assembly (details see section 5.7.1). In brief, Cas9 N-terminal lobe was point mutated into dCas9N. A 3x FLAG tag sequence was inserted upstream of the dCas9N sequence. The two final dCas9N plasmids constructed in this work have different promoters: SMVP (CMV enhancer + CMV promoter) and cTnT (cardiac troponin T promoter; table 12). To generate dCas9C-DNMT3A plasmids, a CMV enhancer was inserted upstream of the CMV promoter to enhance its activity, or the CMV promoter was replaced by cTNT promoter, respectively. The Cas9 C-terminal lobe was then point mutated into dCas9C. The VPR region of the original plasmid was replaced by DNMT3A, DNM3A-2ABFP or DNM3A-2Apuro. Moreover, DNMT3A was point mutated into catalytically inactive DNMT3A (E756A). The two fusion proteins contained BFP for blue fluorescent protein or puro for puromycin resistance protein (table 12). Since the size of the TET1 catalytic domain is 2.1 kb, the packaging capacity did not allow for addiction of the CMV enhancer. Therefore, to generate the dCas9-TET1 plasmid, only Cas9C was mutated to dCas9C and VPR was replaced with TET1 (table 12). All plasmid maps are shown in supplement section (figure S2, S3).

Table 12: overview of final dCas9N and dCas9C plasmids

Index	Plasmid name
1	pAAV-SMVP-FLAG-dCas9**N**
2	pAAV-cTnT-FLAG-dCas9**N**
3	pAAV-SMVP-dCas9**C**-DNMT3A
4	pAAV-SMVP-dCas9**C**-DNMT3A-2ABFP
5	pAAV-SMVP-dCas9**C**-DNMT3A-2Apuro
6	pAAV-SMVP-dCas9**C**-inactiveDNMT3A-2Apuro
7	pAAV-cTNT-dCas9**C**-DNMT3A
8	pAAV-CMV-dCas9**C**-TET1

7.3.3 Reconstitution of dCas9N and dCas9C-DNMT3A

First, to verify if dCas9N and dCas9C were able to reconstitute to full-length dCas9, the dCas9N and dCas9C-DNMT3A plasmids were co-transfected into HEK 293 cells. A full-length dCas9-DNMT3A plasmid was used as a positive control. Western blot probing the FLAG tag revealed that co-transfection of dCas9N and dCas9C-DNMT3A yielded a similar band as full-length dCas9-DNMT3A (figure 55).

1: Untransfected, 2: FLAG-dCas9-DNMT3A, 3: FLAG-dCas9N+dCas9C-DNMT3A, 4: FLAG-dCas9N
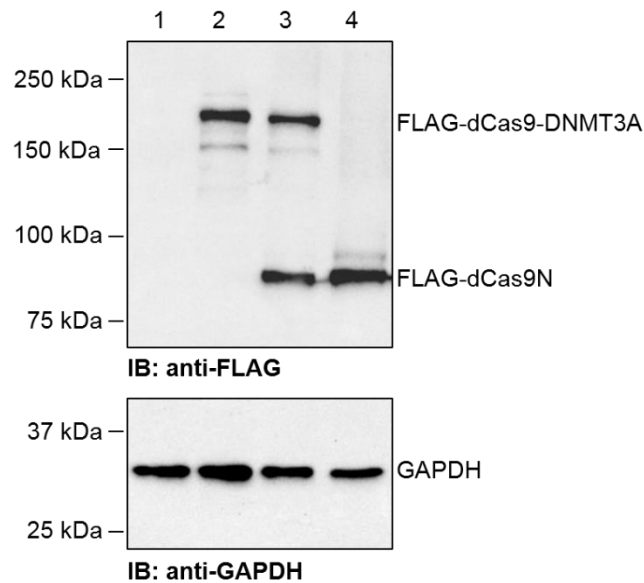
Figure 55: Western blot analysis. Lane 1: Untransfected. Lane 2: FLAG-dCas9-DNMT3A. Lane 3: FLAG-dCas9N+dCas9C-DNMT3A. Lane 4: FLAG-dCas9N. Immunoblotting with anti-FLAG antibody indicated full-length dCas9-DNMT3A and dCas9N. Immunoblotting with anti-GAPDH antibody was used as loading control.

7.3.4 Functional analysis of split-dCas9-DNMT3A

We initially examined the function of split-dCas9-DNMT3A plasmids (containing dCas9N and dCas9C-DNMT3A plasmids) without delivery by AAV. Split-dCas9 plasmids were tested with a group of previously published gRNAs, which had been shown to drive full-length dCas9-DNMT3A to the promoter region of *ILST6* and increase the methylation level in HEK 293 cells (Vojta et al. 2016). After co-transfection of dCas9N with gRNAs and dCas9-DNMT3A constructs into HEK 293 cells, genomic DNA was extracted, and methylation was assessed by sodium bisulfite conversion

and Sanger sequencing. 40 CpGs were analyzed around the gRNAs target region. One group containing active split-dCas9-DNMT3A and non-targeting gRNA; and another group containing inactive methyltransferase constructs (split-dCas9-inactive-DNMT3A) but active *ILST6*-gRNAs were used as negative controls. The results showed that the active split-dCas9-DNMT3A plasmids + *ILST6*-gRNAs significantly increased the methylation level compared to both control (non-targeting and inactive DNMT3A) groups (figure 56A). The groups DNMT3A+*ILST6* gRNAs and inactive-DNMT3A+*ILST6* gRNAs both displayed a significantly lower expression level compared to the non-targeting group (figure 54B). However, gene *IL6ST* expression did not differ between DNMT3A+*IL6ST* gRNAs and inactive-DNMT3A+*ILST6* gRNAs groups (figure 56B). Taken together, split-dCas9-DNMT3A plasmids were able to lead to expression of full-length and active dCas9-DNMT3A protein and methylate the targeted region. However, methylation and expression did not correlate, as active and inactive DNMT3A were equally able to repress expression, which could be due to dCas9 complex binding to the promoter region and blocking transcription factors.
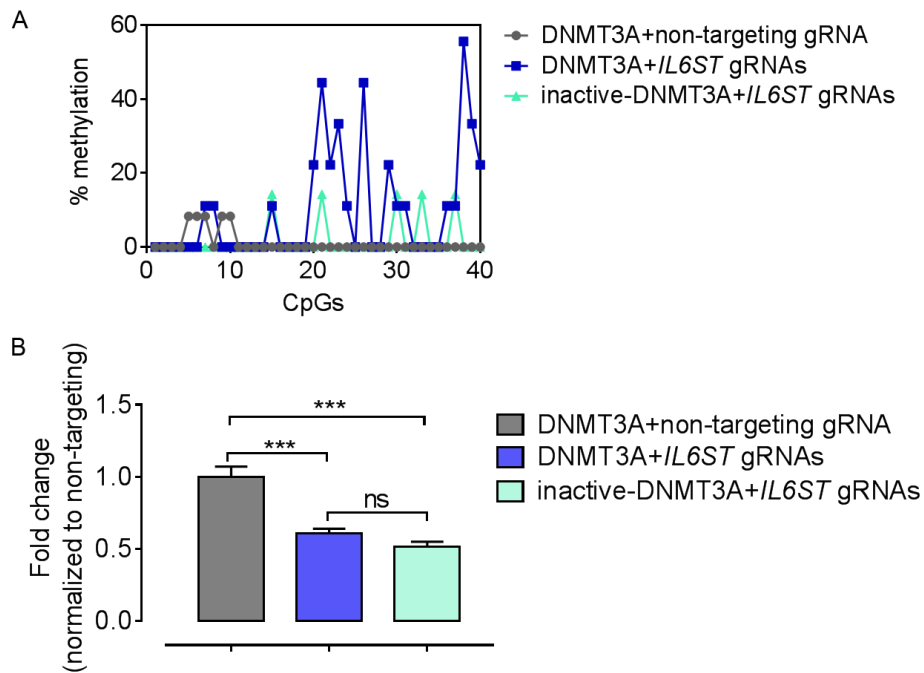
Figure 56: Functional analysis of split-dCas9-DNMT3A. (A) Methylation level of the *IL6ST* promoter region in HEK293 cells transduced with the indicated plasmid combinations. (B) Fold change of *IL6ST* mRNA by qPCR from the same experiment. n=3 per group. Ct values of target genes were normalized to housekeeping gene *GUSB* and to Control. Data are presented as mean ± SEM. ns: not significant, ***p<0.001 by one-way ANOVA plus Bonferroni's multiple comparisons test.

7.3.5 Targeting *COL1A1* in cardiac fibroblasts by AAV-split-dCas9-DNMT3A

Next, we assessed whether split-dCas9-DNMT3A could be delivered by AAV and methylate the promoter region of *COL1A1* in CFs as a treatment for fibrosis. 6 gRNAs were designed to cover several CpGs across the promoter region, 5' UTR and first intron of the human *COL1A1* gene. Non-targeting and targeting gRNAs were separately cloned into the pSMVP-FLAG-dCas9N plasmid, and the respective AAV serotype DJ (AAV-DJ) was produced. After co-transduction with AAV-DJ carrying SMVP-dCas9C-DNMT3A-2Apuro in the CFs, puromycin selection was carried out. COL1A1 expression was assessed at the protein level for two different time points by Western blot. Compared with the non-targeting gRNA group, the COL1A1 protein level did not differ between the targeted and non-targeted gRNAs groups at two time points (figure 57B). This could have been related to disappearance of the dCas9-DNMT3A, but full-length dCas9-DNMT3A was detectable over the entire time (figure 57A). Thus, the data indicated that split-dCas9-DNMT3A was successfully delivered to CFs by AAV-DJ. Moreover, dCas9N and dCas9C-DNMT3A were expressed and reconstituted to the full-length dCas9-DNMT3A fusion protein in the cells. However, in order to obtain meaningful repression of COL1A1 expression, the efficiency of gRNA and AAV-DJ delivery still need to be optimized.
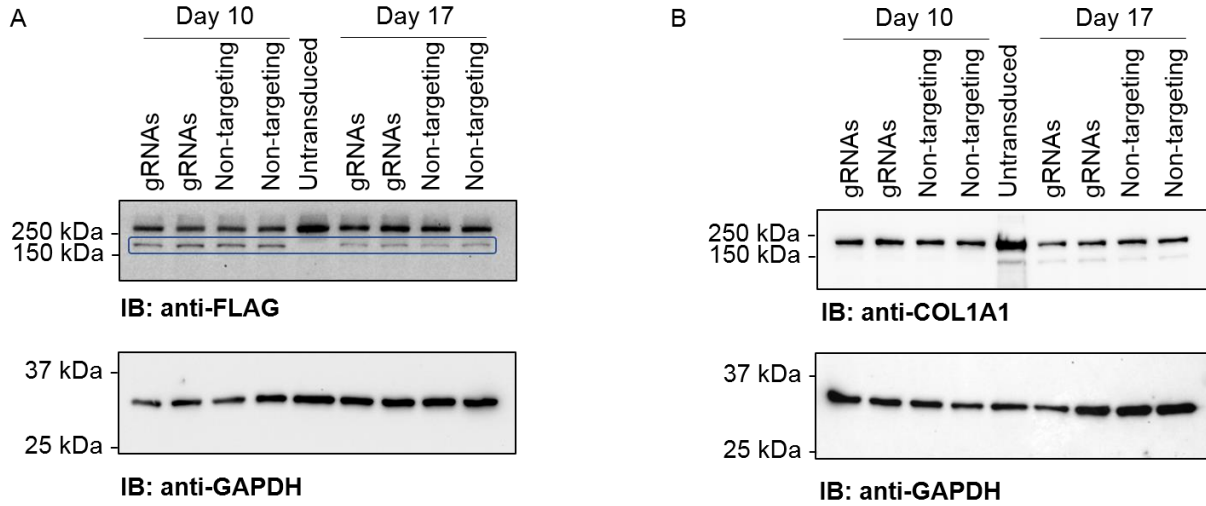
Figure 57: Western blot analysis of dCas9-DNMT3A and COL1A1 in cardiac fibroblasts. Cells were harvested 10 days and 17 days after transduction. gRNAs: gRNAs targeting *COL1A1* promoter region. (A) Immunoblotting with anti-FLAG antibody represents full-length dCas9-DNMT3A (bands in blue box). (B) Immunoblotting with anti-COL1A1 antibody was used to detect COL1A1 expression after targeting. Immunoblotting with anti-GAPDH antibody was used as loading control.

8   Discussion

8.1   VChR1-iPSC generated by CRISPR/Cas9

The overall goal of the thesis was to model AF by chronic tachypacing of atrial-like EHTs, optimize both an EHT model of cardiac fibrosis and an EHT model of cardiac hypertrophy, and eventually investigate targeted manipulation of DNA methylation as a therapeutic approach for AF and HF. In the first part of the study, we aimed to establish an atrial-like EHT tachypacing model and investigate transcriptome and chromatin remodelling in atrial CMs as a consequence of a high beating frequency, as observed in AF. The question was to be answered in an in vitro model, by generation of a ChR knock-in hiPSC line, differentiation of hiPSCs into atrial-like CMs, chronic optical tachypacing of atrial-like EHTs and evaluation of the respective consequences of tachypacing as compared with unpaced controls.

In order to obtain atrial-like EHTs expressing ChR, the first step of this part was to generate a hiPSC line expressing ChR. One of the first reports of a successful combination of optogenetics and cardiac tissue engineering to control beating frequency had been reported from the same institution. This data was based on lentiviral transduction of ChR2/H134R into EHTs (Lemme et al. 2020). However, gene delivery by viral vectors has its downsides, including potential safety issues, complicated handling, as well as low transduction efficiency, and inconsistent expression rate. Thus, to generate EHTs derived from iPSCs that stably express a suitable ChR would be preferable. Creating stable cell lines by lentiviral transduction results in random transgene integration and uncertain copy numbers in the genome (Kim et al. 2021), while CRISPR/Cas9 mediated genome editing allows to insert a transgene into a specific site in the genome (Ran et al. 2013). Therefore, in the present study, we generated the VChR1-iPSC line by CRISPR/Cas9 mediated transgene knock-in at a genomic "safe harbor" AAVS1 locus, which enables stable transgene expression and avoids dysregulation of endogenous genes (Ogata et al. 2003; Oceguera-Yanez et al. 2016). The expression of the transgene was driven by a strong and ubiquitously active promoter CAG promoter. VChR1 was fused to EYFP and luciferase (figure 8). The fusion protein combines a light-emitting luciferase and a light-sensing ChR, so that the activity of the channels can be controlled by either adding a substrate of luciferase or by excitation with light of a certain wavelength (Park et al. 2020). The luciferase was not used in this study and did not affect the optical pacing procedures. Fusion of VChR1 with the fluorescent protein EYFP facilitated detection of VChR1 expression and localization in the cells. Hence, this cell line which had been initially designed for a different project, appeared sufficiently suitable for this study.

Next, we performed a detailed characterization and quality control of this cell line. Cell banking of hiPSCs with good quality control assures reproducibility in basic research or clinical applications (Andrews et al. 2015; Shibamiya et al. 2020). Initially, both master and working cell banks of the VChR1-iPSC line were created by others from the same institute. Meanwhile, quality control was conducted in the present study. PCR reactions using genomic DNA as template identified the clone as heterozygous (figure 9). Flow cytometry analysis and confocal microscopy confirmed the expression of VChR1-EYFP (figure 10). The sterility, pluripotency and genetic integrity were subsequently examined. The VChR-iPSCs expressed a panel of pluripotency markers (SSEA-3, NANOG and KLF4) at a sufficient level and over 90% of cells were positive (figure 12). A NanoString nCounter-based karyotyping was used to quantify chromosome number and detect aneuploidy by quantifying invariant regions crossing all chromosomes (NanoString Technology). Microscopy-based chromosome inspection by G-banding is routinely used in clinical cytogenetics laboratories for identification of human chromosomes and detection of aneuploidy and large structural rearrangements. Both methods were employed and revealed no detectable chromosome abnormalities (figure 13).

Although the 20 nt gRNA governs the site-specificity of Cas9, potential off-target cleavage activity could still happen due to base pair mismatches of gRNA - target DNA site (Cong et al. 2013; Fu et al. 2013). Off-targets could be point mutations, deletions, insertions and translocations. The detection of off-target mutations is still missing in this study. However, in this study, the CRISPR/Cas9 editing was performed by choosing the proposed gRNA with the highest precision and lowest off-target values suggested by the gRNA designing tool CRISPOR and using the gRNA-Cas9 ribonucleoprotein particle-based method (Kim et al. 2014), which is considered to cause low off-target activity. Nevertheless, to really exclude off-target effects in this cell line, a targeted sequencing of the top 10 to 20 predicted off-target sites or whole genome sequencing should be ideally performed in the future.

8.2   Generation and characterization of atrial-like EHTs

The next part of this project aimed to obtain human atrial-like EHTs from hiPSC-derived CMs, which resemble both transcription and electrophysiological properties of the human atrium. Most standard CM differentiation protocols for human pluripotent stem cells result in heterogenous CMs that are mainly consisting of a ventricular-like CM population (Blazeski et al. 2012; Burridge et al. 2012). Substantial evidence indicates that addition of RA (the active metabolite of vitamin A)

during the standard CM differentiation can induce atrial lineage specification (Gassanov et al. 2008; Devalla et al. 2015; Lee et al. 2017; Cyganek et al. 2018; Lemme et al. 2018). However, the observed phenotype of the cells or EHTs varies between studies and sometimes also in the same study. Moreover, none of the papers described CMs or EHTs with a truly human adult atrial phenotype. We therefore attempted to optimize the established EB-based atrial differentiation protocol and additionally establish a monolayer-based atrial differentiation protocol. Furthermore, VChR1-RA-CMs/EHTs were deeply characterized for atrial properties at the transcriptional, functional and electrophysiological level.

8.2.1 Optimization of atrial differentiation protocols

Although previously established RA-EHTs in the institute had displayed atrial transcription profiles, AP shapes of these RA-EHTs showed triangular atrial AP characteristic of AF rather than the spike-and-dome shaped APs with steep initial repolarization phase and low plateau potential in sinus rhythm (Amos et al. 1994; Van Wagoner et al. 1999; Wettwer et al. 2004). To overcome this limitation, optimization of the existing EB-based atrial protocol and establishment of new protocols were carried out in this study. In addition to the atrial subtype promoted by RA signaling at the cardiac induction stage, Lee and colleagues demonstrated that atrial CMs could derive from a specific mesoderm population, induced by a lower concentration of activin A (2 ng/mL) compared with their standard condition (6 ng/mL) in an EB-based differentiation method (Lee et al. 2017). Importantly, the combination of 3 ng/mL BMP4 and 2 ng/mL activin A (3B/2A) was shown to be an optimal condition for atrial subtype specification in this study. Compared with this, 10 ng/mL BMP4 and 3 ng/mL activin A (10B/3A) are used during our standard EB-based differentiation protocol (Breckwoldt et al. 2017).The atrial differentiation was previously established based on this protocol, only with the addition of RA (Lemme et al. 2018). In the present study, we evaluated 10B/3A, 6B/2A and 3B/2A in our standard protocol, together with RA-treatment. CMs from all RA groups did not display differences in the expression of atrial/ventricular chamber markers, and EHTs from all RA groups had faster spontaneous beating rates than EHTs from the control group. These observations are in line with previously established RA-EHTs in the institute (Lemme et al. 2018). However, RA-EHTs from the present study displayed different electrophysiological properties. Previous RA-EHTs had triangular AP shapes, while our new RA-EHTs exhibited regular spike-and-dome AP shapes. In the human atrium, the ultra-rapid delayed rectifier potassium current I_{Kur} is a major repolarizing current and contributes to the low plateau potential (Wettwer et al. 2004). With more negative plateau potentials and shorter APD_{20}, EHTs from the

3B/2A+RA group had more pronounced typical atrial AP shapes than EHTs from the other two RA groups (figure 15). In the presence of the I_{Kur} blocker 4-AP (50 μM), plateau potential was shifted upwards, and APD_{20} was prolonged, which was in line with the reaction of the human atrium to 4-AP. The previously reported changes of the APD_{90} in response to 4-AP had been inconsistent in different models. Prolonged APD_{90} was found in atrial-like CMs or EHTs derived from human stem cell (Devalla et al. 2015; Lemme et al. 2018). In contrast, APD_{90} was shortened by 4-AP in the human atrium in sinus rhythm (Lemme et al. 2018). However, this shortening of APD90 was not observed in the human atrium in AF (Wettwer et al. 2004). In this study, EHTs from the 3B/2A+RA group showed significant shortening of APD_{90} and were thus similar to the human atrium (figure 16C). A possible explanation for the shortening of APD_{90} upon I_{kur} block could be an association with alterations in other ion currents, for example, an increase of the delayed rectifier current I_{kr}. When I_{kr} was blocked by E-4031 (1 μM), 4-AP did not shorten but rather prolong APD_{90} (Wettwer et al. 2004). Another atrial-selective potassium current $I_{K,ACh}$ was shown to be present in EHTs from all RA groups in our study. In line with previous studies, activation of muscarinic receptors by CCh shortened APD (figure 17). In conclusion, RA-EHTs from CMs produced from 3B/2A+RA protocol resembled the human atrium in sinus rhythm more than other RA groups or previously published atrial-like engineered tissues.

Our current EB-based protocol relies on a special experimental setup: spinner flasks with glass bulb impellers and stirrers. The scale of the differentiation is rather large, as it starts with at least 300 million hiPSCs for each round. The whole differentiation procedure takes approximately 5 weeks including iPSCs expansion and cardiac differentiation (Breckwoldt et al. 2017). Therefore, establishing a small scale and simple differentiation protocol was an appealing option for the less often used atrial-like CMs. Generally, an established monolayer-based differentiation can be achieved in a 6-well plate, starting with about 6 million hiPSCs and only takes 2-3 weeks. We thus set out to establish a monolayer-based atrial differentiation method in the present study which would meet the standards discussed above. Our well-established in-house monolayer-based protocol is based on BMP4/activin A-based mesoderm induction (Mosqueira et al. 2018). Here, the success rate of the differentiation in general largely depends on the concentration of BMP4 and activin A. Paying respect to this caveat, in the present study, we only applied RA-treatment without changing the concentrations of BMP4 and activin A. Meanwhile, another well-known monolayer-based method involving CHIR99021-induced mesoderm was tested with the addition of RA as well (Lian et al. 2013; Cyganek et al. 2018). Ventricular and atrial marker expression and RA-EHT spontaneous beating rate were similar to previous results (figure 19, 20). However,

APs from RA-EHTs from monolayer-based differentiation batches displayed triangular shapes, with long APD_{20} and positive plateau voltage (figure 21). Taken together, adding 0.5 µM or 1 µM of RA at day 3 to day 5 (cardiac induction stage) during monolayer-based differentiation was able to induce atrial markers expression but also an atypical not sufficiently atrial electrical phenotype. Thus, further optimization of monolayer-based protocols would be required in the future, for example, with regard to the time window of RA-treatment and mesodermal populations (Devalla et al. 2015; Lee et al. 2017).

Of note, another study has been conducted in our institute in parallel to investigate the effects of different concentrations of RA (0.01, 0.1 and 1 µM) in the EB-based protocol with reduced growth factors. The authors found that only treatment with 1 µM RA, but not less, faithfully reproduced human atrial AP shape. Collectively, concentrations of growth factors (BMP4 and activin A) and RA, and probably the format of differentiation (2D and 3D) all contribute to the chamber specificity of CMs derived from hiPSC.

8.2.2   Characterization of atrial-like VChR1-EHTs

Generation of a homogeneous population of atrial CMs and their comprehensive phenotyping were crucial for AF modelling and AF mechanism studies. Thus, the 3B/2A+RA EB-based protocol was employed to produce atrial-like CMs from VChR1-hiPSCs and then generate atrial-like EHTs for tachypacing to study AF. First, atrial-like VChR1-EHTs were deeply characterized. The standard EB-based protocol with 10B/3A was used to produce more ventricular-like control CMs and EHTs. Gene expression analysis demonstrated that VChR1-RA-EHTs had significantly higher expression of atrial markers (*NPPA*, *MYL7*), transcription factors (*NR2F1*, *NR2F2*, *PITX2*), and ion channels (*KCNJ3*, *KCNA5*), but lower expression of ventricular specific markers (*MYL2* and *IRX4*), compared with VChR1-Ctrl-EHTs (figure 23). This is consistent with previous findings in atrial-like CMs derived from hiPSC (Cyganek et al. 2018; Lemme et al. 2018) and in the human heart (Barth et al. 2005; Asp et al. 2012). Immunofluorescence and immunohistochemistry results confirmed this chamber-specific expression pattern on the protein level (figure 22, figure 24). Importantly, baseline APs of VChR1-RA-EHTs were typical atrial spike-and-dome shapes with low plateau potential and short APD_{20} (figure 25). Unfortunately, further pharmacological experiments during AP recording could not be successfully carried out due to the unstable AP signals. While more successful AP recording had been possible on ChR2/H134R-Ctrl-EHTs (Lemme et al. 2020), the difficulties could be related to general limitations of VChR1, including

high susceptibility to ambient light resulting from a broad excitation spectrum and slow kinetics of the channel (Zhang et al. 2008; Lin 2011). Moreover, ChR2/H134R-EHTs contained 25.7% ChR2/H134R positive cells (Lemme et al. 2020), while VChR1-RA-EHTs consisted of 100% VChR1 positive cells. The strong overexpression of VChR1 in EHTs might have conferred additional difficulties for AP recording.

Contractility recording showed that VChR1-RA-EHTs had higher beating frequency and faster contraction/relaxation kinetics than VChR1-Ctrl-EHTs (figure 26). This is in line with previously published data of RA-CMs/EHTs (Cyganek et al. 2018; Lemme et al. 2018), and also resembles the faster kinetics in human atrial myofibrils compared to ventricular myofibrils (Piroddi et al. 2007). Before reaching the force plateau phase, VChR1-RA-EHTs developed lower force than VChR1-Ctrl-EHTs (figure 27), which is similar to RA-EHTs from the previous study in our institute. However, VChR1-RA-EHT eventually reached the same plateau force as VChR1-Ctrl-EHT, which suggested that VChR1-RA-EHT had a slower force development. Moreover, VChR1-RA-EHTs displayed a positive force-frequency relationship at lower frequencies and a negative force-frequency relationship at higher frequencies, as had been observed in ERC001-RA-EHTs (Lemme et al. 2018). Additionally, expression of VChR1 channel protein was still detectable in 100 days old EHTs. This enables further chronic optical pacing experiments, for which long-term culture of EHTs is required. Taken together, our data showed that VChR1-RA-EHTs are similar to previous atrial-like RA-EHTs regarding molecular and functional characteristics. Importantly, our RA-EHTs resemble the human atrium in terms of electrophysiological properties and these properties were further improved, compared to previous attempts at atrial tissue engineering.

8.3 Optical stimulation of VChR1-RA-EHTs

Chronic atrial tachypacing is commonly used in animals for AF modelling. It can induce electrical and structural remodelling processes which resemble those observed in human AF (Wijffels et al. 1995; Yue et al. 1999). However, long-term electrical stimulation of hiPSC-CMs in 2D or 3D culture causes formation of hypochlorous acid, oxygen-derived free radicals, and pH alterations (Hirt et al. 2014). Chronic tachypacing with optogenetic tools could overcome these constraints.

First, we established a simple and cost-effective customized digital optogenetic pacing platform from readily available components (figure 30). In contrast to the previously used optical device (Lemme et al. 2020), the new device was controlled by a digital microcontroller instead of an analogue trigger box coupled to an external stimulus generator. VChR1-RA-EHTs could follow

pacing from 2.5 to 5 Hz with 60 ms-long blue light pulses at 0.12 mW/mm^2 or green light pulses at 0.08 mW/mm^2. The excitation wavelength of VChR1 is red-shifted compared to ChR2/H134R (Zhang et al. 2008). Thus, possible effects of the red light, used for illumination of the EHTs during contractility analysis, were assessed on VChR1-RA-EHTs by comparing baseline contractility without optical pacing at different red light intensities. Our data demonstrated that red light did not have a significant effect on contractility of VChR1-RA-EHTs (figure 32).

Electrical pacing had been previously shown to improve the maturity of hiPSC-CMs (Hirt et al. 2014; Ronaldson-Bouchard et al. 2018). Considering this point, we evaluated the optimal onset of pacing after EHT casting. Too early pacing prevented VChR1-RA-EHT structural and contractile development (figure 33A). In line with previous observations that continuous optical pacing induced VChR1 desensitization (Lin 2011; Lemme et al. 2020), intermittent tachypacing had to be carried out in this study. Interestingly, when pacing burst time was the same as the interval time, pacing did not affect the contractile force of EHTs (figure 33B), which was in line with a previous study of tachypacing in RA-EHT (Lemoine et al. 2020). However, atrial contractile dysfunction is a hallmark of AF remodelling (Schotten et al. 2002). We observed decreased force when the pacing duration was longer than the interval (figure 33C). Moreover, when optically paced short-term at high frequencies from 3.0 Hz to 6.5 Hz, VChR1-RA-EHTs displayed a negative FFR. This negative FFR had also been observed in previous RA-EHTs (Lemme 2019). As a consequence, we chose the pacing frequency of 5 Hz, which caused a reduction of contractile force to 80% of baseline (figure 34), probably sufficiently stressing the EHTs but without reducing force extremely enough to prevent contractility analysis, and without causing significant cell death. Taken together, a pattern of 10 seconds of break alternating with 25-90 s of pacing at 5 Hz was applied in this study.

8.4 Effects of chronic optical tachypacing

In this study, VChR1-RA-EHTs were optically paced at 5 Hz for about 40 days. We next aimed to probe whether chronic tachypacing would cause AF-like remodelling in VChR1-RA-EHTs, to assess how well our model recapitulates human AF before moving on to employ it to investigate chromatin biology. Experimental and clinical studies have shown that AF induces atrial contractile dysfunction (Daoud et al. 1999; Schotten et al. 2003). In contrast to previous results from tachypaced EHTs (Lemme et al. 2020), we recapitulated the impairment of contractile force of VChR1-RA-EHTs by chronic tachypacing (figure 36). Moreover, chronic tachypacing increased

the release of troponin I from CMs into the culture medium (figure 37), which is in line with the observation of elevated plasma concentrations of cardiac troponin in patients with AF (Costabel et al. 2017; Kaura et al. 2020).

Previous studies have demonstrated that AF correlates with alterations in CM energy metabolism (Ghezelbash et al. 2015; Opacic et al. 2016; Harada et al. 2017). In our standard EHT culture medium, glucose as the main energy substrate can be utilized to produce ATP by CMs in two different ways: (1) anaerobic glycolysis with the production of lactate, and (2) aerobic oxidative metabolism (Ulmer et al. 2018). Lactate can also serve as energy substrate by entering aerobic oxidative metabolism for CMs. The rapid contraction rate of the atria acutely increases ATP consumption early at the onset of AF. However, patients with permanent AF showed mitochondrial dysfunction and a fetal phenotype of energy metabolism, in which glycolysis is the major energy source (Harada et al. 2017). In our results, paced EHTs displayed higher glucose consumption and lower ratio of glucose consumption/lactate production than unpaced EHTs (figure 38). This indicates that tachypaced EHTs may have more aerobic metabolism and produce more ATP and thus resemble an early phase of AF. With a high atrial contraction frequency, AF acutely increases atrial oxygen consumption. A previous study showed that pacing-induced AF in a sheep model acutely increased mitochondrial F0F1-ATPase activity, arguing for higher energy demand (Barbey et al. 2000).

In addition to contractile and metabolic remodelling, possible structural remodelling was also investigated in this study. Histological analysis showed that CMs were predominantly located at the surface of the EHTs with cellular alignment in parallel to the force lines (figure 39, 40), which is similar to many previous observations in EHT (Mannhardt et al. 2016). In a limited number of EHT samples, we did not observe obvious differences between unpaced and paced groups. One explanation could be the lack of specific non-cardiomyocytes in our VChR1-RA-EHTs, such as immune cells and CFs. As mentioned before, these non-cardiomyocytes play an important role in atrial structural remodelling, for example, by secreting fibrogenic mediators. However, more EHTs should be evaluated to confirm this conclusion in the future. The assessment of sarcomere structure and mitochondria should also be included.

To first obtain a global molecular overview of the consequences of tachypacing, bulk RNAseq, ATACseq and histone acetylation H3K27ac ChIPseq were performed in paced and unpaced EHTs to investigate alterations in transcriptome and open and active chromatin regions. The integrative analysis of the RNAseq dataset by PCA revealed that at the PC1 axis, paced EHTs were clearly separated from unpaced EHTs. At the PC2 axis, within the same group, individual

EHTs were more separated from each other in the paced than in the unpaced group (figure 41A), indicating wider variance in the paced group than that in the unpaced group. Of note, on the gene expression level we observed DE gene changes between the unpaced and the paced group (figure 41B), revealing that tachypacing induced global transcriptomic changes. Furthermore, GO enrichment analysis showed that DE gene changes were related to different cellular components, for example, collagen-containing extracellular matrix, cation channel complex and cell-cell contact zone, microtubule and condensed chromosome (figure 42). This data was closely related to the structural and electrical remodelling observed in man. qPCR was further used to validate differential expression of a selection of genes. Upregulation of *NPPA* (encoding atrial natriuretic peptide, ANP) and *NPPB* (encoding brain natriuretic peptide, BNP) were indeed upregulated in paced EHTs (figure 43), both also serve as biomarkers of AF (Zografos and Katritsis 2013). Atrial electrical remodelling in AF includes alterations in ion channel expression. In line with previous studies in human samples (Allessie et al. 2002; Nattel and Dobrev 2012), paced EHTs also displayed lower expression of *KCNJ3* ($I_{K,ACh}$) and higher expression of *KCNJ12* (I_{K1}; figure 43). Additionally, ATACseq and ChIPseq of histone acetylation H3K27ac were used to analyze open and active chromatin regions. We observed that paced EHTs lost peaks in both ATACseq and ChIPseq datasets, compared with unpaced EHTs (figure 44), suggesting that open chromatin regions were fewer in the tachypaced group. Unfortunately, due to insufficient sequencing reads in the ATACseq experiment and lacking replicates in the ChIPseq experiment, we could not further identify specific altered regions in the chromatin.

Last, gene expression analysis showed that chronic tachypacing decreased fibrosis markers (figure 58), which is in line with observations from tachypaced ChR2-Ctrl-EHTs (Lemme 2019), but opposing changes in human AF. Hirt and colleagues had also demonstrated that chronic (electrical) pacing was associated with reduced ECM production and improved maturation (Hirt et al. 2014). We thus concluded that the properties of our model are in themselves partially contradictory as we observed both signs of AF-like pathological remodelling, but also signs of improved maturation. We nevertheless used the model, as many aspects of AF could be faithfully recapitulated and went on to study chromatin dynamics in our model.
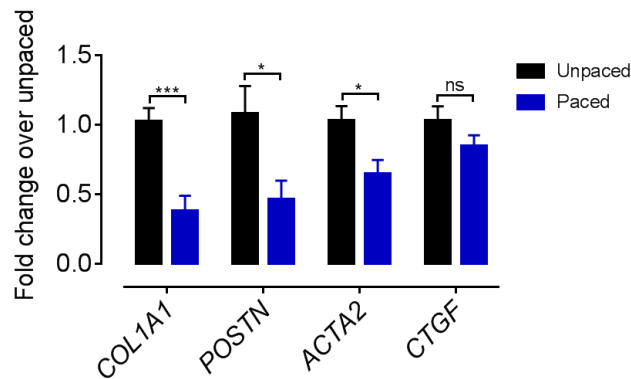
Figure 58: Gene expression analysis of unpaced and paced EHTs by qPCR. n=7 EHTs from 2 batches. Ct values of target genes were normalized to housekeeping gene GUSB and to the upaced group. Data are presented as mean ± SEM. *p<0.05, ***p<0.001, ns: not significant, by unpaired t-test.

8.5   Human EHT disease models to evaluate targeted DNA methylation editing

The progression of heart diseases is also associated with aberrant gene expression. Many of these changes in gene expression have long been known to be detrimental (Tham et al. 2015). Thus, correcting this aberrant transcription, rather than targeting downstream effects might be a promising potential therapeutic approach. As mentioned previously, manipulation of DNA methylation can regulate gene expression. In the second part of this thesis, the aim was to evaluate the therapeutic potential of targeted DNA methylation manipulation for different aspects of HF and AF. Potential advantages of epigenetic manipulation over other therapies could be the possibility of precise targeting, the possibility to address pathways that do not comprise druggable targets and the expected long-term effect over weeks or months. Specifically, compared to gene therapy, gene regulation by epigenetic manipulation is not permanent. In order to start our experiments already with a potential for clinical application, we used AAV as the delivery form of choice for the targeted DNA methylation machinery. To this end, we generated an EHT model of cardiac fibrosis and an EHT model of cardiac hypertrophy based on our robust ventricular-like EHT platform to serve as disease models to evaluate this approach first. And an AAV-based targeted DNA methylation tool was developed for targeted DNA methylation editing.

8.5.1 Generation of fibroblast-EHT

CFs regulate the composition of the extracellular matrix, which contributes to both cardiac function and pathological remodelling. We suspected that fibroblasts could serve as an interesting first target (Rurik et al. 2022) for targeted DNA methylation manipulation, as fibroblasts are regularly over-activated in heart disease and from a technical perspective, gene silencing by de novo-methylation appeared more promising than gene reactivation by demethylation. While demethylation is permissive for gene expression, but not sufficient per se, methylation is sufficient for silencing (Jones 2012). Although CFs in the heart are heterogeneous and have different origins, several studies have identified that CFs can be derived via the epicardial lineage from human pluripotent stem cells (Witty et al. 2014; Iyer et al. 2015; Zhang et al. 2019). This observation led to the establishment of several protocols for CF differentiation from hiPSC. For the present study, CFs were produced through the following procedures: generation of cells from the epicardial lineage from hiPSC-derived mesoderm, by activating BMP and WNT signaling pathways, followed by the epicardium undergoing an epithelial-to-mesenchymal transition toward fibroblast-like cells in response to bFGF (Witty et al. 2014).The mesoderm induction was carried out with the same standard EB-based protocol as for CMs. In our results, gene expression analysis revealed that hiPSC-CFs highly expressed typical fibroblast markers (*COL1A1*, *CNN1*, *DDR2*, *POSTN*, *VIM*), compared with CMs and primary fibroblasts (figure 41). This is in line with the results from several published CF differentiation protocols (Witty et al. 2014; Zhang et al. 2019).

The aim of this part was to manipulate DNA methylation of the *COL1A1* promoter region in an EHT-based fibrosis model. To this end, CF-EHTs containing CFs and CMs were generated. Previous studies had shown that introducing CFs into EHT would improve force generation and CM maturation (Matsuura et al. 2011; Liau et al. 2017; Tiburcy et al. 2017), while others reported that in vitro expanded adult CFs can induce fibrosis-like effects in engineered heart tissues. (Li et al. 2017). Probable signs of fibrosis in EHT may include lower force, lower relaxation velocity, and structural remodelling, such as increased collagen content. In the present study, three batches of CF-EHTs with different CF content (5%, 10%, 20%) were generated and characterized. Interestingly, the morphology and force-generation of CF-EHTs were different among three batches. In Batch A (figure 47), increment of CF content led to a progressive and exaggerated decline in CF-EHT diameter. Accordingly, 20% CF-EHTs became very thin and ripped at an early stage of remodelling. In contrast, 5% and 10% CF-EHTs developed significantly higher contractile force than control EHTs, without differences between the 5% and 10% groups at the plateau

phase. These observations indicated that CFs could indeed promote contractile force development. In contrast, CFs induced shortening of CF-EHTs in Batch B and C (figure 48, 49). With an increasing number of CFs, CF-EHTs reached a shorter final length and developed lower force accordingly. CF-EHTs from Batch B with 20% FB became very short and were eventually not able to deflect the silicone mounting posts further. These observations demonstrate how CFs can both increase and decrease force, depending on the exact conditions and thus confer both positive and negative effects in EHTs. To evaluate if the low force generation was caused by CF activation and fibrosis, 10% CF-EHTs were treated with the TGF-β1 receptor inhibitor SB-431542. TGF-β1 is a principal pro-fibrotic factor and is alone sufficient to activate CFs, contributing to fibrosis (Leask 2007). As expected, the contractile force of treated 10% CF-EHTs was higher than that of untreated 10% CF-EHTs. Most likely CFs in Batch B and C were in a more activated status, associated with proliferation and collagen deposition, causing weaker contractions and higher tissue stiffness. Therefore, we successfully established fibrotic CF-EHT, in which activation state of the fibroblasts should be additionally controlled by TGF receptor signaling manipulation. This model could serve as a platform for manipulation of DNA methylation of *COL1A1* promoter region.

8.5.2   Pro-hypertrophic EHT model

The goal of this part of the work was to use the EHT model of pathological hypertrophy to obtain first evidence on whether targeted manipulation of DNA methylation may represent a therapy for heart failure. In this part of the work, the specific aim was to manipulate DNA methylation directly in CMs rather than in CFs as before. This part of the work was considered more challenging, as very few genes are repressed in heart failure and the fetal gene programme mainly includes reactivation of fetal genes (Dorn et al. 2003). Thus, selection of genes would have been either limited to the few repressed genes, such as SERCA2a or would have to include reactivation by demethylation, as discussed above.

As mentioned above, cardiac hypertrophy precedes the onset of HF. In this study, a pro-hypertrophic EHT model was harnessed to provide a suitable disease model. EHTs from dKatushka2-labeled red fluorescent CMs were treated with pro-hypertrophic compounds PE and ET-1 as previously described (Madsen et al. 2021). With regard to the well-established paradigm of the reactivation of the fetal gene program, both PE and ET-1 had been shown to induce a hypertrophic response via activation of AKT, ERK and calcineurin/NFAT signaling pathways, resulting in expression of hypertrophy-associated genes such as ANP (encoded by *NPPA*) and

BNP (encoded by *NPPB*) and repression of calcium handling protein encoding genes such as SERCA2a (Shubeita et al. 1990; Rolfe et al. 2005). Moreover, SERCA2a (encoded by *ATP2A2*) had been previously shown to be downregulated in several HF experimental models, arguing for the suitability of our model (Hasenfuss et al. 1994; Huang et al. 2014). In line with previous results, we indeed observed changes in the expression of hypertrophy-associated genes in treated EHTs compared with untreated EHTs, such as upregulation of *NPPA* and *NPPB*, and downregulation of *ATP2A2* (figure 53). Repression of SERCA2a results in impaired calcium clearance from the cytosol, further contributing to contractile dysfunction (Hasenfuss et al. 1994). Treatment of CMs with the α-adrenergic agonist PE is positively chronotropic in isolated rabbit CMs (Srivastava et al. 1977). These data are in line with our observation that treated dKatushka2-EHTs showed lower force and higher beating frequency compared to controls (figure 51, 52). Taken together, we successfully reproduced and adjusted the pro-hypertrophic EHT model on dKatushka2-EHTs. Our next step was therefore targeted DNA methylation editing of specific hypertrophic genes.

8.6   Targeted DNA methylation manipulation

In order to manipulate DNA methylation site-specifically with the goal to activate or repress gene expression, we attempted to develop a CRISPR/dCas9-based DNA methylation editing tool and deliver it to human EHTs with AAV. In 2016, a construct fusing the functional domain of the DNA methyltransferase DNMT3A with a catalytically inactive Cas9 (dCas9) for targeted CpG methylation was first published (Vojta et al. 2016). By transfecting plasmids co-expressing dCas9-DNMT3A and gRNA, CpG sites within the promoter of the gene *BACH2* or *IL6ST* were methylated efficiently and specifically. In another study, Liu and colleagues fused the functional domains of either the demethylating enzyme TET1 or DNMT3A with a dCas9 to demethylate or methylate target DNA sequences (Liu et al. 2016). These editing tools were delivered to mice via lentiviral injection and shown to change the methylation state of target DNA sequences. In the present study, we aimed to package dCas9-TET1 or dCas9-DNMT3A into an AAV gene delivery system and test the feasibility of targeted DNA methylation editing based therapeutic approaches in heart disease.

Generally, the packaging capacity of AAV as a vector for DNA delivery is limited to ~5.0 kb. However, the size of the most commonly used dCas9, derived from *Streptococcus pyogenes* Cas9 is 4.2 kb, which makes additional packaging of the catalytic domain of TET1 (2.1 kb) or DNMT3A (0.9 kb) very challenging. Chew and colleagues have established an AAV-split-Cas9

platform for gene editing and transcription regulation, by splitting Cas9 at site V713-D718 (Chew et al. 2016). We applied this platform in the present study, as it seemed suitable for overcoming the packaging capacity limitations (figure 54). First, Cas9N and Cas9C were point mutated to dCas9N and dCas9C, respectively. Then, the catalytic domain of TET1 or DNMT3A was fused with dCas9C at the C-terminal. In line with the published results of splitting Cas9, dCas9N and dCas9C could also be successfully shown to reconstitute to full-length dCas9 by split-intein protein trans-splicing in transfected HEK 293 cells (figure 55). Moreover, after packaging split-dCas9 into AAV of the serotype DJ, full-length dCas9 was detected in AAV-DJ transduced CFs (figure 57A).

We further assessed the methylation activity of split-dCas9-DNMT3A constructs in HEK 293 cells. Similar to full-length dCas9-DNMT3A in the previous study (Vojta et al. 2016), split-dCas9-DNMT3A also induced an increase in CpG methylation in the presence of the same specific gRNAs targeting the *IL6ST* promoter region. In contrast, the methylation of the same region was very low in cells treated under the same conditions but with a non-targeting gRNA. Vojta and colleagues reported a slight increment of DNA methylation in cells treated with the full-length dCas9-inactive DNMT3A. A similar result was observed in our split-dCas9-inactive DNMT3A group. This could be explained on the grounds of the hypothesis that the catalytical domain of inactive DNMT3A might dimerize with an active endogenous partner and contribute to the residual DNA methylation activity (Jia et al. 2007; Van Emburgh and Robertson 2011). To assess whether targeted DNA methylation editing could regulate gene expression, the transcript abundance of the gene *IL6ST* from all three groups was analyzed. Compared with the non-targeting group, the active DNMT3A group had a significantly lower expression level of *IL6ST* which was in concordance with the results published by Vojta and colleagues (2016). However, the inactive DNMT3A group also displayed significantly lower expression of *IL6ST* compared with non-targeting control and showed no significant difference from the active DNMT3A group. The silencing of *IL6ST* in both, the active and inactive DNMT3A groups, can likely be explained by CRISPR interference, the phenomenon that the dCas9 complex competes with transcription factors binding to the promoter region (Qi et al. 2013). Unfortunately, we could thus not draw the conclusion that increased DNA methylation repressed *IL6ST* expression from our existing data. Moreover, the level of silencing with split-dCas9-DNMT3A was less than 2-fold in our hands, while Vojta and colleagues had reported more than 2-fold changes with full-length dCas9-DNMT3A. The discrepancy could be due to the possibly incomplete reconstitution efficiency of dCas9N and dCas9C in the cells. In figure 55, the dCas9N fragment was still detectable in cells with co-

transfection of dCas9N and dCas9C (lane 3). As a result, the methylation level might not have been sufficient to induce gene silencing. In the future, the ratio of dCas9N and dCas9C would have to be further optimized. As proof of principle, however, we successfully demonstrated that our split-dCas9 tool worked when delivered both by plasmid transfection and AAV-DJ transduction. With the assistance of protein inteins, dCas9N and dCas9C were shown to assemble to full-length dCas9. Moreover, dCas9N-gRNA and dCas9C-DNMT3A were able to methylate targeted DNA loci.

Despite the inconclusive relation between methylation and gene expression from our experiments with cultured HEK293 cells, we attempted to utilize our split-dCas9-DNMT3A tool to manipulate DNA methylation of the *COL1A1* promoter region and silence the expression of *COL1A1* in CFs. To this end, 6 different gRNAs targeting the *COL1A1* promoter region with dCas9N and dCas9C-DNMT3A were packaged into AAV-DJ and delivered to CFs. Western blot analysis successfully confirmed the presence of COL1A1 and dCas9-DNMT3A at the protein level (figure 57). However, with the conditions used here, we could not observe a significant reduction of COL1A1 expression. This could be explained by low AAV transduction efficiency in CF, resulting in low expression of dCas9-DNMT3A and consecutively low additional methylation of the *COL1A1* promoter region. Moreover, we had no prior information about which CpG sites could impact most on the regulation of *COL1A1* transcription. In the future, the MOI of AAV-DJ and gRNA targeting sites need to be further optimized. Interestingly, the protein level of dCas9-DNMT3A dropped from day 10 to day 17, which is line with the findings by Vojta and colleagues (2016). This observation could provide a clue for further optimization experiments to find the time point with the maximum expression level of dCas9-DNMT3A.

8.7   Conclusion and future perspectives

The pathophysiological processes that cause AF are still not well understood and the lack of suitable in vitro models limits the evaluation of new potential therapies. Understanding chromatin structure modifications in AF could lead to novel therapeutic strategies. In the first part of this study, we aimed to build a chronically tachypaced atrial-like EHT model for AF modelling and chromatin structure analysis. After optimization of atrial cardiomyocyte differentiation by growth factor adjustment, our RA-EHTs consisting of atrial-like CMs displayed remarkable similarities to the human atrium on the transcriptional and electrophysiological level. A suitable optogenetic device was then built for long-term optical stimulation of EHTs expressing VChR1. After

intermittent chronic tachypacing of VChR1-RA-EHTs, we observed contractile dysfunction, and changes in transcriptome and chromatin accessibility in paced EHTs. We thus improved the specificity of atrial-like differentiation of CMs derived from hiPSCs and established a chronic optical tachypacing-based atrial-like EHT model that partially recapitulated pathological processes observed in AF. Thus, this human atrial-like EHT model could be a valuable in vitro model to study underlying mechanisms of AF and test anti-arrhythmic therapies or pro-arrhythmic drugs in the future.

Despite these qualities, a number of aspects of the model and its analysis may be improved. Atrial remodelling in AF is multifaceted and associated with non-cardiomyocytes in the atrium. In the future, implementation of non-cardiomyocytes into this atrial-like EHT model could create a more pathophysiologically relevant AF substrate and enhance in vitro structural remodelling. Moreover, in our study, the intermittent chronic tachypacing was necessary due to the desensitization of VChR1. New ChR candidates should be tested to achieve continuous chronic tachypacing in the future. Last, in order to better understand changes in transcriptome and chromatin accessibility, and to fully exploit the advantages of our tachypaced atrial-like model, more experiments need to be carried out to improve the sequencing data quality with regard to ATACseq and ChIPseq. A detailed analysis of ATACseq and ChIPseq data is required to assess chromatin remodelling related to tachypacing. For example, differential peaks analysis, transcription factor motif analysis and integration of ATACseq and ChIPseq data with RNAseq data will allow for the identification of important or novel pathways involved in AF.

In the second part of this thesis, we further adapted and optimized two further EHT models and aimed to investigate targeted DNA methylation editing as a potential therapeutic approach for different stages of HF. First, a fibroblast-EHT (CF-EHT) model and a pro-hypertrophic EHT model were successfully generated by capitalizing on previously established methods in our institute (Werner 2018; Madsen et al. 2021). For fibrosis modelling, a detailed characterization, especially regarding possible inventions to activate CFs in CF-EHT still need to be carried out in the future. As gene expression can be regulated by epigenetic changes, we aimed to manipulate DNA methylation at specific genes that are related to the pathophysiology of heart failure. As a first step towards this goal, we established an AAV-based delivery system for the dCas9-based DNA methylation manipulation machinery. To overcome the AAV packaging limit, split-dCas9-DNMT3A and split-dCas9-TET1 were created by splitting dCas9 into two parts and fusing them with protein interns. We observed full-length of dCas9-DNMT3A protein and higher methylation level in the promoter region of a published target gene after co-transfecting split-dCas9-DNMT3A

plasmids into HEK 293 cells. In the next step, we unfortunately did not observe clear repression of the gene *COL1A1* in CFs via AAV delivery of split-dCas9-DNMT3A. Owing to superseding variability, in order to achieve our goal of regulating gene expression by targeted DNA methylation editing in EHT disease models, choosing more efficient gRNAs to the targeted region, testing an optimized ratio of dCas9N and dCas9C and optimization of AAV transduction efficiency in 2D-cultured CFs needs to be performed, before again venturing into 3D tissue culture.

Once targeted DNA methylation manipulation as a potential therapeutic approach is established in our robust ventricular-like EHT models, we could apply this strategy to our tachypacing-based atrial-like EHT model to explore AF treatment. For example, split-dCas9-DNMT3A could be used to repress the expression of atrial selective channels (I_{Kur}, $I_{K,Ach}$) instead of using channel blockers, known for the adverse cardiac side effects complicating therapy. In addition, we would induce CFs into atrial-like EHTs to model atrial fibrosis during AF, and then down-regulate COL1A1 by split-dCas9-DNMT3A.

9   Bibliography

Aimé-Sempé C, Folliguet T, Rücker-Martin C, et al (1999) Myocardial cell death in fibrillating and dilated human right atria. J Am Coll Cardiol 34:1577–1586. https://doi.org/10.1016/S0735-1097(99)00382-4

Allessie M, Ausma J, Schotten U (2002) Electrical, contractile and structural remodeling during atrial fibrillation. Cardiovasc Res 54:230–246. https://doi.org/10.1016/S0008-6363(02)00258-4/2/54-2-230-GR10.GIF

Allessie MA, Bonke FIM, Schopman FJG (1977) Circus movement in rabbit atrial muscle as a mechanism of tachycardia. III. The "leading circle" concept: a new model of circus movement in cardiac tissue without the involvement of an anatomical obstacle. Circ Res 41:9–18. https://doi.org/10.1161/01.RES.41.1.9

Amos GJ, Wettwer E, Li Q, et al (1994) Differences in outward currents of human atrial and ventricular myocytes. Circulation 90:I–581

Andrade J, Khairy P, Dobrev D, Nattel S (2014) The clinical profile and pathophysiology of atrial fibrillation: Relationships among clinical features, epidemiology, and mechanisms. Circ Res 114:1453–1468. https://doi.org/10.1161/CIRCRESAHA.114.303211

Andrews PW, Baker D, Benvinisty N, et al (2015) Points to consider in the development of seed stocks of pluripotent stem cells for clinical applications: International Stem Cell Banking Initiative (ISCBI). Regen Med 10:1–44. https://doi.org/10.2217/rme.14.93

Arrenberg AB, Stainier DYR, Baier H, Huisken J (2010) Optogenetic control of cardiac function. Science (80-) 330:971–974. https://doi.org/10.1126/science.1195929

Asp J, Synnergren J, Jonsson M, et al (2012) Comparison of human cardiac gene expression profiles in paired samples of right atrium and left ventricle collected in vivo. Physiol Genomics 44:89–98. https://doi.org/10.1152/PHYSIOLGENOMICS.00137.2011/SUPPL_FILE/TABLES1.XLS

Barbey O, Pierre S, Duran MJ, et al (2000) Specific up-regulation of mitochondrial F0F1-ATPase activity after short episodes of atrial fibrillation in sheep. J Cardiovasc Electrophysiol 11:432–438. https://doi.org/10.1111/J.1540-8167.2000.TB00339.X

Bardet AF, He Q, Zeitlinger J, Stark A (2011) A computational pipeline for comparative ChIP-seq analyses. Nat Protoc 2012 71 7:45–61. https://doi.org/10.1038/nprot.2011.420

Barth AS, Merk S, Arnoldi E, et al (2005) Functional profiling of human atrial and ventricular gene expression. Pflugers Arch Eur J Physiol 450:201–208. https://doi.org/10.1007/S00424-005-1404-8/FIGURES/1

Bedada FB, Chan SSK, Metzger SK, et al (2014) Acquisition of a Quantitative, Stoichiometrically Conserved Ratiometric Marker of Maturation Status in Stem Cell-Derived Cardiac Myocytes. Stem Cell Reports 3:594–605. https://doi.org/10.1016/J.STEMCR.2014.07.012

Benser ME, Walcott GP, Killingsworth CR, et al (2001) Atrial defibrillation thresholds of electrode configurations available to an atrioventricular defibrillator. J Cardiovasc Electrophysiol 12:957–964. https://doi.org/10.1046/j.1540-8167.2001.00957.x

Benzoni P, Campostrini G, Landi S, et al (2020) Human iPSC modelling of a familial form of atrial fibrillation reveals a gain of function of If and ICaL in patient-derived cardiomyocytes. Cardiovasc Res 116:1147–1160. https://doi.org/10.1093/CVR/CVZ217

Berglund K, Birkner E, Augustine GJ, Hochgeschwender U (2013) Light-Emitting Channelrhodopsins for Combined Optogenetic and Chemical-Genetic Control of Neurons. PLoS One 8:e59759. https://doi.org/10.1371/JOURNAL.PONE.0059759

Bernardo BC, Weeks KL, Pretorius L, McMullen JR (2010) Molecular distinction between physiological and pathological cardiac hypertrophy: Experimental findings and therapeutic strategies. Pharmacol Ther 128:191–227. https://doi.org/10.1016/j.pharmthera.2010.04.005

Blazeski A, Zhu R, Hunter DW, et al (2012) Electrophysiological and contractile function of cardiomyocytes derived from human embryonic stem cells. Prog Biophys Mol Biol 110:178–195. https://doi.org/10.1016/j.pbiomolbio.2012.07.012

Boyden ES, Zhang F, Bamberg E, et al (2005) Millisecond-timescale, genetically targeted optical control of neural activity. Nat Neurosci 2005 89 8:1263–1268. https://doi.org/10.1038/nn1525

Bragazzi NL, Zhong W, Shu J, et al (2021) Burden of heart failure and underlying causes in 195 countries and territories from 1990 to 2017. Eur J Prev Cardiol 28:1682–1690. https://doi.org/10.1093/EURJPC/ZWAA147

Breckwoldt K, Letuffe-Brenière D, Mannhardt I, et al (2017) Differentiation of cardiomyocytes and generation of human engineered heart tissue. Nat Protoc 12:1177–1197. https://doi.org/10.1038/nprot.2017.033

Buenrostro JD, Wu B, Chang HY, Greenleaf WJ (2015) ATAC-seq: A Method for Assaying Chromatin Accessibility Genome-Wide. Curr Protoc Mol Biol 109:21.29.1. https://doi.org/10.1002/0471142727.MB2129S109

Burridge PW, Anderson D, Priddle H, et al (2007) Improved Human Embryonic Stem Cell Embryoid Body Homogeneity and Cardiomyocyte Differentiation from a Novel V-96 Plate Aggregation System Highlights Interline Variability. Stem Cells 25:929–938. https://doi.org/10.1634/STEMCELLS.2006-0598

Burridge PW, Keller G, Gold JD, Wu JC (2012) Production of De Novo Cardiomyocytes: Human Pluripotent Stem Cell Differentiation and Direct Reprogramming. Cell Stem Cell 10:16–28. https://doi.org/10.1016/J.STEM.2011.12.013

Camelliti P, Borg TK, Kohl P (2005) Structural and functional characterisation of cardiac fibroblasts. Cardiovasc Res 65:40–51. https://doi.org/10.1016/J.CARDIORES.2004.08.020/2/65-1-40-FIG8.GIF

Carlson S, Helterline D, Asbe L, et al (2017) Cardiac macrophages adopt profibrotic/M2 phenotype in infarcted hearts: Role of urokinase plasminogen activator. J Mol Cell Cardiol 108:42–49. https://doi.org/10.1016/J.YJMCC.2016.05.016

Chew WL, Tabebordbar M, Cheng JKW, et al (2016) A multifunctional AAV-CRISPR-Cas9 and its host response. Nat Methods 13:868–874. https://doi.org/10.1038/nmeth.3993

Comtois P, Kneller J, Nattel S (2005) Of circles and spirals: Bridging the gap between the leading circle and spiral wave concepts of cardiac reentry. Europace 7

Cong L, Ran FA, Cox D, et al (2013) Multiplex genome engineering using CRISPR/Cas systems. Science (80-) 339:819–823. https://doi.org/10.1126/SCIENCE.1231143/SUPPL_FILE/PAPV2.PDF

Costabel JP, Burgos LM, Trivi M (2017) The Significance Of Troponin Elevation In Atrial Fibrillation. J Atr Fibrillation 9:. https://doi.org/10.4022/JAFIB.1530

Cyganek L, Hasenfuss G, Guan K, et al (2018) Deep phenotyping of human induced pluripotent stem cell – derived atrial and ventricular cardiomyocytes Find the latest version : Deep phenotyping of human induced pluripotent stem cell – derived atrial and ventricular cardiomyocytes. JCI insight 3:e99941

Daoud EG, Marcovitz P, Knight BP, et al (1999) Short-Term Effect of Atrial Fibrillation on Atrial Contractile Function in Humans. Circulation 99:3024–3027.

https://doi.org/10.1161/01.CIR.99.23.3024

de Wit E, de Laat W (2012) A decade of 3C technologies: insights into nuclear organization. Genes Dev 26:11–24. https://doi.org/10.1101/GAD.179804.111

Devalla HD, Schwach V, Ford JW, et al (2015) Atrial-like cardiomyocytes from human pluripotent stem cells are a robust preclinical model for assessing atrial-selective pharmacology. EMBO Mol Med 7:394–410. https://doi.org/10.15252/emmm.201404757

Dobrev D, Friedrich A, Voigt N, et al (2005) The G protein-gated potassium current I(K,ACh) is constitutively active in patients with chronic atrial fibrillation. Circulation 112:3697–3706. https://doi.org/10.1161/CIRCULATIONAHA.105.575332

Dorn GW, Robbins J, Sugden PH (2003) Phenotyping Hypertrophy. Circ Res 92:1171–1175. https://doi.org/10.1161/01.RES.0000077012.11088.BC

Dwenger M, Kowalski WJ, Ye F, et al (2019) Chronic optical pacing conditioning of h-iPSC engineered cardiac tissues. J Tissue Eng 10:. https://doi.org/10.1177/2041731419841748

Eschenhagen T, Fink C, Remmers U, et al (1997) Three-dimensional reconstitution of embryonic cardiomyocytes in a collagen matrix: a new heart muscle model system. FASEB J 11:683–694. https://doi.org/10.1096/FASEBJ.11.8.9240969

Fang L, Murphy AJ, Dart AM (2017) A Clinical Perspective of Anti-Fibrotic Therapies for Cardiovascular Disease. Front Pharmacol 8:186. https://doi.org/10.3389/FPHAR.2017.00186

Fatica A, Bozzoni I (2013) Long non-coding RNAs: new players in cell differentiation and development. Nat Rev Genet 2013 151 15:7–21. https://doi.org/10.1038/nrg3606

Frangogiannis NG (2012) Matricellular proteins in cardiac adaptation and disease. Physiol Rev 92:635–688. https://doi.org/10.1152/PHYSREV.00008.2011/ASSET/IMAGES/LARGE/Z9J0021226120011.JPEG

Frank S, Zhang M, Schöler HR, Greber B (2012) Small molecule-assisted, line-independent maintenance of human pluripotent stem cells in defined conditions. PLoS One 7:. https://doi.org/10.1371/journal.pone.0041958

Fu Y, Foden JA, Khayter C, et al (2013) High-frequency off-target mutagenesis induced by CRISPR-Cas nucleases in human cells. Nat Biotechnol 2013 319 31:822–826.

https://doi.org/10.1038/nbt.2623

Funken M, Malan D, Sasse P, Bruegmann T (2019) Optogenetic hyperpolarization of cardiomyocytes terminates ventricular arrhythmia. Front Physiol 10:498. https://doi.org/10.3389/FPHYS.2019.00498/FULL

Fusaki N, Ban H, Nishiyama A, et al (2009) Efficient induction of transgene-free human pluripotent stem cells using a vector based on Sendai virus, an RNA virus that does not integrate into the host genome. Proc Jpn Acad Ser B Phys Biol Sci 85:348. https://doi.org/10.2183/PJAB.85.348

Gasparovic H, Cikes M, Kopjar T, et al (2014) Atrial apoptosis and fibrosis adversely affect atrial conduit, reservoir and contractile functions. Interact Cardiovasc Thorac Surg 19:223–230. https://doi.org/10.1093/ICVTS/IVU095

Gassanov N, Er F, Zagidullin N, et al (2008) Retinoid acid-induced effects on atrial and pacemaker cell differentiation and expression of cardiac ion channels. Differentiation 76:971–980. https://doi.org/10.1111/j.1432-0436.2008.00283.x

Ghezelbash S, Molina CE, Dobrev D (2015) Altered atrial metabolism: An underappreciated contributor to the initiation and progression of atrial fibrillation. J Am Heart Assoc 4:1808. https://doi.org/10.1161/JAHA.115.001808

Glezeva N, Moran B, Collier P, et al (2019) Targeted DNA Methylation Profiling of Human Cardiac Tissue Reveals Novel Epigenetic Traits and Gene Deregulation Across Different Heart Failure Patient Subtypes. Circ Heart Fail 12:. https://doi.org/10.1161/CIRCHEARTFAILURE.118.005765

Grobarczyk B, Franco B, Hanon K, Malgrange B (2015) Generation of Isogenic Human iPS Cell Line Precisely Corrected by Genome Editing Using the CRISPR/Cas9 System. Stem cell Rev reports 11:774–787. https://doi.org/10.1007/S12015-015-9600-1

Haas J, Frese KS, Park YJ, et al (2013) Alterations in cardiac DNA methylation in human dilated cardiomyopathy. EMBO Mol Med 5:413–429. https://doi.org/10.1002/EMMM.201201553

Hanna RE, Doench JG (2020) Design and analysis of CRISPR–Cas experiments. Nat. Biotechnol. 38:813–823

Hansen A, Eder A, Bönstrup M, et al (2010) Development of a drug screening platform based on engineered heart tissue. Circ Res 107:35–44. https://doi.org/10.1161/CIRCRESAHA.109.211458

Harada M, Melka J, Sobue Y, Nattel S (2017) Metabolic Considerations in Atrial Fibrillation - Mechanistic Insights and Therapeutic Opportunities. Circ J 81:1749–1757. https://doi.org/10.1253/CIRCJ.CJ-17-1058

Hasenfuss G, Reinecke H, Studer R, et al (1994) Relation Between Myocardial Function and Expression of Sarcoplasmic Reticulum Ca2+-ATPase in Failing and Nonfailing Human Myocardium From the Medizinische Klink III (G

Hirt MN, Boeddinghaus J, Mitchell A, et al (2014) Functional improvement and maturation of rat and human engineered heart tissue by chronic electrical stimulation. J Mol Cell Cardiol 74:151–161. https://doi.org/10.1016/j.yjmcc.2014.05.009

Hochbaum DR, Zhao Y, Farhi SL, et al (2014) All-optical electrophysiology in mammalian neurons using engineered microbial rhodopsins. Nat Methods 2014 118 11:825–833. https://doi.org/10.1038/nmeth.3000

Hong L, Zhang M, Ly OT, et al (2021) Human induced pluripotent stem cell-derived atrial cardiomyocytes carrying an SCN5A mutation identify nitric oxide signaling as a mediator of atrial fibrillation. Stem Cell Reports 16:1542–1554. https://doi.org/10.1016/J.STEMCR.2021.04.019

Huang H, Joseph LC, Gurin MI, et al (2014) Extracellular signal-regulated kinase activation during cardiac hypertrophy reduces sarcoplasmic/endoplasmic reticulum calcium ATPase 2 (SERCA2) transcription. J Mol Cell Cardiol 75:58–63. https://doi.org/10.1016/j.yjmcc.2014.06.018

Ito S, Shen L, Dai Q, et al (2011) Tet proteins can convert 5-methylcytosine to 5-formylcytosine and 5-carboxylcytosine. Science (80-) 333:1300–1303. https://doi.org/10.1126/SCIENCE.1210597/SUPPL_FILE/ITO.SOM.PDF

Iwasaki YK, Nishida K, Kato T, Nattel S (2011) Atrial fibrillation pathophysiology: Implications for management. Circulation 124:2264–2274. https://doi.org/10.1161/CIRCULATIONAHA.111.019893

Iyer D, Gambardella L, Bernard WG, et al (2015) Robust derivation of epicardium and its differentiated smooth muscle cell progeny from human pluripotent stem cells. Dev 142:1528–1541. https://doi.org/10.1242/DEV.119271/VIDEO-1

January CT, Wann LS, Alpert JS, et al (2014) 2014 AHA/ACC/HRS guideline for the management of patients with atrial fibrillation: A report of the American college of

Cardiology/American heart association task force on practice guidelines and the heart rhythm society. J Am Coll Cardiol 64:e1–e76. https://doi.org/10.1016/j.jacc.2014.03.022

Jia D, Jurkowska RZ, Zhang X, et al (2007) Structure of Dnmt3a bound to Dnmt3L suggests a model for de novo DNA methylation. Nat 2007 4497159 449:248–251. https://doi.org/10.1038/nature06146

Jiang C, Li HT, Zhou YM, et al (2018) Cardiac optogenetics: a novel approach to cardiovascular disease therapy. EP Eur 20:1741–1749. https://doi.org/10.1093/EUROPACE/EUX345

Jinek M, Chylinski K, Fonfara I, et al (2012) A programmable dual-RNA-guided DNA endonuclease in adaptive bacterial immunity. Science (80-) 337:816–821. https://doi.org/10.1126/science.1225829

Jones PA (2012) Functions of DNA methylation: islands, start sites, gene bodies and beyond. Nat Rev Genet 2012 137 13:484–492. https://doi.org/10.1038/nrg3230

Jonsson MKB, Hartman RJG, Ackers-Johnson M, et al (2016) A Transcriptomic and Epigenomic Comparison of Fetal and Adult Human Cardiac Fibroblasts Reveals Novel Key Transcription Factors in Adult Cardiac Fibroblasts. JACC Basic to Transl. Sci. 1:590–602

Kannel WB, Wolf PA, Benjamin EJ, Levy D (1998) Prevalence, incidence, prognosis, and predisposing conditions for atrial fibrillation: population-based estimates. Am J Cardiol 82:2N-9N. https://doi.org/10.1016/S0002-9149(98)00583-9

Karle CA, Zitron E, Zhang W, et al (2002) Human cardiac inwardly-rectifying K+ channel Kir(2.1b) is inhibited by direct protein kinase C-dependent regulation in human isolated cardiomyocytes and in an expression system. Circulation 106:1493–1499. https://doi.org/10.1161/01.CIR.0000029747.53262.5C

Kato T, Iwasaki YK, Nattel S (2012) Connexins and atrial fibrillation: Filling in the gaps. Circulation 125:203–206. https://doi.org/10.1161/CIRCULATIONAHA.111.075432

Kaura A, Arnold AD, Panoulas V, et al (2020) Prognostic significance of troponin level in 3121 patients presenting with atrial fibrillation (The nihr health informatics collaborative trop-af study). J Am Heart Assoc 9:. https://doi.org/10.1161/JAHA.119.013684

Kim HS, Hwang GH, Lee HK, et al (2021) CReVIS-Seq: A highly accurate and multiplexable method for genome-wide mapping of lentiviral integration sites. Mol Ther - Methods Clin Dev 20:792–800. https://doi.org/10.1016/J.OMTM.2020.10.012/ATTACHMENT/442E79C4-E3AD-466D-8D39-4347F138F9AC/MMC3.XLSX

Kim S, Kim D, Cho SW, et al (2014) Highly efficient RNA-guided genome editing in human cells via delivery of purified Cas9 ribonucleoproteins. Genome Res 24:1012–1019. https://doi.org/10.1101/gr.171322.113

Kirchhof P, Benussi S, Kotecha D, et al (2016) 2016 ESC Guidelines for the management of atrial fibrillation developed in collaboration with EACTS. Eur Heart J 37:2893–2962. https://doi.org/10.1093/eurheartj/ehw210

Komor AC, Kim YB, Packer MS, et al (2016) Programmable editing of a target base in genomic DNA without double-stranded DNA cleavage. Nat 2015 5337603 533:420–424. https://doi.org/10.1038/nature17946

Kornej J, Benjamin EJ, Magnani JW (2021) Atrial fibrillation: Global burdens and global opportunities. Heart 107:516–518. https://doi.org/10.1136/heartjnl-2020-318480

Kostin S, Klein G, Szalay Z, et al (2002) Structural correlate of atrial fibrillation in human patients. Cardiovasc Res 54:361–379. https://doi.org/10.1016/S0008-6363(02)00273-0

Lajiness JD, Conway SJ (2014) Origin, development, and differentiation of cardiac fibroblasts. J Mol Cell Cardiol 70:2–8. https://doi.org/10.1016/j.yjmcc.2013.11.003

Laksman Z, Wauchop M, Lin E, et al (2017) Modeling Atrial Fibrillation using Human Embryonic Stem Cell-Derived Atrial Tissue. Sci Reports 2017 71 7:1–11. https://doi.org/10.1038/s41598-017-05652-y

Leask A (2007) TGFβ, cardiac fibroblasts, and the fibrotic response. Cardiovasc Res 74:207–212. https://doi.org/10.1016/J.CARDIORES.2006.07.012/2/74-2-207-FIG2.GIF

Lee DP, Tan WLW, Anene-Nzelu CG, et al (2019) Robust CTCF-Based Chromatin Architecture Underpins Epigenetic Changes in the Heart Failure Stress-Gene Response. Circulation 139:1937–1956. https://doi.org/10.1161/CIRCULATIONAHA.118.036726

Lee HC (2013) Electrical remodeling in human atrial fibrillation. Chin Med J (Engl) 126:2380–2383. https://doi.org/10.3760/cma.j.issn.0366-6999.20130546

Lee JH, Protze SI, Laksman Z, et al (2017) Human Pluripotent Stem Cell-Derived Atrial and Ventricular Cardiomyocytes Develop from Distinct Mesoderm Populations. Cell Stem Cell 21:179-194.e4. https://doi.org/10.1016/j.stem.2017.07.003

Lee KK, Workman JL (2007) Histone acetyltransferase complexes: one size doesn't fit all. Nat Rev Mol Cell Biol 2007 84 8:284–295. https://doi.org/10.1038/nrm2145

Lemme M (2019) Establishment of human engineered atrial heart tissue and an optogenetic arrhythmia model

Lemme M, Braren I, Prondzynski M, et al (2020) Chronic intermittent tachypacing by an optogenetic approach induces arrhythmia vulnerability in human engineered heart tissue. Cardiovasc Res 116:1487–1499. https://doi.org/10.1093/cvr/cvz245

Lemme M, Ulmer BM, Lemoine MD, et al (2018) Atrial-like Engineered Heart Tissue: An In Vitro Model of the Human Atrium. Stem Cell Reports 11:1378–1390. https://doi.org/10.1016/j.stemcr.2018.10.008

Lemoine MD, Lemme M, Ulmer BM, et al (2020) Intermittent Optogenetic Tachypacing of Atrial Engineered Heart Tissue Induces Only Limited Electrical Remodelling. J Cardiovasc Pharmacol 77:291–299. https://doi.org/10.1097/FJC.0000000000000951

Lemoine MD, Mannhardt I, Breckwoldt K, et al (2017) Human iPSC-derived cardiomyocytes cultured in 3D engineered heart tissue show physiological upstroke velocity and sodium current density. Sci Rep 7:1–11. https://doi.org/10.1038/s41598-017-05600-w

Li D, Fareh S, Leung TK, Nattel S (1999) Promotion of atrial fibrillation by heart failure in dogs: Atrial remodeling of a different sort. Circulation 100:87–95. https://doi.org/10.1161/01.CIR.100.1.87

Li Y, Asfour H, Bursac N (2017) Age-dependent functional crosstalk between cardiac fibroblasts and cardiomyocytes in a 3D engineered cardiac tissue. Acta Biomater 55:120–130. https://doi.org/10.1016/J.ACTBIO.2017.04.027

Lian X, Zhang J, Azarin SM, et al (2013) Directed cardiomyocyte differentiation from human pluripotent stem cells by modulating Wnt/β-catenin signaling under fully defined conditions. Nat Protoc 8:162–175. https://doi.org/10.1038/nprot.2012.150

Liau B, Jackman CP, Li Y, Bursac N (2017) Developmental stage-dependent effects of cardiac fibroblasts on function of stem cell-derived engineered cardiac tissues. Sci Rep 7:. https://doi.org/10.1038/SREP42290

Lin H, Yin X, Xie Z, et al (2017) Methylome-wide Association Study of Atrial Fibrillation in Framingham Heart Study. Sci Reports 2017 71 7:1–9. https://doi.org/10.1038/srep40377

Lin JY (2012) A User's Guide to Channelrhodopsin Variants. Exp Physiol 96:19–25. https://doi.org/10.1113/expphysiol.2009.051961.A

Lin JY (2011) A user's guide to channelrhodopsin variants: features, limitations and future developments. Exp Physiol 96:19–25. https://doi.org/10.1113/EXPPHYSIOL.2009.051961

Lin JY, Lin MZ, Steinbach P, Tsien RY (2009) Characterization of engineered channelrhodopsin variants with improved properties and kinetics. Biophys J 96:1803–1814. https://doi.org/10.1016/J.BPJ.2008.11.034

Lip GYH, Fauchier L, Freedman SB, et al (2016) Atrial fibrillation. Nat Rev Dis Prim 2:1–26. https://doi.org/10.1038/nrdp.2016.16

Lippi G, Sanchis-Gomar F (2020) Global epidemiology and future trends of heart failure. AME Med J 5:15–15. https://doi.org/10.21037/amj.2020.03.03

Liu CF, Tang WHW (2019) Epigenetics in Cardiac Hypertrophy and Heart Failure. JACC Basic to Transl Sci 4:976–993. https://doi.org/10.1016/j.jacbts.2019.05.011

Liu F, Levin MD, Petrenko NB, et al (2008) Histone-deacetylase Inhibition Reverses Atrial Arrhythmia Inducibility and Fibrosis in Cardiac Hypertrophy Independent of Angiotensin. J Mol Cell Cardiol 45:715. https://doi.org/10.1016/J.YJMCC.2008.08.015

Liu XS, Wu H, Ji X, et al (2016) Editing DNA Methylation in the Mammalian Genome. Cell 167:233-247.e17. https://doi.org/10.1016/j.cell.2016.08.056

Liu XS, Wu H, Krzisch M, et al (2018) Rescue of Fragile X Syndrome Neurons by DNA Methylation Editing of the FMR1 Gene. Cell 172:979-992.e6. https://doi.org/10.1016/j.cell.2018.01.012

Locher MR, Razumova M V., Stelzer JE, et al (2011) Effects of low-level α-myosin heavy chain expression on contractile kinetics in porcine myocardium. Am J Physiol Heart Circ Physiol 300:. https://doi.org/10.1152/AJPHEART.00452.2010

Madsen A, Krause J, Höppner G, et al (2021) Hypertrophic signaling compensates for contractile and metabolic consequences of DNA methyltransferase 3A loss in human cardiomyocytes. J Mol Cell Cardiol 154:115–123. https://doi.org/10.1016/j.yjmcc.2021.02.002

Mahida S (2014) Genetic Discoveries in Atrial Fibrillation and Implications for Clinical Practice. Arrhythmia Electrophysiol Rev 3:69. https://doi.org/10.15420/AER.2014.3.2.69

Mannhardt I, Breckwoldt K, Letuffe-Brenière D, et al (2016) Human Engineered Heart Tissue: Analysis of Contractile Force. Stem Cell Reports 7:29–42.

https://doi.org/10.1016/j.stemcr.2016.04.011

Mannhardt I, Saleem U, Benzin A, et al (2017) Automated contraction analysis of human engineered heart tissue for cardiac drug safety screening. J Vis Exp 2017:1–10. https://doi.org/10.3791/55461

Mannhardt I, Saleem U, Mosqueira D, et al (2020) Comparison of 10 Control hPSC Lines for Drug Screening in an Engineered Heart Tissue Format. Stem cell reports 15:983–998. https://doi.org/10.1016/J.STEMCR.2020.09.002

Matsuura K, Masuda S, Haraguchi Y, et al (2011) Creation of mouse embryonic stem cell-derived cardiac cell sheets. Biomaterials 32:7355–7362. https://doi.org/10.1016/J.BIOMATERIALS.2011.05.042

McDonagh TA, Metra M, Adamo M, et al (2021) 2021 ESC Guidelines for the diagnosis and treatment of acute and chronic heart failureDeveloped by the Task Force for the diagnosis and treatment of acute and chronic heart failure of the European Society of Cardiology (ESC) With the special contribution of the Heart Failure Association (HFA) of the ESC. Eur Heart J 42:3599–3726. https://doi.org/10.1093/EURHEARTJ/EHAB368

Meder B, Haas J, Sedaghat-Hamedani F, et al (2017) Epigenome-Wide Association Study Identifies Cardiac Gene Patterning and a Novel Class of Biomarkers for Heart Failure. Circulation 136:1528–1544. https://doi.org/10.1161/CIRCULATIONAHA.117.027355

Meyer M, Schillinger W, Pieske B, et al (1995) Alterations of Sarcoplasmic Reticulum Proteins in Failing Human Dilated Cardiomyopathy. Circulation 92:778–784. https://doi.org/10.1161/01.CIR.92.4.778

Morillo CA, Klein GJ, Jones DL, Guiraudon CM (1995) Chronic Rapid Atrial Pacing. Circulation 91:1588–1595. https://doi.org/10.1161/01.CIR.91.5.1588

Morin DP, Bernard ML, Madias C, et al (2016) The State of the Art: Atrial Fibrillation Epidemiology, Prevention, and Treatment. Mayo Clin Proc 91:1778–1810. https://doi.org/10.1016/J.MAYOCP.2016.08.022/ATTACHMENT/8A4CFA94-2BEE-4756-9E3E-3143ACE45BFE/MMC1.MP4

Mosqueira D, Mannhardt I, Bhagwan JR, et al (2018) CRISPR/Cas9 editing in human pluripotent stemcell-cardiomyocytes highlights arrhythmias, hypocontractility, and energy depletion as potential therapeutic targets for hypertrophic cardiomyopathy. Eur Heart J 39:3879–3892. https://doi.org/10.1093/eurheartj/ehy249

Movassagh M, Choy MK, Knowles DA, et al (2011) Distinct epigenomic features in end-stage failing human hearts. Circulation 124:2411–2422. https://doi.org/10.1161/CIRCULATIONAHA.111.040071/-/DC1

Nagel G, Brauner M, Liewald JF, et al (2005) Light activation of channelrhodopsin-2 in excitable cells of Caenorhabditis elegans triggers rapid behavioral responses. Curr Biol 15:2279–2284. https://doi.org/10.1016/J.CUB.2005.11.032

Nakamura M, Sadoshima J (2018) Mechanisms of physiological and pathological cardiac hypertrophy. Nat Rev Cardiol 2018 157 15:387–407. https://doi.org/10.1038/s41569-018-0007-y

Nattel S (2002) New ideas about atrial fibrillation 50 years on. Nat 2002 4156868 415:219–226. https://doi.org/10.1038/415219a

Nattel S, Dobrev D (2016) Electrophysiological and molecular mechanisms of paroxysmal atrial fibrillation. Nat Rev Cardiol 13:575–590. https://doi.org/10.1038/nrcardio.2016.118

Nattel S, Dobrev D (2012) The multidimensional role of calcium in atrial fibrillation pathophysiology: mechanistic insights and therapeutic opportunities. Eur Heart J 33:1870–1877. https://doi.org/10.1093/EURHEARTJ/EHS079

Nattel S, Harada M (2014) Atrial remodeling and atrial fibrillation: Recent advances and translational perspectives. J. Am. Coll. Cardiol. 63:2335–2345

Nattel S, Heijman J, Zhou L, Dobrev D (2020) Molecular Basis of Atrial Fibrillation Pathophysiology and Therapy: A Translational Perspective. Circ Res 127:51–72. https://doi.org/10.1161/CIRCRESAHA.120.316363

Nattel S, Xiong F, Aguilar M (2017) Demystifying rotors and their place in clinical translation of atrial fibrillation mechanisms. Nat Rev Cardiol 2017 149 14:509–520. https://doi.org/10.1038/nrcardio.2017.37

Neef S, Dybkova N, Sossalla S, et al (2010) CaMKII-Dependent diastolic SR Ca2+ leak and elevated diastolic Ca2+ levels in right atrial myocardium of patients with atrial fibrillation. Circ Res 106:1134–1144. https://doi.org/10.1161/CIRCRESAHA.109.203836

Nielsen JB, Thorolfsdottir RB, Fritsche LG, et al (2018) Biobank-driven genomic discovery yields new insight into atrial fibrillation biology. Nat Genet 2018 509 50:1234–1239. https://doi.org/10.1038/s41588-018-0171-3

Oceguera-Yanez F, Kim S Il, Matsumoto T, et al (2016) Engineering the AAVS1 locus for consistent and scalable transgene expression in human iPSCs and their differentiated derivatives. Methods 101:43–55. https://doi.org/10.1016/j.ymeth.2015.12.012

Ogata T, Kozuka T, Kanda T (2003) Identification of an Insulator in AAVS1, a Preferred Region for Integration of Adeno-Associated Virus DNA. J Virol 77:9000–9007. https://doi.org/10.1128/jvi.77.16.9000-9007.2003

Okano M, Bell DW, Haber DA, Li E (1999) DNA methyltransferases Dnmt3a and Dnmt3b are essential for de novo methylation and mammalian development. Cell 99:247–257. https://doi.org/10.1016/S0092-8674(00)81656-6

Opacic D, Van Bragt KA, Nasrallah HM, et al (2016) Atrial metabolism and tissue perfusion as determinants of electrical and structural remodelling in atrial fibrillation. Cardiovasc Res 109:527–541. https://doi.org/10.1093/CVR/CVW007

Paci M, Passini E, Klimas A, et al (2020) All-Optical Electrophysiology Refines Populations of In Silico Human iPSC-CMs for Drug Evaluation. Biophys J 118:2596–2611. https://doi.org/10.1016/J.BPJ.2020.03.018

Paik DT, Chandy M, Wu JC (2020) Patient and Disease–Specific Induced Pluripotent Stem Cells for Discovery of Personalized Cardiovascular Drugs and Therapeutics. Pharmacol Rev 72:320–342. https://doi.org/10.1124/PR.116.013003

Pandit S V., Jalife J (2013) Rotors and the dynamics of cardiac fibrillation. Circ Res 112:849–862. https://doi.org/10.1161/CIRCRESAHA.111.300158

Park SY, Song SH, Palmateer B, et al (2020) Novel luciferase–opsin combinations for improved luminopsins. J Neurosci Res 98:410–421. https://doi.org/10.1002/jnr.24152

Perez-Pinera P, Kocak DD, Vockley CM, et al (2013) RNA-guided gene activation by CRISPR-Cas9-based transcription factors. Nat Methods 10:973. https://doi.org/10.1038/NMETH.2600

Peterson CL, Laniel MA (2004) Histones and histone modifications. Curr Biol 14:R546–R551. https://doi.org/10.1016/J.CUB.2004.07.007

Piccini JP, Hammill BG, Sinner MF, et al (2012) Incidence and prevalence of atrial fibrillation and associated mortality among medicare beneficiaries: 1993-2007. Circ Cardiovasc Qual Outcomes 5:85–93. https://doi.org/10.1161/CIRCOUTCOMES.111.962688

Piroddi N, Belus A, Scellini B, et al (2007) Tension generation and relaxation in single myofibrils from human atrial and ventricular myocardium. Pflugers Arch 454:63–73. https://doi.org/10.1007/S00424-006-0181-3

Polyakova V, Miyagawa S, Szalay Z, et al (2008) Atrial extracellular matrix remodelling in patients with atrial fibrillation. J Cell Mol Med 12:189–208. https://doi.org/10.1111/J.1582-4934.2008.00219.X

Ponikowski P, Voors AA, Anker SD, et al (2016) 2016 ESC Guidelines for the diagnosis and treatment of acute and chronic heart failure. Eur Heart J 37:2129-2200m. https://doi.org/10.1093/EURHEARTJ/EHW128

Qi LS, Larson MH, Gilbert LA, et al (2013) Repurposing CRISPR as an RNA-Guided Platform for Sequence-Specific Control of Gene Expression. Cell 152:1173. https://doi.org/10.1016/J.CELL.2013.02.022

Qi XY, Yeh YH, Xiao L, et al (2008) Cellular signaling underlying atrial tachycardia remodeling of L-type calcium current. Circ Res 103:845–854. https://doi.org/10.1161/CIRCRESAHA.108.175463

Ran FA, Hsu PD, Wright J, et al (2013) Genome engineering using the CRISPR-Cas9 system. Nat Protoc 8:2281. https://doi.org/10.1038/NPROT.2013.143

Rietbrock S, Heeley E, Plumb J, van Staa T (2008) Chronic atrial fibrillation: Incidence, prevalence, and prediction of stroke using the Congestive heart failure, Hypertension, Age >75, Diabetes mellitus, and prior Stroke or transient ischemic attack (CHADS2) risk stratification scheme. Am Heart J 156:57–64. https://doi.org/10.1016/J.AHJ.2008.03.010

Rolfe M, McLeod LE, Pratt PF, Proud CG (2005) Activation of protein synthesis in cardiomyocytes by the hypertrophic agent phenylephrine requires the activation of ERK and involves phosphorylation of tuberous sclerosis complex 2 (TSC2). Biochem J 388:973. https://doi.org/10.1042/BJ20041888

Ronaldson-Bouchard K, Ma SP, Yeager K, et al (2018) Advanced maturation of human cardiac tissue grown from pluripotent stem cells. Nat 2018 5567700 556:239–243. https://doi.org/10.1038/s41586-018-0016-3

Roth GA, Mensah GA, Johnson CO, et al (2020) Global Burden of Cardiovascular Diseases and Risk Factors, 1990-2019: Update From the GBD 2019 Study. J Am Coll Cardiol 76:2982–3021. https://doi.org/10.1016/j.jacc.2020.11.010

Rurik JG, Tombácz I, Yadegari A, et al (2022) CAR T cells produced in vivo to treat cardiac injury. Science (80-) 375:91–96. https://doi.org/10.1126/SCIENCE.ABM0594/SUPPL_FILE/SCIENCE.ABM0594_MDAR_REPRODUCIBILITY_CHECKLIST.PDF

Saleem U, Meer BJV, Katili PA, et al (2020) Blinded, Multicenter Evaluation of Drug-induced Changes in Contractility Using Human-induced Pluripotent Stem Cell-derived Cardiomyocytes. Toxicol Sci 176:103–123. https://doi.org/10.1093/TOXSCI/KFAA058

Savarese G, Becher PM, Lund LH, et al (2022) Global burden of heart failure: A comprehensive and updated review of epidemiology. Cardiovasc Res. https://doi.org/10.1093/CVR/CVAC013

Schaaf S, Shibamiya A, Mewe M, et al (2011) Human engineered heart tissue as a versatile tool in basic research and preclinical toxicology. PLoS One 6:. https://doi.org/10.1371/journal.pone.0026397

Scholz B, Schulte JS, Hamer S, et al (2019) HDAC (Histone Deacetylase) Inhibitor Valproic Acid Attenuates Atrial Remodeling and Delays the Onset of Atrial Fibrillation in Mice. Circ Arrhythmia Electrophysiol 12:. https://doi.org/10.1161/CIRCEP.118.007071

Schotten U, Duytschaever M, Ausma J, et al (2003) Electrical and contractile remodeling during the first days of atrial fibrillation go hand in hand. Circulation 107:1433–1439. https://doi.org/10.1161/01.CIR.0000055314.10801.4F

Schotten U, Greiser M, Benke D, et al (2002) Atrial fibrillation-induced atrial contractile dysfunction: a tachycardiomyopathy of a different sort. Cardiovasc Res 53:192–201. https://doi.org/10.1016/S0008-6363(01)00453-9

Schüttler D, Bapat A, Kääb S, et al (2020) Animal Models of Atrial Fibrillation. Circ Res 127:91–110. https://doi.org/10.1161/CIRCRESAHA.120.316366

Shi Y, Zhang H, Huang S, et al (2022) Epigenetic regulation in cardiovascular disease: mechanisms and advances in clinical trials. Signal Transduct Target Ther 2022 71 7:1–28. https://doi.org/10.1038/s41392-022-01055-2

Shibamiya A, Schulze E, Krauß D, et al (2020) Cell Banking of hiPSCs: A Practical Guide to Cryopreservation and Quality Control in Basic Research. Curr Protoc Stem Cell Biol 55:1–26. https://doi.org/10.1002/cpsc.127

Shubeita HE, McDonough PM, Harris AN, et al (1990) Endothelin induction of inositol

phospholipid hydrolysis, sarcomere assembly, and cardiac gene expression in ventricular myocytes. A paracrine mechanism for myocardial cell hypertrophy. J Biol Chem 265:20555–20562. https://doi.org/10.1016/s0021-9258(17)30538-0

Song S, Zhang R, Mo B, et al (2019) EZH2 as a novel therapeutic target for atrial fibrosis and atrial fibrillation. J Mol Cell Cardiol 135:119–133. https://doi.org/10.1016/j.yjmcc.2019.08.003

Song Y, Shryock JC, Belardinelli L (2008) An increase of late sodium current induces delayed afterdepolarizations and sustained triggered activity in atrial myocytes. Am J Physiol - Hear Circ Physiol 294:2031–2039. https://doi.org/10.1152/AJPHEART.01357.2007/SUPPL_FILE/FIGURE

Srivastava RD, Kalitha M, Varma P, Bhatnagar VM (1977) A mechanism of action of phenylephrine on heart. Indian J Physiol Pharmacol 21:167–74

Stenzig J, Schneeberger Y, Löser A, et al (2018) Pharmacological inhibition of DNA methylation attenuates pressure overload-induced cardiac hypertrophy in rats. J Mol Cell Cardiol 120:53–63. https://doi.org/10.1016/J.YJMCC.2018.05.012

Stöhr A, Friedrich FW, Flenner F, et al (2013) Contractile abnormalities and altered drug response in engineered heart tissue from Mybpc3-targeted knock-in mice. J Mol Cell Cardiol 63:189–198. https://doi.org/10.1016/J.YJMCC.2013.07.011

Stüdemann T, Rössinger J, Manthey C, et al (2021) Contractile force of transplanted cardiomyocytes contributes to heart function after injury. bioRxiv 2021.11.23.469715

Takahashi K, Tanabe K, Ohnuki M, et al (2007) Induction of pluripotent stem cells from adult human fibroblasts by defined factors. Cell 131:861–872. https://doi.org/10.1016/J.CELL.2007.11.019

Tan NGA, Wu W, Seifalian AM (2015) Optogenetics: Lights, camera, action! A ray of light, a shadow unmasked. Appl Nanosci Photomed 185–203. https://doi.org/10.1533/9781908818782.185

Tan WLW, Anene-Nzelu CG, Wong E, et al (2020) Epigenomes of human hearts reveal new genetic variants relevant for cardiac disease and phenotype. Circ Res 761–777. https://doi.org/10.1161/CIRCRESAHA.120.317254

Thakore PI, D'Ippolito AM, Song L, et al (2015) Highly specific epigenome editing by CRISPR-Cas9 repressors for silencing of distal regulatory elements. Nat Methods 2015 1212

12:1143–1149. https://doi.org/10.1038/nmeth.3630

Tham YK, Bernardo BC, Ooi JYY, et al (2015) Pathophysiology of cardiac hypertrophy and heart failure: signaling pathways and novel therapeutic targets. Arch Toxicol 2015 899 89:1401–1438. https://doi.org/10.1007/S00204-015-1477-X

Tiburcy M, Hudson JE, Balfanz P, et al (2017) Defined Engineered Human Myocardium with Advanced Maturation for Applications in Heart Failure Modelling and Repair. Circulation 135:1832. https://doi.org/10.1161/CIRCULATIONAHA.116.024145

Ulmer BM, Stoehr A, Schulze ML, et al (2018) Contractile Work Contributes to Maturation of Energy Metabolism in hiPSC-Derived Cardiomyocytes. Stem Cell Reports 10:834–847. https://doi.org/10.1016/j.stemcr.2018.01.039

Van Emburgh BO, Robertson KD (2011) Modulation of Dnmt3b function in vitro by interactions with Dnmt3L, Dnmt3a and Dnmt3b splice variants. Nucleic Acids Res 39:4984–5002. https://doi.org/10.1093/nar/gkr116

Van Wagoner DR, Pond AL, Lamorgese M, et al (1999) Atrial L-type Ca2+ currents and human atrial fibrillation. Circ Res 85:428–436. https://doi.org/10.1161/01.RES.85.5.428

Verheule S, Wilson E, Everett IV T, et al (2003) Alterations in atrial electrophysiology and tissue structure in a canine model of chronic atrial dilatation due to Mitral Regurgitation. Circulation 107:2615–2622. https://doi.org/10.1161/01.cir.0000066915.15187.51

Vest JA, Wehrens XHT, Reiken SR, et al (2005) Defective cardiac ryanodine receptor regulation during atrial fibrillation. Circulation 111:2025–2032. https://doi.org/10.1161/01.CIR.0000162461.67140.4C

Vojta A, Dobrinic P, Tadic V, et al (2016) Repurposing the CRISPR-Cas9 system for targeted DNA methylation. Nucleic Acids Res 44:5615–5628. https://doi.org/10.1093/nar/gkw159

Wakili R, Voigt N, Kääb S, et al (2011) Recent advances in the molecular pathophysiology of atrial fibrillation. J Clin Invest 121:2955. https://doi.org/10.1172/JCI46315

Waks JW, Josephson ME (2014) Mechanisms of Atrial Fibrillation – Reentry, Rotors and Reality. Arrhythmia Electrophysiol Rev 3:90. https://doi.org/10.15420/AER.2014.3.2.90

Weber K, Thomaschewski M, Benten D, Fehse B (2012) RGB marking with lentiviral vectors for multicolor clonal cell tracking. Nat Protoc 7:839–849. https://doi.org/10.1038/nprot.2012.026

Werner T (2018) Humanes künstliches Herzgewebe aus mehreren Zelltypen zur Untersuchung kardialer Hypertrophie. Univ Hamburg, http//ediss.sub.uni-hamburg.de/volltexte/2018/9072

Wettwer E, Hála O, Christ T, et al (2004) Role of IKur in controlling action potential shape and contractility in the human atrium: Influence of chronic atrial fibrillation. Circulation 110:2299–2306. https://doi.org/10.1161/01.CIR.0000145155.60288.71

Wijffels MCEF, Kirchhof CJHJ, Dorland R, Allessie MA (1995) Atrial fibrillation begets atrial fibrillation. A study in awake chronically instrumented goats. Circulation 92:1954–1968. https://doi.org/10.1161/01.CIR.92.7.1954

Witty AD, Mihic A, Tam RY, et al (2014) Generation of the epicardial lineage from human pluripotent stem cells. Nat Biotechnol 32:1026–1035. https://doi.org/10.1038/NBT.3002

Wu Z, Yang H, Colosi P (2010) Effect of genome size on AAV vector packaging. Mol Ther 18:80–86. https://doi.org/10.1038/mt.2009.255

Xia Y, Lee K, Li N, et al (2009) Characterization of the inflammatory and fibrotic response in a mouse model of cardiac pressure overload. Histochem Cell Biol 131:471–481. https://doi.org/10.1007/S00418-008-0541-5

Xiao D, Dasgupta C, Chen M, et al (2014) Inhibition of DNA methylation reverses norepinephrine-induced cardiac hypertrophy in rats. Cardiovasc Res 101:373–382. https://doi.org/10.1093/CVR/CVT264

Youn JY, Zhang J, Zhang Y, et al (2013) Oxidative Stress in Atrial Fibrillation: An Emerging Role of NADPH Oxidase. J Mol Cell Cardiol 62:72. https://doi.org/10.1016/J.YJMCC.2013.04.019

Yue L, Melnyk P, Gaspo R, et al (1999) Molecular Mechanisms Underlying Ionic Remodeling in a Dog Model of Atrial Fibrillation. Circ Res 84:776–784. https://doi.org/10.1161/01.RES.84.7.776

Yue L, Xie J, Nattel S (2011) Molecular determinants of cardiac fibroblast electrical function and therapeutic implications for atrial fibrillation. Cardiovasc Res 89:744–753. https://doi.org/10.1093/CVR/CVQ329

Zgierski-Johnston CM, Ayub S, Fernández MC, et al (2020) Cardiac pacing using transmural multi-LED probes in channelrhodopsin-expressing mouse hearts. Prog Biophys Mol Biol 154:51–61. https://doi.org/10.1016/J.PBIOMOLBIO.2019.11.004

Zhang D, Wu CT, Qi XY, et al (2014) Activation of histone deacetylase-6 induces contractile dysfunction through derailment of α-tubulin proteostasis in experimental and human atrial fibrillation. Circulation 129:346–358. https://doi.org/10.1161/CIRCULATIONAHA.113.005300

Zhang F, Prigge M, Beyrière F, et al (2008) Red-shifted optogenetic excitation: a tool for fast neural control derived from Volvox carteri. Nat Neurosci 11:631. https://doi.org/10.1038/NN.2120

Zhang H, Tian L, Shen M, et al (2019) Generation of quiescent cardiac fibroblasts from human induced pluripotent stem cells for in vitro modeling of cardiac fibrosis. Circ Res 125:552–566. https://doi.org/10.1161/CIRCRESAHA.119.315491

Zhou Y, Liu J, Qian L (2019) Epigenomic Reprogramming in Cardiovascular Disease. Elsevier Inc.

Zimmermann WH, Fink C, Kralisch D, et al (2000) Three-dimensional engineered heart tissue from neonatal rat cardiac myocytes. Biotechnol Bioeng 68:106–114. https://doi.org/10.1002/(SICI)1097-0290(20000405)68:1<106::AID-BIT13>3.0.CO;2-3

Zimmermann WH, Schneiderbanger K, Schubert P, et al (2002) Tissue engineering of a differentiated cardiac muscle construct. Circ Res 90:223–230. https://doi.org/10.1161/HH0202.103644

Zografos TA, Katritsis DG (2013) Natriuretic Peptides as Predictors of Atrial Fibrillation Recurrences Following Electrical Cardioversion. Arrhythmia Electrophysiol Rev 2:109. https://doi.org/10.15420/AER.2013.2.2.109

10 Appendix

10.1 Security information

The experiments were all conducted in certified security standard S1 and S2 laboratories. All chemicals, buffers, and solutions were handled and disposed of according to their security data sheets in appropriate containers. Cell-containing or contaminated material was autoclaved before disposal. All surfaces that have been possibly contaminated with genetically modified organisms were cleaned with 70% ethanol, PurSept disinfectant or hypochloric acid as appropriate.

Table S1: Security information of all used substances

Substance	CAS #	H-statements	P-statements
1,4-Dithiothreitol (DTT)	3483-12-3	H: 302, 315, 319, 412	P: 264, 270, 273, 280, 337+313, 501
1-Thioglycerol	96-27-5	H: 302-311-315-319-335	P: 261-280-305+351+338+312
2-Mercaptoethanol	60-24-2	H: 301+331, 310, 315, 317, 318, 373, 410	P: 270, 280, 302+352, 330, 304+340, 305+351+338, 310
2-Propanol	67-63-0	H: 225, 319, 336	P: 210, 261, 305+351+338
Acetic acid	64-19-7	H: 226-290-314	P: 210-280-301+330+331-305+351+338-308+310
Acrylamide/Bis solution, 29:1, 40%	79-06-1 110-26-9	H: 302, 312, 315, 319, 317, 340, 350, 361, 372	P: 260, 280, 281, 305+351+338, 405, 501
Ammonium persulfate (APS)	7727-54-0	H: 272, 302, 315, 317, 319, 334, 335	P: 221, 210, 285, 405 305+P351+P338, 501
Ampicillin trihydrate	7177-48-2	H: 317-334	P: 280-285, 302+352-304+341-333+313-342+311
Calcium chloride dihydrate	10035-04-8	H: 319	P: 305+351+388
Carbachol	51-83-2	H: 300	P: 308+310
Dimethyl Formamide	68-12-2	H: 226, 312+332, 319, 360D	P: 210, 261, 280, 302+352, 305+351+338, 312, 370+378, 403+235, 501

Digitonin	11024-24-1	H: 301, 311, 331	P: 261, 280, 301+310, 302+352, 304+340
Dorsomorphin	866405-64-3	H: 302, 312, 332	P: 301+312, 304+340, 302+352, 261, 280, 264, 270, 271, 330, 501, 363
EDTA	6381-92-6	H: 332, 373	P: 260, 314
Ethanol, absolute	64-17-5	H: 225, 319	P: 210, 240, 305+351+338, 403+233
Formaldehyde	50-00-0	H: 351-331-311-301-314-317	P: 301+310-303+361+353-305+351+338, 320-361-405-501
IGEPAL CA-630	9002-93-1	H: 302, 315, 318, 410	P: 264, 273, 280, 301+312, 302+352, 305+351+338
Lipid mix	64-17-5	H: 225, 319	P210, 280, 305+351+338, 337+313, 403+235
MEM non-essential amino acid solution	n/a	H: 315, 319	P: 280,264, 302+352, 305+351+338, 332+313, 337+313
Midori Green	n/a		P: 261, 280
N,N,N',N'-Tetramethyl ethylenediamine (TEMED)	110-18-9	H: 225, 332, 302, 314	P: 210, 233, 280, 301+330+331, 305+351+338, 308, 310
Nitrogen, liquid (N_2)	7727-37-9	H: 281	P: 282, 336+315, 403
Penicillin	61-33-6	H: 317	P: 280
Potassium di-hydrogen Phosphate	7778-77-0	--	P: 260
Proteinase K	39450-01-6	H: 334	P: 304+340, 261, 342+311, 284
RNase A	9001-99-4	H: 334	P: 261sh, 342+311
Roti-Histofix 4%	50-00-0 67-56-1	H: 302, 317, 341, 350	P: 261, 280, 302+352, 308+313
Saponin	8047-15-2	H: 319, 335	P 261, 305+351+338
Sodium azide	26628-22-8	H: 300-400-410	P: 273–309-310

Sodium hydroxide	1310-73-2	H: 314	P: 280–301+330+331–309–310-305+351+338
Sodium selenite	10102-18-8	H: 300+330, 315, 317, 319, 411	P: 260, 273, 280, 301+330+331+310, 302+352, 304+340+310, 305+351+338, 403+233
Streptomycin	57-92-1	H: 302	--
Thrombin	9002-04-4	H: 315, 319, 334, 335	P: 261, 305+351+338, 342+311
trans-4-(Aminomethyl)cyclohexanecarboxylic acid	1197-18-8	H: 315, 319, 335	P261, 305+351+338
TRIS-Hydrochloride (Tris-HCl)	1185-53-1	H: 315, 319, 335	P: 280, 302+352, 305+351+338
Triton X-100	9002-93-1	H: 302-318-411	P: 273-280-305+351+338
TRIzol reagent	108-95-2 593-84-0 1762-95-4	H: 301+311+331, 314, 335, 341, 373, 412	P: 201, 261, 261, 280, 273, 301+310, 302+352
Trypan blue	72-57-1	H: 350	P: 201-308+313
Y-27632	331752-47-7	H: 302-312-332	P: 280

10.2 Devices, materials and substances

10.2.1 Devices

4D-Nucleofector Core Unit	Lonza
4D-Nucleofector X Unit	Lonza
AbiPrism7900HT cycler	Applied Biosystems
Analytic Scale Genius	Sartorius AG
BD FACSAria IIIu	BD Biosciences
BD FACSCanto II	BD Biosciences
Bioanalyzer 2100	Agilent
C25 Incubator Shaker	New Brunswick Scientific
Cell culture incubator CB 220	Binder
Cell culture incubators HERAcell 240	Thermo Fischer Scientific

Cell culture incubators MCO-19M & MCO-20AIC	Sanyo
Centrifuges 5415 R & 5810 R	Eppendorf
Centrifuge Avanti JXN-26	Beckmann
Centrifuges Rotanta/RP & Universal 30 RF	Hettich
ChemiDoc Touch Imaging System	Bio-Rad Laboratories
Electrophoretic Transfer Cell Mini Trans-Blot cell	Bio-Rad Laboratories
Gel electrophoresis cell Mini-PROTEAN 3 Cell	Bio-Rad Laboratories
Gel electrophoresis tank Sub-cell GT	Bio-Rad Laboratories
Zeiss LSM 800 Airyscan	Zeiss
LEICA DMD 108	Leica
Leica VT1000 S Vibrating blade microtome	Leica
Magnetic stirring and heating plate IKA Combimag RET	Janke & Kunkel GmbH & Co KG
Magnetic stirring plate Variomag / Cimarec Biosystem Direct	Thermo Scientific
Magnetic stirring plate Variomag / Cimarec Biosystem 4 Direct	Thermo Scientific
Microscope Axioskop 2 with AxioCam Color	Zeiss
Microscope EVOS FL Cell Imaging System	Thermo Fischer Scientific
Microscope T1-SM Nikon Eclipse TS100	Nikon
NanoDrop ND-1000 Spectrophotometer	Thermo Fischer Scientific
nCounter SPRINT	NanoString
pH meter, digital	Mettler Toledo
Pipettes 10 / 100 / 1000 µL	Eppendorf
Pipette controller Accu-jet pro	Brand
Power supply PowerPac Bacic	Bio-Rad Laboratories
Precision Advanced Scale	Ohaus
S88X dual output square pulse stimulator	Grass
Safety workbench HeraSafe	Heraeus
Safety workbench Safe 2020	Thermo Fischer Scientific
Safire 2 multi-detection plate reader	TECAN
Sequencer HiSeq 2500	Illumina
Qubit 3.0 Fluorometer	Life technologies
Thermal cycler Hybaid PCR Sprint	Thermo Fischer Scientific
Thermal cycler vapo.protect	Eppendorf
Thermomixer comfort	Eppendorf

TissueLyser	QIAGEN
Video-optical EHT analysis system	EHT Technologies
Ventana Benchmark XT	Ventana
Vortex Genie	Scientific Industries
Warming cabinet Kelvitron T	Heraeus

10.2.2 Software

Arduino	Open-source hardware
CLC Main Workbench 20	GIAGEN
Chart5.5.6	AD Instruments
FACSDiva	BD Biosciences
FlowJo V7	BD Biosciences
Image Lab	Bio-Rad Laboratories
nCounter CNV Collector Tool	Nanostring
Prism 7	GraphPad
RStudio	
SDS 2.4.1	Applied Biosystems
ZEN 2012	Zeiss

10.2.3 Materials and equipment

250 mL Vacuum Filtration "rapid"-Filtermax	TPP, 99250
500 mL Vacuum Filtration "rapid"-Filtermax	TPP, 99500
Aspiration pipette 2 mL	Sarstedt, 86.1252.011
Cell culture flask T75 for suspension culture	Sarstedt, 83.3911.502
Cell culture flask T175 for suspension culture	Sarstedt, 83.3912.502
Cell culture microplate 96 well µClear black CELLSTAR	Greiner Bio-One, 655090
Cell culture plate 6 / 12 / 24-well	Nunc
Cell scraper	Sarstedt, 83.1830
Cell strainer 100 µm	Falcon, 352360
Cryovial CryoPure 1.6 mL	Sarstedt, 72.380
Circuit board for LEDs	JLCPCB
Flow cytometry tubes	Sarstedt, 55.1579

HistoBond microscope slides	Marienfeld, 0810000
Neubauer counting chamber	Karl-Hecht
Nunc EasYFlask Cell Culture Flasks T75 cm^2 Nunclon Delta Surface	Thermo Fisher Scientific, 156499
Pacing adapter/cables	EHT Technologies GmbH, P0002
Pacing electrode carbon	EHT Technologies GmbH, P0001
Pipette tips	Sarstedt
Pipette tips with Biosphere filter	Sarstedt
Reaction tube graduated 15 mL	Sarstedt, 62.554.502
Reaction tubes conical 15 / 50 mL	Sarstedt
Reaction tubes Safe Lock 0.2 - 2 mL	Eppendorf
Round bottom tube 12 mL (for EHT casting)	Greiner Bio-One, 163160
Serological pipettes 1 / 2 / 5 / 10 / 25 / 50 mL	Sarstedt
Silicone rack	EHT Technologies, C0001
Spinner flasks 1000 mL	Integra Biosciences, 182101
Syringe filtration unit Filtropur S 0.2 µm	Sarstedt, 83.1826.001
Teflon spacer	EHT Technologies, C0002
Tri-color light-emitting diode	APA102
TissueLyser steel beads	QIAGEN, 69989
V-shaped sedimentation rack	Custom made at UKE, Hamburg

10.2.4 Media and serum

Basal medium, neurobasal	Thermo Fisher Scientific, 21103-049
DMEM-low glucose	Sigma, D5546-500ML
DMEM (PAN)	PAN Biotech, P04-01501
DMEM/F-12 without Glutamine	Gibco, 21331-046
DMEM powder for 2x DMEM	Gibco, 52100-021
Fetal Calf Serum superior, FCS	Biochrom, S0615
Goat serum	Thermo Fisher Scientific, 16210064
Horse serum	Life Technologies, 26050-088
Human serum albumin	Biological Industries, 05-720-1B
mTeSR1	StemCell Technologies, 05825
RPMI 1640	Gibco, 21875-034

StemPro-34 SFM — Life Technologies, 10639011

10.2.5 Reagents

1,4-Dithiothreitol (DTT)	Roth, 6908.2
1-Thioglycerol	Sigma-Aldrich, M6145
2-Mercaptoethanol	Sigma-Aldrich, M6250
2-Propanol	Merck Millipore, 107022
4-aminopyridine	Sigma-Aldrich, 275875
6x DNA loading dye	Thermo Fisher Scientific, R0611
Accutase Cell Dissociation Reagent	Sigma-Aldrich, A6964
Acrylamide/Bis 40%	Bio-Rad Laboratories, 161-0146
Activin A	R&D Systems, 338-AC
Agarose	Invitrogen, 15510-027
Ammoniumpersulfate	APS, Bio-Rad Laboratories, 161-0700
Aprotinin	Genaxxon bioscience, M6361.1010
Aqua	B. Braun
Bacto Agar	BD, 214010
Bacto Tryptone	BD, 211705
Bacto Yeast Extract	BD, 212750
bFGF	R&D Systems, 233-FB
BMP4	R&D Systems, 314-BP
BSA Fraction V IgG free, FA-poor	Fisher Scientific, 30036578
BTS (N-benzyl-p-toluenesulfonamide)	TCI, B3082-25G
Biotin	Sigma-Aldrich, B4639-100MG
$CaCl_2$ x $2H_2O$	Merck, 1.02382
Catalase	Sigma-Aldrich, C40-100MG
Carbachol	Sigma-Aldrich, Y0000113
CHIR99012	Cayman, 13122
CloneR 10x Cloning Supplement	StemCell Technologies, 0588
Collagenase II	Worthington, LS004176
Corticosterone	Sigma-Aldrich, C2505-500MG
D+-galactose	Sigma-Aldrich, G0625-100G
D(+)-Glucose anhydrous	Roth, X997.2

DAPI	Biochemica, A1001 0025
Digitonin	Promega, G9441
Dimethyl Formamide (DMF)	Merck, 103053
DL-alpha tocophercol acetate	Sigma-Aldrich, T3001-10G
DL-alpha tocopherol	Sigma-Aldrich, T3251-5G
DMSO	Sigma-Aldrich, D4540
DNase II type V	Sigma-Aldrich, D8764
Dorsomorphin	Tocris, 3093
EDTA	Roth, 8043.2
Endothelin-1	Sigma-Aldrich, E7764
Ethanol, absolute	Chemsolute, 2246.1000
Ethanolamine	Sigma-Aldrich, E9508-100ML
Fibrinogen	Sigma-Aldrich, F8630
Fluoromount-G	Invitrogen, 00-4958-02
Geltrex	Gibco, A1413302
GeneRuler 1 kb DNA Ladder	Thermo Fisher Scientific, SM0313
GeneRuler 100 bp DNA Ladder	Thermo Fisher Scientific, SM0243
GlutaMax Supplement	Gibco, 35050061
Glutathione	Sigma-Aldrich, G6013-5G
HBSS (-) Ca^{2+}/Mg^{2+}	Gibco, 14175-053
HEPES	Roth, 9105.4
Hydrocortisone	Sigma-Aldrich, H4001
IGEPAL CA-630 (NP40)	Sigma-Aldrich, I8896
Insulin	Sigma-Aldrich, I9278
L-Carnitine	Sigma-Aldrich, C0283-1G
L-Glutamine	Gibco, 25030-081
Linoleic acid	Sigma-Aldrich, L1012-100MG
Linolenic acid	Sigma-Aldrich, L2376-500MG
Lipidmix	Sigma-Aldrich, L5146
Matrigel Basement Membrane Matrix	Corning, 354234
Methanol	J. Baker, 8045
Midori Green	Biozym, 617004
Milk powder	Roth, T145.2
N,N,N',N'-Tetramethylethylenediamine (TEMED)	Bio-Rad Laboratories, 161-0801

Na-selenite	Sigma-Aldrich, T8158
Non-essential amino acids	Gibco, 11140
Paraffin	Sigma-Aldrich, 327204
Papain	Sigma-Aldrich, 76220
Penicillin / streptomycin	Gibco, 15140
Phosphoascorbate (2-Phospho-L-ascorbic acid trisodium salt)	Sigma-Aldrich, 49752
Pluronic F-127	Sigma-Aldrich, P2443
Progesterone	Sigma-Aldrich, P8783-1G
Ponceau S solution	Sigma-Aldrich, P7170-1L
Polyvinyl alcohol	Sigma-Aldrich, P8136
Retinol acetate	Sigma-Aldrich, R7882-1G
(R)-(−)-Phenylephrine hydrochloride	Sigma-Aldrich, P6126
Roti-Histofix 4%	Roth, P087.3
Saponin	Merck, 558255
SB-431542	Cayman, 13031
Sodium azide	Sigma-Aldrich, 71290
Sodium chloride solution 0.9%	B. Braun, 3570210
Sodium hydroxide	Roth, 6771.1
TGF-β1	Peprotech, 100-21
Thrombin	Sigma-Aldrich, T7513
Transferrin	Sigma-Aldrich, S5261
Triiodothyronine	Sigma-Aldrich, T2877-100MG
TRIS-hydrochloride	Roth, 9090.2
Triton X-100	Roth, 3051.3
Trizma base	Sigma-Aldrich, T1503
TRIzol	Life Technologies, 15596026
Trypan Blue	Biochrom, L 6323
Trypsin-EDTA 0.5%	Gibco, 15400054
TurboFect transfection reagent	Thermo Scientific, R0532
Tween 20	Sigma-Aldrich, P1379
VEGF	R&D Systems, 293-VE
XAV939	Tocris, 3748
Y-27632	Biaffin, PKI-Y27632-010

10.2.6 Kits and enzymes

5x HOT FIREPol EvaGreen qPCR Mix Plus ROX	Solis BioDyne, 08-24-00008
Agencourt AMPure XP	Beckman Coulter, A63880
Amaxa P3 Primary Cell 4D-Nucleofector X Kit L	Lonza, V4XP-3024
Amaxa P4 Primary Cell 4D-Nucleofector X Kit L	Lonza, V4XP-4024
AscI	NEB, R0058
BamHI-FastDigest	Thermo Scientific, FD0054
BsaBI	NEB, R0537S
Coomassie dye reagent	Bio-Rad, 5000006
DNeasy Blood & Tissue Kit	QIAGEN, 69504
EcoRV-FastDigest	Thermor Scientific, FD0303
EpiMark Hot Start *Taq* DNA Polymerase	NEB, M0490S
EZ DNA Methylation-Gold Kit	ZYMO RESEARCH, D5005 & D5006
Esp3I	NEB, R0734S
FavorPrep Plasmid Extraction Mini kit	Favorgen
High-Capacity cDNA Reverse Transcription Kit	Applied Biosystems, 4368813
Illumina Tagment DNA Enzyme and Buffer Small Kit	Illumina, 20034197
Mph1103I-FastDigest	Thermor Scientific, FD0734
Monarch DNA Gel Extraction Kit	NEB, T1020L
Monarch PCR & DNA Cleanup Kit	NEB, T1030S
NdeI-FastDigest	Thermor Scientific, FD0583
NheI-FastDigest	Thermor Scientific, FD0973
NEB PCR Cloning Kit	NEB, E1202S
NEBuilder HiFi DNA Assembly	NEB, E2621S
NucleoBond Xtra Maxi Kit	Macherey-Nagel, 740414.10
PmlI-FastDigest	Thermo Scientific, FD0364
Pierce ECL Western Blotting Substrate	Thermo Fisher, 32106
PstI-FastDigest	Thermor Scientific, FD0614
PvuII-FastDigest	Thermor Scientific, FD0634
Q5 High-Fidelity 2X Master Mix	NEB, M0492S
Qubit dsDNA BR Assay kit	Life technologies, Q32850
RNA 6000 Pico Kit	Agilent, 5067-1513
RNeasy Mini Kit	QIAGEN, 74904
SalI-FastDigest	Thermor Scientific, FD0644

SpeI-FastDigest   Thermor Scientific, FD1253

SphI-FastDigest   Thermor Scientific, FD0604

T4 DNA Ligase   NEB, M0202S

TRIzol Reagent   Life Technologies, 15596026

TruSeq Stranded Total RNA Library Prep Kit   Illumina, 20020596

UltraView Universal DAB Detection Kit   Roche, 760-500

XhoI-FastDigest   Thermor Scientific, FD0694

10.2.7 Antibodies

Table S2: Primary and secondary antibodies for Western blot

Antibody	Company and Cat. number	Dilution
Anti-Collagen I	Abcam, Ab138492	1:1000
Anti-FLAG	Sigma-Aldrich, F3165	1:5000
Anti-GAPDH	HyTest, 5G4	1:5000
Anti-mouse IgG peroxidase-conjugated secondary antibody	Sigma-Aldrich, A3682	1:10,000
Anti-rabbit IgG peroxidase-conjugated secondary antibody	Sigma-Aldrich, A0545	1:10,000

Table S3: Primary and secondary antibodies for IF and IHC

Antibody	Company and Cat. number	Dilution
Anti-α-actinin	Sigma-Aldrich, A7811	IF 1:800
Anti-ANP	Santa Cruz, sc-80686	IHC 1:500
Anti-Collagen I	Abcam, Ab138492	IF 1:1500
Anti-dystrophin	Millipore, MAB1645	IHC 1:200
Anti-MLC2A	BD Pharmingen, 565496 Synaptic Systems, 311011	IF 1:500 IHC 1:75
Anti-MLC2V	Proteintech, 10906-1-AP Synaptic Systems, 311111	IF 1:250 IHC 1:3000
Mouse anti- Human NANOG Alexa Fluor 647	BD Pharmingen, 561300	IF: 1:50

Goat anti-mouse Alexa Fluor 546	Invitrogen, A-11003	IF 1:100
Goat anti-rabbit Alexa Fluor 546	Invitrogen, A-11035	IF 1:100
Goat anti-mouse Alexa Fluor 647	Invitrogen, A-21236	IF 1:100

Table S4: Primary and secondary antibodies for flow cytometry

Antibody	Company and Cat. number	Dilution
Anti-hKLF-4 APC	R&D Systems, IC3640A	1:50
Anti-SSEA-3 PE	BD Pharmingen, 560237	1:5
Isotype control PE	BD Pharmingen, 553943	1:50
Anti-SSEA-3 Alexa Fluor 647	BD Pharmingen, 561145	1:50
Isotype control Alexa Fluor 647	BD Pharmingen, 557714	1:50
Mouse anti- Human NANOG Alexa Fluor 647	BD Pharmingen, 561300	1:50
Anti-cardiac troponin-T APC	Miltenyi Biotec, 130-120-403	1:50
REA control antibody APC	Miltenyi Biotec, 130-120-709	1:50
Anti-cardiac troponin-T FITC	Miltenyi Biotec, 130-119-575	1:50
REA control antibody FITC	Miltenyi Biotec, 130-113-437	1:50

10.2.8 Composition of media, reagents, buffer and solutions

Table S5: Tissue culture media

Medium	Composition
FTDA	DMEM/F-12 without glutamine 2 mM L-Glutamine 5 mg/L Transferrin 6.6 µg/L Sodium selenite 1% (v/v) Human serum albumin (HSA) 0.1% (v/v) Lipid mix 5 mg/L Human recombinant insulin 50 nM Dorsomorphin 2.5 µg/L Activin A

	0.5 µg/L Transforming growth factor β1 (TGF-β1)
	The medium was sterile filtered and stored at 4 °C for two weeks. 30 µg/L bFGF was supplemented freshly before usage.
EB-formation medium	FTDA
	3 g/L Polyvinyl alcohol in 1x DPBS
	10 µM Y-27632
	The medium was prepared freshly and sterile filtered. 30 µg/L bFGF was supplemented freshly before usage.
Mesoderm induction medium	RPMI 1640
	4g/L Polyvinyl alcohol in 1x DPBS
	10 mM HEPES, pH 7.4
	5mg/L Transferrin
	6.6 µg/L Sodium selenite
	0.1% (v/v) Lipid mix
	10 µM Y-27632
	250 µM Phosphoascorbate (PAA)
	The medium was sterile filtered and stored at 4 °C for one week. BMP4, activin A and 5 ng/mL bFGF were supplemented freshly before usage. The concentration of BMP4 and activin A depends on the type of cardiac differentiation.
Cardiac differentiation medium I	RPMI 1640
	0.5% (v/v) Penicillin/streptomycin
	10 mM HEPES (pH 7.4)
	0.5% (v/v) HSA
	5 mg/L Transferrin
	6.6 µg/L Sodium selenite
	0.1% (v/v) Lipid mix
	1 µM Y-27632
	250 µM PAA
	The medium was filter-sterilized and stored at 4 °C for one week. 1 µM XAV-939 was added directly before usage.
Cardiac differentiation medium II	RPMI 1640
	0.5% (v/v) Penicillin/streptomycin

	10 mM HEPES (pH 7.4)
	1 μM Y-27632
	500 μM 1-Thioglycerol (MTG)
	The medium was filter-sterilized and stored at 4 °C for two weeks. 2% (v/v) B27 with insulin and 1 μM XAV-939 were added freshly before usage.
Cardiac differentiation medium III	RPMI 1640
	0.5% (v/v) Penicillin/streptomycin
	10 mM HEPES (pH 7.4)
	1 μM Y-27632
	500 μM 1-Thioglycerol
	The medium was filter-sterilized (0.2 μm filter) and stored at 4 °C for two weeks. 2% (v/v) B27 with insulin was added freshly before usage.
Stg0 medium	StemPro-34 SFM + Supplement
	1 μg/L BMP4
	2 mM GlutaMAX
	1% (v/v) Matrigel high growth factor
Stg1 medium	StemPro-34™ SFM + supplement
	8 μg/L Activin A
	10 μg/L BMP-4
	2 mM GlutaMAX
Stg2.1 medium	RPMI 1640
	2% (v/v) B27 minus insulin
	10 μM KY021111
	10 μM XAV939
Stg2.2 medium	RPMI 1640
	2% (v/v) B27 minus insulin
	10 μM KY021111
	10 μM XAV939
	25 μM Insulin
RDM	RPMI 1640
	2% (v/v) B27 minus insulin

	25 µM Insulin
Epi-medium	RPMI 1640
	0.5% Penicillin/streptomycin
	0.1% Lipid mix
	250 µM PAA
	0.01% transferrin-selenium
	1 µM Y-27632
HEK cell medium	DMEM-low glucose
	10% (v/v) FCS
	1% (v/v) Penicillin/streptomycin
	1% (v/v) L-glutamine
EHT casting medium (NKM)	DMEM-low glucose
	1% (v/v) Penicillin/streptomycin
	10% (v/v) Heat inactivated horse serum
	1% (v/v) GlutaMAX
Complete medium (Standard EHT culture medium)	DMEM-low glucose
	1% (v/v) Penicillin/streptomycin
	10% (v/v) Heat inactivated horse serum
	10 mg/L Insulin
	33 mg/L Aprotinin
Serum-free EHT medium	DMEM-low glucose
	1% (v/v) Penicillin/streptomycin
	10 mg/L Insulin
	33 mg/L Aprotinin
	50 ng/mL Hydrocortisone
	0.5 ng/mL T3

Table S4: Reagents / Buffer / Solutions

Reagents / Buffer / Solutions	Composition
Agarose for EHT casting	2% (w/v) Agarose

	300 mL 1x DPBS Sterilized by autoclaving and stored at 60 °C oven
Antibody solution	1% BSA 0.5% Triton X-100 in TBS (pH 7.5)
Aprotinin	33 mg/mL Aprotinin Dissolved in sterile H_2O
ATAC-resuspension buffer	10 mM Tris-HCl pH7.4 10 mM NaCl 3 mM $MgCl_2$ H_2O
Blocking buffer (Dissociation)	RPMI 1640 6 mL/L DNase II type V 1% (v/v) Penicillin/streptomycin
Blocking solution	10% goat serum 1% BSA 0.5% Triton-X100 In TBS
BTS solution	30 mM BTS in DMSO
Dissociation buffer	HBSS (-) calcium/magnesium 200 U/mL Collagenase II 1 mM HEPES 10 µM Y-27632 30 µM BTS
DNase solution	100 mg DNase II, type V 50 mL DPBS Filter-sterilized (0.2 µm filter)
EDTA	250 mM in H_2O NaOH adjust pH to 8
FACS buffer	DPBS

	5% (v/v) FCS
Fibrinogen	200 mg/mL Fibrinogen dissolved in pre-warmed 0.9% NaCl solution
	100 µg/mL Aprotinin
	Mixed by hand shaking at room temperature for 1 hour, then aliquoted and stored at -80 °C
HEPES stock solution	1 M HEPES
	DPBS
	Sodium hydroxide tablet for adjustment of pH to 7.4
Kranias buffer	2 mL Tris (1.5 M, pH 8.8)
	1 mL EDTA (0.5 M)
	6 mL NaF (500mM)
	15 mL SDS (20%)
	10 mL Glycerol
	Add H_2O to 100 mL
Laemmli buffer (6X)	1.2 g SDS
	6 mg Bromophenol blue
	6 g Glycerol
	1.2 mL of 0.5 M Tris (pH 6.8)
	0.93 g DTT
	Add H_2O to 10 mL
LB broth	10 g Tryptone
	5 g Yeast extract
	10 g NaCl
	H_2O top up to 1 L, adjust pH to 7.4.
	Sterilized by autoclaving
LB agar plate	15 g agar/ 1 L LB
	Sterilized by autoclaving
Papain solution	1x EBSS
	10 U/mL Papain
	1 mM EDTA
	5.5 mM L-Cystein-HCl

	Sterilized by filtering
Pluronic F-127 solution	0.1% (v/v) Pluronic F-127 in DPBS Filter-sterilized (0.2 µm filter) and stored at 4 °C
Polyvinyl alcohol (50X)	20 g polyvinyl alcohol Add H_2O to 100 mL
SDS-PAGE electrophoresis buffer (10x)	30.2 g Trizma base 144 g Glycine 10 g SDS Add H_2O to 1 L
Separation gel SDS-PAGE (10%, 10 mL)	4.8 mL H_2O 2.5 mL 40% Acrylamide 2.5 mL 1.5 M Tris pH 8.8 100 µL 10% SDS 100 µL 10% APS 4 µL TEMED
Stacking gel SDS-PAGE (10 mL)	6 mL H_2O 1.25 mL 40% Acrylamide 2.5 mL 0.5 M Tris pH 6.8 100 µL 10% (w/v) SDS 100 µL 10% (w/v) APS 10 µL TEMED
TAE buffer (50x)	242 g Trizma base 37.2 g Titriplex III (EDTA) 57.1 mL concentrated acetic acid Add H_2O to 1 L, pH 8.5
TBS (10x)	1 M Trizma base or Tris-HCl 1.5 M NaCl H_2O; pH 7.5 (adjust with 37% HCl)
Thrombin	100 U/mL Thrombin 60% (v/v) DPBS 40% (v/v) H_2O

Tyrode's solution	127 mM NaCl 4.5 mM KCl 1.5 mM MgCl$_2$ 1.8 mM CaCl$_2$ 10 mM Glucose 22 mM NaHCO$_3$ 0.42 mM Na$_2$HPO$_4$ H$_2$O, pH 7.4
Tris 0.5 M (pH 6.8)	60.6 g Trizma base Add H2O to 1 L, pH6.8
Tris 1.5 M (pH 8.8)	181.7 g Trizma base Add H2O to 1 L, pH 8.8
Western blot transfer buffer (5x)	29 g Trizma base 145 g Glycin Add H$_2$O to 2 L
Western blot transfer buffer (1x)	200 mL Western blot transfer buffer (5x) 200 mL Methonal Add H$_2$O to 1 L

10.2.9 Primers and gRNAs

Table S5: Primer pairs for qPCR

Target (gene name)	Sequence (5'-3')	Product (bp)
ACNT2	F: AAGGGGTGAAACTGGTGTCC R: AGCAGACCTTCTTTGGCAGAT	145
ACTA2	F: TGGAAAAGATCTGGCACCACT R: GGCATAGAGAGACAGCACCG	188
ATP2A2	F: ATCAGCGGGTGGCTCTTTTT R: CACCGTCAGCAGCAATGAAC	100
COL1A1	F: GGCCCAGAAGAACTGGTACA R: CGCTGTTCTTGCAGTGGTAG	200

CNN1	F: TTAAGAACAAGCTGGCCCAGAAG R: ATCTTCTTCACGGAGCCTGG	172
DDR2	F: TTTTTGGGTTGGGGAAACGC R: TCCTCAAAAACAGCTGGCCT	203
GAPDH	F: CCTCAAGATCATCAGCAATGCC R: ATGTTCTGGAGAGCCCCGC	189
GUSB	F: ACGATTGCAGGGTTTCACCA R: CACTCTCGTCGGTGACTGTT	171
IL6ST	F: CCGTCAGTCCAAGTCTTCTCAA R: GCCGCTCCTCTGAATCTAACA	64
IRX4	F: TTGAGAGGTTAAGTTGGGGTTTG R: CCACCCAATTTCTAAAACTAATTACC	281
KCNA5	F: CGAGGATGAGGGCTTCATTA R: CTGAACTCAGGCAGGGTCTC	186
KCNJ3	F: TGCCACGTGATCGATGCCAAA R: TCGAGCTTGACAAGTCATCCCAGT	129
KCNJ12	F: AGGTTGAGGCACTATGGCAC R: AGCCCGACTAGAAGAGAGCA	169
MYL2	F: GCCAACTCCAACGTGTTCTC R: TTTCACGTTCACTCGCCCAA	150
MYL7	F: CACCGTCTTCCTCACGCTCTT R: AGGCACTCAGGATGGCTTC	71
NPPA	F: GCTGCTTCGGGGGCAGGATG R: TGCAGCAGAGACCCCAGGGG	153
NPPB	F: TGCAAGGGTCTGGCTGCTTTGG R: CACTTCAAAGGCGGCCACAGGG	165
NR2F1	F: AAGCCATCGTGCTGTTCAC R: GCTCCTCAGGTACTCCTCCA	107
NR2F2	F: CCGAGTACAGCTGCCTCAA R: TTTTCCTGCAAGCTTTCCAC	91
PITX2	F: AGCCATTCTTGCATAGCTCG R: GTGTGGACCAACCTTACGGA	109
POSTN	F: GAGGCTTGGGACAACTTGGA R: ACAGTGACAACCCCATTAGGA	200

VIM	F: GCAGGAGATGCTTCAGA R: GCAGCTCCTGGATTTCCTCT	167

Table S6: Molecular cloning primers

Primer name	Sequence (5'-3')
AmpN-F	CGGGAAACCTGTCGTGCCAGCTGCATTAATGAATCGGCC
AmpN-R	GTGAGCGTGGAAGCCGCGGTATCATTGC
AmpC-F	ACCGCGGCTTCCACGCTCACCGGCTCCA
AmpC-R	GCACATCCCCCTTTCGCCAGCTGGCGTAATAGCGAAGAGGCCCG
hU6-BsmBI-sgRNA-F	GCAGAAGTATGCAAAGCATGCGAGGGCCTATTTCCCATG
hU6-BsmBI-sgRNA-R	CGAGACCCAAGGTCTCGCGATCAAAAAAGCACCGACTCG
CMV-Intein F	TGCTTTTTTGATCGCGAGACCTTGGGTCTCGGTGATGCGGTTTTGGCAG
dCsa9-EcoRV-R	CCGACGCTGTTTGTGCCGATGGCGAGCCCAATGGAGTAC
dCas9N-SalI-F	GAACCCAGACAACAGCGATGTCGACAAACTCTTTATCCAACTGG
dCas9N-BsaI-R	GAGTGATGGTTTCTTCTGATTTGCGAGTCATC
CMVenhancer-F	AGACCTTGGGTCTCGGGCATTGATTATTGACTAGTTATTAATAG
CMV-R	AAACTACCGCAATAAAGCTACTAGTACCTCTGCTTATATAGACC
FLAG-dCas9N-F	AGGGGTACCGAAGCCGCTAGCGCCACCATGGACTATAAG
FLAG-dCas9N-R	GCCCAATGGAGTACTTCTTGTCGGCTGC
dCas9N-PstI-F	CAAGAAGTACTCCATTGGGCTCGCCATC
dCas9N-PstI-R	ATTACTAAAGATCTCCTGCAGGTAGCAGATCCGATTC
cTNT-F	GGGCATTGATTATTGACTAGTCTCAGTCCATTAGGAGCCAG
cTNT-R	TACCGCAATAAAGCTACTAGTCTGCCGACAGATCCTGGAG
pAAV-CMV NdeI F	TATCTACCCGCTAGCAGGCATATGGTGATGCGGTTTTGGCAG
pAAV-CMV R	CCATGGTGGCACCTCTGCTTATATAGACCTCC
IntC F	AAGCAGAGGTGCCACCATGGCGGCGGCG

Int C dCas9 R	ACTGGGGCACGATGGCATCCACGTCGTAGTCGGAGAGC
dCas9 C F	CGTGGATGCCATCGTGCCCCAGTCTTTTC
dCas9 C R	GAATCGAGAATTTGGGCCACGTGCTTGGTGATCTGGCGTGTC
cas9 C-NLS F	TTTACTCTGACCAACTTGGGCGCGCCTGCAGCCTTCAAGTACTTC
cas9 C-NLS R	GCAGGGATCCCACCTTCCTCTTCTTCTTG
Tet1CD F	GAGGAAGGTGGGATCCCTGCCCACCTGC
Tet1CD-R	GAAGATGGACAGTCCTGTGCTCAGACCCAATGGTTATAGGGCCC
cas9C-NLS-F	TTTACTCTGACCAACTTGGGCGCGCCTGCAGCCTTCAAGTACTTC
cas9C-NLS-Gly4-R	CGCCTCCGCCCACCTTCCTCTTCTTCTTG
DNMT3A-F	GAGGAAGGTGGGCGGAGGCGGGAGCGGA
DNMT3A-R	CAGTCCTGTGCTGATATGCATCACACACACGCAAAATACTCCTTCAGCGGAGC
NdeI-pAAV-CMV-enhancer-F	TATCTACCCGCTAGCAGGCATATGGGCATTGATTATTGACTAG
NdeI-pAAV-CMV-R	AATAGGGGGCGGACTTGGCATATGATACACTTGATGTACTGC
P2A-BFP-F	GGAGTATTTTGCGTGTGTGGCCACGAACTTCTCTCTG
BFP-R	CAGTCCTGTGCTGATATGCATCAATTAAGCTTGTGCCC
T2A-puro-F	GGAGTATTTTGCGTGTGTGGAGGGCAGAGGAAGTCTTC
puro-R	CAGTCCTGTGCTGATATGCATCAGGCACCGGGCTTGCG
dCas9C-DNMT3A-F	AAAAAACCCCATCGACTTTCTCGAGGCGAAAGGATATAAAGAGGTCAAAAAG
dCas9C-DNMT3A-R	AGAAGAAGGGGCGATCATCTCCCTCCTTG
in-DNMT3A-F'	AGATGATCGCCCCTTCTTCTGGCTCTTTGCGAATG
in-DNMT3A-R	caatcatcacagggttggactcgagAAATCGCGAGATGTCCCTC

Table S7: gRNA sequence

Name	Target region	Sequence (5'-3')
Non-targeting 1	-	F: caccgACGGAGGCTAAGCGTCGCAA R: aaacTTGCGACGCTTAGCCTCCGTc
COL1A1_293Rev	Intron 1	F: caccGAGGAAAGCACGTCGAAGAT R: aaacATCTTCGACGTGCTTTCCTC
COL1A1_494Rev	Intron 1	F: caccgTCTATATCGCGCCTTGCGCT R: aaacAGCGCAAGGCGCGATATAGAc
COL1A1_718Rev	5' UTR	F: caccgCAGGAGGCACGCGGAGTGTG R: aaacCACACTCCGCGTGCCTCCTGc
COL1A1_715Rev	5' UTR	F: caccGGTTAGCGTCCGCTCATGCG R: aaacCGCATGAGCGGACGCTAACC
COL1A1_747Rev	Promoter	F: caccgCAGACGGGAGTTTCTCCTCG R: aaacCGAGGAGAAACTCCCGTCTGc
COL1A1_772Rev	Promoter	F: caccgAAGGGGCCCGGGCCAGTCGT R: aaacACGACTGGCCCGGGCCCCTTc
IL6ST-gRNA1	Promoter/exon 1	F: caccGCCACCCCAGTCCCGCGGCG R: aaacCGCCGCGGGACTGGGGTGGC
IL6ST-gRNA2	Exon 1	F: caccgATCTGACAGTGTTCCGGAGC R: aaacGCTCCGGAACACTGTCAGATc
IL6ST-gRNA3	Exon 1	F: caccgCGCACGAACCCCTTGGCGCC R: aaacGGCGCCAAGGGGTTCGTGCGc
IL6ST-gRNA4	Exon 1	F: caccGCCAAGGGGTTCGTGCGCTG R: aaacCAGCGCACGAACCCCTTGGC

Table S8: Primers for bisulfite-conversion amplification

Primer name	Sequence (5'->3')
IL6ST-For	GAGAAGGATTTGATAGTGT
IL6ST-Rev_Btn	CCTCCTCACCTCAAAC
IL6ST-For_F2	TGGGYGTAAAGGGTTTTTTAGGGGTTAATTAG
IL6ST-For_R2	CACCCRACCCCTCCTCACCTCAAAC
IL6ST-For_F1	GATAGGYGGTTATTGGATTAATGTTTGG
IL6ST-For_R1	CCCCTTAACRCCAAACTAAACCAAACCC

Table S9: Genotyping primers and Sanger sequencing primers

| Primer name	Sequence (5'->3')
Gaussia for	AACGCTGCGCGACCTTTG
EYFP rev	CGGACACGCTGAACTTGTGG
HA-L for	TCGACCTACTCTCTTCCGCA
HA-R rev	GGCTCCATCGTAAGCAAACC
HA-L rev	GTACTCGGTCATCTCGAGCC
Tet seq1 R	CTGTCTGCTCCTGTGATG
Amp-seq-F	CTGCGGCCAACTTACTTC
dCas9C-seq-F1	ATAAAAGAACTGGGGTCC
Tet-seq-F2	ATGTTGCCCGAGAATGTC
CMV-rev	AGTAGGAAAGTCCCGTAAGG
U6-fwd	GAGGGCCTATTTCCCATGATTCC

10.3 Supplementary figures and tables
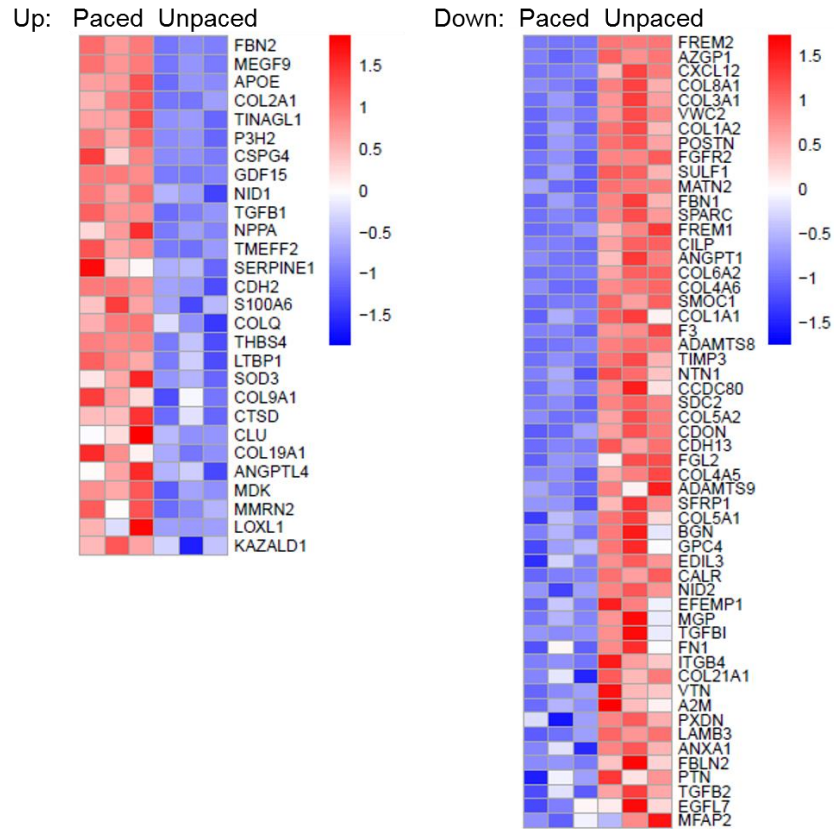
Figure S1: DE genes in collagen-containing extracellular matrix between by Gene Ontology terms analysis. Left: upregulated genes. Right: downregulated genes.

Table S10: Cloning information of dCas9C constructs

Plasmid	Insert		Vector	
	Primer	Template	Backbone	RE
pAAV-cTNT-dCas9C-DNMT3A	cTNT-F cTNT-R	pVC525-pGG2-cTnT-HA-TTL	pAAV-SMVP-dCas9C-DNMT3A	SpeI
pAAV-SMVP-dCas9C-DNMT3A-2ABFP	P2A-BFP-F BFP-R	pFuw-dCas9-Tet1CD-P2A-tagBFP	pAAV-SMVP-dCas9C-DNMT3A	BsaBI
pAAV-SMVP-dCas9C-DNMT3A-2Apuro	T2A-puro-F puro-R	pVC178-pSico-Ef1a-RIP1-2Apuro	pAAV-SMVP-dCas9C-DNMT3A	BsaBI

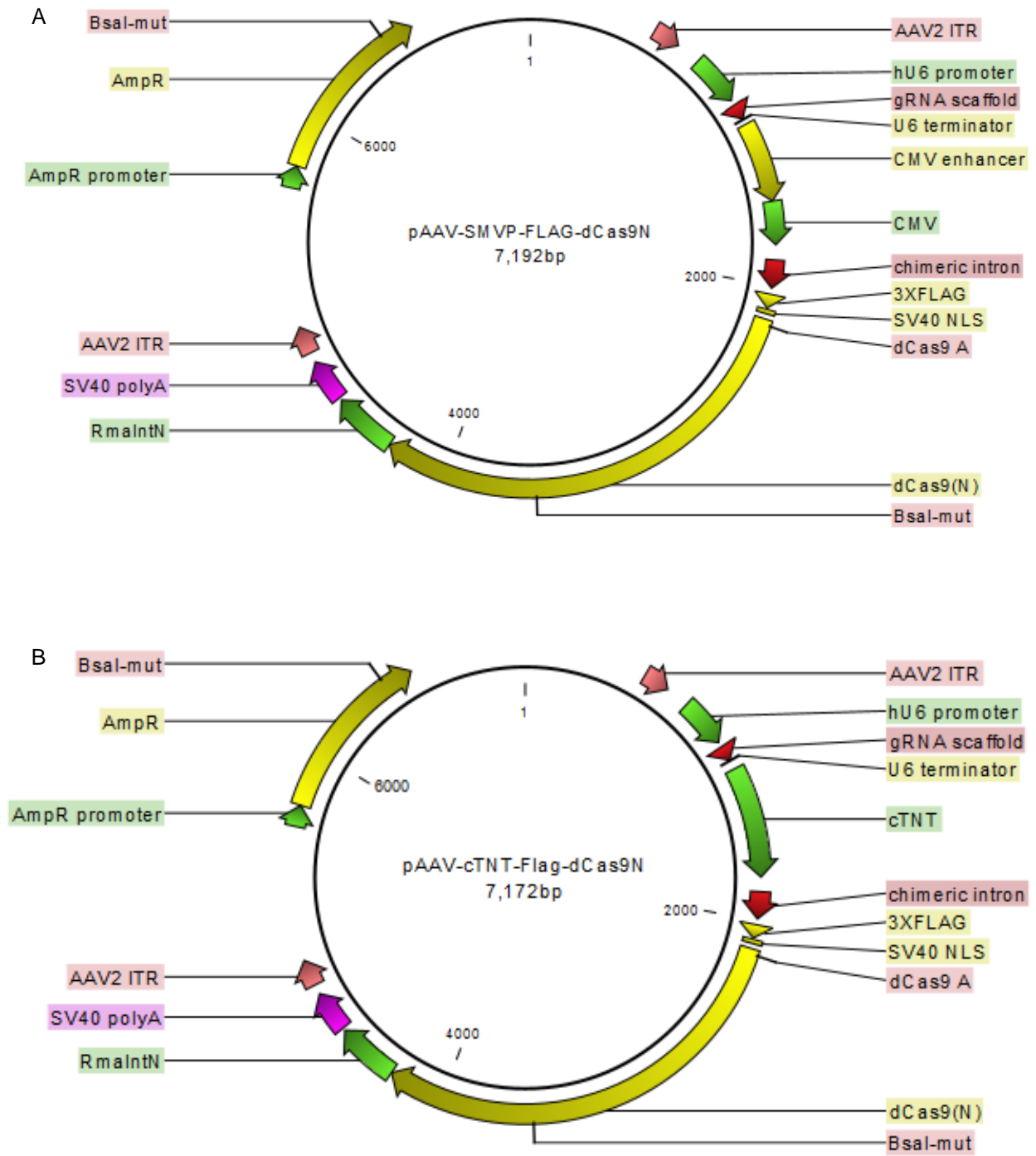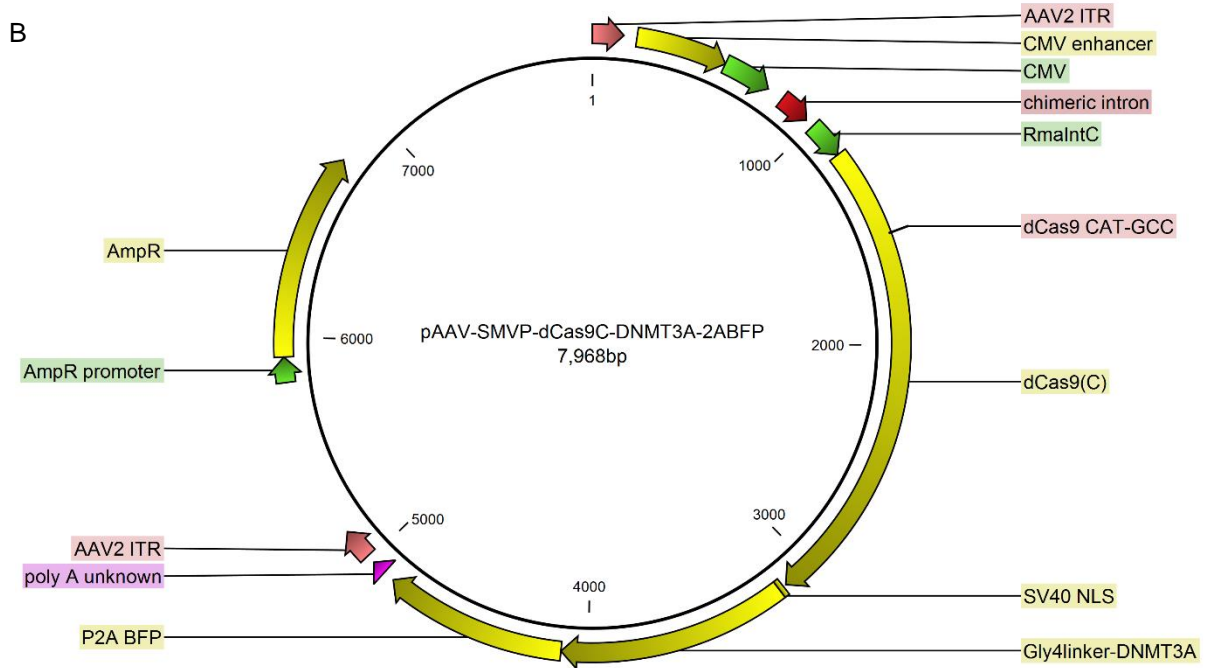| PAav-SMVP-dCas9C-inactiveDNMT3A-2Apuro | dCas9C-DNMT3A-F | pSMVP-dCas9C-gly4DNMT3A | pSMVP-dCas9C-gly4DNMT3A-2Apuro | XhoI |
	dCas9C-DNMT3A-R			
	in-DNMT3A-F'			
	in-DNMT3A-R			

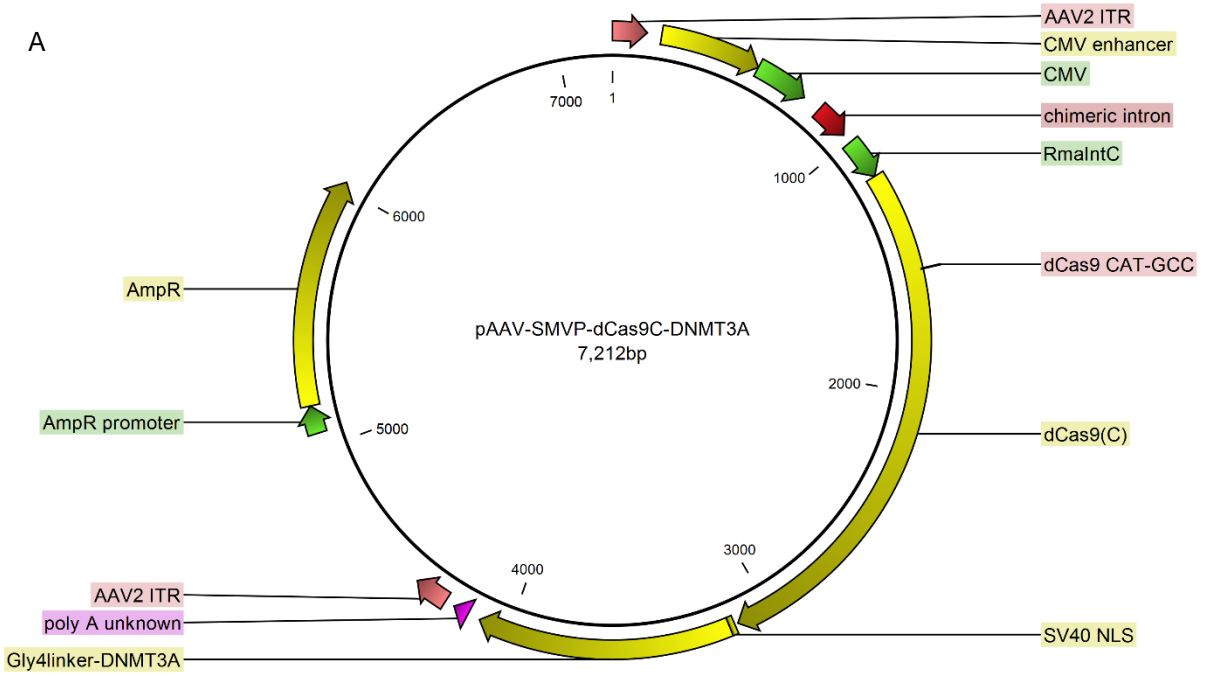**Figure S2: Maps of split-dCas9N plasmids.** (A) pAAV-SMVP-FLAG-dCas9N. (B) pAAV-cTNT-FLAG-dCas9N.

A

pAAV-SMVP-dCas9C-DNMT3A
7,212bp

- AAV2 ITR
- CMV enhancer
- CMV
- chimeric intron
- RmaIntC
- dCas9 CAT-GCC
- dCas9(C)
- SV40 NLS
- AmpR
- AmpR promoter
- AAV2 ITR
- poly A unknown
- Gly4linker-DNMT3A

B

pAAV-SMVP-dCas9C-DNMT3A-2ABFP
7,968bp

- AAV2 ITR
- CMV enhancer
- CMV
- chimeric intron
- RmaIntC
- dCas9 CAT-GCC
- dCas9(C)
- SV40 NLS
- Gly4linker-DNMT3A
- AmpR
- AmpR promoter
- AAV2 ITR
- poly A unknown
- P2A BFP

C

pAAV-SMVP-dCas9C-DNMT3A-2Apuro
7,863bp

- AAV2 ITR
- CMV enhancer
- CMV
- chimeric intron
- RmaIntC
- dCas9 CAT-GCC
- dCas9(C)
- SV40 NLS
- Gly4linker-DNMT3A
- T2A Puro
- poly A unknown
- AAV2 ITR
- AmpR promoter
- AmpR

D

pAAV-SMVP-dCas9C-inactiveDNMT3A-2Apuro
7,863bp

- AAV2 ITR
- CMV enhancer
- CMV
- chimeric intron
- RmaIntC
- dCas9 CAT-GCC
- dCas9(C)
- SV40 NLS
- Gly4linker-inactive DNMT3A
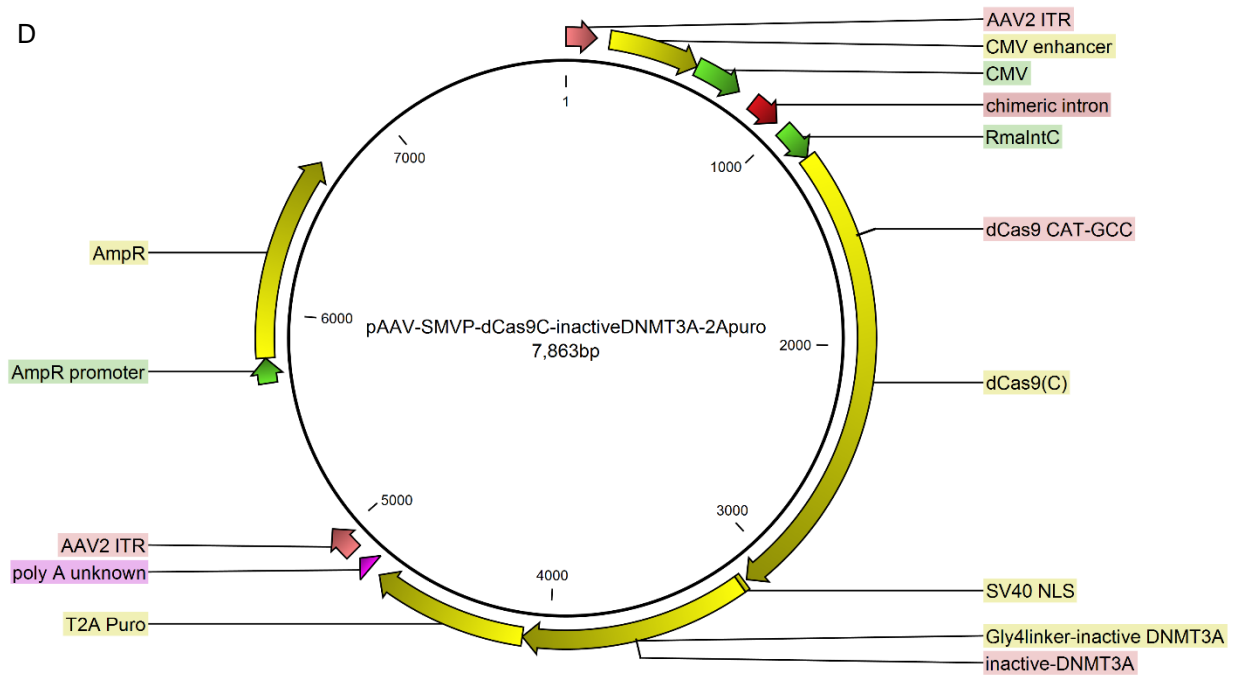- inactive-DNMT3A
- T2A Puro
- poly A unknown
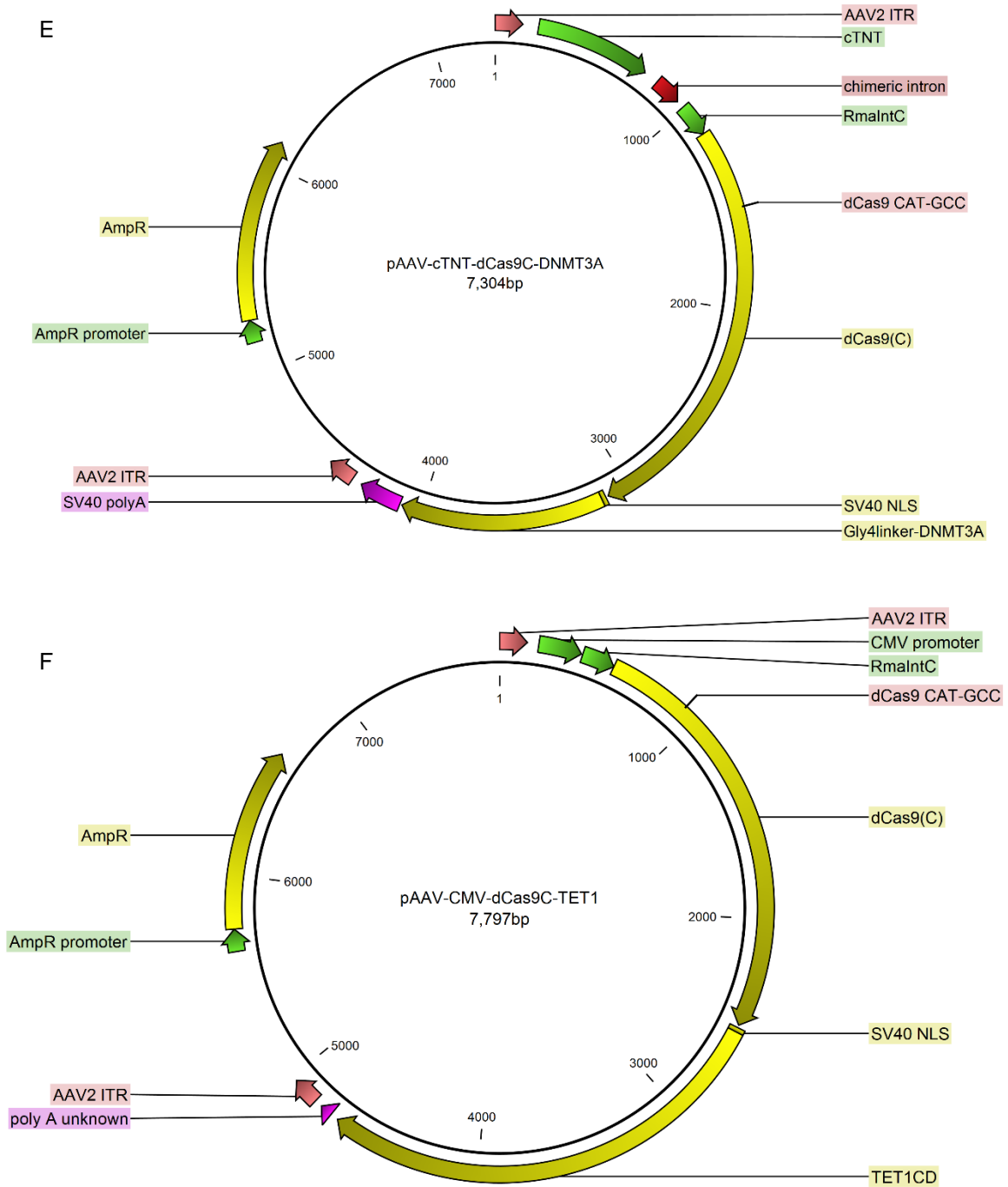- AAV2 ITR
- AmpR promoter
- AmpR

Figure S3: Maps of split-dCas9C plasmids. (A) pAAV-SMVP-dCas9C-DNMT3A. (B) pAAV-SMVP-dCas9C-DNMT3A-2ABFP. (C) pAAV-SMVP-dCas9C-DNMT3A-2Apuro. (D) pAAV-SMVP-dCas9C-inactiveDNMT3A-2Apuro. (E) pAAV-cTNT-dCas9C-DNMT3A. (F) pAAV-CMV-dCas9C-TET1.

11 Acknowledgments

I am incredibly grateful for all the support of many people I have received along the way. This thesis would not have been possible without their help. I sincerely apologise for not being able to personally mention every name here.

First, I would like to express my heartfelt gratitude to supervisors. I want to thank Prof. Thomas Eschenhagen for selflessly sharing his experience and knowledge with me and thank Prof. Elke Oetjen for supervising my doctoral thesis on behalf of the Department of Chemistry. My sincere thanks also go to Dr. Justus Stenzig for giving me the opportunity to pursue a doctoral degree, supervising my work and providing all the support during the last 3.5 years.

Special thanks are addressed to colleagues from AG Stenzig. I am also very grateful to be able to work together with everyone else from the institute who offered help whenever I needed it. I would like to highlight the contribution of colleagues from the institute: Grit Höppner for gene expression analysis, Dr. Torsten Christ for his expertise in electrophysiology, Thomas Schulze and Birgit Klampe for the support of stem cell culture and differentiation, Dr. Florian Weinberger and Dr. Tim Stüdemann for providing the CRISPR cell line, June Uebeler and Anna Steenpass for mycoplasma test. Additionally, I would like to thank many people from other laboratories in the UKE: Mouse Pathology Core Facility for immunohistochemistry analysis, Vector Core Facility and Stem Cell Transplantation Research for providing virus, NanoString Core Facility and the Institute of Human Genetics for karyotyping, Molecular Cardiology for troponin I assay.

I am very grateful to my previous colleagues from National University of Singapore and Genome Institute of Singapore. I appreciate the 4-years scientific training in Prof. Dr. Roger Foo's laboratory before my doctoral study and thank for his continuous support for my doctoral thesis. I would also like to thank Dr. George Anene-Nzelu, Dr. Mick Lee and Dr. Zhu Yike for their help with next-generation sequencing, and Dr. Matias Autio for the help with split dCas9 plasmids.

I would like to thank Julius Hansen from University of Vienna and Sarcura GmbH for his scientific input for the optical device and optical pacing. Another big thank goes to Dr. Wen Wang from Tong Ji University in Shanghai for analysing ATACseq data.

最后，我要感谢我挚爱的家人，我的爷爷奶奶、爸爸妈妈、姐姐和哥哥，感谢他们一直以来支持我在海外求学。由于疫情影响，我已经两年半没有见过他们，深感愧疚，感谢他们的理解和在背后默默的付出，在此，祝愿他们身体健康。

12 Declaration of on Oath

I hereby declare on oath that this doctoral thesis entitled

"Atrial fibrillation modelling and targeted DNA methylation editing in human engineered heart tissue-based disease models"

is written independently and solely by my own based on the original work of my PhD and has not been sued other than the acknowledged resources and aids. The submitted version corresponds to the version on the electronic storage medium. I declare that the present dissertation was prepared maintaining the Rules of Good Scientific Practice of the German Research Foundation and it has never been submitted in the present form or similar to any other University or board of examiners.

Hamburg, 15.12.2022   Pan, Bangfen

Hiermit versichere ich an Eides statt, die vorliegende Dissertation mit dem Titel

"Atrial fibrillation modelling and targeted DNA methylation editing in human engineered heart tissue-based disease models"

selbst verfasst und keine anderen als die angegebenen Hilfsmittel benutzt zu haben. Die eingereichte schriftliche Fassung entspricht der auf dem elektronischen Speichermedium. Ich versichere, dass diese Dissertation nicht in einem früheren Promotionsverfahren eingereicht wurde."

Hamburg, den 15.12.2022   Pan, Bangfen